MAX PLANCK INSTITUTE
FOR POLYMER RESEARCH

JOHANNES GUTENBERG
UNIVERSITÄT MAINZ

Synthesis of Bioresponsive Peptides for Controlled Intracellular Structure Formation

Dissertation

zur Erlangung des Grades

Doctor rerum naturalium (Dr. rer. nat.)

der Fachbereiche:
08 - Physik, Mathematik und Informatik
09 - Chemie, Pharmazie und Geowissenschaften,
10 – Biologie,
Universitätsmedizin
der Johannes Gutenberg-Universität Mainz

Sarah Chagri
geboren in Köln

Mainz, Oktober 2024

Max Planck Graduate Center
mit der Johannes Gutenberg-Universität

First Reviewer [redacted]

Second Reviewer [redacted]

Date of defense: December 5, 2024

This work was carried out at the Max Planck Institute for Polymer Research in the research group of Prof. Dr. Tanja Weil from July 2020 to October 2024.

In accordance with § 11 (4) of the doctoral regulations dated May 26, 2009:

I hereby declare that I wrote the dissertation submitted without any unauthorized external assistance and used only sources acknowledged in the work. All textual passages which are appropriated verbatim or paraphrased from published and unpublished texts as well as all information obtained from oral sources are duly indicated and listed in accordance with bibliographical rules. In carrying out this research, I complied with the rules of standard scientific practice as formulated in the statutes of Johannes Gutenberg University Mainz to ensure standard scientific practice.

Mainz, October 2024 

Sarah Chagri

Acknowledgement

[redacted]

[redacted]

Abstract

The development of bioresponsive nanomaterials for intracellular assembly addresses the challenge of creating synthetic structures within living cells, enabling the modulation of cellular processes and behaviors. This thesis explores the design, synthesis and characterization of bioresponsive isopeptides for the *in situ* construction of intracellular nanostructures and investigates their impact on cellular functions.

Isopeptides are a class of programmable assembly precursors. Their kinked, non-linear structure, which arises from an ester bond at a serine side chain instead of the conventional amide linkage, effectively prevents premature peptide assembly. Introducing a bioresponsive protecting group at the serine amino function allows for the triggered rearrangement of the isopeptide into a linear, self-assembling peptide in response to a specific physiological stimulus. This chemical design strategy provides control over the assembly process within complex cellular environments.

Within this thesis, the development of glutathione-responsive isopeptides for intracellular assembly is presented, including their application for synthetic structure formation in human cytotoxic T cells. These peptide nanostructures were found to enhance T cell effector function, significantly increasing the cytotoxic activity of T cells against cancer cells. Correlative light and electron microscopy confirmed the presence of synthetic peptide assemblies within the cytosol and perinuclear region of T cells. Additionally, real-time deformation cytometry revealed increased cell stiffness and reduced deformability, critical parameters for effective interactions with target cells. Further analysis demonstrated that T cells treated with these isopeptides exhibited an altered protein phosphorylation profile of signaling proteins associated with cellular activation. These findings suggest that

synthetic intracellular nanostructures can modulate T cell behavior and enhance their activity, highlighting their potential for advancing immunotherapeutic strategies.

Furthermore, the impact of the glutathione-responsive isopeptides on drug-resistant MDA-MB-231 breast cancer cells was examined, focusing on their effects on mitochondrial function. Live-cell imaging and oxygen consumption measurements assessed how peptide assembly formation disrupts mitochondrial integrity and respiration. This study also employed a three-dimensional tumor spheroid model, revealing that intracellular peptide assembly resulted in reduced spheroid size due to increased cell death. This approach provided insights into the effects of peptide structures in a three-dimensional cellular network, better mimicking in vivo tumor conditions.

Additionally, the thesis presents the development of an enzyme-responsive kinked isopeptide designed for controlled nanostructure formation through proteolytic transformation. The protease furin effectively cleaves the kinked isopeptide, leading to its rearrangement into a linear peptide capable of forming fibrillar nanostructures. This isopeptide-based system demonstrates the potential of enzyme-mediated transformation for creating supramolecular nanostructures.

In summary, this thesis highlights the versatility of bioresponsive isopeptides as precursors for intracellular structure formation and their potential in modulating cellular functions and behaviors.

Zusammenfassung

Die Entwicklung bioresponsiver Nanomaterialien für die intrazelluläre Assemblierung zielt darauf ab, synthetische Strukturen innerhalb lebender Zellen zu schaffen und damit Zellprozesse und -verhalten zu beeinflussen. Diese Dissertation behandelt das Design, die Synthese und die Charakterisierung bioresponsiver Isopeptide für die *in situ* Bildung intrazellulärer Nanostrukturen und untersucht deren Auswirkungen auf die Funktionen menschlicher Zellen.

Isopeptide sind eine Klasse programmierbarer Assemblierungsvorläufer. Ihre geknickte, nicht-lineare Struktur, die durch eine Esterbindung an der Serin-Seitenkette anstelle der konventionellen Amidbindung entsteht, verhindert effektiv eine vorzeitige Peptidassemblierung. Die Einführung einer bioresponsive Schutzgruppe an der Aminogruppe des Serins ermöglicht die durch einen spezifischen physiologischen Stimulus ausgelöste Umlagerung des Isopeptids in ein lineares, selbstassemblierendes Peptid. Diese chemische Designstrategie erlaubt die Kontrolle über den Assemblierungsprozess in komplexen zellulären Umgebungen.

Im Rahmen dieser Dissertation wird zunächst die Entwicklung glutathion-sensitiver Isopeptide für die intrazelluläre Assemblierung vorgestellt, sowie deren Anwendung zur Bildung synthetischer Strukturen in menschlichen zytotoxischen T-Zellen. Die Ergebnisse dieser Untersuchung zeigten, dass die Peptid-Nanostrukturen die T-Zell-Effektor-Funktion verbessern und somit die zytotoxische Aktivität gegen Krebszellen steigern. Durch korrelative Licht- und Elektronenmikroskopie sowie Konfokalmikroskopie konnten die synthetischen Peptidstrukturen im Zytosol und in der perinukleären Region der T-Zellen visualisiert werden. Zusätzlich zeigten Messungen mittels Echtzeit-Deformations-Zytometrie eine erhöhte Zellsteifigkeit und reduzierte Verformbarkeit der T-Zellen, was für effektive Interaktionen mit Zielzellen entscheidende Faktoren sind. Weitere Analysen zeigten, dass T-Zellen mit

intrazellulären synthetischen Peptidstrukturen eine erhöhte Phosphorylierung von Signalproteinen aufwiesen, welche mit der T-Zellaktivierung in Verbindung stehen. Die Ergebnisse dieser Studie deuten darauf hin, dass synthetische intrazelluläre Nanostrukturen die T-Zell-Aktivität verbessern können, was bedeutende Implikationen für die Weiterentwicklung der Immuntherapie haben könnte.

Des Weiteren wurde der Effekt der glutathion-sensitiven Isopeptide auf hochinvasive metastasierende MDA-MB-231-Brustkrebszellen untersucht, wobei der Schwerpunkt auf der Untersuchung der Auswirkungen der Nanostrukturbildung auf die mitochondriale Funktion lag. Lebendzell-Imaging und Messungen des Sauerstoffverbrauchs zeigten, wie die intrazelluläre Peptidassemblierung die mitochondriale Integrität und Atmung stört. Die Untersuchung wurde ergänzt durch ein dreidimensionales Tumorsphäroid-Modell, bei dem die intrazelluläre Peptidassemblierung zu einer Verringerung der Sphäroidgröße aufgrund erhöhten Zelltods führte. Dieser Ansatz ermöglichte Einblicke in die Effekte der synthetischen Peptidstrukturen in einem dreidimensionalen Zellnetzwerk, das die physiologischen Bedingungen von Tumoren realistischer nachahmt.

Zusätzlich behandelt diese Arbeit die Entwicklung eines enzym-sensitiven Isopeptids für die kontrollierte Bildung von Nanostrukturen durch proteolytische Transformation. Das Enzym Furin schneidet das enzym-responsive Isopeptid trotz seiner geknickten Struktur effektiv. Dies führt zur Umlagerung des freien Isopeptids in ein lineares Peptid, das fibrilläre Nanostrukturen ausbilden kann. Dieses Isopeptid-basierte System zeigt das Potenzial enzymkatalysierter molekularer Transformation zur Bildung supramolekularer Nanostrukturen.

Zusammenfassend hebt diese Dissertation die Vielseitigkeit bioresponsiver Isopeptide als Vorläufermoleküle für die intrazelluläre Strukturbildung hervor und

unterstreicht deren Potenzial zur Modulation von zellulären Funktionen und Verhalten.

Contents

1. Introduction

Section 1.1. has been reproduced, with changes, from 'Chagri, S., Ng, D. Y. W. & Weil, T. Designing bioresponsive nanomaterials for intracellular self-assembly. *Nat. Rev. Chem.* **6**, 320–338 (2022).'

1.1. Designing bioresponsive nanomaterials for intracellular self-assembly

In nature, the formation of functional structures through the assembly of smaller units can be observed over several structural hierarchies at the macroscopic, microscopic and nanoscopic scales. While spiderwebs are tangible examples of natural constructs built for specific function, eukaryotic cells reveal that similar phenomena also exist on a molecular level: for instance, the cytoskeleton is made from various dynamic protein assemblies that form intricate networks inside the cell, ensuring cellular stability, motility and division[1]. Mimicking these naturally occurring structures by integrating synthetic self-assembled nanostructures in a biological context is an important milestone in supramolecular chemistry, as these systems expand the boundaries of both nanomedicine and synthetic biology. Additionally, the bottom-up approach of creating non-natural assemblies inside cells could help to elucidate molecular mechanisms of naturally occurring cellular processes and provide the foundation to unravel the origin of life[2].

Regarding the potential of synthetic supramolecular nanostructures for therapeutic applications[3], a major appeal is the circumvention of limitations that small molecule

drugs face, such as drug resistance in cancer cells[4]. In contrast to small molecules, systems capable of intracellular self-assembly can form large aggregates inside cells, which forces their accumulation at the target site[5], resulting in improved pharmacokinetics. Additionally, the process of self-assembly can cause mechanical stress due to the disruption of cellular structures, thus, triggering cell death[6]. By instilling bioresponsiveness – in which molecules react to physiological cues – in the design of the assembly precursor, its conversion to an active self-assembling monomer can be precisely tailored to a specific nanoenvironment or microenvironment in the cell. Targeted intracellular stimuli include those that have been widely exploited in state-of-the-art prodrugs and delivery systems, such as pH (refs[7-11]), redox[6,12-15] or enzymes[16-22], in which the respective stimulus is often characteristic for a certain subcellular location (Fig. 1.1). As the considerations to program nanostructure formation within cells are multifaceted, we aim to streamline the design concepts to create greater accessibility and understanding for the scientific community. In this section, we showcase successful molecular design principles to control the assembly of functional nanostructures within mammalian cells, which are triggered by endogenous stimuli.

1.1.1. Cellular compartments as reaction vessels

The eukaryotic cell is an intricate machinery made of lipids, proteins and genetic material, all forming supramolecular structures in an aqueous environment, while dynamic chemical crosstalk between organelles and the extracellular space governs internal processes[23]. The living cell is a non-equilibrium system characterized by compartmentalization and the energy-dependent maintenance of concentration gradients that are essential for proliferation and function[24]. As cellular compartments fulfil different tasks within the cell, they often provide distinct

(bio)chemical environments, such as a certain pH, redox environment, level of molecular crowding or the presence of specific enzymes[23] (Fig. 1.1).

From a chemist's perspective, cellular compartments with their distinct characteristics are analogous to a system of interconnected reaction vessels, each offering different reaction conditions for chemical transformations. When designing synthetic materials for intracellular self-assembly, a knowledge of cell biology is essential to understand and exploit structure-(bio)activity relationships. In terms of molecular design, this means carefully choosing the respective functional groups and other components, such as enzyme recognition sites, to implement selectivity towards a biological or chemical stimulus associated with a target subcellular location. For example, the decrease in pH associated with the endocytic pathway can be exploited by using pH-sensitive materials that can undergo supramolecular transformations inside the acidic endosomal or lysosomal environments due to protonation or isomerization[7-11]. Similarly, the reducing medium of the cytosol can induce the chemical conversion of reduction-sensitive precursors into active monomers upon cell entry[12,15], while the higher concentration of reactive oxygen species (ROS) near the mitochondria can lead to oxidation-driven self-assembly in the vicinity of these organelles[14].

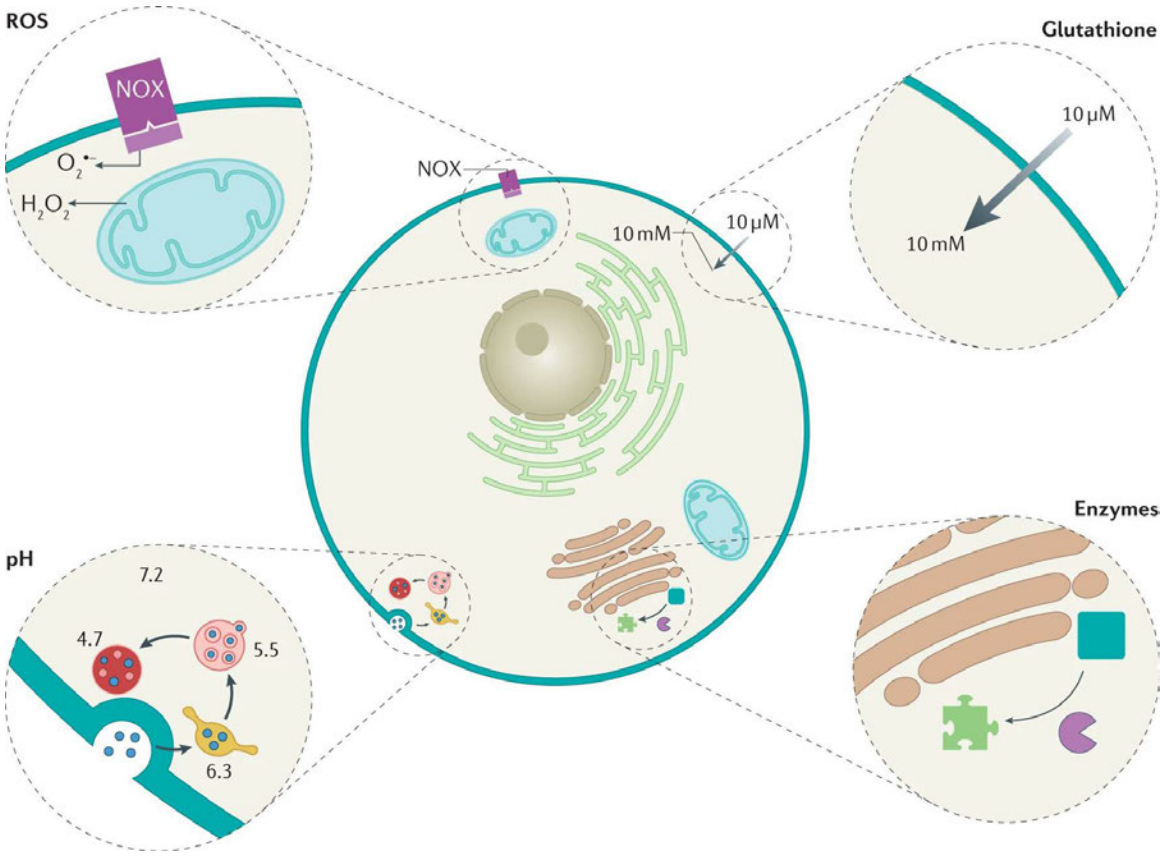

Figure 1.1 The eukaryotic cell and its compartments as interconnected reaction vessels. The conditions for chemical transformation of bioresponsive nanomaterials in terms of pH, redox environment and enzyme catalysis differ widely, depending on the subcellular location. While reactive oxygen species (ROS) are mainly generated in the mitochondria[25], as well as, to a lesser degree, by the membrane-bound NADPH oxidase (NOX)[26], the cellular reducing agent glutathione is present in high concentration (10 mM) throughout the cytosol[27]. During the endocytic pathway, the pH inside the vesicles decreases significantly from 6.3 in the early endosomes to 5.5 in the late endosomes to 4.7 in the lysosomes, whereas the cytosolic pH is typically neutral, at around 7.2 (ref.[28]). The localization of enzymes within the cells depends on their respective biocatalytic function, meaning that they are often associated with specific organelles.

Besides the influence of different reaction conditions associated with intracellular location, the cell type also affects the efficiency of chemical transformations, as cells from different tissues have evolved to behave in specific ways that contribute to the survival of the whole organism. For example, liver cells, which are in charge of detoxification, display a comparatively high cytosolic concentration of glutathione, a cellular antioxidant and nucleophile essential for scavenging harmful electrophilic compounds and ROS[29]. Moreover, the gene expression profile of cells also varies depending on the tissue, which includes the expression levels of certain enzymes, such as proteases, that catalyze biochemical transformations.

Alterations in the genetic code can cause cells to cease following expected patterns and instead start displaying an opportunistic, self-serving behaviour targeted at sustained growth and evasion of cell death[30]. These cancerous cells can emerge from different tissues and often show an upregulation of pro-proliferative and pro-angiogenic factors, as well as an elevated cellular metabolism[31]. While cancer cells are not uniform in their biological and chemical characteristics, there are some common properties of aggressively growing cancers, for example: the acidification of the tumour extracellular microenvironment because of their enhanced glycolytic rate, a tendency to develop low oxygen level in tissue, called hypoxia, due to limited oxygen supply inside the tumour and the overexpression of certain proteases that aid cell invasion and metastasis[30]. Regarding the great challenges associated with drug-resistant cancers, upregulated efflux pumps, such as P-glycoprotein[32], and elevated glutathione levels in the cytosol[33] play critical roles in treatment failure due to drug inactivation and efficient removal. Therefore, in addition to using targeting moieties that are recognized by specific cell surface receptors, the aforementioned distinct features of cancerous cells can facilitate the design of novel cancer-specific drugs or imaging agents with less toxic side effects on healthy cells or tissue[34]. Consequently, these considerations are also relevant for controlling the bioresponsive formation of synthetic nanostructures within cancer cells, which offers entirely new avenues to potentially revolutionize bioimaging and cancer therapy.

1.1.2. Nanomaterials for intracellular self-assembly

Creating synthetic supramolecular assemblies in a biological environment requires molecular design strategies that fulfil necessary criteria regarding biocompatibility, environmental responsiveness and the propensity for self-assembly within crowded and complex environments. For instance, the assembly precursor must enter cells without premature disruption of cellular functions or causing cell death, since a

lack of biocompatibility at this stage would impede the formation of nanostructures at the desired cellular location. Efficient cell uptake of the precursor can be achieved by including structural elements that promote cell entry in the molecular design, such as cell-penetrating peptides (CPPs)[6,8] or ligands of certain cell surface receptors[5,35,36]. CPPs comprise 40 or less amino acids and they can be conjugated covalently or non-covalently to cargo to facilitate their delivery into the cell[37,38]. Besides direct translocation into the cytosol as a result of attractive electrostatic interaction with the negatively charged plasma membrane[38], CPPs and their conjugates can also be internalized through various endocytic pathways[39]. While some aspects of the cell uptake mechanisms remain elusive, prominent examples of cationic CPPs such as the HIV-derived peptide transactivator of transcription or polyarginine peptides have been shown to enter cells through a variety of pathways, depending on the cell type and the conjugated cargo[40-42]. However, using CPPs for intracellular delivery of assembly precursors can come with the limitation of lacking cell selectivity, whereas the introduction of certain ligands for receptor-mediated endocytosis can tailor the system towards a more targeted effect[5,35,36]. For example, the tripeptide RGD serves as a recognition motif for integrin cell surface receptors, such as αvβ3, which are overexpressed in many cancer cells[43]. Therefore, assembly precursors that are modified with the linear or cyclic version of the targeting peptide have been employed for cancer-specific targeting both in vitro[10,35,36] and in vivo[5].

For the in vivo application of nanomaterials for intracellular structure formation, achieving tissue selectivity by active or passive targeting is one of the key objectives. Besides the use of tumour-specific recognition motifs[44], the so-called enhanced permeability and retention effect in solid tumours with high vascular density and high endothelial permeability[45] contributes to the passive accumulation of macromolecular precursors at the desired location[12]. In general, the administration

of compounds for intracellular self-assembly comes with similar challenges in terms of pharmacokinetics and immunogenicity as observed for small molecule drugs[44]; however, these pro-assembling systems can possess greater selectivity and avoid affecting healthy cells. This is due to the bioresponsive mode of action of the assembly precursors, which require the presence of a specific stimulus inside the cells and confines the assembly formation to the intracellular space[44,46].

Within the cell, the activated self-assembling monomer resulting from intracellular chemical conversion needs to display a critical aggregation concentration that is sufficiently low for self-assembly under physiological conditions, which is usually in the micromolar range[9,47]. The critical aggregation concentration of the active monomer is determined by the self-assembly propensity of the material, which is based on attractive intermolecular interactions. Since the intracellular environment displays a high degree of macromolecular crowding due to, for example, soluble proteins, densely packed filamentous structures and phase-separated components, this increases diffusional obstacles and further enhances the inherent aggregation tendency of the monomers[48,49]. However, this abundance of biomacromolecules with reactive groups, such as proteins with surface-exposed cysteines[50], as well as other ubiquitous molecules such as glutathione[27] or ROS[51], mandates the need for biorthogonality of the assembly precursor to prevent unwanted interactions. This biorthogonality is also important for achieving spatial control over the subcellular structure formation, which can additionally be aided by introducing organelle-specific targeting groups to the precursor that ferry the pro-assembling material through the cellular environment to the desired compartment[52].

Generally, there are four material classes that are commonly used for intracellular self-assembly: peptides, polyaromatic compounds, polymers and metal nanoparticles (Fig. 1.2). While there are only a few examples of polymers[14,53] or metal nanoparticles[54-56] that have shown intracellular structure formation, many

peptide-based and polyaromatic materials readily undergo stimuli-responsive self-assembly in cellular environments, providing new perspectives for diagnostic or therapeutic applications.

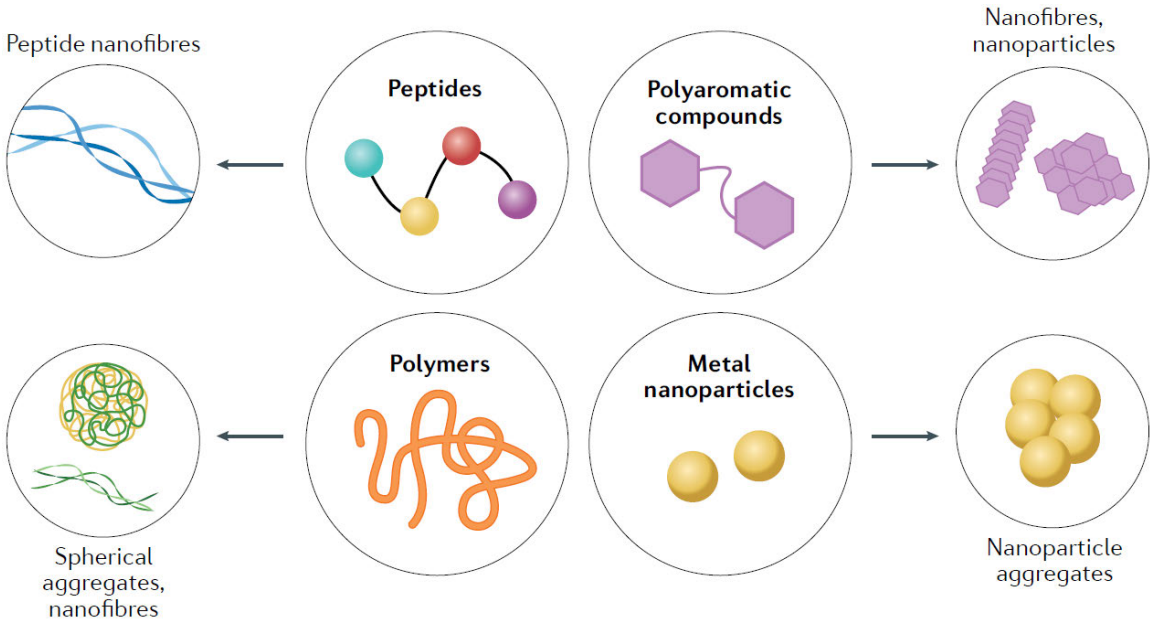

Figure 1.2 Material classes for intracellular self-assembly. Peptides represent the largest subset of nanomaterials for intracellular structure formation and can self-assemble into peptide nanofibres due to hydrogen bonding and π-π stacking caused by aromatic amino acid residues[35]. In the case of peptide amphiphiles, hydrophobic interactions of alkyl chains also contribute to the self-assembly propensity[57,58]. Polyaromatic compounds form fibrous structures or nanoparticles because of aromatic interactions between the monomers[9,59-64]. Polymers, such as polyvinyl alcohol, transform into spherical aggregates or fibres[14,53], whereas metal nanoparticles can aggregate into larger assemblies due to covalent crosslinking of their coating[54-56]

Peptides, more specifically, β-sheet forming so-called amyloid-like peptides, constitute one of the most popular scaffold materials: they are characterized by amphiphilicity caused by an alternating sequence pattern of polar and nonpolar amino acids, which supports the intermolecular hydrogen bonding necessary for adopting β-sheet secondary structures[65]. Moreover, they usually display a high content of aromatic amino acids, such as phenylalanine, required for self-assembly due to π-π stacking and van der Waals interactions[49,66]. Often, an aromatic moiety or fluorophore at the amino terminus further adds to their π-π stacking tendency, supporting their assembly into stable nanostructures[65]. For instance, certain peptides can form ordered β-sheet-rich nanofibres of a few nanometers in width and

micrometers in length that show similarities to naturally occurring β-amyloid aggregates present in various neurodegenerative illnesses, such as Alzheimer disease[65]. Amphiphilic peptide conjugates are another subcategory of peptide-based nanomaterials consisting of a peptide sequence prone to hydrogen bonding and a nonpolar alkyl chain (fatty acid) engaging in hydrophobic interactions. Because of their fast assembly into dynamic but stable nanostructures and their gelation propensity[67], these biocompatible amphiphilic conjugates have been studied extensively for various medical applications, including tissue regeneration[68] and wound healing[69]. Besides extracellular applications, their potential for intracellular structure formation and gelation has been used for enzyme-responsive and pH-responsive self-assembly inside cancer cells[57,58].

Polyaromatic compounds can form intracellular aggregates because of π-π aromatic interactions within the aqueous cytoplasm, which has been exploited for the creation of supramolecular imaging agents[15] and drugs for photodynamic therapy[36]. Prominent examples include bispyrene-based systems that rely on the formation of highly fluorescent *J*-aggregates[59,60] and luminogens that display aggregation-induced emission (AIE) properties[61-64]. Aside from fluorophores and AIE luminogens that display a constant number of aromatic rings both in the precursor and in the self-assembling monomer, there are also systems that rely on the intracellular formation of new aromatic units due to chemical transformation. For instance, the intracellular condensation reaction between a deprotected aminothiol and an aromatic nitrile can be used to generate self-assembling aminoluciferin-based macrocycles inside cells[9,70]. This approach relies on the intracellular creation of polyaromatic cyclic oligomers that can self-assemble into fluorescent nanoaggregates via π-π stacking[9].

Stimuli-induced chemical transformations yielding a self-assembling monomer can be grouped by different levels of complexity, depending on the length of the reaction

sequence (Fig. 1.3). Generally, the molecular design concepts for bioresponsive self-assembly can be divided into three categories: structures that undergo a purely morphological transformation (Fig. 1.3a), pro-assembling monomers that transform into active monomers due to the removal of a hydrophilic group (Fig. 1.3b) and molecules that rely on the bioresponsive deprotection of reactive groups causing a multistep reaction cascade (Fig. 1.3c). While the macrocyclization-based systems fit the last category, the most common strategy for controlled intracellular self-assembly uses the chemical or enzymatic removal of a hydrophilic unit to trigger the aggregation of the remaining less polar fragment. By contrast, purely morphological transformations comprise systems that do not require the breakage of chemical bonds to transform into active monomers but instead rely on pH-induced isomerization or protonation.

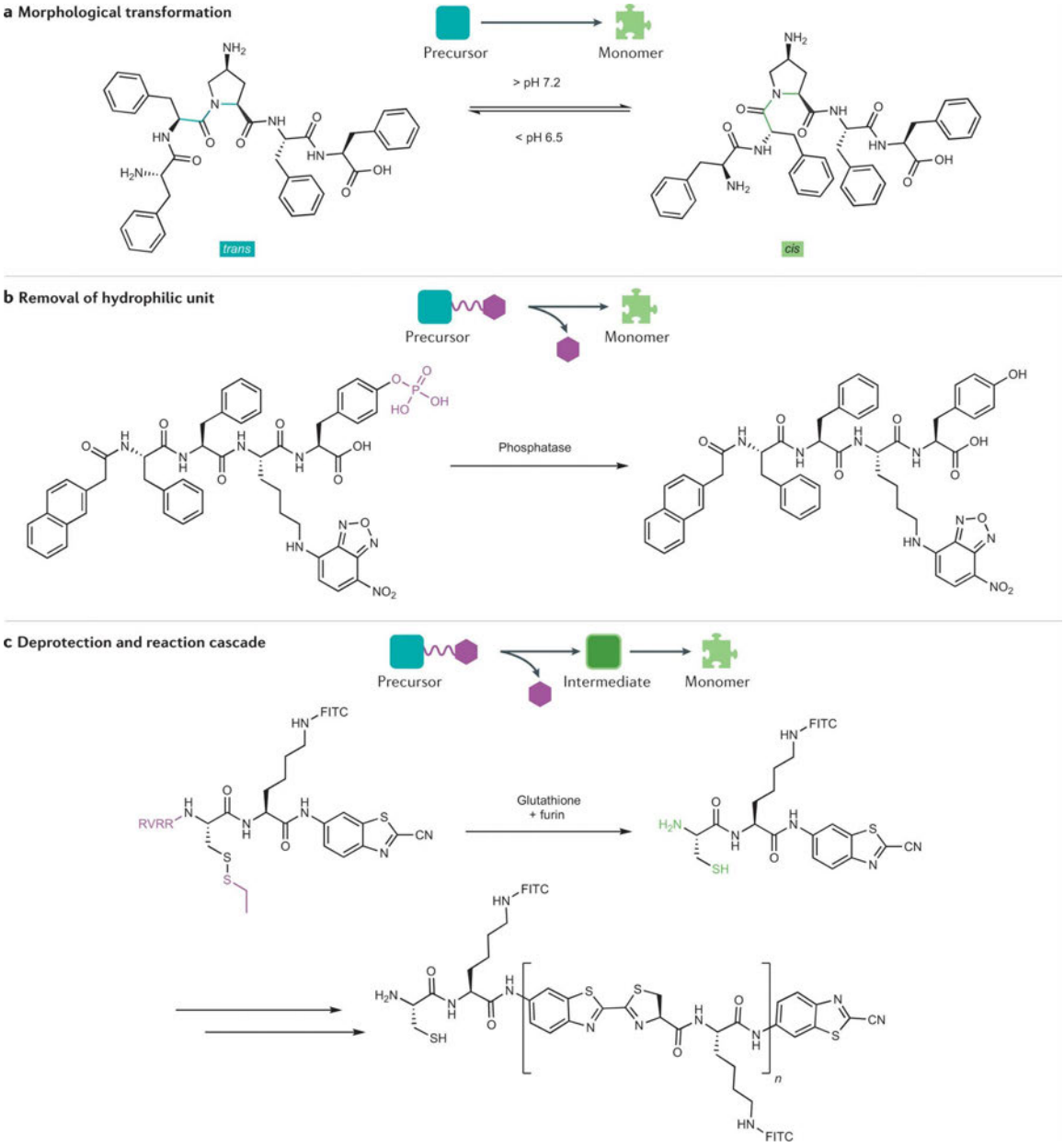

Figure 1.3 Differences in complexity of the chemical transformation for intracellular self-assembly. a | Morphology transformation due to *trans/cis*-amide isomerization[71]. b | Removal of a hydrophilic group in a phospho-tyrosine-containing peptide[18]. c | Deprotection of a bioresponsive cyclization precursor and following reaction cascade[9]. FITC, fluorescein isothiocyanate.

Apart from materials that rely on bioresponsive transformations for self-assembly, local accumulation can also lead to aggregation, which does not depend on any specific endogenous stimulus[72]. A subcellular accumulation occurs by integrating organelle-specific targeting groups into the nanomaterial design, which can be exploited to locally exceed the critical aggregation concentration. For example, the positively charged targeting group triphenylphosphonium (TPP) has been used to

induce the mitochondria-specific accumulation of short aromatic peptides, which leads to cellular dysfunction and cancer cell death[73-75]. Besides TPP, methylpyridinium-substituted materials also target the mitochondria: a methylpyridinium-containing oligothiophene conjugate revealed time-dependent and temperature-dependent accumulation and self-assembly first in the mitochondria, followed by the perinuclear region. The aggregation process was indicated by changes in fluorescence due to a bathochromic shift upon formation of superstructures[76]. For targeting the nucleus, lysine-rich peptides that bind to RNA can direct the self-assembling material to the desired organelle[77].

1.1.3. Physiological stimuli

Although a high local concentration of active monomers is the basis for assembly, the specificity and control over structure formation can be enhanced by leveraging physiological cues. The next sections are dedicated to the exploration of strategies for bioresponsive stimuli-induced self-assembly and the ways in which it allows for spatiotemporal control over the formation of intracellular nanostructures. Thus, the following sections are divided according to the respective chemical or biological stimulus that triggers the conversion of a pro-assembling precursor into an active monomer that can form supramolecular structures inside living cells.

1.1.3.1. Glutathione

Glutathione is the most abundant low-molecular-weight peptide in eukaryotic cells and consists of three amino acids: glutamate, cysteine and glycine[33]. Due to the reactive thiol group of its cysteinyl moiety, it acts as a reducing agent, a nucleophile and a cell-protective antioxidant, ensuring redox homeostasis by scavenging free radicals, such as ROS, lipid peroxides and heavy metals[78]. Normal levels of glutathione in human tissues range from 0.1 mM to 10 mM (ref.[27]), in which 85% to 90% of reduced glutathione is localized in the cytosolic–nuclear compartment[79],

transforming it into a reducing environment for both endogenous compounds and xenobiotics. Many cancers exhibit elevated levels of intracellular glutathione that correlate with higher cellular proliferation and metastatic activity[80,81], as well as multidrug resistance caused by an increased efflux of glutathionylated chemotherapeutics[82]. Glutathione, therefore, constitutes an attractive endogenous stimulus for controlled intracellular self-assembly, due to its ubiquity in cells, its capability of efficiently reducing disulfide bonds and the significant difference in its distribution inside and outside of the cell[83].

The reduction and cleavage of a disulfide bond by glutathione can cause the removal of a hydrophilic aggregation-inhibitive unit, thereby releasing the self-assembling component to form the designated nanostructures inside the cell[12,15,53,84]. An example for this strategy is the glutathione-responsive fluorescence probe that is composed of a bispyrene linked to a positively charged cyanine dye via a disulfide bridge[15]. Glutathione-induced cleavage of the disulfide in the cytosol causes the separation of the two fluorophores, thereby, allowing the free bispyrene to form large, highly fluorescent *J*-aggregates[59] in vitro and in vivo[15]. Aside from this small molecule probe for the imaging of glutathione levels, glutathione-responsive polymer–peptide conjugates have also been synthesized[53]. These conjugates consist of a thermoresponsive poly(*N*-isopropylacrylamide) backbone covalently linked to a hydrophilic cell-penetrating peptide by a disulfide bond (Fig. 1.4a). Upon glutathione-induced cleavage, the polymer conjugate exhibits a decrease in lower critical solution temperature to below 37 °C, which causes a transition from a random-coil state into spherical aggregates inside the cell. In addition, this system can be tuned to respond to different endogenous stimuli, including the proteolytic cleavage of the hydrophilic peptide by various enzymes, for example, caspase-3[53].

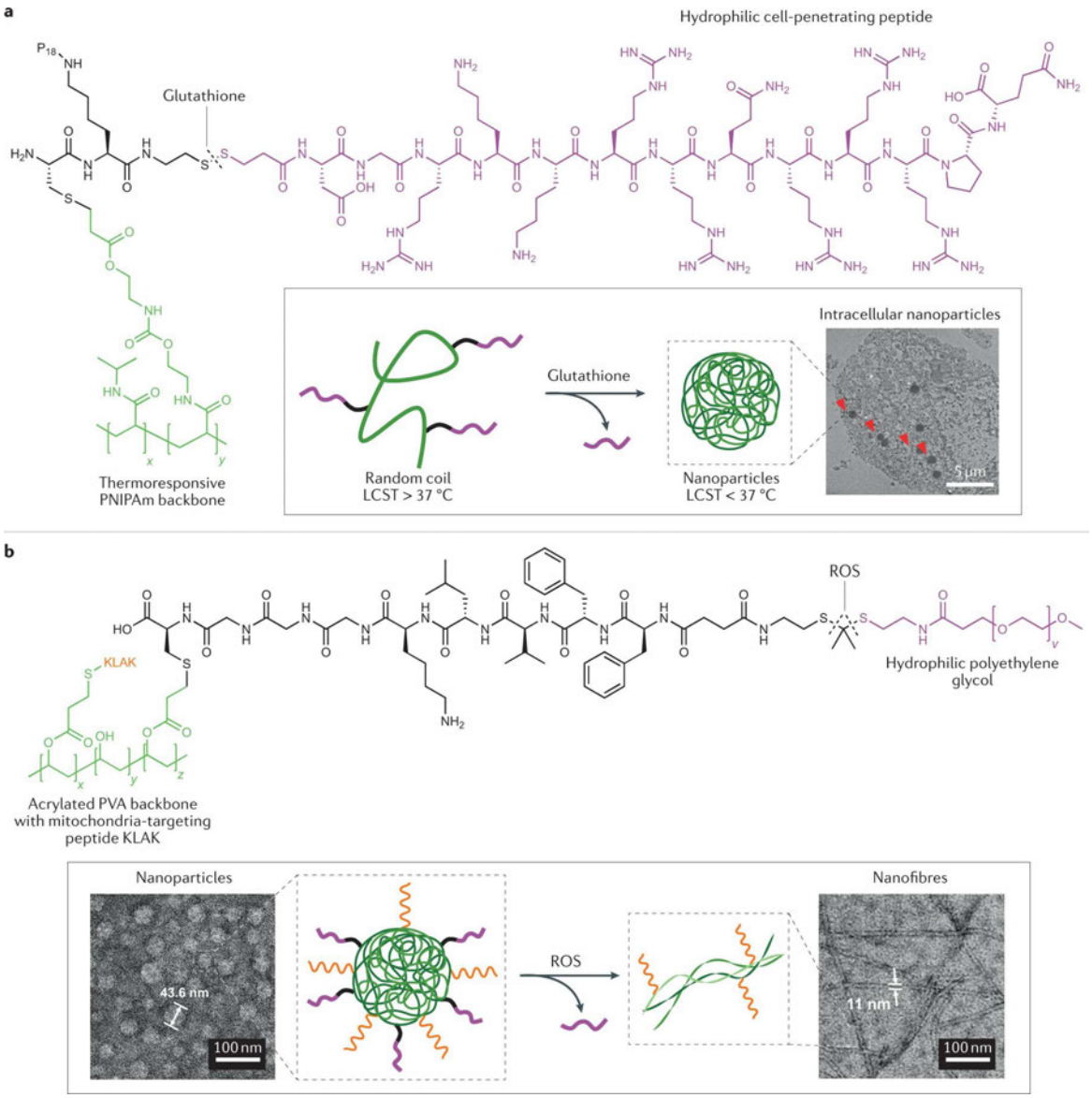

Figure 1.4 Redox-induced intracellular self-assembly. a | Glutathione-induced cleavage of a disulfide bond changes the lower critical solution temperature (LCST) behaviour of a polymer conjugate, causing it to form intracellular nanoaggregates[53]. Bio-transmission electron microscopy of MC7 cells shows the presence of intracellular nanoparticle. b | Cleavage of a reactive oxygen species (ROS)-sensitive thioketal group induces fibre formation[14]. Transmission electron microscopy images show ROS-induced transformation from nanoparticles to nanofibres in hydrogen-peroxide-containing phosphate buffer. KLAK, mitochondria-targeting peptide; P18, purpurin 18; PNIPAm, poly(N-isopropylacrylamide); PVA, polyvinyl alcohol. Part a (right) is adapted with permission from ref.[53], American Chemical Society. Part b (bottom left and right) is adapted with permission from ref.[14], American Chemical Society.

1.1.3.2. Reactive oxygen species

ROS are generated during mitochondrial oxidative metabolism[51] and as a cellular response to xenobiotics, cytokines and bacterial invasion[26,85]. Controlled ROS production inside the cell fulfils many biological purposes, such as the regulation of signal transduction[51,86] with regards to angiogenesis[26] and insulin metabolism[87].

However, overproduction of ROS leads to oxidative stress and is linked to various pathological phenomena[88], including abnormal cell growth that can perpetuate cancer initiation and progression[89,90].

Targeting cancer cells with high levels of ROS[91] for oxidation-driven self-assembly is a relatively new strategy to create supramolecular architectures inside cells[6,14]. The mitochondria produce ROS by means of the electron transport chain[25], thereby, influencing the immediate redox environment of the organelle and making it an attractive subcellular target for ROS-sensitive materials. Thioketals are an example of a ROS-sensitive functionality that can be degraded in the presence of sufficient amounts of cellular oxidants[92]. For instance, using a thioketal linker to attach a hydrophilic polyethylene glycol (PEG) chain to a self-assembling peptide on a polymer backbone, that is also decorated with a mitochondria-targeting peptide (KLAK), gives rise to a multifunctional platform for mitochondria-specific accumulation, morphology transformation and assembly[14] (Fig. 1.4b). This polymer–peptide conjugate consisting of two different polymers (PEG side chain and polyvinyl alcohol backbone), as well as two different peptides (KLAK and β-sheet-forming peptide), can enter the cells as a nanoparticle and undergoes a transformation into a fibrous network in the proximity of ROS-overproducing mitochondria. The morphological transformation is designed in a way that a lipophilic β-sheet-forming sequence is flanked by two hydrophilic polymers, KLAK-functionalized polyvinyl alcohol and PEG. In this initial state, the chains collapse into spherical aggregates, where the steric component of two bulky hydrophilic polymers prevents molecular interaction between the β-sheet peptides. Upon oxidation by high amounts (μM) of ROS, the PEG segment is cleaved, transforming the molecule into an amphiphilic structure. Hence, the steric hindrance is relieved and chain flexibility promotes intermolecular interactions between interchain β-sheet peptides to afford a fibrillar morphology. The ROS-sensitive supramolecular

system exhibits significantly higher cytotoxicity towards HeLa cervical cancer cells than towards normal cells, both in vitro and in vivo[14].

1.1.3.3. Enzymes

Biocatalytic reactions carried out by enzymes enrich the chemical depth of cellular pathways, allowing molecules and biopolymers to be processed within the environmental limitations of a living system. Besides converting natural substrates, many enzymes have also been exploited for the intracellular transformation of synthetic precursors into self-assembling monomers[18,46,93,94] (Table 1.1). For this purpose, enzyme-specific recognition motifs can be included in the molecular design of the precursor to tailor its bioresponsiveness towards a certain enzyme within the cell (Fig. 1.6). The following sections highlight the use of various types of intracellular enzymes to instruct targeted structure formation at different subcellular locations.

Table 1.1 Enzyme-instructed intracellular self-assembly

Enzyme	Transformation site	Cellular localization	Refs
Furin	RVRR_	Golgi	9,21,55,56,95-101
Caspase-3/7	DEVD_	Cytosol	16,22,35,44,46,53,54,102,103
ENTK	DYKDDDDK_	Mitochondria	94,104-106
ATG4B	TFG_F	Cytosol	53,107
Cathepsin B	GF_LG	Lysosome	5,36
ALP	Yp	Cell membrane	17,18,20,49,52,108-117
PTP1B	Yp	ER	17,18,108,109,114,118
β-Galactosidase	β-Gal-aromatic	Lysosome	16,119
γGT	γ-E_	Cell membrane	120
Nitroreductase	$-NO_2 \rightarrow -NH_2$	Cytosol	121
Transglutaminase	$\rightarrow$ ε-(γ-Q)-K	Cytosol, ER, mitochondria	93

Carboxylesterase	Ester bond	ER	47,122-125

γGT, γ-glutamyltransferase; ALP, alkaline phosphatase; ATG4B, autophagy-related 4B cysteine peptidase; ENTK, enterokinase; ER, endoplasmic reticulum; PTP1B, protein tyrosine phosphatase 1B.

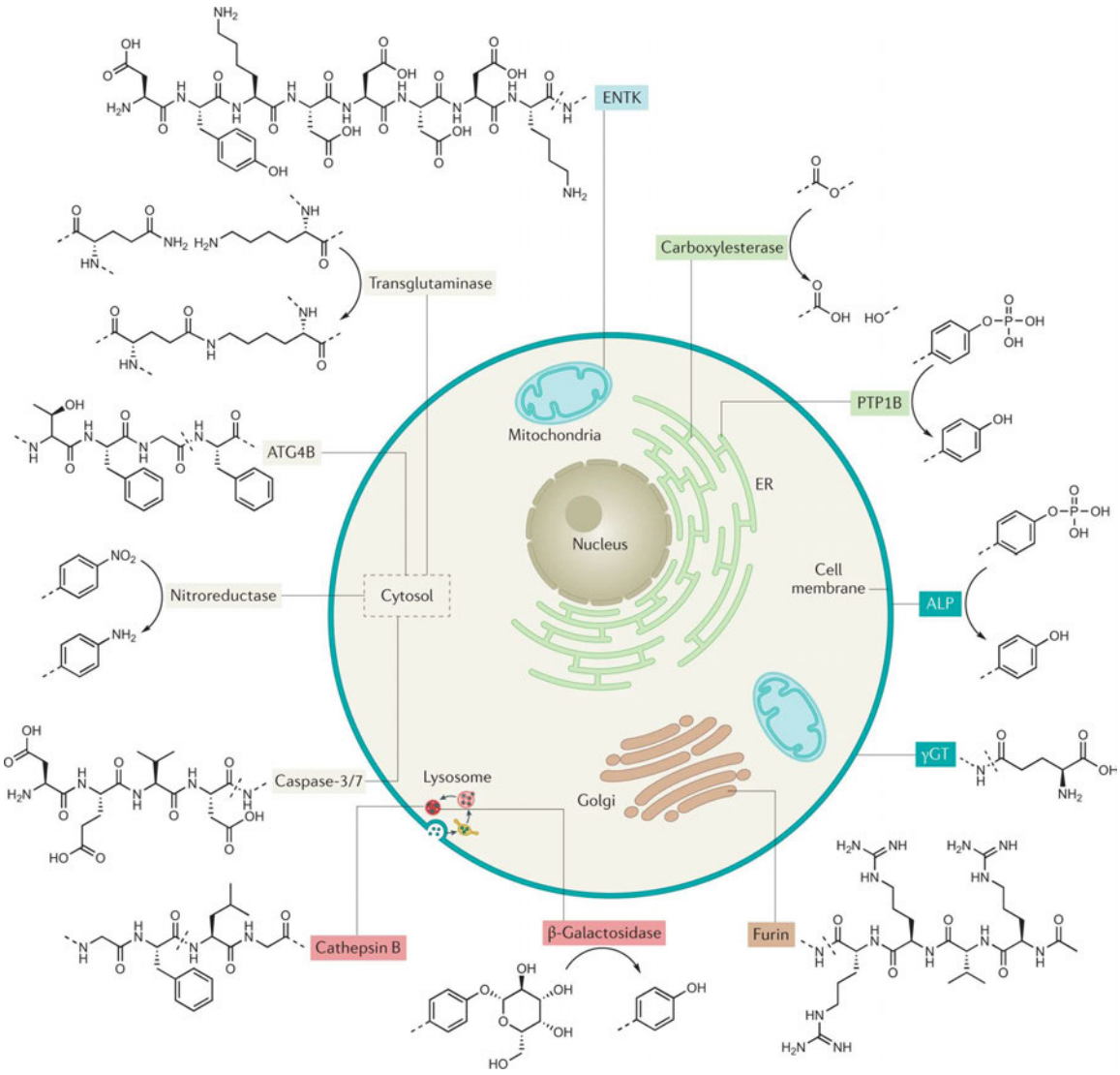

Figure 1.5 Cellular localization of enzymes for self-assembly and their respective recognition and transformation sites. γGT, γ-glutamyltransferase; ALP, alkaline phosphatase; ATG4B, autophagy-related 4B cysteine peptidase; ENTK, enterokinase; ER, endoplasmic reticulum; PTP1B, protein tyrosine phosphatase 1B.

Proteases

Proteolytic enzymes catalyse the hydrolysis of peptide bonds[126], making them an attractive biological tool for the activation of bioresponsive nanomaterials. The diversity of proteases in terms of their subcellular localization, level of expression

in different cell types, as well as their specificity for a certain cleavage site, facilitates spatiotemporal programming of enzyme-instructed self-assembly.

Furin is an endoprotease that is associated with the Golgi apparatus in eukaryotic cells. Belonging to the enzyme family of proprotein convertases, it catalyses downstream peptide cleavage of the polybasic motif RX(R/K)R for the bioactivation of certain proteins[127]. This enzymatic cleavage reaction plays an essential role in pathogenesis, as the enzyme activity of furin has been linked to cancer progression[128,129], as well as viral diseases[130], including SARS-CoV-2 infection[131]. Therefore, the imaging of furin activity inside cells or tumour tissue is an attractive target that can be addressed using bioresponsive supramolecular chemistry. For example, the intracellular condensation reaction between an aminothiol and a cyanobenzothiazole for the formation of self-assembling macrocyclic dimers was first realized using a furin-sensitive precursor (Fig. 1.3c). By adding the four amino acids RVRR to the amino-terminal cysteine, they serve not only as an enzyme-cleavable protecting group (Fig. 1.6a) for the amino function but also facilitate cell entry of the precursor due to the positively charged side chain residues[9]. Further investigation of the intracellular reaction cascade showed that the furin-induced proteolytic cleavage near the Golgi apparatus constitutes the rate-limiting step for the formation of active monomers, which correlates to the subcellular localization of the resulting nanostructures at this site[21]. This enzyme-instructed intracellular aggregation also enables in vivo imaging of furin activity inside furin-overexpressing tumor tissue, since it can promote the accumulation and retention of an imaging agent that is covalently linked to the self-assembling monomer. A variety of techniques that exploit this effect have been applied for diagnostic purposes, such as photoacoustic imaging[95], micro-positron emission tomography[96], use of radiotracers[97], Raman imaging[98] and magnetic resonance imaging[99]. In all these studies, the imaging agent was introduced to the

precursor molecule via side chain modification of a lysine positioned between the cyanobenzothiazole and the cysteine. The use of this strategy for the chemical modification of the condensation precursor has also been used for the conjugation of the chemotherapeutic drug, Taxol, which helps to prevent undesired drug efflux and promotes sustained drug release due to the furin-induced self-assembly of Taxol nanoparticles[100]. Aside from the attachment of small organic molecules, metal-based nanoparticles can also be decorated with the bioresponsive precursor by using the amino group of the lysine side chain for amide coupling reactions on a carboxyl-modified particle surface[55,56]. The resulting metal-based pro-assembling nanomaterials can form aggregates of gold or iron oxide nanoparticles inside furin-overexpressing cells as a result of particle crosslinking caused by enzyme-triggered condensation reactions.

Caspases are proteolytic enzymes that play an essential role in the initiation and execution of apoptosis, a mode of programmed cell death[132]. These endoproteases contain a characteristic nucleophilic cysteine as a central part of a polybasic substrate-binding pocket[133]. The chemical structure of their active site enables them to catalyse the hydrolytic cleavage of proteins for the controlled dismantling of the cell. Within the intricate activation cascade of different caspases, the so-called 'effector' caspases-3, 6 and 7 carry out most of the proteolysis during apoptosis and can, therefore, be considered biomarkers for programmed cell death[134]. Since caspase-3 and caspase-7 both exhibit similar preferential downstream cleavage of the motif DEVD in synthetic substrates[135], many supramolecular systems have been designed to include this sequence as a bioresponsive moiety for intracellular self-assembly[16,22,35,44,46,53,54,102,103,136] (Fig. 1.5). For example, a fluorescent probe for the real-time imaging of apoptosis in drug-treated cancer cells was combined with the hydrophobic tetraphenylethene (TPE) with the hydrophilic peptide motif DEVD_K via azide–alkyne click chemistry[102]. After enzymatic cleavage by

caspase-3/7, the polyaromatic fragment TPE-K can self-assemble inside cells, which results in AIE caused by the restriction of intramolecular rotation of its phenyl rings[137]. These so-called AIE luminogens[138] – which exhibit a turn-on fluorescence upon aggregation – can be useful reporters of enzyme activity in cancer cells, especially when they are part of a multifunctional theranostic nanomaterial[35].

A sequential approach to the caspase-induced formation of intracellular nanostructures uses systems containing tumor-specific recognition motifs able to trigger apoptosis[22,44]. A peptide-based precursor, containing a biomimetic sequence that can bind and inactivate the X-linked inhibitor of apoptosis protein (XIAP)[139], promotes the activation of caspase-3/7 through the manipulation of intracellular signal transduction[140]. The activated pro-apoptotic proteases can then remove the non-assembling XIAP-recognition motif, thereby, inducing the self-assembly of the remaining β-sheet-forming peptide–drug conjugate[44] or peptide–cyanine dye conjugate[22]. This sophisticated system selectively causes assembly formation in cancerous tissue both in animal models and in ex vivo human bladders that were taken from patients with late-stage bladder cancer[44]. The latter experiment shows the potential clinical use of the caspase-sensitive assembly precursor, as it could help detect tumor boundaries during image-guided surgery.

For quantitative imaging of caspase-3/7 activity in live animals, a condensation-driven system was developed, in which the enzymatic activation of the precursor is decoupled from a subsequent imaging tag immobilization[46]. The pro-assembling molecule consists of the amino-terminal protecting group DEVD (Fig. 1.6a) linked to a cysteine, a lysine with a clickable *trans*-cyclooctene (TCO) on its side chain, as well as a pyrimidinecarbonitrile as the aromatic nitrile for the enzyme-instructed macrocyclization. Since this caspase-3/7-responsive molecule can form stable intracellular nanoaggregates, subsequent addition or injection of a tetrazine-functionalized fluorophore leads to an immobilization of the imaging probe due to

inverse electron demand Diels–Alder reactions between the tetrazine and the aggregated TCO-bearing monomers.

Enterokinase (ENTK) (also known as enteropeptidase)[141] is a membrane-bound protease that is essential for digestion[142]. Its main physiological purpose is the cleavage of the acidic motif DDDDK in the pancreatic proenzyme trypsinogen, which leads to the activation of trypsin[143]. There are multiple reasons as to why ENTK is an interesting enzyme candidate for programming cell-specific and organelle-specific self-assembly[94,104-106]: firstly, its role in the activation of trypsin has been linked to matrix degradation and migration of lung, colorectal and glioblastoma cancer cells[144]; secondly, it allows cell-specific targeting of the mitochondria in cancer cell lines, such as HeLa (cervical cancer), Saos-2 (bone cancer) and HepG2 (liver cancer)[105]; and, thirdly, it enables the enzyme-driven release of cargo from a supramolecular vehicle at the organelle surface[104]. The ENTK-sensitive systems consist of the cleavable FLAG-tag DYKDDDDK covalently linked to a self-assembling peptide sequence[94,104,105] or a lipid-like moiety[106]. The chemical design of the peptide-based precursor is a branched structure that is important for mitochondria targeting[104]. After entering the cell in a micellar form by clathrin-mediated endocytosis[105], the supramolecular precursors escape the endosome facilitated by pH buffering of the carboxylic acid groups[106]. The subsequent subcellular accumulation at the mitochondria is promoted by the increased mitochondrial membrane potential in cancer cells and the electrostatic interaction between the negatively charged FLAG-tag and voltage-dependent anion channels at the organelle surface[106]. The enzymatic cleavage of the hydrophilic tag by ENTK initiates the local conversion from micelles to peptide nanofibres[94,104,105] (or more lipophilic micelles in the case of the peptide–lipid conjugates)[106]. This supramolecular transformation causes an increase in perimitochondrial viscosity and enables the organelle-specific delivery of drugs[104,106], proteins[94] or gene vectors[105].

Trypsin is a potent serine protease that has been the subject of ongoing biomedical research due to its role in the invasion and metastasis of various cancers, such as ovarian[145], colorectal[146,147], lung[148] and prostate cancer[149]. The overexpression of different trypsin isoforms by tumors leads to the amplified degradation of extracellular proteins[150] and the increased activation of other matrix-associated proteases[145,151,152]. The preferential cleavage of trypsin at the carboxy terminal of lysine or arginine can be exploited as an enzymatic trigger for the self-assembly of synthetic monomers, as shown by a trypsin-responsive precursor molecule[19]. Similar to the ENTK-responsive systems, the branched pro-assembling peptide consists of an aromatic tetrapeptide backbone and a hydrophilic lysine-rich sequence KYDKKKKDG that can be cleaved in trypsin 1-overexpressing ovarian cancer cells (OVSAHO). As these particular cells exhibit an abnormally high activity of the protease at the endoplasmic reticulum (ER), the resulting formation of cytotoxic nanofibres is not only cell specific but also organelle specific, despite high concentrations of the supramolecular precursor being necessary.

Cathepsin B is a lysosomal protease that has been linked to the invasiveness of several types of cancer[153], including colorectal[154] and breast cancer[155]. This pro-angiogenic enzyme[156] recognizes and cleaves the sequence GFLG in synthetic substrates, which has made it a useful biological tool for cancer-specific drug delivery[157]. Combining the technology of AIE luminogens with a cathepsin B-cleavable peptide led to a light-up imaging probe and photosensitizer for the detection and ablation of breast cancer cells[36]. The precursor consists of a tetraphenylethylene derivative with two azido groups that are each 'clicked' to a bioactive peptide composed of the cathepsin B-responsive sequence GFLG, a hydrophilic linker (DDD) and the targeting moiety cyclo-RGD. The double-substituted AIE imaging probe can form fluorescent aggregates in the lysosomes of breast cancer cells (MDA-MB 231), which facilitates the quantification of enzyme

activity, as well as photodynamic therapy[36]. To study the autocatalytic growth of intracellular nanofibres, a cathepsin B-responsive prodrug was developed that could undergo a morphology transformation from nanoparticles to fibrous networks in vitro and in vivo: after shedding a hydrophilic PEG-RGD unit, the remaining self-assembling peptide–drug conjugate undergoes β-sheet-driven fibrillation inside HeLa cells, which is accelerated by the presence of previously formed fibrils[5].

Matrix metalloproteinase 7 (MMP7) is a protease involved in the degradation of extracellular matrix proteins[158], contributing to cancer cell migration[159]. To initiate cancer cell death by intracellular self-assembly, a peptide–lipid conjugate susceptible to cleavage by MMP7 was developed, an enzyme that is secreted by HeLa cells[58]. The palmitoylated peptide consists of a glycine-rich nonpolar sequence, an MMP7 cleavage site (PLG_L) and a hydrophilic carboxy-terminal fragment (_LARK) that inhibits unspecific aggregation before enzymatic conversion. After incubation with the precursor, HeLa cells exhibited decreased viability caused by the cancer-cell-specific formation of intracellular peptide–lipid nanofibres[58].

ATG4B is a cysteine protease that contributes to autophagy, during which protein aggregates and damaged organelles are digested and recycled[160]. While it is essential for homeostasis in healthy tissue, dysregulated autophagy is associated with pathogenesis, such as tumorigenesis[161,162] and neurodegeneration[163]. Since ATG4B is crucial for the formation of autophagosomes[164], its activity was monitored using a bioresponsive supramolecular probe[107]. The chemical design of this imaging agent combines a self-assembling bispyrene with a peptide displaying the ATG4B cleavage site TFG_F[107], as well as a highly cationic poly(amidoamine) dendrimer that enables cell entry and provides water solubility. After the enzymatic cleavage in MCF-7 breast cancer cells, the free bispyrene units self-assemble into fluorescent nanoparticles due to the formation of *J*-aggregates[59], before transforming into cytosolic nanofibres over time[107].

1.1.4. Multistep conversion for self-assembly

The most common chemical design strategy for bioresponsive molecules for supramolecular assembly focuses on the combination of a cleavable hydrophilic unit with a more hydrophobic self-assembling moiety, such as a β-sheet-forming peptide or a polyaromatic group. In this general approach, the stimulus-induced separation of the two building blocks directly triggers the formation of synthetic structures inside cells (Fig. 1.3b). However, given the complexity of the cellular environment and the many potential endogenous stimuli, systems for intracellular self-assembly can also be made to undergo a more complex multistep transformation to the final monomer. The idea of having a reaction sequence or cascade rather than a single transformative step also offers the opportunity to implement more than one bioresponsive element into the chemical design of the precursor, which can increase spatial control over the assembly formation.

The latter can be achieved, for example, by combining an enzyme-responsive unit on one part of the molecule with a redox-sensitive group on another part of the molecule (Fig. 1.6a). This combination has been used for the condensation reaction between a deprotected aminothiol and a cyanobenzothiazole for the formation of self-assembling macrocycles[70]. As both the amino group and the thiol group of the amino-terminal aminothiol are necessary for condensation and self-assembly, choosing complementary bioresponsive protecting groups helps to tailor the system towards a specific intracellular behavior. For example, the amino group of the aminothiol can be attached to an enzyme-responsive peptide sequence that is cleavable by a protease (for example, furin[9,21,95] or caspase-3/7 (refs[16,46,103])), while the thiol group can be protected via a disulfide bond to a small molecule such as ethanethiol (Fig. 1.6a). Upon cell entry, this disulfide bond is cleaved by intracellular glutathione in the reducing environment of the cytosol. Consequently, the determining step for the formation of the reactive intermediate, which can

transform into the self-assembling monomer, is the final deprotection of the *N*-terminal amino group. As this can only occur at the subcellular localization of the targeted enzyme, spatial control over the structure formation is achieved by careful selection of the enzyme-responsive moiety in the precursor. This strategy is not only applicable to proteases but also works for other enzymes such as β-galactosidase[16] or nitroreductase[121] if a self-immolative benzyl-carbamate-derived protecting group is chosen for the amino terminus (Fig. 1.6a). The cyanobenzothiazole moiety can also be substituted for other less electrophilic aromatic nitriles, which lowers the risk of potential side reactions with endogenous aminothiols[16]. Aside from implementing bioresponsive groups that control self-assembly, additional enzyme cleavage sites can be included in the center of the molecule that allow the programmed disassembly of intracellularly formed nanostructures by proteolysis later on[16,17]. For biomedical purposes, the cyclization precursor can be modified to include photothermal agents that are activated by condensation-mediated and assembly-mediated quenching[13] or chemotherapeutic drugs that can slowly be released inside tumor cells[100].

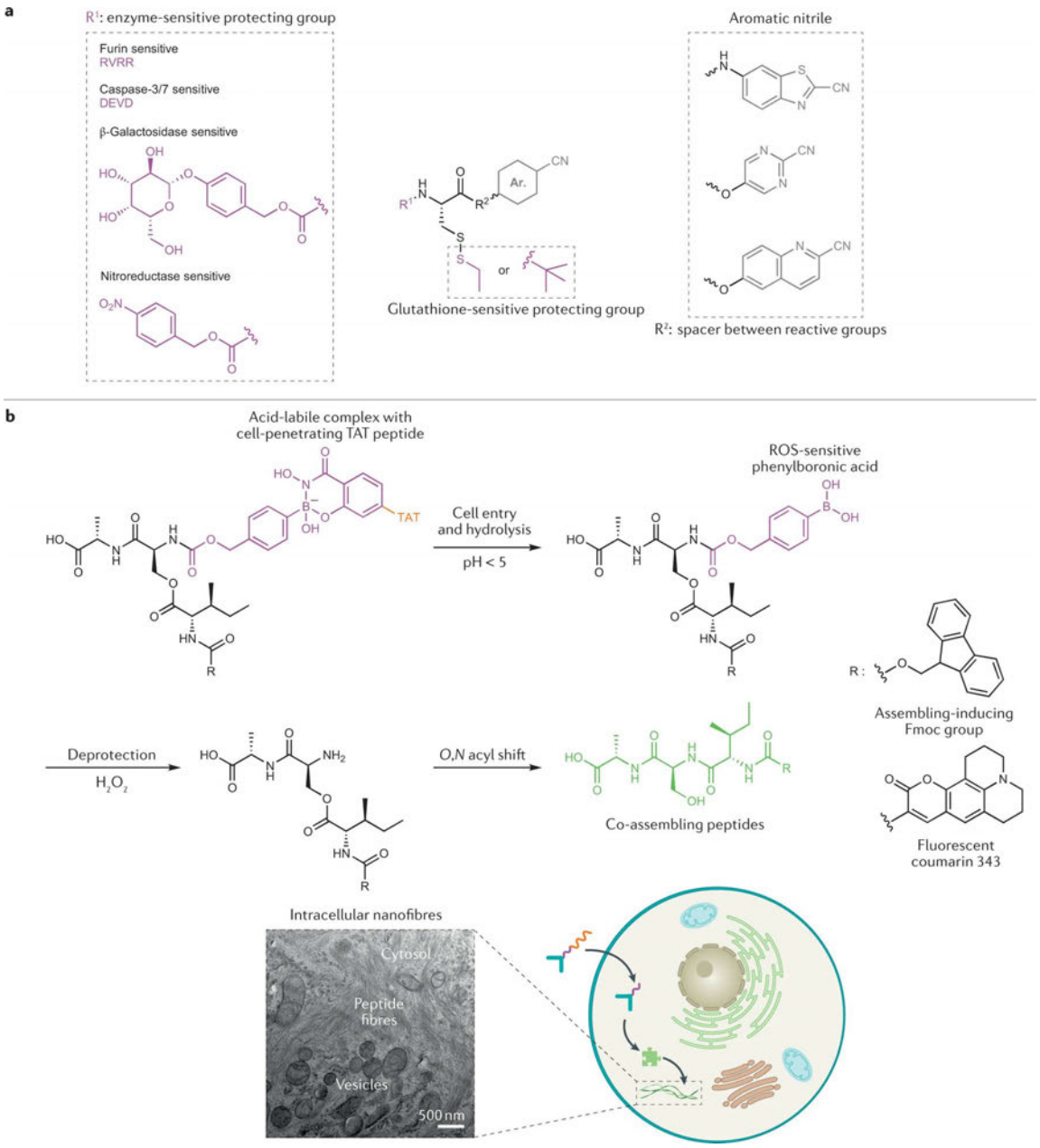

Figure 1.6 Multistep transformation for intracellular self-assembly. a | Structures of assembly precursors for macrocyclization-based self-assembly. The amino protecting group determines the sensitivity to a specific enzyme, such as furin[9,21,95], caspase-3/7 (refs[16,46,103]), β-galactosidase[16] or nitroreductase[121]. The peptide-based spacer R^2 between the reactive functionalities can contain fluorophores, drugs or other bioactive compounds. b | Multistep reaction sequence of intracellular conversion pH-sensitive and reactive oxygen species (ROS)-sensitive isopeptides into linear co-assembling peptides. The targeting group contains cell-penetrating peptide TAT (transactivator of transcription) and enables cell entry, upon which the acid-labile dynamic covalent bond between the salicyl hydroxamate of targeting peptide and the phenylboronic acid group of the isopeptides is hydrolyzed in the endosomes. The hydrogen-peroxide-induced deprotection via self-immolation of the phenylboronic acid group reveals a reactive amino group that can attack the adjacent ester bond. This rearrangement due to an *O,N* acyl shift results in the linearized co-assembling peptides. The formation of peptide nanofibres inside A549 cells can be visualized with bio-transmission electron microscopy. Part b (bottom left) is adapted with permission from ref.[6], American Chemical Society.

For programming peptide fiber formation inside cancer cells, a multiresponsive system was designed that is pH sensitive and ROS sensitive[6]. The peptide-based precursors contain a phenylboronic acid trigger group, which serves as both a ROS-sensitive cage for the amino group of an esterified serine and as a handle for the attachment of a cell-penetrating peptide via an acid-labile dynamic covalent bond (Fig. 1.6b). In the acidic environment of the endosome, the cell-penetrating peptide is removed. After endosomal escape, cytosolic ROS causes the degradation of the self-immolative phenylboronic acid group, revealing a free reactive amine. In the neutral pH of the cytosol, the nucleophilic amino group can perform an intramolecular attack on the adjacent ester bond of the serine side chain, yielding linearized peptides that can co-assemble into cytotoxic peptide fibres inside ROS-overproducing cancer cells[6]. These decoupled steps of the reaction cascade – the initial activation by deprotection and the following transformation to the monomer – take place under different chemical conditions and display individual reaction kinetics. Therefore, the multistep approach offers more opportunities to modulate the speed of the transformation of a precursor into a self-assembling monomer, in contrast to most systems for intracellular self-assembly that rely on a singular transformative step.

1.1.5. Perspective

Synthetic supramolecular chemistry in a cellular environment uses a strategic implementation of bioresponsiveness in chemical design to achieve control over the formation of nanoscale architectures. In this section, we discussed various chemical scaffolds, such as peptides, polyaromatic molecules and polymers, that can undergo a triggered transformation into assemblies due to endogenous stimuli. Tailoring the reactivity of the nanomaterial towards a specific intracellular cue can be realized by incorporating redox-sensitive or pH-sensitive groups, as well as enzyme recognition motifs that allow biocatalytic transformations. These stimulus-dependent mechanisms of self-assembly come with numerous advantages for therapeutic or diagnostic application. For example, the bioresponsive properties of the materials contribute to cell and tissue specificity in vivo, while also allowing for spatial control over the structure formation inside cells by targeting organelle-specific enzymes. Another therapeutic advantage of systems for intracellular self-assembly is the circumvention of multidrug resistance in certain cancers due to an impaired efflux of the intracellularly formed nanostructures compared with small molecules. Moreover, this accumulation effect can also contribute to the concentration of fluorescent agents inside the targeted cells, enabling more efficient bioimaging. Compared with ex situ self-assembled materials, such as therapeutic nanoparticles, the monomeric assembly precursors generally display an easier clearance from the liver, spleen or kidneys, thereby, reducing their systemic toxicity[165].

However, there are also several challenges regarding the potential clinical translation that need to be addressed. For example, a detailed pharmacokinetic and pharmacodynamic analysis of nanomaterials for intracellular self-assembly is necessary to ensure a favorable biodistribution and circulation time of precursors, as well as low immunogenicity. The chemical stability of the precursor molecule is

crucial for its in vivo application, as, for instance, the proteolysis of peptide-based materials prior to cell entry and self-assembly needs to be avoided. Additionally, the eventual clearance of the in situ-formed nanostructures must be considered thoroughly, since stable assemblies, particularly amyloid-like β-sheet peptide assemblies, could potentially cause negative side effects over time as a result of their systemic accumulation. Generally, the morphology, stability and overall physiological impact of synthetic nanostructures need to be closely monitored and evaluated, which is still a challenge for current methods of in vivo analysis.

In the future, further exploration of the existing toolbox of functionalities that can be reduced by glutathione, oxidized by ROS or that are labile to acidification could broaden the scope of potential precursors for intracellular self-assembly. With systems for enzyme-instructed self-assembly being prominent in recent years, the investigation of other enzymes beyond the commonly used phosphatases and proteases could not only help to diversify strategies but also contribute to a more cell-specific approach that could benefit the targeted therapy of cancer or other diseases with a characteristic dysregulation of enzyme expression. For this purpose, the study of molecular pathology is essential to lay the foundations for the design of novel enzyme-responsive materials. Moreover, including more than one bioresponsive group can increase the spatial control over the structure formation, as well as cell specificity, since multiple endogenous stimuli need to be present for assembly to occur. Adding other bioactive components to the molecular design, such as signaling peptides[44,111] or small molecule drugs[166], can further enhance the impact of the system on cellular processes leading to potentially synergistic therapeutic effects.

Many existing systems rely on thermodynamic control as the primary driving force to construct the intracellular architectures. Advanced methodologies involving non-equilibrium assemblies[167,168] coupled to cellular feedback dynamics would be highly

attractive to induce reversible changes in cellular behavior, as cell death is not always the desired outcome. From this perspective, there is also room to explore intracellular structures that boost cellular functions, possibly to address cell senescence (ageing) and environmental adaptation. The creation of such biomimetic materials that imitate reversibly formed biological supramolecular assemblies would be a milestone in synthetic biology and challenge frontiers in biomedical science.

1.2. Cell-Material Interactions

Programming the interaction between synthetic materials and different types of eukaryotic cells is a fundamental goal of biomedical research.[34] Insights into how synthetic materials influence complex biological environments and how to modulate the cellular response to these engineered materials are essential for advancing a wide range of applications, including tissue engineering, drug delivery, cancer therapy and immunotherapy. As discussed in previous sections, tailoring the bioresponsiveness of synthetic materials requires a deep understanding of the chemical and biological conditions present in different cell types and their respective microenvironments.[169] For instance, cancer cells can exhibit markedly different features compared to healthy cells[30,170,171], such as immune cells. As characteristics of cancer cells and their interactions with synthetic materials, including endogenous cues for intracellular material transformation, have been extensively covered in the first section of the introduction, the following subsection will focus on immune cells, namely T cells, and provide examples of T cell-material interactions pursued for immunotherapeutic applications.

1.2.2. T cell-material interactions

The interplay between T cells and synthetic materials is particularly relevant for the development of advanced immunotherapies.[172] Understanding these interactions is essential for designing materials that leverage the potential of T cells to combat diseases, particularly cancer. This section explores the key aspects of T cell-material interactions, focusing first on the classification and properties of T cells and second on the implications of T cell-material interactions for cancer immunotherapy.

1.2.2.1. General classification and functions of T cells

T cells are a central element of the adaptive immune system, classified into two major types based on their surface markers and functions: $CD4^+$ T cells and $CD8^+$ T cells. Both types originate from hematopoietic precursor stem cells in the bone marrow and mature in the thymus, where they undergo selection to ensure self-tolerance and functional competence (Fig. 1.8).[173,174]

$CD4^+$ T cells, or helper T cells, are characterized by the expression of the CD4 glycoprotein on their surface as a co-receptor of the T cell receptor.[175] They primarily function to regulate and coordinate the immune response by secreting cytokines that influence other immune cells.[175] $CD4^+$ T cells are further divided into several subsets, each with distinct roles[176]: for instance, T_h1 cells enhance cellular immunity against intracellular pathogens by activating macrophages and $CD8^+$ T cells; T_h2 cells control extracellular microorganisms and assist in humoral immunity by promoting B cell differentiation and antibody production; T_h17 cells are involved in inflammation and defense against extracellular pathogens; and T_{reg} cells maintain immune tolerance and prevent autoimmunity.[175,177-179]

$CD8^+$ T cells, also known as cytotoxic T cells, are identified by the expression of the CD8 glycoprotein on their membranes.[173] They are specialized in directly eliminating infected or malignant cells. $CD8^+$ T cells recognize antigens presented by Major Histocompatibility Complex (MHC) class I molecules on target cells.[173] Upon recognition, they form so-called immunological synapses[180] connecting them to the target cell surface and execute their cytotoxic function through the release of cytotoxic granules containing perforin and granzymes.[181] Perforin forms calcium-dependent pores in the target cell membrane, triggering a repair response that allows granzymes to enter the cytoplasm and induce apoptosis.[182] This direct killing

mechanism induced by $CD8^+$ T cells is crucial for controlling intracellular pathogens and cancer cells.

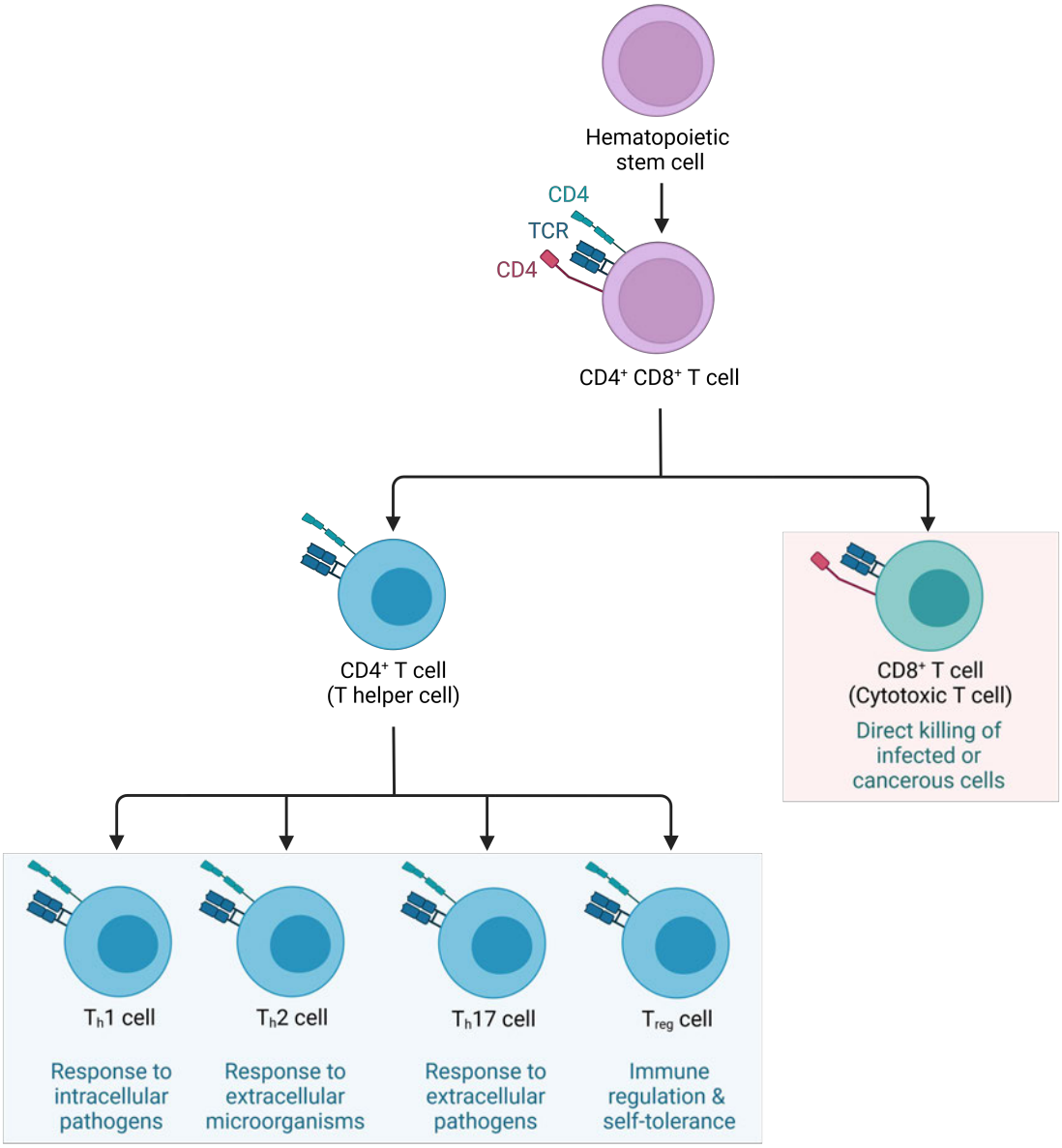

Figure 1.8 Schematic overview of T cell differentiation into various functional T cell types.[173,174]

Understanding the various classifications and functions of T cells is crucial for comprehending immune responses. While $CD4^+$ T cells play essential regulatory and helper roles, $CD8^+$ T cells are central to the direct elimination of infected or aberrant cells.[174] Insights into these cells' properties and behaviors contribute to efforts of designing synthetic materials for immunotherapeutic strategies.

1.2.2.2. T cell-material interactions for immunotherapy

Cancer immunotherapy aims to harness the immune system, particularly T cells, to target and eliminate malignant cells. Currently, key strategies for cancer immunotherapy include adoptive cell transfer, checkpoint inhibitors and cancer vaccines.[183]

Adoptive cell transfer involves two main approaches aimed at enhancing T cell efficacy.[184] The first approach involves expanding tumor-infiltrating lymphocytes (TILs) isolated directly from the patient's tumor and reintroducing them to the bloodstream[185,186]; the second approach involves genetically engineering T cells with chimeric antigen receptors (CARs) to precisely target cancer-specific antigens.[187,188] This CAR-T cell therapy has shown significant clinical impact in recent years, especially in treating hematologic malignancies.[189]

Checkpoint inhibitors are antibodies designed to block immune checkpoint proteins, such as PD-1 and CTLA-4, which are receptors found on the surface of T cells.[190,191] These checkpoint proteins suppress T cell activity, thereby, enabling cancer cells to evade immune detection and response.[192,193] By binding and inhibiting checkpoint proteins, checkpoint inhibitors enhance the ability of T cells to recognize and eliminate cancer cells.[194]

In contrast, therapeutic cancer vaccines stimulate T cell responses by introducing cancer-specific antigens identified through tumor cell DNA sequencing, thereby training the immune system to target and destroy cancer cells.[195]

Despite the recent progress, the strategies for cancer immunotherapy still face significant challenges, including difficulties in T cell trafficking to tumors caused by physical barriers[196] and immunosuppressive environments[197]. Additionally, the hostile tumor microenvironment often leads to T cell exhaustion and death[198], while genetic mutations in tumors can result in the loss of target antigen expression[199].

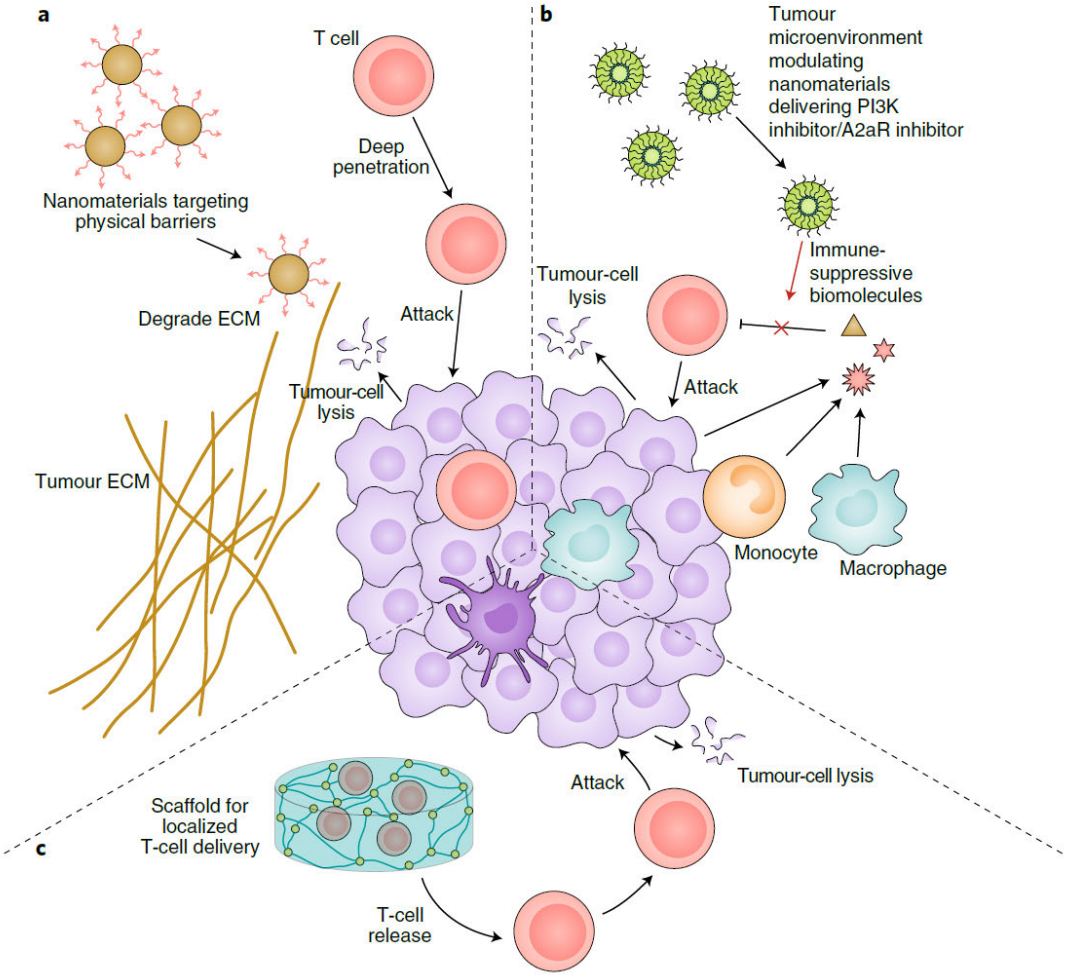

Figure 1.9 Examples of synthetic nanomaterials that promote T cell efficacy in cancer immunotherapy. Figure is reproduced with permission from ref.[172], Springer Nature.

Therefore, using synthetic nanomaterials to address these challenges through their interactions with T cells could significantly advance cancer immunotherapy.[172] Generally, nanomaterial-based immunotherapeutic systems offer several possible benefits: 1) their morphology and surface characteristics can help them overcome pathophysiological barriers, improving both accumulation and penetration at the tumor site; 2) they can enable site-specific delivery and release of immunomodulators, triggering anti-tumor immunity while reducing the risk of unwanted autoimmune responses; 3) they can facilitate the co-delivery of other therapeutic agents, including antibodies, chemotherapeutics, nucleic acids and

therapeutic proteins or peptides; and 4) they can promote immune normalization by concurrently targeting various immune evasion pathways.[200]

To address the issue of pathophysiological barriers in the tumor microenvironment, recent studies have explored the use of nanomaterials to overcome the fibrotic extracellular matrix in solid tumors, which inhibits effective immune cell infiltration (Fig. 1.9a).[172] One such approach involves the development of a dual mechanism core–shell calcium phosphate liposome nanomaterial designed to deliver an antifibrotic drug directly to the tumor site, as well as an immune-enhanced cytokine that can further stimulate cytotoxic T cell activation and infiltration.[201]

Nanomaterials can also be used to counteract the immunosuppressive environment within solid tumors to support T cell therapy.[172,202] For instance, lipid nanoparticles coated with a tumor-targeting peptide and loaded with a PI3K inhibitor and an α-GalCer agonist can shift the tumor microenvironment from suppressive to stimulatory.[202] The PI3K inhibitor targets immunosuppressive tumor cells, while the α-GalCer agonist enhances the activity of therapeutic T cells (Fig. 1.9b). This combination creates a therapeutic window, enabling tumor-specific CAR-T cells to home to the lesion, expand and cause tumor regression.[202]

Biomaterial scaffolds also represent a significant application in T cell-based therapies (Fig. 1.9c).[203] These scaffolds are made from materials such as hydrogels[204] or porous structures like polysaccharides scaffolds functionalized with adhesion molecules[205] and provide physical and biochemical support to T cells. By offering a conducive environment for T cell growth, expansion, and survival, these scaffolds enhance the cells' functionality and longevity, thereby improving the outcomes of adoptive cell therapies.[203]

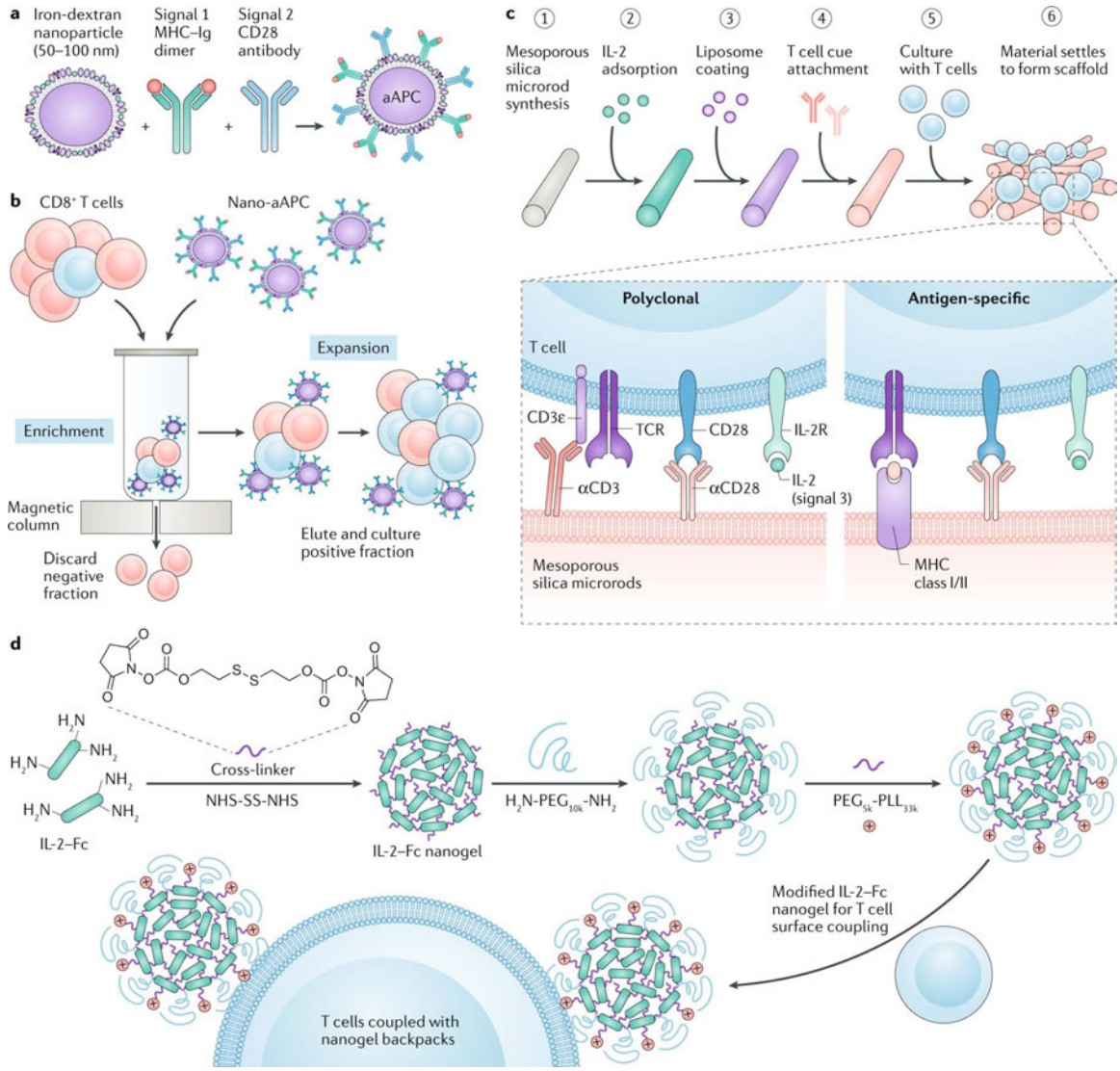

Figure 1.10 Nanomaterials for the enhancement of T cell expansion and function in adoptive cell therapy. a | Artificial antigen-presenting cells (aAPCs) prime and enrich antigen-specific T cells. b | aAPCs enable the isolation of CD8+ T cells from bulk leukocytes. c | Lipid- and antibody-coated mesoporous silica microrods (αCD3, αCD28) drive T cell expansion. d | Nanogel 'backpacks' on T cells release cytokines in tumors, boosting T cell function while minimizing systemic side effects. Figure is reproduced with permission from ref.[206], Springer Nature.

Another advancement in T cell-material interactions is the development of artificial antigen presentation platforms using synthetic materials (Fig. 1.10a-c).[206] These platforms are designed to mimic the natural antigen-presenting cells (APCs) that play a crucial role in T cell activation.[207,208] For instance, van Hest and co-workers developed a poly(ethylene glycol)-block-poly(D,L-lactide) polymersomes with varying morphological and surface properties which were used to present antigens in a manner that closely resembles physiological processes, thereby boosting T cell

activation.[207] Similarly, another artificial APC system was developed using mesoporous silica microrods coated with liposome shells to attach CD3 and CD28 antibodies to their surfaces, which promote T cell activation and survival (Fig. 1.10c).[209] The three-dimensional scaffold facilitated more effective proliferation of both mouse and human T cells compared to a commercially available T cell expansion system.[209]

An emerging strategy to further enhance T cell therapies involves conjugating nanoparticles loaded with immunotherapeutic agents directly onto T cells as so-called 'backpacks' (Fig. 1.10d).[206] In contrast to passive nanoparticles, T cells actively move along chemokine gradients, enabling them to concentrate their payloads in tumors more effectively than free nanoparticles. One example of this 'backpacking' approach is a system using protein nanogel-based particles conjugated to T cells which contain an interleukin-15 agonist complex.[210] This delivery strategy significantly increased the dosage of the cytokine at the tumor site, leading to substantial tumor clearance and prompting the initiation of a clinical trial.[206,210]

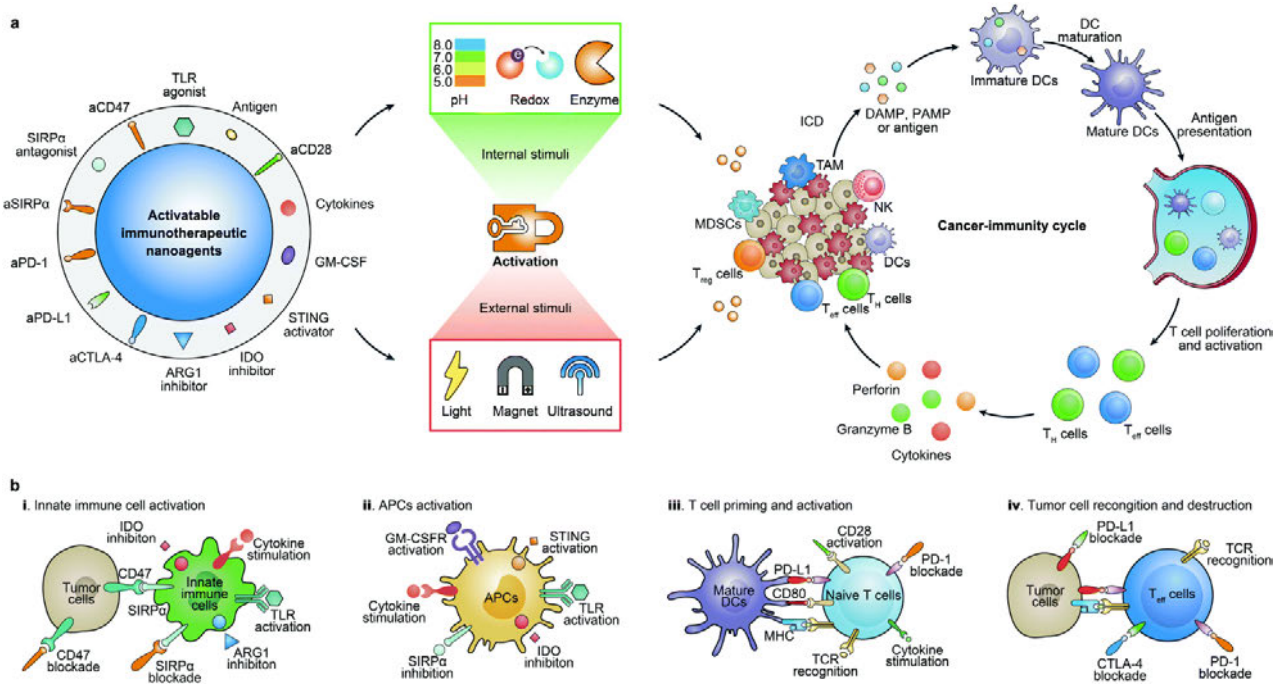

Figure 1.11 Nanomaterial-based delivery systems for stimulus-induced cargo release and immunomodulation. a | Schematic representation of potential stimulus-responsive mechanisms exploited for the activation of cancer immunotherapy nanoagents and depiction of the cancer-immunity cycle. b | Overview of four key strategies for inducing antitumor immunity by targeting and modulating

different immune cell populations, including naïve and activated T cells (iii, iv). Figure is reproduced with permission from ref.[211], the Royal Society of Chemistry.

Despite the promising potential of the 'backpacking' approach, where nanomaterials loaded with immunotherapeutic agents are directly attached to T cells,[206] traditional nanomaterial-mediated delivery systems continue to be widely employed. These systems represent diverse platforms for the tumor-targeted and often stimulus-responsive delivery of immunomodulatory agents such as cytokines, checkpoint inhibitors or nucleic acids used in the genetic engineering of T cells (Fig. 1.11).[211]

An example of a polymer-based delivery system for immunomodulation involves poly(lactic-co-glycolic acid) (PLGA) microparticles functionalized with interleukin-2, which significantly enhances T cell proliferation compared to non-encapsulated cytokines.[212] Similarly, carbohydrate-based nanogels co-loaded with the chemotherapeutic drug paclitaxel and interleukin-2 have shown synergistic therapeutic effects.[213] These nanogels use a pH-sensitive release mechanism to deliver low doses of paclitaxel in the acidic tumor microenvironment, triggering immunogenic cell death and antigen release from tumor cells. This effect is amplified by the delivery of interleukin-2, which directly promotes the expansion of activated T cells, further boosting the immune response.[213]

Nanomaterials designed for in situ genetic reprogramming of T cells have also emerged as a strategy, allowing T cells to be engineered directly within the body, bypassing the need for ex vivo manipulation.[214] One approach utilizes poly(β-amino ester) (PBAE) polymers, which are functionalized with T cell-specific antibodies and nuclear localization signals to facilitate nuclear delivery of the cargo.[215] In this method, the cargo was a plasmid encoding a leukemia-specific chimeric antigen receptor (CAR), consequently triggering sustained CAR expression in T cells. Upon

intravenous injection, these nanoparticles successfully reprogrammed endogenous T cells into leukemia-specific CAR-T cells.[215]

In summary, programming functional T cell-synthetic material interactions is a rapidly evolving and diverse field.[206,212,214,216,217] While much of the research to date has concentrated on extracellular T cell-material interactions – such as biomaterial scaffolds for cell delivery[203], artificial antigen presentation platforms[207] and systems for the targeted delivery and release of immunomodulators[210] – there is still significant untapped potential in exploiting intracellular material-cell interactions to further enhance T cell function. These intracellular approaches could offer new avenues to augment the efficacy of immunotherapies by modulating cellular processes from within T cells. As research into nanomaterials for immunotherapeutic applications continues to evolve, deeper investigation of both extracellular and intracellular T cell-material interactions will be essential for the strategic development of new synthetic nanomaterials that can further advance the field of cancer immunotherapy.

References

1 Alberts, B. *et al. Molecular Biology of the Cell.* 6. edn, (W. W. Norton & Company, 2014).

2 Tu, Y. *et al.* Mimicking the Cell: Bio-Inspired Functions of Supramolecular Assemblies. *Chem. Rev.* **116**, 2023–2078 (2016).

3 Qi, G.-B., Gao, Y.-J., Wang, L. & Wang, H. Self-Assembled Peptide-Based Nanomaterials for Biomedical Imaging and Therapy. *Adv. Mater.* **30**, 1703444 (2018).

4 Bradshaw, D. M. & Arceci, R. J. Clinical relevance of transmembrane drug efflux as a mechanism of multidrug resistance. *J. Clin. Oncol.* **16**, 3674–3690 (1998).

5 Cheng, D.-B. *et al.* Autocatalytic Morphology Transformation Platform for Targeted Drug Accumulation. *J. Am. Chem. Soc.* **141**, 4406–4411 (2019).

6 Pieszka, M. *et al.* Controlled Supramolecular Assembly inside Living Cells by Sequential Multi-staged Chemical Reactions. *J. Am. Chem. Soc.* **142**, 15780-15789 (2020).

7 Yang, P.-P. *et al.* Host Materials Transformable in Tumor Microenvironment for Homing Theranostics. *Adv. Mater.* **29**, 1605869 (2017).

8 Waqas, M. *et al.* pH-Dependent In-Cell Self-Assembly of Peptide Inhibitors Increases the Anti-Prion Activity While Decreasing the Cytotoxicity. *Biomacromolecules* **18**, 943–950 (2017).

9 Liang, G., Ren, H. & Rao, J. A biocompatible condensation reaction for controlled assembly of nanostructures in living cells. *Nat. Chem.* **2**, 54–60 (2009).

10 Dong, B. *et al.* Reversible Self-Assembly of Nanoprobes in Live Cells for Dynamic Intracellular pH Imaging. *ACS Nano* **13**, 1421–1432 (2019).

11 Cheng, Z. *et al.* Self-assembly of pentapeptides into morphology-adaptable nanomedicines for enhanced combinatorial chemo-photodynamic therapy. *Nano Today* **33**, 100878 (2020).

12 Guo, W.-W. *et al.* Intracellular Restructured Reduced Glutathione-Responsive Peptide Nanofibers for Synergetic Tumor Chemotherapy. *Biomacromolecules* **21**, 444–453 (2020).

13 Du, W. *et al.* Increasing Photothermal Efficacy by Simultaneous Intra- and Intermolecular Fluorescence Quenching. *Adv. Funct. Mater.* **30**, 1908073 (2020).

14 Cheng, D.-B. *et al.* Endogenous Reactive Oxygen Species-Triggered Morphology Transformation for Enhanced Cooperative Interaction with Mitochondria. *J. Am. Chem. Soc.* **141**, 7235–7239 (2019).

15 An, H.-W. *et al.* Bio-orthogonally Deciphered Binary Nanoemitters for Tumor Diagnostics. *ACS Appl. Mater. Interfaces* **8**, 19202-19207 (2016).

16 Chen, Z. *et al.* Exploring the Condensation Reaction between Aromatic Nitriles and Amino Thiols To Optimize In Situ Nanoparticle Formation for the Imaging of Proteases and Glycosidases in Cells. *Angew. Chem. Int. Ed.* **59**, 3272-3279 (2020).

17 Feng, Z. *et al.* Enzymatic Assemblies Disrupt the Membrane and Target Endoplasmic Reticulum for Selective Cancer Cell Death. *J. Am. Chem. Soc.* **140**, 9566–9573 (2018).

18 Gao, Y., Shi, J., Yuan, D. & Xu, B. Imaging enzyme-triggered self-assembly of small molecules inside live cells. *Nat. Commun.* **3**, 1033 (2012).

19 Kim, B. J., Fang, Y., He, H. & Xu, B. Trypsin-Instructed Self-Assembly on Endoplasmic Reticulum for Selectively Inhibiting Cancer Cells. *Adv. Healthcare Mater.* **10**, 2000416 (2021).

20 Wu, C., Zhang, R., Du, W., Cheng, L. & Liang, G. Alkaline Phosphatase-Triggered Self-Assembly of Near-Infrared Nanoparticles for the Enhanced Photoacoustic Imaging of Tumors. *Nano Lett.* **18**, 7749–7754 (2018).

21 Ye, D., Liang, G., Ma, M. L. & Rao, J. Controlling Intracellular Macrocyclization for the Imaging of Protease Activity. *Angew. Chem. Int. Ed.* **50**, 2275–2279 (2011).

22 Zheng, R. *et al.* Controllable Self-Assembly of Peptide-Cyanine Conjugates In Vivo as Fine-Tunable Theranostics. *Angew. Chem. Int. Ed.* **60**, 7809 –7819 (2021).

23 Krauss, G. *Biochemistry of Signal Transduction and Regulation*. 5. edn, (Wiley-VCH, 2014).

24 Ornes, S. Core Concept: How nonequilibrium thermodynamics speaks to the mystery of life. *Proc. Natl. Acad. Sci. U.S.A.* **114**, 423–424 (2017).

25 Dickinson, B. C. & Chang, C. J. Chemistry and biology of reactive oxygen species in signaling or stress responses. *Nat. Chem. Biol.* **7**, 504–511 (2011).

26 Geiszt, M. & Leto, T. L. The Nox Family of NAD(P)H Oxidases: Host Defense and Beyond. *J. Biol. Chem.* **279**, 51715–51718 (2004).

27 Estrela, J. M., Obrador, E., Navarro, J., De La Vega, M. C. L. & Pellicer, J. A. Elimination of Ehrlich tumours by ATP-induced growth inhibition, glutathione depletion and X-rays. *Nat. Med.* **1**, 84–88 (1995).

28 Casey, J. R., Grinstein, S. & Orlowski, J. Sensors and regulators of intracellular pH. *Nat. Rev. Mol. Cell Biol.* **11**, 50–61 (2009).

29 Kaplowitz, N. The importance and regulation of hepatic glutathione. *Yale J. Biol. Med.* **54**, 497 (1981).

30 Hanahan, D. & Weinberg, R. A. The Hallmarks of Cancer. *Cell* **100**, 57–70 (2000).

31 Martínez-Reyes, I. & Chandel, N. S. Cancer metabolism: looking forward. *Nat. Rev. Cancer* **21**, 669–680 (2021).

32 Bradley, G. & Ling, V. P-glycoprotein, multidrug resistance and tumor progression. *Cancer Metastasis Rev.* **13**, 223–233 (1994).

33 Estrela, J. M., Ortega, A. & Obrador, E. Glutathione in Cancer Biology and Therapy. *Crit. Rev. Clin. Lab. Sci.* **43**, 143–181 (2006).

34 Lu, Y., Aimetti, A. A., Langer, R. & Gu, Z. Bioresponsive materials. *Nat. Rev. Mater.* **2**, 16075 (2016).

35 Yuan, Y., Kwok, R. T. K., Tang, B. Z. & Liu, B. Targeted Theranostic Platinum(IV) Prodrug with a Built-In Aggregation-Induced Emission Light-Up Apoptosis Sensor for Noninvasive Early Evaluation of Its Therapeutic Responses in Situ. *J. Am. Chem. Soc.* **136**, 2546-2554 (2014).

36 Yuan, Y. *et al.* Specific Light-Up Bioprobe with Aggregation-Induced Emission and Activatable Photoactivity for the Targeted and Image-Guided Photodynamic Ablation of Cancer Cells. *Angew. Chem. Int. Ed.* **54**, 1780–1786 (2015).

37 Shi, Y., Conde, J. & Azevedo, H. S. in *Peptides and Peptide-based Biomaterials and their Biomedical Applications. Advances in Experimental Medicine and Biology* Vol. 1030 (eds Sunna Anwar, Andrew Care, & Peter L. Bergquist) 265–278 (Springer, 2017).

38 Copolovici, D. M., Langel, K., Eriste, E. & Langel, Ü. Cell-Penetrating Peptides: Design, Synthesis, and Applications. *ACS Nano* **8**, 1972–1994 (2014).

39 Walrant, A., Bechara, C., Alves, I. D. & Sagan, S. Molecular partners for interaction and cell internalization of cell-penetrating peptides: how identical are they? *Nanomedicine* **7**, 133–143 (2011).

40 Richard, J. P. *et al.* Cellular Uptake of Unconjugated TAT Peptide Involves Clathrin-dependent Endocytosis and Heparan Sulfate Receptors. *J. Biol. Chem.* **280**, 15300–15306 (2005).

41 Duchardt, F., Fotin-Mleczek, M., Schwarz, H., Fischer, R. & Brock, R. A Comprehensive Model for the Cellular Uptake of Cationic Cell-penetrating Peptides. *Traffic* **8**, 848–866 (2007).

42 LeCher, J. C., Nowak, S. J. & McMurry, J. L. Breaking in and busting out: cell-penetrating peptides and the endosomal escape problem. *Biomol. Concepts* **8**, 131–141 (2017).

43 Caswell, P. T., Vadrevu, S. & Norman, J. C. Integrins: masters and slaves of endocytic transport. *Nat. Rev. Mol. Cell Biol.* **10**, 843–853 (2009).

44 An, H.-W. *et al.* A tumour-selective cascade activatable self-detained system for drug delivery and cancer imaging. *Nat. Commun.* **10**, 4861 (2019).

45 Fang, J., Nakamura, H. & Maeda, H. The EPR effect: Unique features of tumor blood vessels for drug delivery, factors involved, and limitations and augmentation of the effect. *Adv. Drug Delivery Rev.* **63**, 136–151 (2011).

46 Chen, Z., Chen, M., Zhou, K. & Rao, J. Pre-targeted Imaging of Protease Activity through In Situ Assembly of Nanoparticles. *Angew. Chem. Int. Ed.* **59**, 7864–7870 (2020).

47 Li, J. *et al.* Enzyme-Instructed Intracellular Molecular Self-Assembly to Boost Activity of Cisplatin Against Drug-Resistant Ovarian Cancer Cells. *Angew. Chem. Int. Ed.* **54**, 13307–13311 (2015).

48 Ellis, R. J. Macromolecular crowding: an important but neglected aspect of the intracellular environment. *Curr. Opin. Struct. Biol.* **11**, 114–119 (2001).

49 Feng, Z. *et al.* Artificial Intracellular Filaments. *Cell Rep. Phys. Sci.* **1**, 100085 (2020).

50 Hansen, R. E., Roth, D. & Winther, J. R. Quantifying the global cellular thiol–disulfide status. *Proc. Natl. Acad. Sci. U.S.A.* **106**, 422–427 (2009).

51 Veal, E. A., Day, A. M. & Morgan, B. A. Hydrogen Peroxide Sensing and Signaling. *Mol. Cell* **26**, 1–14 (2007).

52 Wang, H. *et al.* Integrating Enzymatic Self-Assembly and Mitochondria Targeting for Selectively Killing Cancer Cells without Acquired Drug Resistance. *J. Am. Chem. Soc.* **138**, 16046–16055 (2016).

53 Qiao, S.-L., Ma, Y., Wang, Y., Lin, Y.-X. & Wang, H. General Approach of Stimuli-Induced Aggregation for Monitoring Tumor Therapy. *ACS Nano* **11**, 7301–7311 (2017).

54 Yuan, Y. *et al.* Casp3/7-Instructed Intracellular Aggregation of Fe3O4 Nanoparticles Enhances T2 MR Imaging of Tumor Apoptosis. *Nano Lett.* **16**, 2686–2691 (2016).

55 Ding, Z. *et al.* Furin-Controlled Fe3O4 Nanoparticle Aggregation and 19F Signal "Turn-On" for Precise MR Imaging of Tumors. *Adv. Funct. Mater.* **29**, 1903860 (2019).

56 Chen, J. *et al.* Furin-Instructed Intracellular Gold Nanoparticle Aggregation for Tumor Photothermal Therapy. *Adv. Funct. Mater.* **30**, 2001566 (2020).

57 Yamamoto, S. *et al.* Microenvironment pH-Induced Selective Cell Death for Potential Cancer Therapy Using Nanofibrous Self-Assembly of a Peptide Amphiphile. *Biomacromolecules* **22**, 2524–2531 (2021).

58 Tanaka, A. *et al.* Cancer cell death induced by the intracellular self-assembly of an enzyme-responsive supramolecular gelator. *J. Am. Chem. Soc.* **137**, 770-775 (2015).

59 He, P.-P., Li, X.-D., Wang, L. & Wang, H. Bispyrene-Based Self-Assembled Nanomaterials: In Vivo Self-Assembly, Transformation, and Biomedical Effects. *Acc. Chem. Res.* **52**, 367-378 (2019).

60 Wang, L. *et al.* Supramolecular Nano-Aggregates Based on Bis(Pyrene) Derivatives for Lysosome-Targeted Cell Imaging. *J. Phys. Chem. C* **117**, 26811–26820 (2013).

61 Wang, D. *et al.* Highly Efficient Photosensitizers with Far-Red/Near-Infrared Aggregation-Induced Emission for In Vitro and In Vivo Cancer Theranostics. *Adv. Mater.* **30**, 1802105 (2018).

62 Zheng, Z. *et al.* Bright Near-Infrared Aggregation-Induced Emission Luminogens with Strong Two-Photon Absorption, Excellent Organelle Specificity, and Efficient Photodynamic Therapy Potential. *ACS Nano* **2018**, 8145–8159 (2018).

63 Niu, G. *et al.* Highly photostable two-photon NIR AIEgens with tunable organelle specificity and deep tissue penetration. *Biomaterials* **208**, 8145–8159 (2019).

64 Zhang, T. *et al.* In Situ Monitoring Apoptosis Process by a Self-Reporting Photosensitizer. *J. Am. Chem. Soc.* **141**, 5612–5616 (2019).

65 Levin, A. *et al.* Biomimetic peptide self-assembly for functional materials. *Nat. Rev. Chem.* **4**, 615-634 (2020).

66 Wang, H., Feng, Z. & Xu, B. Assemblies of Peptides in a Complex Environment and their Applications. *Angew. Chem. Int. Ed.* **58**, 10423–10432 (2019).

67 Hendricks, M. P., Sato, K., Palmer, L. C. & Stupp, S. I. Supramolecular Assembly of Peptide Amphiphiles. *Acc. Chem. Res.* **50**, 2440–2448 (2017).

68 Bakshi, R. *et al.* A Chemotactic Functional Scaffold with VEGF-Releasing Peptide Amphiphiles Facilitates Bone Regeneration by BMP-2 in a Large-Scale Rodent Cranial Defect Model. *Plast. Reconstr. Surg.* **147**, 386–397 (2020).

69 Zhou, S. *et al.* Bioactive peptide amphiphile nanofiber gels enhance burn wound healing. *Burns* **45**, 1112–1121 (2019).

70 Yuan, Y. & Liang, G. A biocompatible, highly efficient click reaction and its applications. *Org. Biomol. Chem.* **12**, 865–871 (2014).

71 Li, M. *et al.* Proline Isomerization-Regulated Tumor Microenvironment-Adaptable Self-Assembly of Peptides for Enhanced Therapeutic Efficacy. *Nano Lett.* **19**, 7965–7976 (2019).

72 Kuang, Y. & Xu, B. Disruption of the Dynamics of Microtubules and Selective Inhibition of Glioblastoma Cells by Nanofibers of Small Hydrophobic Molecules. *Angew. Chem. Int. Ed.* **52**, 6944–6948 (2013).

73 Jin, S. *et al.* Spatiotemporal Self-Assembly of Peptides Dictates Cancer-Selective Toxicity. *Biomacromolecules* **21**, 4806–4813 (2020).

74 Jeena, M. T. *et al.* Heterochiral Assembly of Amphiphilic Peptides Inside the Mitochondria for Supramolecular Cancer Therapeutics. *ACS Nano* **13**, 11022-11033 (2019).

75 Jeena, M. T. *et al.* Mitochondria localization induced self-assembly of peptide amphiphiles for cellular dysfunction. *Nat. Commun.* **8**, 26 (2017).

76 Ng, D. Y. W. *et al.* Directing intracellular supramolecular assembly with N-heteroaromatic quaterthiophene analogues. *Nat. Commun.* **8**, 1850 (2017).

77 Wang, H., Feng, Z., Tan, W. & Xu, B. Assemblies of d-Peptides for Targeting Cell Nucleolus. *Bioconjugate Chem.* **30**, 2528-2532 (2019).

78 Sies, H. Glutathione and its role in cellular functions. *Free Radical Biol. Med.* **27**, 916–921 (1999).

79 Lu, S. C. Regulation of hepatic glutathione synthesis: current concepts and controversies. *FASEB J.* **13**, 1169–1183 (1999).

80 Carretero, J. *et al.* Growth-associated changes in glutathione content correlate with liver metastatic activity of B16 melanoma cells. *Clin. Exp. Metastasis* **17**, 567–574 (1999).

81 Gamcsik, M. P., Kasibhatla, M. S., Teeter, S. D. & Colvin, O. M. Glutathione levels in human tumors. *Biomarkers* **17**, 671–691 (2012).

82 Depeille, P., Cuq, P., Passagne, I., Evrard, A. & Vian, L. Combined effects of GSTP1 and MRP1 in melanoma drug resistance. *Br. J. Cancer* **93**, 216–223 (2005).

83 Quinn, J. F., Whittaker, M. R. & Davis, T. P. Glutathione responsive polymers and their application in drug delivery systems. *Polym. Chem.* **8**, 97–126 (2016).

84 Zhan, J., Cai, Y., He, S., Wang, L. & Yang, Z. Tandem Molecular Self-Assembly in Liver Cancer Cells. *Angew. Chem. Int. Ed.* **57**, 1813–1816 (2018).

85 Spooner, R. & Yilmaz, Ö. The Role of Reactive-Oxygen-Species in Microbial Persistence and Inflammation. *Int. J. Mol. Sci.* **12**, 334 (2011).

86 D'Autréaux, B. & Toledano, M. B. ROS as signalling molecules: mechanisms that generate specificity in ROS homeostasis. *Nat. Rev. Mol. Cell Biol.* **8**, 813–824 (2007).

87 Houstis, N., Rosen, E. D. & Lander, E. S. Reactive oxygen species have a causal role in multiple forms of insulin resistance. *Nature* **440**, 944–948 (2006).
88 Touyz, R. M. & Schiffrin, E. L. Reactive oxygen species in vascular biology: implications in hypertension. *Histochem. Cell Biol.* **122**, 339–352 (2004).
89 Behrend, L., Henderson, G. & Zwacka, R. M. Reactive oxygen species in oncogenic transformation. *Biochem. Soc. Trans.* **31**, 1441–1444 (2003).
90 Wu, W.-S. The signaling mechanism of ROS in tumor progression. *Cancer Metastasis Rev.* **25**, 695–705 (2006).
91 Trachootham, D., Alexandre, J. & Huang, P. Targeting cancer cells by ROS-mediated mechanisms: a radical therapeutic approach? *Nat. Rev. Drug Discovery* **8**, 579–591 (2009).
92 Liu, B. & Thayumanavan, S. Mechanistic Investigation on Oxidative Degradation of ROS-Responsive Thioacetal/Thioketal Moieties and Their Implications. *Cell Rep. Phys. Sci.* **1**, 100271 (2020).
93 Li, L.-L. *et al.* Intracellular construction of topology-controlled polypeptide nanostructures with diverse biological functions. *Nat. Commun.* **8**, 1276 (2017).
94 He, H., Guo, J., Lin, X. & Xu, B. Enzyme-Instructed Assemblies Enable Mitochondria Localization of Histone H2B in Cancer Cells. *Angew. Chem. Int. Ed.* **59**, 9330–9334 (2020).
95 Dragulescu-Andrasi, A., Kothapalli, S.-R., Tikhomirov, G. A., Rao, J. & Gambhir, S. S. Activatable Oligomerizable Imaging Agents for Photoacoustic Imaging of Furin-Like Activity in Living Subjects. *J. Am. Chem. Soc.* **135**, 11015–11022 (2013).
96 Liu, Y. *et al.* Enzyme-Controlled Intracellular Self-Assembly of 18F Nanoparticles for Enhanced MicroPET Imaging of Tumor. *Theranostics* **5**, 1058 (2015).
97 Miao, Q. *et al.* Intracellular self-assembly of nanoparticles for enhancing cell uptake. *Chem. Commun.* **48**, 9738–9740 (2012).
98 Yuan, Y. *et al.* Furin-Mediated Self-Assembly of Olsalazine Nanoparticles for Targeted Raman Imaging of Tumors. *Angew. Chem. Int. Ed.* **60**, 3923–3927 (2020).
99 Yuan, Y. *et al.* Furin-mediated intracellular self-assembly of olsalazine nanoparticles for enhanced magnetic resonance imaging and tumour therapy. *Nat. Mater.* **18**, 1376–1383 (2019).
100 Yuan, Y. *et al.* Intracellular Self-Assembly of Taxol Nanoparticles for Overcoming Multidrug Resistance. *Angew. Chem. Int. Ed.* **54**, 9700–9704 (2015).
101 Hai, Z. *et al.* Smart Dual Quenching Strategy Enhances the Detection Sensitivity of Intracellular Furin. *Anal. Chem.* **90**, 1520–1524 (2018).
102 Shi, H. *et al.* Real-Time Monitoring of Cell Apoptosis and Drug Screening Using Fluorescent Light-Up Probe with Aggregation-Induced Emission Characteristics. *J. Am. Chem. Soc.* **134**, 17972–17981 (2012).
103 Ye, D. *et al.* Bioorthogonal cyclization-mediated in situ self-assembly of small-molecule probes for imaging caspase activity in vivo. *Nat. Chem.* **6**, 519–526 (2014).

104 He, H. *et al.* Enzymatic Cleavage of Branched Peptides for Targeting Mitochondria. *J. Am. Chem. Soc.* **140**, 1215–1218 (2018).
105 He, H. *et al.* Enzymatic Noncovalent Synthesis for Mitochondrial Genetic Engineering of Cancer Cells. *Cell Rep. Phys. Sci.* **1**, 100270 (2020).
106 He, H., Lin, X., Guo, J., Wang, J. & Xu, B. Perimitochondrial Enzymatic Self-Assembly for Selective Targeting the Mitochondria of Cancer Cells. *ACS Nano* **14**, 6947–6955 (2020).
107 Lin, Y.-X. *et al.* An in Situ Intracellular Self-Assembly Strategy for Quantitatively and Temporally Monitoring Autophagy. *ACS Nano* **11**, 1826–1839 (2017).
108 Gao, Y. *et al.* Probing Nanoscale Self-Assembly of Nonfluorescent Small Molecules inside Live Mammalian Cells. *ACS Nano* **7**, 9055–9063 (2013).
109 Gao, Y. *et al.* Imaging self-assembly dependent spatial distribution of small molecules in a cellular environment. *Langmuir* **29**, 15191–15200 (2013).
110 Tan, W. *et al.* Enzymatic Assemblies of Thiophosphopeptides Instantly Target Golgi Apparatus and Selectively Kill Cancer Cells. *Angew. Chem. Int. Ed.* **60**, 12796–12801 (2021).
111 He, H., Liu, S., Wu, D. & Xu, B. Enzymatically Formed Peptide Assemblies Sequestrate Proteins and Relocate Inhibitors to Selectively Kill Cancer Cells. *Angew. Chem. Int. Ed.* **59**, 16445–16450 (2020).
112 Yao, Q. *et al.* Synergistic enzymatic and bioorthogonal reactions for selective prodrug activation in living systems. *Nat. Commun.* **9**, 5032 (2018).
113 Yang, S. *et al.* Enzyme-triggered self-assembly of gold nanoparticles for enhanced retention effects and photothermal therapy of prostate cancer. *Chem. Commun.* **54**, 9841–9844 (2018).
114 Wang, J. *et al.* Cell-Compatible Nanoprobes for Imaging Intracellular Phosphatase Activities. *ChemBioChem* **20**, 526–531 (2019).
115 Tang, W., Yang, J., Zhao, Z., Lian, Z. & Liang, G. Intracellular coassembly boosts the anti-inflammation capacity of dexamethasone. *Nanoscale* **9**, 17717–17721 (2017).
116 Huang, A. *et al.* In situ enzymatic formation of supramolecular nanofibers for efficiently killing cancer cells. *RSC Adv.* **6**, 32519–32522 (2016).
117 Dong, L., Miao, Q., Hai, Z., Yuan, Y. & Liang, G. Enzymatic Hydrogelation-Induced Fluorescence Turn-Off for Sensing Alkaline Phosphatase in Vitro and in Living Cells. *Anal. Chem.* **87**, 6475–6478 (2015).
118 Feng, Z., Wang, H. & Xu, B. Instructed Assembly of Peptides for Intracellular Enzyme Sequestration. *J. Am. Chem. Soc.* **140**, 16433–16437 (2018).
119 Xu, T. *et al.* β-Galactosidase instructed supramolecular hydrogelation for selective identification and removal of senescent cells. *Chem. Commun.* **55**, 7175–7178 (2019).
120 Hai, Z. *et al.* γ-Glutamyltranspeptidase-Triggered Intracellular Gadolinium Nanoparticle Formation Enhances the T 2-Weighted MR Contrast of Tumor. *Nano Lett.* **19**, 2428–2433 (2019).
121 Zhang, M. *et al.* Directly observing intracellular nanoparticle formation with nanocomputed tomography. *Sci. Adv.* **6**, eaba3190 (2020).

122 Yang, Z. M., Xu, K. M., Guo, Z. F., Guo, Z. H. & Xu, B. Intracellular Enzymatic Formation of Nanofibers Results in Hydrogelation and Regulated Cell Death. *Adv. Mater.* **19**, 3152–3156 (2007).

123 Zhou, J., Du, X., Li, J., Yamagata, N. & Xu, B. Taurine Boosts Cellular Uptake of Small D-Peptides for Enzyme-Instructed Intracellular Molecular Self-Assembly. *J. Am. Chem. Soc.* **137**, 10040-10043 (2015).

124 Li, J. *et al.* Selectively Inducing Cancer Cell Death by Intracellular Enzyme-Instructed Self-Assembly (EISA) of Dipeptide Derivatives. *Adv. Healthcare Mater.* **6**, 1601400. (2017).

125 Li, J. *et al.* Kinetic Analysis of Nanostructures Formed by Enzyme-Instructed Intracellular Assemblies against Cancer Cells. *ACS Nano* **12**, 3804–3815 (2018).

126 López-Otín, C. & Bond, J. S. Proteases: Multifunctional Enzymes in Life and. *J. Biol. Chem.* **283**, 30433 (2008).

127 Molloy, S. S., Bresnahan, P. A., Leppla, S. H., Klimpel, K. R. & Thomas, G. Human furin is a calcium-dependent serine endoprotease that recognizes the sequence Arg-X-X-Arg and efficiently cleaves anthrax toxin protective antigen. *J. Biol. Chem.* **267**, 16396–16402 (1992).

128 Jaaks, P. & Bernasconi, M. The proprotein convertase furin in tumour progression. *Int. J. Cancer* **141**, 654–663 (2017).

129 Bassi, D. E., Fu, J., de Cicco, R. L. & Klein-Szanto, A. J. P. Proprotein convertases: "Master switches" in the regulation of tumor growth and progression. *Mol. Carcinog.* **44**, 151–161 (2005).

130 Ozden, S. *et al.* Inhibition of Chikungunya Virus Infection in Cultured Human Muscle Cells by Furin Inhibitors. *J. Biol. Chem.* **283**, 21899 - 21908 (2008).

131 Bestle, D. *et al.* TMPRSS2 and furin are both essential for proteolytic activation of SARS-CoV-2 in human airway cells. *Life Sci. Alliance* **3**, e202000786 (2020).

132 Li, J. & Yuan, J. Caspases in apoptosis and beyond. *Oncogene* **27**, 6194–6206 (2008).

133 Riedl, S. J. & Shi, Y. Molecular mechanisms of caspase regulation during apoptosis. *Nat. Rev. Mol. Cell Biol.* **5**, 897–907 (2004).

134 McComb, S. *et al.* Efficient apoptosis requires feedback amplification of upstream apoptotic signals by effector caspase-3 or -7. *Sci. Adv.* **5**, eaau9433 (2019).

135 Walsh, J. G. *et al.* Executioner caspase-3 and caspase-7 are functionally distinct proteases. *Proc. Natl. Acad. Sci. U.S.A.* **105**, 12815–12819 (2008).

136 Huang, R. *et al.* Multifunctional Fluorescent Probe for Sequential Detections of Glutathione and Caspase-3 in Vitro and in Cells. *Anal. Chem.* **85**, 6203-6207 (2013).

137 Tong, H. *et al.* Protein Detection and Quantitation by Tetraphenylethene-Based Fluorescent Probes with Aggregation-Induced Emission Characteristics. *J. Phys. Chem. B* **111**, 11817–11823 (2007).

138 Niu, G. *et al.* AIE luminogens as fluorescent bioprobes. *Trends Anal. Chem.* **123**, 115769 (2020).

139 Sharma, S. K., Straub, C. & Zawel, L. Development of Peptidomimetics Targeting IAPs. *Int. J. Pept. Res. Ther.* **12**, 21–32 (2006).

140 Deveraux, Q. L., Takahashi, R., Salvesen, G. S. & Reed, J. C. X-linked IAP is a direct inhibitor of cell-death proteases. *Nature* **388**, 300–304 (1997).

141 Blanco, G. & Blanco, A. *Medical Biochemistry*. (Academic Press, 2017).

142 Light, A. & Janska, H. Enterokinase (enteropeptidase): comparative aspects. *Trends Biochem. Sci.* **14**, 110–112 (1989).

143 Kitamoto, Y., Yuan, X., Wu, Q., McCourt, D. W. & Sadler, J. E. Enterokinase, the initiator of intestinal digestion, is a mosaic protease composed of a distinctive assortment of domains. *Proc. Natl. Acad. Sci. U.S.A.* **91**, 7588–7592 (1994).

144 Luengo-Gil, G. *et al.* Antithrombin controls tumor migration, invasion and angiogenesis by inhibition of enteropeptidase. *Sci. Rep.* **6**, 27544 (2016).

145 Moilanen, M. *et al.* Tumor-Associated Trypsinogen-2 (Trypsinogen-2) Activates Procollagenases (MMP-1, -8, -13) and Stromelysin-1 (MMP-3) and Degrades Type I Collagen. *Biochemistry* **42**, 5414–5420 (2003).

146 Yamamoto, H. *et al.* Association of trypsin expression with tumour progression and matrilysin expression in human colorectal cancer. *J. Pathol.* **199**, 176–184 (2003).

147 Soreide, K., Janssen, E. A., Körner, H. & Baak, J. Trypsin in colorectal cancer: molecular biological mechanisms of proliferation, invasion, and metastasis. *J. Pathol.* **209**, 147–156 (2006).

148 Miyata, S. *et al.* Expression of trypsin in human cancer cell lines and cancer tissues and its tight binding to soluble form of Alzheimer amyloid precursor protein in culture. *J. Biochem.* **125**, 1067–1076 (1999).

149 Hockla, A. *et al.* PRSS3/Mesotrypsin Is a Therapeutic Target for Metastatic Prostate Cancer. *Mol. Cancer Res.* **10**, 1555–1566 (2012).

150 Koivunen, E. *et al.* Tumor-associated Trypsin Participates in Cancer Cell-mediated Degradation of Extracellular Matrix. *Cancer Res.* **51**, 2107–2112 (1991).

151 Sorsa, T. *et al.* Activation of Type IV Procollagenases by Human Tumor-associated Trypsin-2. *J. Biol. Chem.* **272**, 21067–21074 (1997).

152 Vilen, S.-T. *et al.* Intracellular co-localization of trypsin-2 and matrix metalloprotease-9: possible proteolytic cascade of trypsin-2, MMP-9 and enterokinase in carcinoma. *Exp. Cell Res.* **314**, 914–926 (2008).

153 Podgorski, I. & Sloane, B. F. Cathepsin B and its role(s) in cancer progression. *Biochem. Soc. Symp.* **70**, 263–276 (2003).

154 Campo, E. *et al.* Cathepsin B expression in colorectal carcinomas correlates with tumor progression and shortened patient survival. *Am. J. Pathol.* **145**, 301–309 (1994).

155 Bengsch, F. *et al.* Cell type-dependent pathogenic functions of overexpressed human cathepsin B in murine breast cancer progression. *Oncogene* **33**, 4474–4484 (2014).

156 Malla, R. R. *et al.* Cathepsin B and uPAR knockdown inhibits tumor-induced angiogenesis by modulating VEGF expression in glioma. *Cancer Gene Ther.* **18**, 419–434 (2011).

157 Dheer, D., Nicolas, J. & Shankar, R. Cathepsin-sensitive nanoscale drug delivery systems for cancer therapy and other diseases. *Adv. Drug Delivery Rev.* **151-152**, 130–151 (2019).
158 Quantin, B., Murphy, G. & Breathnach, R. Pump-1 cDNA codes for a protein with characteristics similar to those of classical collagenase family members. *Biochemistry* **28**, 5327–5334 (1989).
159 Polette, M., Nawrocki-Raby, B., Gilles, C., Clavel, C. & Birembaut, P. Tumour invasion and matrix metalloproteinases. *Crit. Rev. Oncol. Hematol.* **49**, 179–186 (2004).
160 Xu, D. *et al.* Identification of New ATG4B Inhibitors Based on a Novel High-Throughput Screening Platform. *SLAS Discovery* **22**, 338–347 (2016).
161 Guo, J. Y., Xia, B. & White, E. Autophagy-Mediated Tumor Promotion. *Cell* **155**, 1216–1219 (2013).
162 Mathew, R., Karantza-Wadsworth, V. & White, E. Role of autophagy in cancer. *Nat. Rev. Cancer* **7**, 961–967 (2007).
163 Nixon, R. A. The role of autophagy in neurodegenerative disease. *Nat. Med.* **19**, 983–997 (2013).
164 Fujita, N. *et al.* An Atg4B Mutant Hampers the Lipidation of LC3 Paralogues and Causes Defects in Autophagosome Closure. *Mol. Biol. Cell* **19**, 4651–4659 (2008).
165 Yang, J., An, H.-W. & Wang, H. Self-Assembled Peptide Drug Delivery Systems. *ACS Appl. Bio Mater.* **4**, 24–46 (2021).
166 Gao, Y. *et al.* Enzyme-Instructed Molecular Self-assembly Confers Nanofibers and a Supramolecular Hydrogel of Taxol Derivative. *J. Am. Chem. Soc.* **131**, 13576-13577 (2009).
167 Debnath, S., Roy, S. & Ulijn, R. V. Peptide Nanofibers with Dynamic Instability through Nonequilibrium Biocatalytic Assembly. *J. Am. Chem. Soc.* **135**, 16789–16792 (2013).
168 Boekhoven, J., Hendriksen, W. E., Koper, G. J. M., Eelkema, R. & van Esch, J. H. Transient assembly of active materials fueled by a chemical reaction. *Science* **349**, 1075–1079 (2015).
169 Chagri, S., Ng, D. Y. W. & Weil, T. Designing bioresponsive nanomaterials for intracellular self-assembly. *Nat. Rev. Chem.* **6**, 320-338 (2022).
170 Hanahan, D. & Weinberg, R. A. Hallmarks of Cancer: The Next Generation. *Cell* **144**, 646–674 (2011).
171 Hanahan, D. Hallmarks of Cancer: New Dimensions. *Cancer Discov.* **12**, 31–46 (2022).
172 Gong, N., Sheppard, N. C., Billingsley, M. M., June, C. H. & Mitchell, M. J. Nanomaterials for T-cell cancer immunotherapy. *Nat. Nanotechnol.* **16**, 25–36 (2021).
173 Raskov, H., Orhan, A., Christensen, J. P. & Gögenur, I. Cytotoxic CD8+ T cells in cancer and cancer immunotherapy. *Br. J. Cancer* **124**, 359–367 (2021).
174 Germain, R. N. T-cell development and the CD4–CD8 lineage decision. *Nat. Rev. Immunol.* **2**, 309–322 (2002).
175 Luckheeram, R. V., Zhou, R., Verma, A. D. & Xia, B. CD4+T Cells: Differentiation and Functions. *J. Immunol. Res.*, 925135 (2012).

176 Wilson, C. B., Rowell, E. & Sekimata, M. Epigenetic control of T-helper-cell differentiation. *Nat. Rev. Immunol.* **9**, 91–105 (2009).
177 Erber, J. & Herndler-Brandstetter, D. Regulation of T cell differentiation and function by long noncoding RNAs in homeostasis and cancer. *Front. Immunol.* **14**, 1181499 (2023).
178 Kanno, Y., Vahedi, G., Hirahara, K., Singleton, K. & O'Shea, J. J. Transcriptional and Epigenetic Control of T Helper Cell Specification: Molecular Mechanisms Underlying Commitment and Plasticity. *Annu. Rev. Immunol.* **30**, 707–731 (2012).
179 Toscano, M. A. *et al.* Differential glycosylation of TH1, TH2 and TH-17 effector cells selectively regulates susceptibility to cell death. *Nat. Immunol.* **8**, 825–834 (2007).
180 Stinchcombe, J. C., Bossi, G., Booth, S. & Griffiths, G. M. The Immunological Synapse of CTL Contains a Secretory Domain and Membrane Bridges. *Immunity* **15**, 751–761 (2001).
181 Basu, R. *et al.* Cytotoxic T Cells Use Mechanical Force to Potentiate Target Cell Killing. *Cell* **165**, 100–110 (2016).
182 Thiery, J. *et al.* Perforin pores in the endosomal membrane trigger the release of endocytosed granzyme B into the cytosol of target cells. *Nat. Immunol.* **12**, 770–777 (2011).
183 Waldman, A. D., Fritz, J. M. & Lenardo, M. J. A guide to cancer immunotherapy: from T cell basic science to clinical practice. *Nat. Rev. Immunol.* **20**, 651–668 (2020).
184 Rosenberg, S. A. & Restifo, N. P. Adoptive cell transfer as personalized immunotherapy for human cancer. *Science* **348**, 62–68 (2015).
185 Rosenberg, S. A. *et al.* Use of Tumor-Infiltrating Lymphocytes and Interleukin-2 in the Immunotherapy of Patients with Metastatic Melanoma. *N. Engl. J. Med.* **319**, 1676-1680 (1988).
186 Rosenberg, S. A. *et al.* Durable Complete Responses in Heavily Pretreated Patients with Metastatic Melanoma Using T-Cell Transfer Immunotherapy. *Clin. Cancer Res.* **17**, 4550–4557 (2011).
187 Porter, D. L., Levine, B. L., Kalos, M., Bagg, A. & June, C. H. Chimeric Antigen Receptor–Modified T Cells in Chronic Lymphoid Leukemia. *N. Engl. J. Med.* **365**, 725-733 (2011).
188 June, C. H., O'Connor, R. S., Kawalekar, O. U., Ghassemi, S. & Milone, M. C. CAR T cell immunotherapy for human cancer. *Science* **359**, 1361–1365 (2018).
189 Lu, J. & Jiang, G. The journey of CAR-T therapy in hematological malignancies. *Mol. Cancer* **21**, 194 (2022).
190 Gong, J., Chehrazi-Raffle, A., Reddi, S. & Salgia, R. Development of PD-1 and PD-L1 inhibitors as a form of cancer immunotherapy: a comprehensive review of registration trials and future considerations. *J. ImmunoTher. Cancer* **6**, 8 (2018).
191 Pardoll, D. M. The blockade of immune checkpoints in cancer immunotherapy. *Nat. Rev. Cancer* **12**, 252–264 (2012).

192 Fife, B. T. & Bluestone, J. A. Control of peripheral T-cell tolerance and autoimmunity via the CTLA-4 and PD-1 pathways. *Immunol. Rev.* **224**, 166–182 (2008).

193 Intlekofer, A. M. & Thompson, C. B. At the Bench: Preclinical rationale for CTLA-4 and PD-1 blockade as cancer immunotherapy. *J. Leukocyte Biol.* **94**, 25–39 (2013).

194 Leach, D. R., Krummel, M. F. & Allison, J. P. Enhancement of Antitumor Immunity by CTLA-4 Blockade. *Science* **271**, 1734–1736 (1996).

195 Sahin, U. & Türeci, Ö. Personalized vaccines for cancer immunotherapy. *Science* **359**, 1355–1360 (2018).

196 Caruana, I. *et al.* Heparanase promotes tumor infiltration and antitumor activity of CAR-redirected T lymphocytes. *Nat. Med.* **21**, 524–529 (2015).

197 Motz, G. T. *et al.* Tumor endothelium FasL establishes a selective immune barrier promoting tolerance in tumors. *Nat. Med.* **20**, 607–615 (2014).

198 Chang, C.-H. *et al.* Metabolic Competition in the Tumor Microenvironment Is a Driver of Cancer Progression. *Cell* **162**, 1229–1241 (2015).

199 Hamieh, M. *et al.* CAR T cell trogocytosis and cooperative killing regulate tumour antigen escape. *Nature* **568**, 112–116 (2019).

200 Wang, W. *et al.* Endogenous Stimuli-Activatable Nanomedicine for Immune Theranostics for Cancer. *Adv. Funct. Mater.* **31**, 2100386 (2021).

201 Huang, Y. *et al.* Dual-mechanism based CTLs infiltration enhancement initiated by Nano-sapper potentiates immunotherapy against immune-excluded tumors. *Nat. Commun.* **11**, 622 (2020).

202 Zhang, F. *et al.* Nanoparticles That Reshape the Tumor Milieu Create a Therapeutic Window for Effective T-cell Therapy in Solid Malignancies. *Cancer Res.* **78**, 3718–3730 (2018).

203 Dellacherie, M. O., Seo, B. R. & Mooney, D. J. Macroscale biomaterials strategies for local immunomodulation. *Nat. Rev. Mater.* **4**, 379–397 (2019).

204 Stachowiak, A. N. & Irvine, D. J. Inverse opal hydrogel-collagen composite scaffolds as a supportive microenvironment for immune cell migration. *J. Biomed. Mater. Res. Part A* **85A**, 815–828 (2008).

205 Stephan, S. B. *et al.* Biopolymer implants enhance the efficacy of adoptive T-cell therapy. *Nat. Biotechnol.* **33**, 97–101 (2015).

206 Goldberg, M. S. Improving cancer immunotherapy through nanotechnology. *Nat. Rev. Cancer* **19**, 587–602 (2019).

207 Wauters, A. C. *et al.* Artificial Antigen-Presenting Cell Topology Dictates T Cell Activation. *ACS Nano* **16**, 15072–15085 (2022).

208 Perica, K. *et al.* Enrichment and Expansion with Nanoscale Artificial Antigen Presenting Cells for Adoptive Immunotherapy. *ACS Nano* **9**, 6861–6871 (2015).

209 Cheung, A. S., Zhang, D. K. Y., Koshy, S. T. & Mooney, D. J. Scaffolds that mimic antigen-presenting cells enable ex vivo expansion of primary T cells. *Nat. Biotechnol.* **36**, 160–169 (2018).

210 Tang, L. *et al.* Enhancing T cell therapy through TCR-signaling-responsive nanoparticle drug delivery. *Nat. Biotechnol.* **36**, 707–716 (2018).

211 Zhang, C. & Pu, K. Molecular and nanoengineering approaches towards activatable cancer immunotherapy. *Chem. Soc. Rev.* **49**, 4234–4253 (2020).
212 Li, F. *et al.* Nanomedicine for T-Cell Mediated Immunotherapy. *Adv. Mater.* **36**, 2301770 (2024).
213 Song, Q. *et al.* Tumor Microenvironment Responsive Nanogel for the Combinatorial Antitumor Effect of Chemotherapy and Immunotherapy. *Nano Lett.* **17**, 6366–6375 (2017).
214 Nie, S., Qin, Y., Ou, L., Chen, X. & Li, L. In Situ Reprogramming of Immune Cells Using Synthetic Nanomaterials. *Adv. Mater.* **36**, 2310168 (2024).
215 Smith, T. T. *et al.* In situ programming of leukaemia-specific T cells using synthetic DNA nanocarriers. *Nat. Nanotechnol.* **12**, 813–820 (2017).
216 Luo, Z. & Liu, X. Nanomaterials for cancer immunotherapy, what is the next? *Next Nanotechnology* **1**, 100006 (2023).
217 Parra-Nieto, J. *et al.* Stimuli-Responsive Nanocarriers as Active Enhancers of Antitumoral Immunotherapy. *Adv. Mater. Interfaces*, 2400343 (2024).

2. Motivation and Conceptual Design

Nature excels at creating biological functionality through structure formation across various scales, from the organization of multicellular tissues to the assembly of the cytoskeleton through dynamic protein interactions. These complex systems emerge from the collective behavior of many small units, with each component playing a critical role in achieving and maintaining overall function. Emulating this natural phenomenon using synthetic structures in complex biological environments has been a long-standing challenge in biomedical sciences and synthetic biology. Achieving this goal could pave the way for innovative therapeutic and diagnostic applications, leveraging synthetic nanostructures in areas such as tissue engineering and cancer therapy.

To construct synthetic assemblies in cellular environments for biological applications, various self-assembling molecules have been explored, each with distinct supramolecular properties. Among these, peptides, which are composed of amino acids, stand out as versatile bioinspired materials. Depending on their amino acid sequence and functionalization, peptides can be engineered to form a wide range of supramolecular structures, including coacervates, nanoparticles and nanofibers. The chemical design of these peptides is crucial, as it directly influences material properties and, consequently, material-cell interactions.

Creating synthetic functional structures within living cells presents significant challenges due to the highly complex, dynamic and crowded nature of the cellular

environment. In particular, successful programmed structure formation inside cells requires several prerequisites: the assembly precursor must enter the cell in a monomeric, non-assembled state; its transformation into the structure-forming monomer must be triggered by an intrinsic cue, such as changes in pH, reduction by glutathione or enzymatic conversion; and the resulting structures must functionally interact with natural cellular components to elicit the desired biological responses.

Current approaches for bioresponsive intracellular structure formation typically rely on a one-step transformation of the assembly precursor, often via the cleavage of a hydrophilic unit. However, a multi-step transformation strategy offers several advantages, as it allows for the incorporation of multiple bioresponsive elements into the chemical design of the precursor and provides greater control over the kinetics of monomer generation through individual reaction steps. Moreover, while existing systems have primarily aimed at disrupting cellular processes to induce damage and cell death, expanding this focus to include the creation of synthetic structures that can positively interact with cellular components opens new possibilities for programming material-cell interactions to enhance or modify cellular functions.

To address the challenge of creating functional synthetic assemblies in complex biological environments, this thesis focuses on two primary goals: first, designing peptide-based nanomaterials with tailored bioresponsiveness for triggered intracellular structure formation, and second, analyzing the impact of the resulting material-cell interactions on cellular functions (Fig. 2.1).

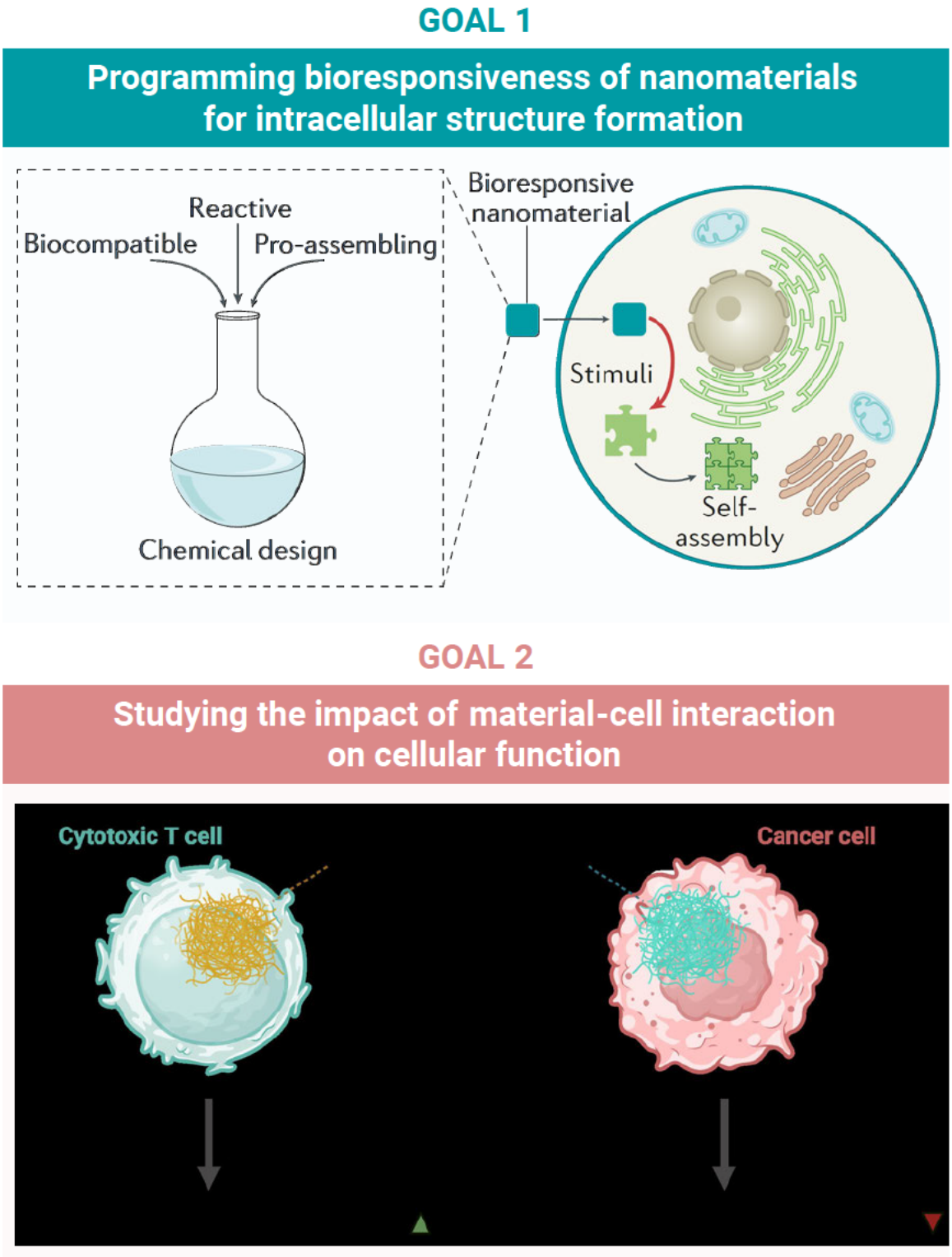

Figure 2.1 Scope of this thesis and overview of the two main goals.

To achieve the first goal, the chemical design of kinked isopeptides as assembly precursors was adapted to tune their responsiveness to different intracellular biological cues. These isopeptides feature an ester bond at a serine side chain,

replacing the conventional amide bond to the adjacent amino acid, thereby introducing a kinked molecular structure (Fig. 2.2). This kink serves a dual purpose: it prevents premature assembly and allows for the attachment of a bioresponsive protecting group to the amino group of the esterified serine. Upon removal of this protecting group, triggered by an intracellular stimulus, the isopeptide undergoes a rearrangement transforming into its linear isomer. To exploit this mechanism, glutathione, a reducing agent present in high concentrations within mammalian cells, was used as an intracellular trigger. A glutathione-responsive disulfide bridge was incorporated into an amino-protecting group at the central serine of the isopeptide, allowing for reductive cleavage. The reduction of this disulfide bridge and the subsequent removal of the protecting group in the reducing intracellular environment lead to the formation of self-assembling linear peptide monomers, which then assemble into supramolecular peptide nanostructures. This glutathione-responsive nanomaterial was used in two distinct projects: first, for stimulating the effector function of cytotoxic T cells to enhance their ability to kill cancer cells (Chapter 3) and second, for directly disrupting cellular processes inside drug-resistant breast cancer cells both in 2D cell culture and within 3D tumor spheroids (Chapter 4).

Additionally, an enzyme-responsive isopeptide design was developed featuring a sequence susceptible to proteolytic cleavage by the endoprotease furin (Chapter 5). Furin, a Golgi-associated protease overexpressed in many cancerous cells, is responsible for several aspects of disease development and progression. Incorporating the furin-specific cleavage sequence RVRR as an assembly-preventing unit in a kinked isopeptide expands the toolbox of bioresponsive moieties available for the chemical design of isopeptide assembly precursors. This diversification is crucial for tailoring nanomaterials to specific cellular and subcellular environments.

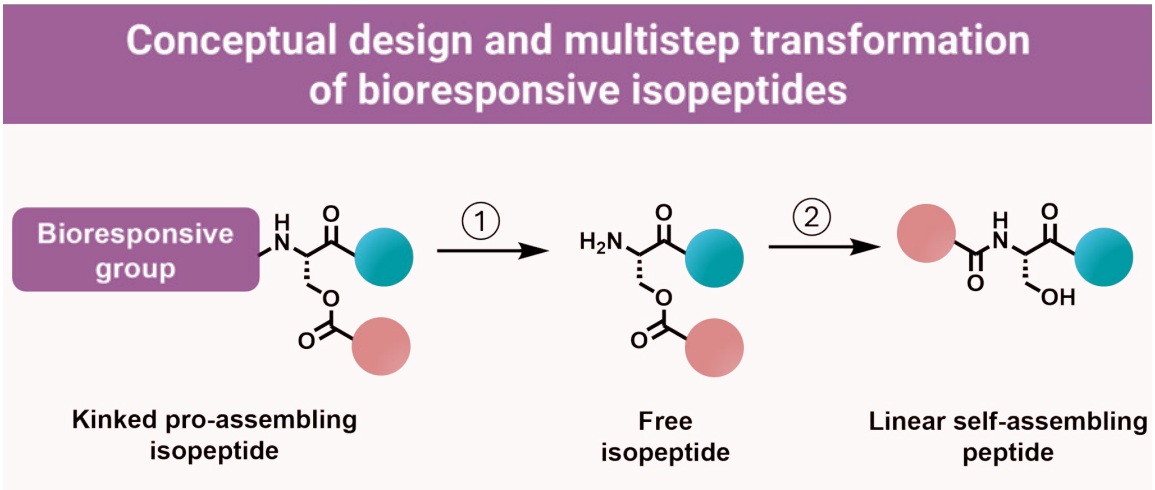

Figure 2.2 Design and bioresponsive transformation of a kinked pro-assembling isopeptide. The removal of the bioresponsive protecting group via a physiological stimulus (e.g., glutathione or furin) results in the formation of the free isopeptide (step 1). The rearrangement of the free isopeptide through an *O,N* acyl shift yields the linear self-assembling peptide (step 2). As the final product of the multistep transformation, the linear peptide can form supramolecular nanostructures inside cellular environments.

The second goal of studying the biological impact of the material-cell interactions of the intracellular nanostructures was pursued in the two aforementioned distinct cell types: cytotoxic T cells (Chapter 3) and cancer cells (Chapter 4).

Cytotoxic T cells are central to the targeted immune response against cancerous and virus-infected cells, making the stimulation of their cytotoxic effector function a key objective in immunotherapy. While recent advances in modulating T cell function have largely focused on genetic engineering and extracellular interactions with synthetic materials, such as scaffolding hydrogels for adoptive cell therapies or synthetic antigen-presenting platforms, the role of interactions with intracellular synthetic nanostructures remains unexplored. One of the objectives of this thesis was to address this gap by investigating the formation and biological impact of intracellular peptide nanostructures within cytotoxic T cells (Chapter 3). To assess the stimulatory potential of these synthetic assemblies, their effect on T cell cytotoxicity towards cancer cells was quantified. Mechanistic insights were further gained by analyzing mechanobiological changes in T cells with intracellular peptide nanostructures, along with alterations in protein phosphorylation, compared to

untreated cells. These insights can contribute to the field of immunotherapy by demonstrating how synthetic supramolecular materials can modulate immune cell function.

In cancer cells, intracellular peptide assembly offers a different therapeutic avenue by disrupting key organelles, such as mitochondria, leading to a significant reduction in mitochondrial respiration and metabolic activity (Chapter 4). The cytotoxic effect of intracellular structure formation was studied in both 2D cultured cells and 3D tumor spheroids, leading to a notable reduction in tumor spheroid size. These findings underscore the potential of peptide-based nanomaterials to directly disrupt cancer cells from within.

In summary, this thesis presents new approaches to developing peptide-based nanomaterials capable of forming functional supramolecular structures within living cells. By strategically designing and applying isopeptides with tailored bioresponsiveness, this interdisciplinary research bridges chemical design, material science and cellular biology, thereby advancing our understanding of programmed material-cell interactions.

3. Synthetic intracellular nanostructures enhance cytotoxic T cell function via assembly-driven chemical engineering

Authors

Sarah Chagri, Anna Burgstaller, Claudia Schirra, Julian Link, Zhixuan Zhou, Raphael Meyer, Jana Fetzer, Patrick Roth, Yong Ren, Shutian Si, Francesca Mazzotta, Manfred Wagner, Ingo Lieberwirth, Katharina Landfester, David Y.W. Ng, Oskar Staufer, Tanja Weil

Reproduced, with minor changes, from preprint 'Chagri, S.; Burgstaller, A.; Schirra, C.; Link, J.; Zhou, Z.; Roth, P.; Meyer, R.; Fetzer, J.; Ren, Y.; Si, S.; Mazzotta, F.; Wagner, M.; Lieberwirth, I.; Landfester, K.; Ng, D. Y. W.; Staufer, O.; Weil, T. Synthetic intracellular nanostructures enhance cytotoxic T cell function via assembly-driven chemical engineering. *ChemRxiv*, doi:10.26434/chemrxiv-2024-3lxgk (2024).'

Contributions

Sarah Chagri: Conceptualization, molecular design of peptides and planning of synthesis and experiments. Synthesis and characterization of peptides and associated molecules. LC-MS kinetic analysis, CD measurements and NMR analysis. Data analysis and interpretation of results. Writing of the manuscript.

Anna Burgstaller: RT-DC measurements and interpretation of results.

Claudia Schirra: CLEM measurements and interpretation of results.

Julian Link: Synthesis of peptides and TEM measurements for the analysis of peptide structure formation and interpretation of results.

Zhixuan Zhou: LC-MS kinetic analysis and interpretation of results.

Raphael Meyer: CD measurements and interpretation of results.

Patrick Roth: TEM measurements for the analysis of peptide structure formation and interpretation of results.

Jana Fetzer: Synthesis of peptides.

Yong Ren: Synthesis of peptides.

Manfred Wagner: Measuring and interpretation NMR spectra.

Shutian Si, Francesca Mazzotta, Ingo Lieberwirth, Katharina Landfester: Cryo-EM measurements and interpretation of results.

Oskar Staufer: Conceptualization and planning of experiments. Cell uptake experiments, imaging via CLSM, cytotoxicity assays and proteome profiler analysis. Editing of the manuscript.

David Y. W. Ng: Design and discussion on the concept and results. Editing of the manuscript.

Tanja Weil: Acquiring funding for the project, design and discussion of the concept and results. Editing of the manuscript.

Abstract

Nature achieves diverse biological functions through structure formation. Inspired by the controlled formation of polypeptide nanostructures in cells, synthetic methods have been developed to assemble artificial nanostructures and organelle-like compartments within living cells. While these synthetic intracellular assemblies have mostly been used to disrupt cellular processes, their potential to induce a gain of function within cells remains unexplored. Here, we introduce redox-sensitive *iso*peptides that transform into self-assembling linear peptides inside human cytotoxic T cells in response to intracellular levels of glutathione. The *in situ* formation of synthetic peptide nanostructures in cytotoxic T cells leads to cellular stiffening, establishing a direct interface between biochemically driven peptide assembly and mechanobiological effects. This change in biophysical properties, along with increased phosphorylation of signaling proteins associated with T cell activation, correlates with a significant enhancement in the efficacy of cytotoxic T cells to eliminate cancer cells. Our findings elucidate the cellular impact of synthetic peptide nanostructures assembled within living cytotoxic T cells and demonstrate their ability to modulate and enhance effector immune cell responses.

3.1. Introduction

Naturally occurring intracellular nanostructures, such as microtubules, actin filaments, and intermediate filaments that form the cytoskeleton, play a critical role in fundamental cellular processes, including metabolism, division and motility.[1] These complex, dynamic protein assemblies span the cytosol and provide a blueprint for the development of synthetic materials designed to form nanostructures in synthetic cells, a growing frontier in biomolecular engineering.[2] Moreover, the creation of synthetic architectures inside the complex environment of mammalian cells represents a significant milestone in nanomedicine and synthetic biology, providing a bottom-up approach that mimics natural intracellular assemblies and opens new avenues for supramolecular drug design.[3]

To date, advances in the creation of intracellular assemblies have primarily focused on the formation of synthetic nanostructures within cancerous cells with the goal of disrupting cellular metabolism and inducing apoptosis.[4,5] State-of-the-art strategies involve the use of bioresponsive molecules that can undergo chemical transformations in response to endogenous stimuli, enabling spatiotemporal control and selectivity over the assembly formation.[3,6-10] However, these efforts to construct synthetic intracellular nanostructures have so far been limited to malignant cells[4,5], leaving the potential to modulate the behavior of non-cancerous cells, particularly immune cells, unexplored.

Our work explores a new direction in this field by harnessing synthetic intracellular nanostructures for the immunomodulation of cytotoxic T cells. Cytotoxic $CD8^+$ T cells play a crucial role in the immune response by directly targeting and eliminating cancerous or virus-infected cells.[11] The unmatched specificity of T cells in recognizing target cells is a key advantage in T cell-based therapies and their efficacy in inducing apoptosis is tightly linked to their activation status, which

involves complex intracellular signaling pathways.[12] High cytotoxic effector function in T cells is desirable, as it enables a more robust and effective response against tumors, contributing to better therapeutic outcomes in adoptive cell therapy. The mechanical properties of T cells, such as stiffness and deformability, correlate with their activation and migration capabilities, as well as their ability to interact with target cells.[13] Enhancing the functional capacity of cytotoxic T cells by biochemical and biophysical means is therefore a central goal in immunotherapy.

In current clinical approaches, T cells are often modified outside the body through genetic engineering before being reinfused into the patient to combat cancer.[14,15] While ongoing efforts aim to enhance T cell efficacy by refining genetic engineering techniques, fewer strategies explore modulation of T cells through chemical engineering, for instance, via extracellular interactions with nanomaterials.[16-18] In our work, we propose a complementary strategy by intracellular chemical engineering: the *in situ* self-assembly of synthetic nanostructures within cytotoxic T cells to enhance T cell cytotoxicity. This approach holds the potential to further enhance T cell functionality beyond the limits of genetic modifications.

In T cells, glutathione, a reducing agent abundant in the cytosol[19], plays a critical role in maintaining redox homeostasis and facilitating metabolic reprogramming during T cell activation. It acts as an antioxidant to counterbalance the increased mitochondrial production of reactive oxygen species (ROS).[20-22] As ROS scavenging is essential for T cell activation, proliferation and effector function, activated T cells have been shown to contain significantly higher levels of intracellular glutathione compared to resting T cells.[21,23] Therefore, the glutathione-induced transformation of a bioresponsive assembly precursor within T cells is a promising strategy for the *in situ* generation of intracellular nanostructures that boost T cell activation dynamics and cytotoxic effector function against cancer cells. Shifting the focus

from disrupting malignant cells to enhancing the beneficial functions of healthy cells, such as cytotoxic T cells, will be a next-generation technology for more sophisticated cell-material interactions. Modulating the behavior of these immune cells through *in situ*-formed artificial nanostructures would also have significant implications for immunotherapy.

Herein, we introduce glutathione-responsive *iso*peptides capable of undergoing a multistep reaction cascade upon cellular entry, resulting in the *in situ* formation of peptide nanostructures inside human cytotoxic T cells (Fig. 3.1). We report a significant stimulatory effect of these peptide nanostructures on cytotoxic T cell function, leading to enhanced cytotoxicity against breast cancer cells. Using confocal laser scanning microscopy (CLSM) and correlative light and electron microscopy (CLEM), we visualize the formation and localization of these nanostructures. Importantly, the enhancement of T cell effector function is directly correlated with intracellular nanostructure formation. Additionally, we examine activation of stimulatory T cell signaling of peptide-treated versus untreated T cells and evaluate the impact of synthetic intracellular nanostructures on T cell mechanical properties. This analysis aims to elucidate the biophysical and molecular mechanisms driving the observed functional enhancements. To our knowledge, this is the first study to demonstrate that synthetic intracellular nanostructures can support and enhance beneficial cellular functions, offering a novel strategy to modulate immune cell responses.

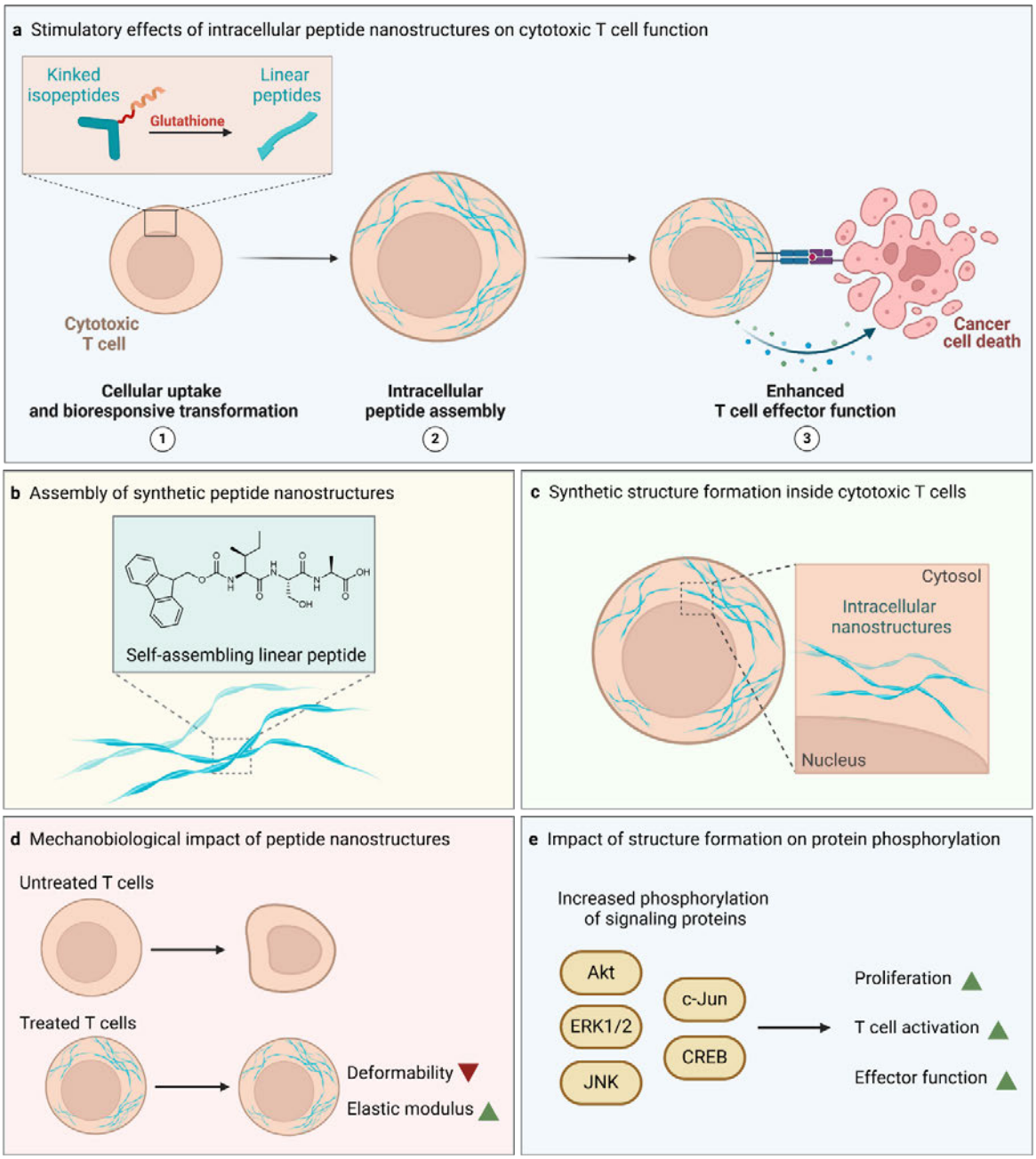

Figure 3.1. Schematic overview of T cell engineering through intracellular synthetic nanostructures. a | Glutathione-responsive kinked *iso*peptides undergo a bioresponsive transformation inside cytotoxic T cells, leading to the formation of linear, self-assembling peptides. This intracellular peptide assembly within human cytotoxic T cells enhances T cell-mediated cytotoxicity against cancer cells. **b** | The supramolecular properties and structural characteristics of the nanofiber-forming peptides were investigated. **c** | The *in situ* structure formation inside cytotoxic T cells was visualized using confocal laser scanning microscopy and correlative light and electron microscopy. **d** | Intracellular structure formation influences the mechanical properties of cytotoxic T cells, reducing their deformability and increasing the elastic modulus. **e** | Increased phosphorylation of key signaling proteins associated with T cell proliferation, activation, and effector function was observed following *in situ* nanostructure formation.

3.2. Results and Discussion

3.2.1. Design, synthesis and transformation of glutathione-responsive isopeptides

The glutathione-responsive *iso*peptide **1a**, along with the control *iso*peptide **1b**, consists of three key structural components: (1) the cell-penetrating peptide sequence TAT (transactivator of transcription) derived from human immunodeficiency virus (HIV), (2) a glutathione-responsive trigger group that can undergo reductive degradation and (3) the kinked *iso*peptide with an aromatic *N*-terminal group (Fig. 3.2a). This *N*-terminal group either promotes supramolecular assembly (Fmoc in **1a**) or prevents assembly of the linear product (NBD in **1b**) resulting from the glutathione-triggered transformation (Fig. 3.2a).

The synthesis of the kinked *iso*peptides **1a** and **1b** was achieved through a combination of solid-phase peptide synthesis and solution-phase synthesis (Scheme S3.1). To analyze the glutathione-induced transformation of the *iso*peptides (Fig. 3.2b), we investigated the kinetics of this multistep reaction cascade (Fig. 3.2b) using liquid chromatography-mass spectrometry (LC-MS) (Fig. 3.2c). By analyzing the *m/z* values of the emerging peaks in the LC traces, we identified and assigned the reactive intermediates and final products of the glutathione-induced conversion (Fig. 3.2c,d).

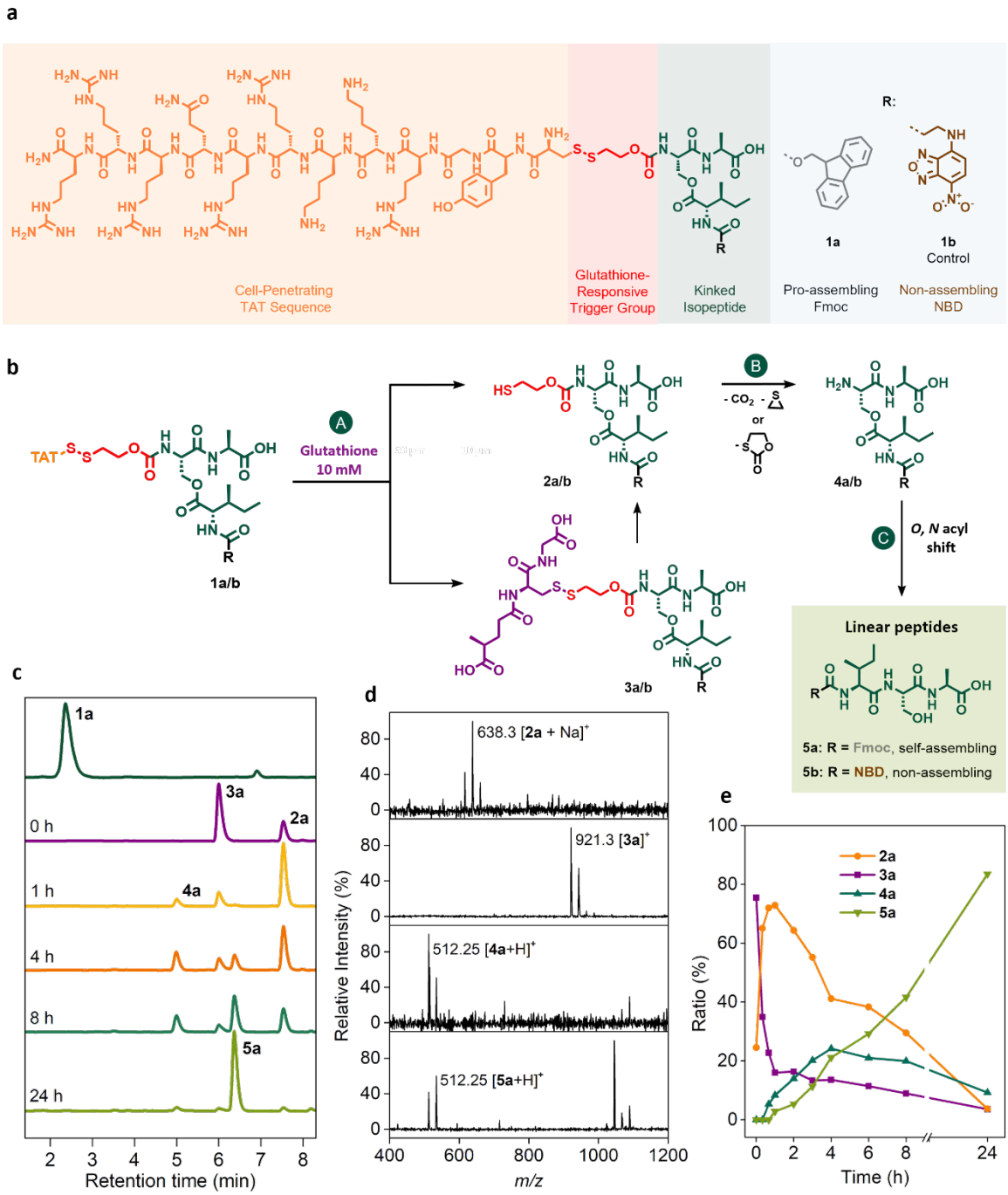

Figure 3.2. Chemical structure and multistep conversion of glutathione-responsive *iso*peptides. **a|** Chemical structures of glutathione-responsive *iso*peptides **1a** (with a Fmoc (9-fluorenylmethoxycarbonyl) group) and **1b** (with an NBD (nitrobenzodiazole) unit). **b|** Reaction scheme illustrating the multistep conversion of pro-assembling *iso*peptides **1a** or the control isopeptide **1b** into the self-assembling linear peptide **5a** or the non-assembling linear peptide **5b**. **c |** LC-MS kinetic analysis of the glutathione-induced linearization of **1a** in NH_4HCO_3 buffer (50 mM, pH 7.4) and methanol (v/v 1:1) in the presence of intracellular concentrations of glutathione (reduced glutathione: 10 mM; oxidized glutathione: 1 mM) at room temperature. **d |** Convoluted MS spectra identifying the intermediates **2a** (t_R = 7.53 min), **3a** (t_R = 6.00 min) and **4a** (t_R = 4.98 min) as well as the final linear peptide **5a** (t_R = 6.37 min) during the LC-MS analysis. **e |** Molar ratio of intermediates **2a**, **3a**, **4a** and final product **5a** after the addition of glutathione-containing buffer, based on the peak integration at 254 nm.

In the presence of intracellular levels of glutathione (reduced glutathione: 10 mM; oxidized glutathione: 1 mM)[24] in NH_4HCO_3 buffer (50 mM, pH 7.4), *iso*peptide **1a** underwent instant degradation, so that upon the first LC-MS injection, its signal (t_R = 2.36 min) was no longer detectable (Fig. 3.2c). Instead, two cleavage products, **2a** (t_R = 7.53 min) and **3a** (t_R = 6.00 min), were identified. These two intermediate products result from the nucleophilic attack of glutathione on the disulfide bond of **1a**, occurring at either of the two sulfur atoms (Fig. 3.2b). As the disulfide bond of the glutathione adduct **3a** is similarly susceptible to reductive cleavage, the transformation of **3a** also gave rise to the *iso*peptide with a free thiol group **2a** over time. After one hour, the unprotected *iso*peptide **4a** (t_R = 4.98 min) was detected as the product of the self-immolation of the trigger group (Fig. 2c). The subsequent *O,N* acyl shift caused the linearization of **4a**, indicated by the increasing peak corresponding to the linear peptide **5a** (t_R = 6.37 min). After 24 h, the linear self-assembling Fmoc-ISA **5a** became the most prominent peak in the LC trace (Fig. 3.2c), reflecting a conversion of 84% of the initial *iso*peptide **1a** into the self-assembling linear monomer **5a** (Fig. 3.2e).

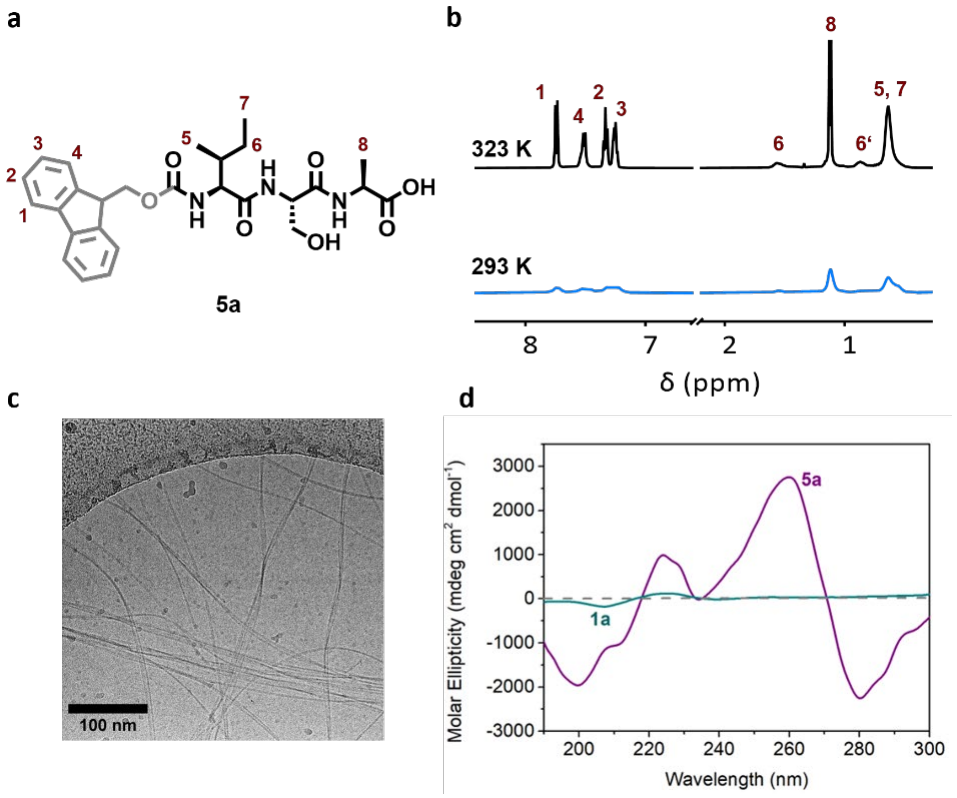

Figure 3.3. Supramolecular assembly of linear peptide. a | Chemical structure of **5a** with labeled protons. **b** | ^{1}H NMR analysis of self-assembly behavior of **5a** (1 mg/ml) in deuterated phosphate buffer (50 mM) and DMSO-d_6 (9:1) at 293 K and 323 K. **c** | Cryo-TEM image of peptide nanofibers formed by linear peptide **5a** (1 mg/ml) in Dulbecco's phosphate buffered saline (DPBS) (pH 7.4) and DMSO (99:1). Scale bar 100 nm. **d** | Circular dichroism spectra of linear peptide **5a** and *iso*peptide **1a** (500 µM each) in phosphate buffer (10 mM, pH 7.4). The spectrum of **5a** shows characteristic signals of attractive peptide backbone interactions and aromatic interactions between Fmoc groups, while the spectrum of **1a** shows no signals indicating chirality.

The supramolecular assembly behavior of the linear peptide **5a** was analyzed using nuclear magnetic resonance (NMR) spectroscopy, circular dichroism (CD) spectroscopy, transmission electron microscopy (TEM) and cryogenic transmission electron microscopy (cryo-TEM) (Fig. 3.3).

Temperature-dependent ^{1}H NMR spectroscopy of the linear peptide **5a** revealed significant peak broadening at room temperature (293 K), which is characteristic of supramolecular interactions between peptide monomers in aqueous solution (deuterated phosphate buffer (50 mM) and DMSO-d_6 (9:1)) (Fig. 3.3b and Fig. S3.21). Upon heating the solution to 323 K, sharp signals corresponding to the

aromatic Fmoc head group and side chain groups of peptide **5a** emerged (Fig. 3.3a,b), indicating a higher amount of detectable monomeric peptide **5a** in solution at elevated temperatures.

CD spectroscopy was used to further characterize the secondary structure of linear Fmoc-ISA **5a** and kinked *iso*peptide **1a** (Fig. 3.3d). The CD spectrum revealed a nanoscale chirality of the self-assembling peptide **5a**, which arises from the chiral arrangement of the peptide monomers within the assembled nanostructure.[25] The spectrum of **5a** displays a maximum at 260 nm that is characteristic for the $\pi \rightarrow \pi^*$ transitions of the aromatic Fmoc groups[26]. Additionally, another maximum was observed at 224 nm indicating a $n \rightarrow \pi^*$ transition of the carbonyl groups in the peptide backbone due to hydrogen bonding.[27,28] In contrast, the non-assembling kinked *iso*peptide **1a** showed no discernable chirality of the secondary structure, underlining the necessity of the transformation from kinked **1a** to linear **5a** to achieve the desired supramolecular interaction required for structure formation (Fig. 3.3d).

Dry-state TEM images of the linear peptide **5a** revealed its ability to self-assemble into long nanofibers in Dulbecco's phosphate buffered saline (DPBS) with 1% DMSO (Fig. S3.23). To investigate the impact of incorporating another linear peptide modified with a fluorophore, which is crucial for detecting nanostructures inside living cells, we studied the co-assembly of fluorescent Coumarin343-functionalized peptide **5c** with **5a** in a 5:1 ratio. TEM images confirmed that the presence of peptide **5c** did not disrupt nanofiber formation (Fig. S3.24). Similarly, when Cyanine5 (Cy5)-functionalized peptide **5d** was co-assembled with peptide **5a** at a 99:1 ratio, the nanofiber integrity was preserved. In contrast, co-assembly of the kinked assembly precursors **1a** and **1c** (Coumarin343-modified) (5:1 ratio) or **1a** and **1d** (Cy5-modified) (99:1 ratio) did not produce any observable superstructures (Fig. S3.24), emphasizing again the importance of the glutathione-

induced linearization to induce self-assembly. Additionally, the more hydrophilic nitrobenzodiazole (NBD)-modified control *iso*peptide **1b** and its corresponding linear peptide **5b** also did not form any nanostructures, which allows evaluating cellular uptake and glutathione-induced rearrangement without subsequent peptide assembly (Fig. S3.24).

Cryo-TEM provided further insights into the peptide nanostructures of the Fmoc-functionalized peptide **5a** in an aqueous environment (DPBS with 1% DMSO). Consistent with dry-state TEM, cryo-TEM images revealed long, thin nanofibers of linear peptide **5a** with a slightly twisted morphology (Fig. 3.3c and Fig. S3.25 and S3.26). The twisted fibers exhibited an average thickness of 6.8±0.3 nm at the twists and 11.0±0.2 nm at the non-twisted regions (Fig. S3.26). The critical aggregation concentration (CAC) of the linear peptides was determined via a Proteostat aggregation assay, which is a fluorescence-based technique used to detect β-sheet driven assembly formation. The CAC for linear peptide **5a** in DPBS with 1% DMSO was found to be 10 µM (Fig. S3.27). For the co-assemblies with either the Coumarin343-containing linear peptide **5c** (5:1 ratio) or the Cy5-modified linear peptide **5d** (99:1 ratio), the CAC was 9.2 µM and 4.6 µM, respectively (Fig. S3.27). These results further confirm that the incorporation of fluorescent monomers **5c** or **5d** does not hinder nanostructure formation.

In summary, our analysis demonstrates that the multistep conversion of kinked *iso*peptide **1a** into the linear self-assembling peptide **5a** can be effectively triggered by physiological levels of glutathione. Physicochemical characterization of linear peptide **5a** further reveals its ability to form peptide nanofibers at low micromolar concentrations, highlighting its potential for the *in situ* formation of synthetic nanostructures in the intracellular environment.

3.1.1. Cellular uptake and *in situ* formation of peptide nanostructures in T cells

Next, we explored the glutathione-induced conversion of the *iso*peptides into the corresponding linear peptides and subsequent nanostructure formation within cytotoxic T cells. First, primary human $CD8^+$ T cells were activated *ex vivo* by isolating them from healthy donors and co-incubating with anti-CD3/CD28 activation beads. This cross-linking of CD3 and CD28 receptors, combined with interleukin 2 (IL-2), induces T cell activation into an effector state and promotes polyclonal expansion.

We then investigated the uptake and co-assembly of the pro-assembling *iso*peptide **1a** together with a fluorescently labeled *iso*peptide (either **1c** with Coumarin343 or **1d** with Cy5) in these *ex vivo* expanded cytotoxic T cells (Fig. 3.4). CLSM of activated T cells treated with the *iso*peptides **1a:1c** (5:1) at 5 µM for 1 hour revealed the formation of fluorescent peptide nanostructures in the cytosol, the nucleus and in the perinuclear region, also visible as high-contrast regions in the brightfield images (Fig. 3.4a).

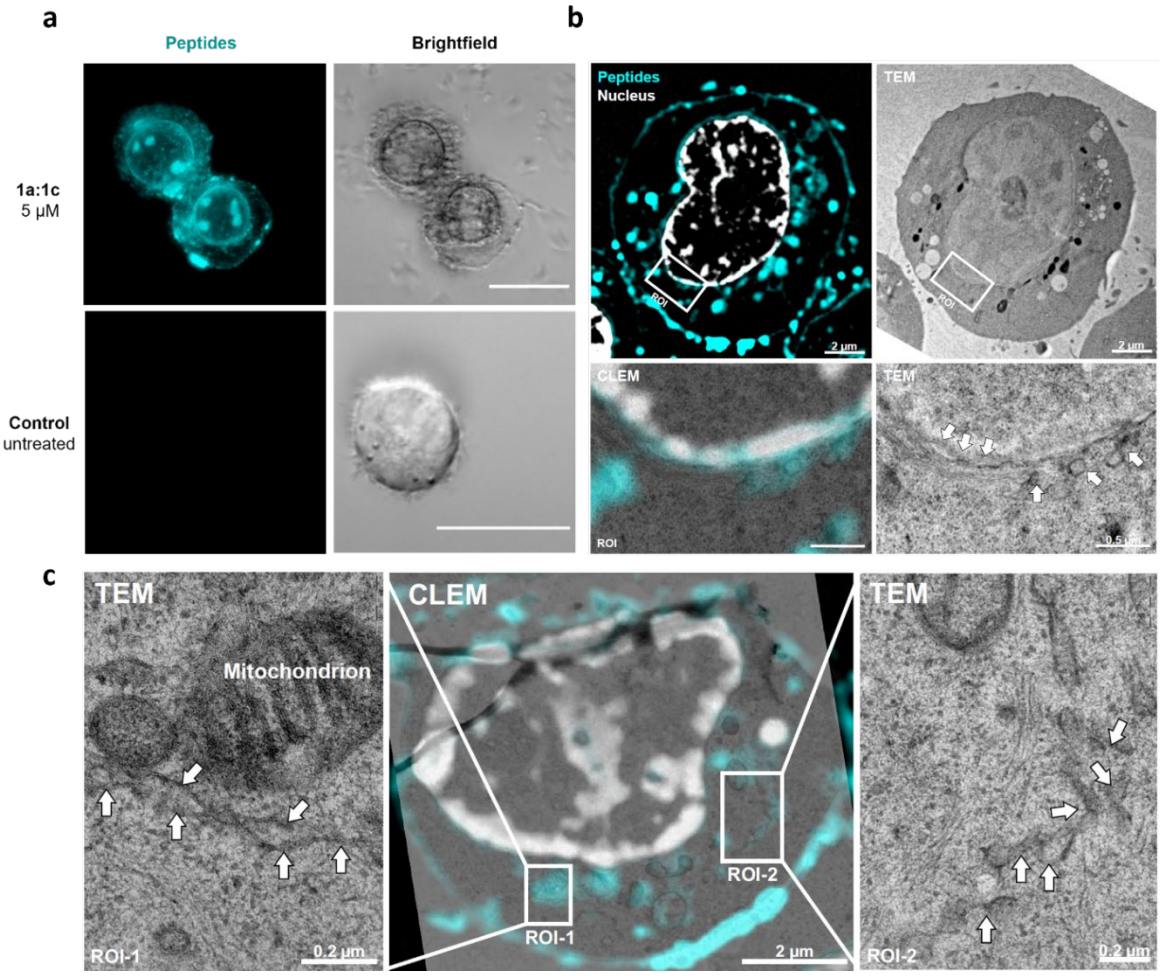

Figure 3.4 Cellular uptake and intracellular peptide nanostructure formation in cytotoxic T cells. **a** | Confocal laser scanning microscopy (CLSM) images of activated T cells incubated with 5 µM of glutathione-responsive isopeptides **1a** and **1c** (5:1) (cyan) for 1 hour, demonstrating the formation of intracellular peptide nanostructures in the cytosol and perinuclear region. Untreated T cells served as controls. Scale bar: 15 µm. **b** | Correlative light and electron microscopy (CLEM) images of activated human $CD8^+$ T cells treated with 5 µM of glutathione-responsive isopeptides **1a** and **1d** (99:1) (cyan) for 1 hour before freezing, highlighting the formation of fluorescent peptide nanostructures at the nuclear membrane and perinuclear region. **c** | CLEM images focusing on the localization of peptide nanostructures within the cytosol. The integrity of subcellular compartments of T cells appear unaffected by intracellular structure formation.

Further validation of in situ peptide assembly was conducted using CLEM (Fig. 3.4b,c). Pre-activated and *ex vivo* expanded cytotoxic T cells treated with *iso*peptides **1a:1d** (99:1) were analyzed, with Cy5-labeled *iso*peptide **1d** selected for co-assembly due to its superior fluorescence properties. CLEM images revealed fluorescent nanostructures distributed throughout the cytosol, perinuclear region, and at the cell membrane (Fig. 3.4b,c). The observed fiber thickness ranged from

approximately 3.5 to 7.5 nm, consistent with the cryo-EM findings for peptide nanofibers in buffered solution (see Fig. 3.3c). Importantly, despite the widespread presence of peptide nanostructures within the cytosol and near the nucleus, the overall integrity of the T cells, including organelles such as mitochondria, remained intact (Fig. 3.4b,c). This indicates that incubation with *iso*peptides **1a:1d** at 5 µM for 1 hour did not significantly disrupt cellular or subcellular structures. These results underscore that the self-assembly of peptides at low concentrations does not compromise the cellular integrity of activated T cells.

In contrast, activated T cells treated with the NBD-functionalized control *iso*peptide **1b** at 5 µM for 1 hour exhibited no nanostructure formation and lower intracellular fluorescence (Fig. S3.34), reflecting the lack of self-assembling capability of the linear NBD-modified peptide **5b** (Fig. S3.24). Cellular uptake analysis of resting, i.e. non-activated, T cells treated with the pro-assembling *iso*peptides **1a:1d** (99:1) at 5 µM for 1 hour showed markedly lower intracellular fluorescence compared to activated T cells treated with the same peptides (Fig. S3.35). This aligns with the observation that fiber assembly is glutathione-dependent and activated T cells have reportedly higher cytosolic glutathione levels.[21,23]

3.2.2. Functional impact of intracellular peptide nanostructures on cytotoxic T cells

Next, we examined how the synthetic intracellular peptide nanostructures impact the morphology and immunological function of cytotoxic T cells, specifically their ability to eliminate cancer cells. To evaluate the cytotoxicity of *ex vivo* pre-activated $CD8^+$ T cells against MCF-7 breast cancer cells, we combined the cytotoxic T cells with a bispecific T cell engager (BiTE) – a dual-targeting antibody that binds both the CD3 complex on T cells and the Human Epidermal Growth Factor Receptor 2 (HER2) on MCF-7 cells – followed by a 24-hour co-culture incubation with the cancer cells.

Treatment of cytotoxic T cells with glutathione-responsive *iso*peptides **1a:1c** (5:1, 5 µM) for 1 hour prior to the addition of BiTE and co-culturing significantly enhanced their cytotoxicity against the cancer cells. T cells pre-treated with these *iso*peptides exhibited a markedly lower IC_{50} value for the bispecific T cell engager of 0.34 pM compared to 3.81 pM in untreated control T cells (Fig. 3.5a,b). Similarly, the use of *iso*peptides **1a:1d** (99:1, 5 µM), which includes the Cy5-labeled peptide used also for CLEM analysis, yielded comparable enhancements in cytotoxicity, indicating that the choice of fluorescent label does not impact the functional efficacy of the synthetic peptide nanostructures (Fig. S3.31). In contrast, T cells pre-treated with control *iso*peptide **1b**, which is internalized but only releases a linear NBD-modified peptide incapable of forming intracellular nanostructures, did not exhibit increased cytotoxicity (Fig. S3.30). These findings suggest that the observed enhancement in cytotoxicity is due to the formation of synthetic intracellular peptide nanostructures.

Towards revealing the functional mechanism behind the increased cytotoxic effect, we analyzed the rheological changes in T cells treated with pro-assembling

*iso*peptides *via* single cell real-time deformation cytometry (RT-DC). T cell activation and adhesion to the antigen expressing cells (in this case the HER2-expressing MCF7 breast cancer cells) is greatly influenced by the mechanical properties of the T cells, which in turn are governed by cytoskeletal tensions and acto-myosin contractions.[29] Both the actin and microtubule cytoskeleton play crucial roles in establishing T cell polarity, migration, formation of the immunological synapse and the directed secretion of cytokines and cytolytic granules.[30] RT-DC measurements revealed that T cells treated with *iso*peptides **1a:1c** for 1 h at 5 µM exhibited notable changes in morphology and stiffness (Fig. 3.5c,d,e). Specifically, these T cells demonstrated significantly reduced deformability (Fig. 3.5c) and an increased elastic modulus (Fig. 3.5d) compared to the untreated controls. This indicates a general stiffening of the activated T cells that results from the presence of synthetic intracellular nanostructures.

To elucidate the downstream signaling effects of peptide nanostructures within T cells, we correlated enhanced T cell effector functions and mechanobiological changes with alterations in signaling protein phosphorylation by a Phospho-Kinase Antibody Arrays (Fig. 3.5f and Fig. S3.32). We observed significant changes in the phosphorylation of key signaling proteins, including Akt, c-Jun, CREB, ERK1/2 and JNK, in cytotoxic T cells treated with pro-assembling *iso*peptides **1a:1c** (Fig. 3.5f). These proteins are integral components of pathways that drive T cell activation, proliferation and effector function. Elevated phosphorylation of Akt, a central kinase in the PI3K/Akt pathway,[31] suggests enhanced survival, along with elevated expression of key adhesion and cytolytic molecules in T cells.[32-34] The increased phosphorylation of c-Jun, a member of the activator protein-1 (AP-1) family, further promotes the expression of genes required for T cell activation and proliferation.[35,36] Similarly, the higher levels of phosphorylated transcription factor CREB were found in peptide-treated T cells, indicating activation of gene

expression essential for T cell effector function and cytokine production.[37] The elevated phosphorylation levels of ERK1/2 and JNK, which are key mitogen-activated protein (MAP) kinases, further support the notion of heightened T cell proliferation and effector function.[38-40] In contrast, T cells treated with the non-assembling control *iso*peptide **1c**, which can enter cells and undergo glutathione-induced transformation but lacks the ability to form assemblies, did not exhibit increased phosphorylation of these proteins (Fig. S3.32). This finding highlights that the observed effects on signaling proteins are specifically associated with the formation of synthetic peptide nanostructures within T cells.

Collectively, these findings demonstrate that the glutathione-triggered formation of peptide nanostructures not only alters the mechanobiological properties of T cells but also potentiates intracellular signaling pathways linked to an enhanced T cell immune response.

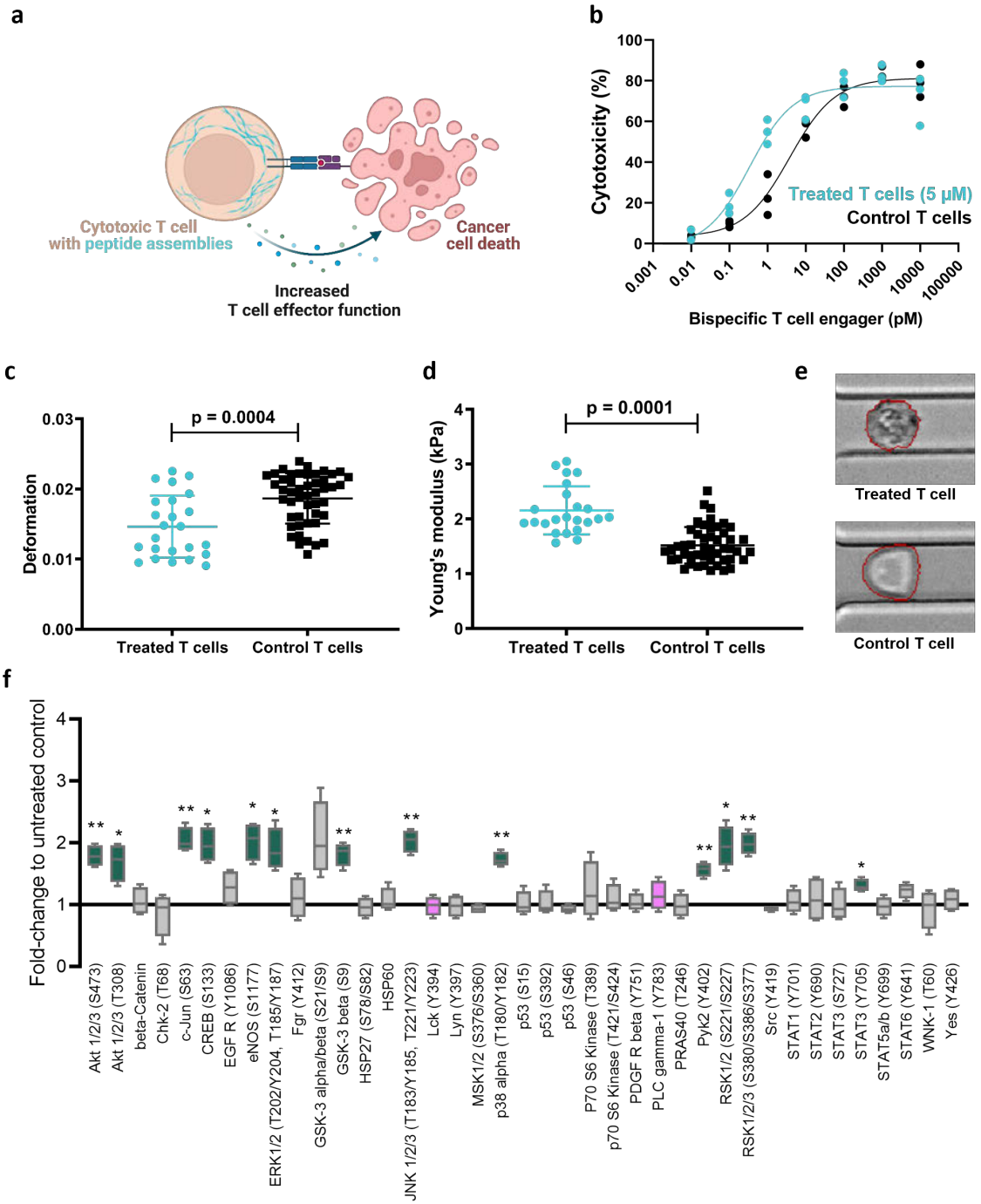

Figure 3.6 Enhancement of T cell cytotoxicity against MCF-7 cancer cells and alterations in mechanobiology and protein phosphorylation by intracellular peptide nanostructures. **a** | Schematic illustration of the co-stimulation of T cell cytotoxicity via intracellular peptide assembly. **b** | Dose-response curve showing the cytotoxic effect of activated T cells against HER2-expressing MCF7 cancer cells in relation to the concentration of a bispecific T cell engager targeting HER2 and CD3. The black curve represents data for untreated T cells, while the blue curve shows data for T cells pre-treated with the *iso*peptides **1a:1c** (5:1) at 5 µM for 1 hour, followed by washing and addition of the bispecific engager (n = 3 donors, mean of 2 technical replicates each). The IC_{50} of the bispecific engager for untreated T cells is 3.81 pM, compared to 0.34 pM for *iso*peptide-treated cells. **c** | Real-time deformability cytometry (RT-DC) analysis showing reduced deformation in T cells pre-treated with the *iso*peptide mixture **1a:1b** (5:1) at 5 µM for 1 hour, relative to untreated controls. **d** | RT-DC measurements indicating an increased Young's modulus in T cells treated with the *iso*peptide mixture,

reflecting enhanced cellular stiffness. **e** | Brightfield images of treated (**1a:1b** (5:1) at 5 μM for 1 hour) and untreated control T cells during RT-DC measurements within a microfluidic channel. **f** | Proteome Profiler Human Phospho-Kinase Antibody Array analysis of T cells treated with the *iso*peptides **1a:1c** (5:1) at 5 μM for 1 hour (n = 2 donors, 2 on-membrane replicates), highlighting differential phosphorylation in a panel of key signaling proteins essential for T cell activation.

3.3. Conclusion

In this study, we have demonstrated the chemical engineering of activated human cytotoxic T cells through the *in situ* formation of intracellular synthetic peptide nanofibers that alter critical T cell functions, ultimately improving the immune response against cancer cells. By using redox-sensitive *iso*peptides, we successfully induced the assembly of synthetic nanostructures within the intracellular environment of cytotoxic T cells, resulting in a significant boost to their cytotoxic effector function. The formation of these peptide nanostructures not only altered the mechanical properties of the T cells, leading to increased stiffness and decreased deformability, but also promoted the phosphorylation of proteins in central signaling pathways involved in the activation and regulation of T cells. This dual impact on both the physical and biochemical attributes of T cells underscores the potential of intracellular nanostructures as a tool for modulating immune cell behavior beyond genetic engineering. By focusing on augmenting the intrinsic functions of healthy immune cells, this work could pave the way for innovations in the field of immunotherapy. The ability to fine-tune immune cell properties through controlled intracellular assembly could potentially open up new possibilities for the design of next-generation therapies targeting complex intracellular environments.

References

1 Alberts, B. *et al. Molecular Biology of the Cell*. 6. edn, (W. W. Norton & Company, 2014).

2 Zhan, P., Jahnke, K., Liu, N. & Göpfrich, K. Functional DNA-based cytoskeletons for synthetic cells. *Nat. Chem.* **14**, 958–963 (2022).

3 Chagri, S., Ng, D. Y. W. & Weil, T. Designing bioresponsive nanomaterials for intracellular self-assembly. *Nat. Rev. Chem.* **6**, 320-338 (2022).

4 Deng, Y., Zhan, W. & Liang, G. Intracellular Self-Assembly of Peptide Conjugates for Tumor Imaging and Therapy. *Adv. Healthcare Mater.* **10**, 2001211 (2021).

5 Guo, R.-C. *et al.* Recent progress of therapeutic peptide based nanomaterials: from synthesis and self-assembly to cancer treatment. *Biomater. Sci.* **8**, 6175–6189 (2020).

6 Pieszka, M. *et al.* Controlled Supramolecular Assembly inside Living Cells by Sequential Multi-staged Chemical Reactions. *J. Am. Chem. Soc.* **142**, 15780-15789 (2020).

7 Zhou, Z. *et al.* In Situ Assembly of Platinum(II)-Metallopeptide Nanostructures Disrupts Energy Homeostasis and Cellular Metabolism. *J. Am. Chem. Soc.* **144**, 12219–12228 (2022).

8 Ren, Y. *et al.* Supramolecular Assembly in Live Cells Mapped by Real-Time Phasor-Fluorescence Lifetime Imaging. *J. Am. Chem. Soc.* **146**, 11991–11999 (2024).

9 Chen, Z., Chen, M., Zhou, K. & Rao, J. Pre-targeted Imaging of Protease Activity through In Situ Assembly of Nanoparticles. *Angew. Chem. Int. Ed.* **59**, 7864–7870 (2020).

10 Zheng, R. *et al.* Controllable Self-Assembly of Peptide-Cyanine Conjugates In Vivo as Fine-Tunable Theranostics. *Angew. Chem. Int. Ed.* **60**, 7809 –7819 (2021).

11 Raskov, H., Orhan, A., Christensen, J. P. & Gögenur, I. Cytotoxic CD8+ T cells in cancer and cancer immunotherapy. *Br. J. Cancer* **124**, 359–367 (2021).

12 Hwang, J.-R., Byeon, Y., Kim, D. & Park, S.-G. Recent insights of T cell receptor-mediated signaling pathways for T cell activation and development. *Exp. Mol. Med.* **52**, 750–761 (2020).

13 Basu, R. *et al.* Cytotoxic T Cells Use Mechanical Force to Potentiate Target Cell Killing. *Cell* **165**, 100–110 (2016).

14 Waldman, A. D., Fritz, J. M. & Lenardo, M. J. A guide to cancer immunotherapy: from T cell basic science to clinical practice. *Nat. Rev. Immunol.* **20**, 651–668 (2020).

15 Rosenberg, S. A. & Restifo, N. P. Adoptive cell transfer as personalized immunotherapy for human cancer. *Science* **348**, 62–68 (2015).

16 Sahin, U. & Türeci, Ö. Personalized vaccines for cancer immunotherapy. *Science* **359**, 1355–1360 (2018).

17 Goldberg, M. S. Improving cancer immunotherapy through nanotechnology. *Nat. Rev. Cancer* **19**, 587–602 (2019).

18 Göpfrich, K., Platten, M., Frischknecht, F. & Fackler, O. T. Bottom-up synthetic immunology. *Nat. Nanotechnol.*, doi:10.1038/s41565-024-01744-9 (2024).
19 Quinn, J. F., Whittaker, M. R. & Davis, T. P. Glutathione responsive polymers and their application in drug delivery systems. *Polym. Chem.* **8**, 97–126 (2016).
20 Rashida Gnanaprakasam, J. N., Wu, R. & Wang, R. Metabolic Reprogramming in Modulating T Cell Reactive Oxygen Species Generation and Antioxidant Capacity. *Front. Immunol.* **9**, 342242 (2018).
21 Mak, T. W. *et al.* Glutathione Primes T Cell Metabolism for Inflammation. *Immunity* **46**, 675–689 (2017).
22 Franchina, D. G., Dostert, C. & Brenner, D. Reactive Oxygen Species: Involvement in T Cell Signaling and Metabolism. *Trends Immunol.* **39**, 489–502 (2018).
23 Lian, G. *et al.* Glutathione de novo synthesis but not recycling process coordinates with glutamine catabolism to control redox homeostasis and directs murine T cell differentiation. *eLife* **7**, e36158 (2018).
24 Estrela, J. M., Ortega, A. & Obrador, E. Glutathione in Cancer Biology and Therapy. *Crit. Rev. Clin. Lab. Sci.* **43**, 143–181 (2006).
25 Smith, D. K. Lost in translation? Chirality effects in the self-assembly of nanostructured gel-phase materials. *Chem. Soc. Rev.* **38**, 684–694 (2009).
26 Tao, K., Levin, A., Adler-Abramovich, L. & Gazit, E. Fmoc-modified amino acids and short peptides: simple bio-inspired building blocks for the fabrication of functional materials. *Chem. Soc. Rev.* **45**, 3935–3953 (2016).
27 Micsonai, A. *et al.* Accurate secondary structure prediction and fold recognition for circular dichroism spectroscopy. *Proc. Natl. Acad. Sci. U.S.A.* **112**, E3095–E3103 (2015).
28 Roth, P. *et al.* Supramolecular assembly guided by photolytic redox cycling. *Nat. Synth.* **2**, 980–988 (2023).
29 Rossy, J., Laufer, J. M. & Legler, D. F. Role of Mechanotransduction and Tension in T Cell Function. *Front. Immunol.* **9**, 2638 (2018).
30 Gomez, T. S. & Billadeau, D. D. T Cell Activation and the Cytoskeleton: *You Can't Have One Without the Other*. In Advances in Immunology, vol. 97, 1–50 (Elsevier, 2008).
31 Xue, L., Chiang, L., Kang, C. & Winoto, A. The role of the PI3K-AKT kinase pathway in T-cell development beyond the β checkpoint. *Eur. J. Immunol.* **38**, 3200–3207 (2008).
32 Cantrell, D. Protein kinase B (Akt) regulation and function in T lymphocytes. *Semin. Immunol.* **14**, 19–26 (2002).
33 Kim, E. H. & Suresh, M. Role of PI3K/Akt signaling in memory CD8 T cell differentiation. *Front. Immunol.* **4**, 39750 (2013).
34 Macintyre, A. N. *et al.* Protein kinase B controls transcriptional programs that direct cytotoxic T cell fate but is dispensable for T cell metabolism. *Immunity* **34**, 224–236 (2011).

35 Hussein, M. S., Li, Q., Mao, R., Peng, Y. & He, Y. TCR T cells overexpressing c-Jun have better functionality with improved tumor infiltration and persistence in hepatocellular carcinoma. *Front. Immunol.* **14**, 1114770 (2023).

36 Lynn, R. C. *et al.* c-Jun overexpression in CAR T cells induces exhaustion resistance. *Nature* **576**, 293–300 (2019).

37 Wen, A. Y., Sakamoto, K. M. & Miller, L. S. The Role of the Transcription Factor CREB in Immune Function. *J. Immunol.* **185**, 6413–6419 (2010).

38 Shah, K., Al-Haidari, A., Sun, J. & Kazi, J. U. T cell receptor (TCR) signaling in health and disease. *Sig. Transduct. Target. Ther.* **6**, 412 (2021).

39 D'Souza, W. N., Chang, C.-F., Fischer, A. M., Li, M. & Hedrick, S. M. The Erk2 MAPK Regulates CD8 T Cell Proliferation and Survival. *J. Immunol.* **181**, 7617–7629 (2008).

40 Behrens, A. *et al.* Jun N-terminal kinase 2 modulates thymocyte apoptosis and T cell activation through c-Jun and nuclear factor of activated T cell (NF-AT). *Proc. Natl. Acad. Sci. U.S.A.* **98**, 1769–1774 (2001).

Supplementary Information

1. General Information

1.1. Materials

Reagents and solvents were purchased from commercial sources and were used without further purification. Peptide synthesis grade reagents were used for synthesizing the peptides. HPLC was performed using acetonitrile (CH_3CN) in HPLC grade (containing 0.1% trifluoroacetic acid (TFA)) and water for HPLC (containing 0.1% TFA) and reactions was obtained from a Millipore purification system. Flash column chromatography was carried out using Macherey-Nagel silica gel 0.04–0.063 mm.

1.2. Instruments

1.2.1. Microwave Peptide Synthesizer

Linear peptides were synthesized in a Liberty Blue Automated Microwave Peptide Synthesizer by CEM Corporation.

1.2.2. High-Performance Liquid Chromatography (HPLC)

The peptides were purified by preparative HPLC using a setup by Shimadzu. For purification either a Zorbax Eclipse XDB-C18 HPLC column (9.4 × 250 mm, 5 μM) was used at a flowrate of 4 ml/min or a Phenomenex Gemini 5 μm NX-C18 110 Å 150 × 30 mm was used at a flowrate of 25 ml/min.

1.2.3. Liquid Chromatography-Mass Spectrometry (LC-MS)

Compounds were analyzed by HPLC-ESI-MS on a LC-MS 2020 by Shimadzu using a Kinetex 2.6 μm EVO C18 100 Å LC 50 × 2.1 mm column. MilliQ water acidified with 0.1% formic acid and CH_3CN were used as solvents for all measurements. The solvent gradient started with 5% CH_3CN and 95% water. This solvent ratio was kept constant for 2 min, then the CH_3CN content was linearly increased to 95% in 14 min. Data were processed in LabSolutions and OriginPro 9.

1.2.4. Atmospheric-Pressure Chemical Ionization Mass Spectrometry (APCI-MS)

All APCI-MS spectra were recorded on a Advion Expression-L Compact mass spectrometer. Data processing was performed in Advion Data Express.

1.2.5. Matrix-Assisted Laser Desorption/Ionisation-Time of Flight Mass Spectrometry (MALDI-TOF)

All MALDI-TOF spectra were recorded on either a rapifleX MALDI-TOF/TOF from Bruker or MALDI Synapt G2-SI from Waters. Samples were mixed with a saturated solution of the matrix S7 α-cyano-4-hydroxycinnamic acid (CHCA) in H_2O/CH_3CN 1/1 + 0.1% TFA. Data processing was performed in mMass and OriginPro 9.

1.2.6. Nuclear Magnetic Resonance Spectroscopy (NMR)

NMR spectra of small molecules and peptides were recorded on a Bruker Avance II 300 MHz spectrometer and a Bruker Avance 400 MHz spectrometer. The solvent signal was used as a reference (deuterated chloroform $CDCl_3$ δ = 7.26 ppm for ^1H, 77.16 ppm for ^{13}C and for DMSO-d_6 2.50 ppm and 39.52 ppm respectively). The data was processed in MestReNova.

1.2.7. Circular Dichroism Spectroscopy (CD)

CD spectra were recorded on a JASCO J-1500 spectrometer in a 0.1 cm High Precision Cell by HellmaAnalytics. The recorded data was processed in Spectra Analysis by JASCO and OriginPro9.

1.2.8. Transmission Electron Microscopy (TEM)

TEM images of the peptide samples were recorded on a JEOL 1400 transmission electron microscope at a voltage of 120 kV. Formvar/carbon-film coated copper grids (300 mesh) by Plano GmbH were used to prepare the samples. The images were processed in Fiji ImageJ or Icy.

1.2.9. Cryogenic Transmission Electron Microscopy (cryo-TEM)

For cryo-TEM examination the samples were vitrified using a Vitrobot Mark V (Thermo Fisher, Hilsboro Oregon) plunging device. 3 µl of the sample dispersion was applied to a Quantifoil® R 1.2/1.3 300 Mesh, Cu, that has been glow discharged in an oxygen plasma

cleaner (Diener Nano®, Diener electronic, Germany) shortly before. After removing excess sample solution with a filter paper, the grid is immediately plunged into liquid ethane. For the subsequent examination, the specimen is transferred to a TEM (FEI Titan Krios G4) keeping cryogenic conditions. Conventional TEM imaging was done using an acceleration voltage of 300 kV. Micrographs were acquired with a 4k Direct Electron Detection Camera (Gatan K3) under low dose conditions.

2. Synthesis

2.1. Synthesis of glutathione-responsive isopeptides

2.1.1. Synthesis of isopeptides with activated disulfide bond

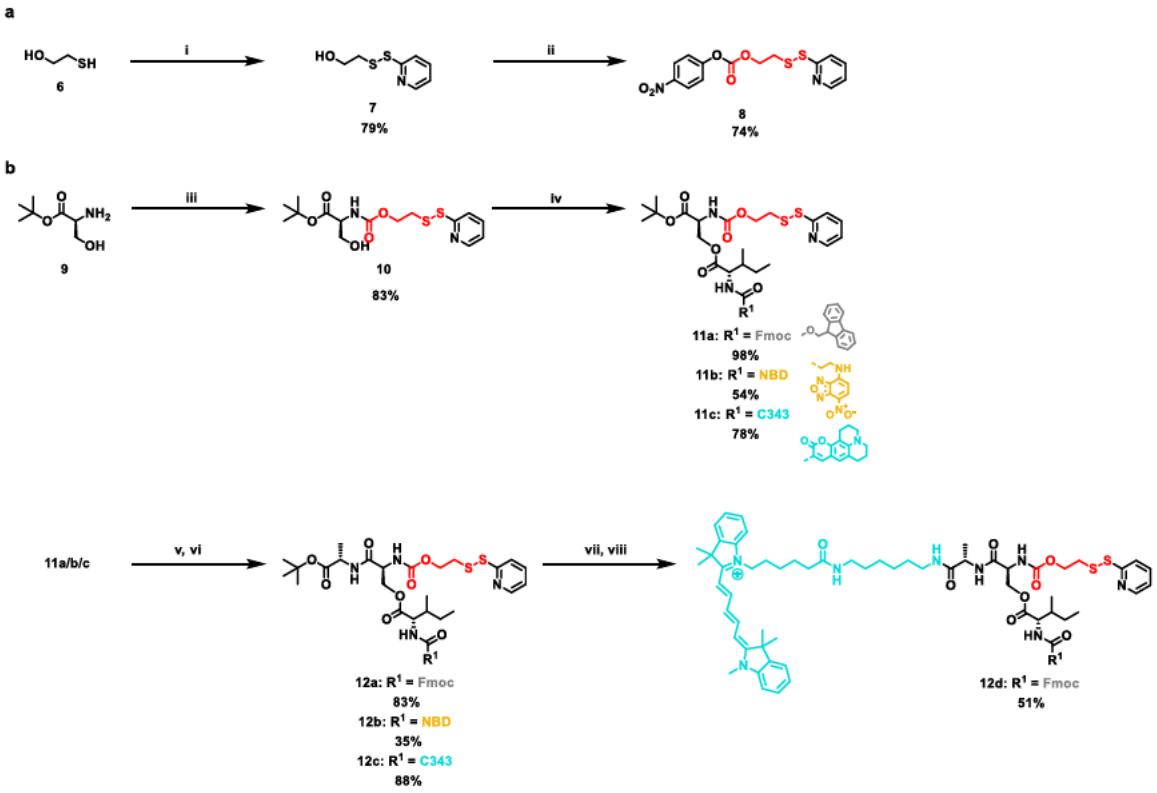

Scheme S3.1 Synthesis of isopeptides with activated disulfide-bonds. a | Synthesis of reactive carbonate 8: i) 2,2'-dipyridyldisulfide, MeOH, AcOH, 24 h, RT; ii) 4-nitrophenyl chloroformate, TEA, THF, 2 h, 0 °C-RT. b | Synthesis of isopeptides with activated disulfide-bonds 12a/b/c/d: iii) 4-nitrophenyl 2-(pyridin-2-yldisulfanyl)ethyl carbonate 8, DIPEA, DCM, overnight, RT; iv) Fmoc/C343/NBD-Ile, DIC, DMAP, DCM, overnight, RT; v) TFA, DCM, 4 h, RT; vi) Ala-tBuO, PyBOP, DIPEA, DCM, 3 h, RT; vii) TFA, DCM, 4 h, RT; viii) Cyanine5-amine, PyBOP, DIPEA, DCM, 3 h, RT.

2.1.1.1. Synthesis of compound 7

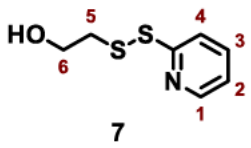

7

In a round-bottom flask 2-mercaptoethan-1-ol **6** (500 mg, 450 µl, 6.40 mmol, 1 eq.) was dissolved in MeOH under N_2 (30 ml) and AcOH (1.7 ml) was added. 2,2'-Dipyridyldisulfide (2.82 g, 12.8 mmol, 2 eq.) dissolved in MeOH (10 ml) was added dropwise to the reaction mixture. The solution was stirred for 24 h at room temperature. Afterwards, the solvent

was removed in vacuo. Purification via flash chromatography (cHex:EA 3:2) yielded compound **7** as a colorless oil (951 mg, 5,07 mmol, 79%).

^{1}H NMR (300 MHz, $CDCl_3$) δ 8.53 – 8.52 (m, 1H, H-1), 7.59 (td, J = 7.8, 1.9 Hz, 1H, H-3), 7.42 – 7.39 (m, 1H, H-4), 7.18– 7.14 (m, 1H, H-2), 3.81 (t, J = 5.1 Hz, 2H, H-6), 2.96 (t, J = 5.1 Hz, 2H, H-5).

^{13}C NMR (75 MHz, $CDCl_3$) δ 159.20, 149.88, 137.11, 122.16, 121.70, 58.36, 42.86.

APCI-MS: m/z 188.0 (calculated for $[M+H]^+$: 188.02)

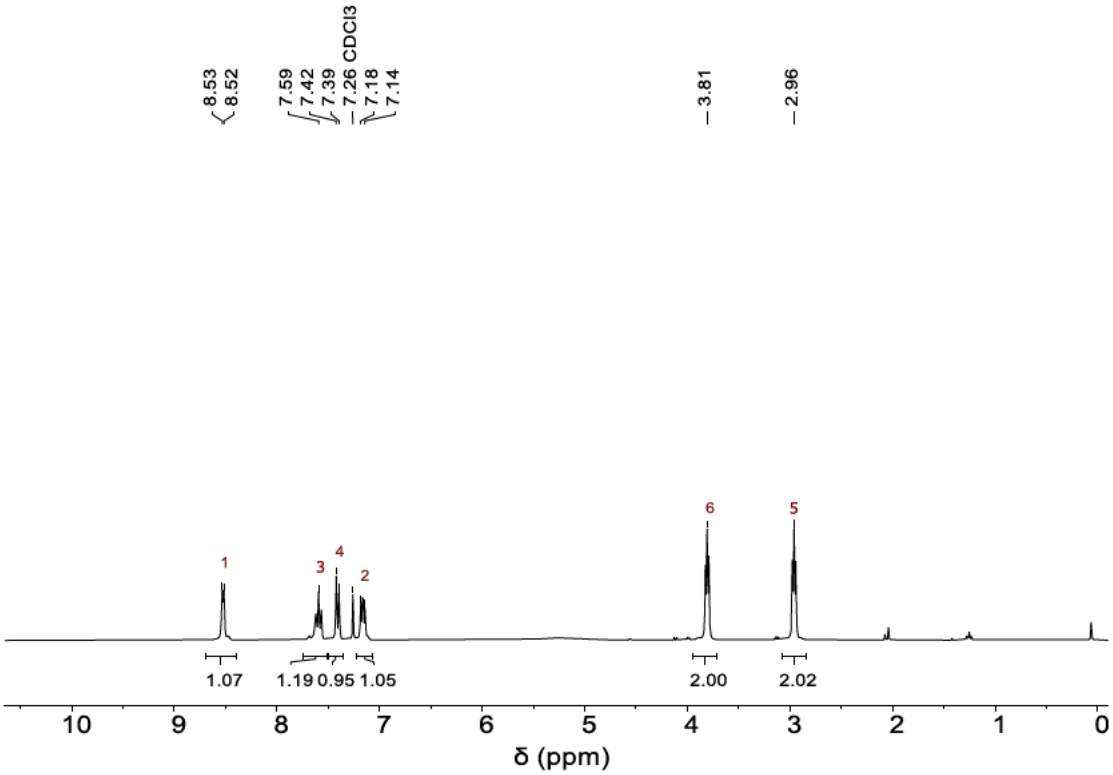

Figure S3.1 ^{1}H NMR spectrum (300 MHz, $CDCl_3$, 298 K) of compound 7.

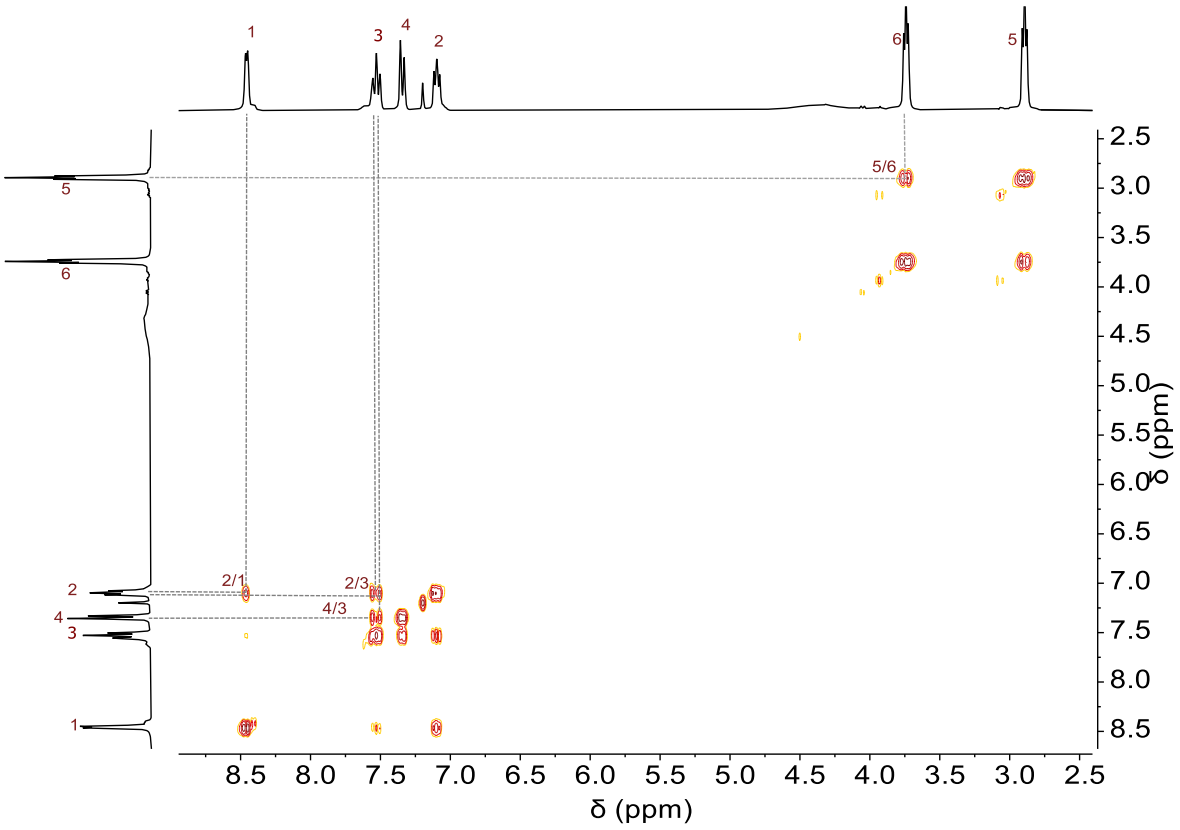

Figure S3.2 Partial $^{1}H,^{1}H$ COSY NMR spectrum (300 MHz, CDCl3, 298 K) of compound 7.

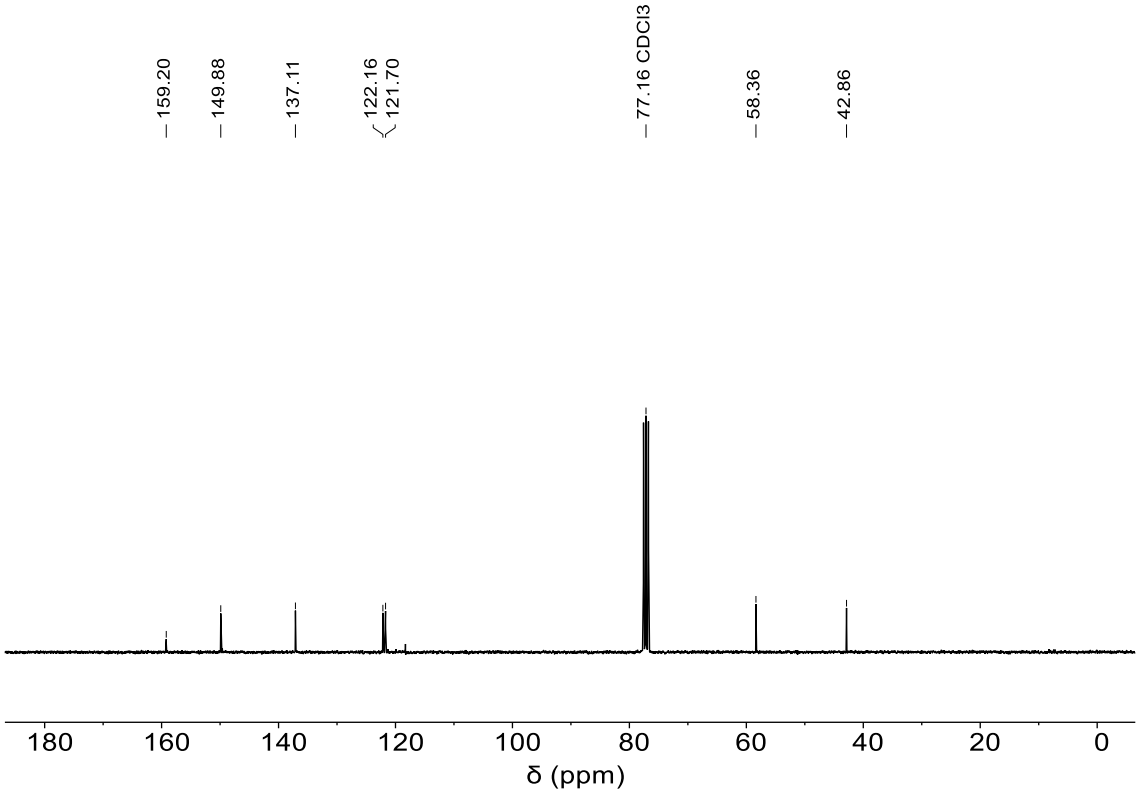

Figure S3.3 ^{13}C NMR spectrum (75 MHz, $CDCl_3$, 298 K) of compound 7.

2.1.1.2. Synthesis of compound 8

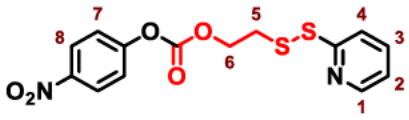

8

In a round-bottom flask 4-nitrochloroformate (1.40 g, 1.4 eq.) was dissolved in dry THF (30 ml) under N_2. The solution was cooled to 0 °C using an ice bath. Compound **7** (930 mg, 4.97 mmol, 1 eq.) and TEA (1.01 g, 1.38 ml, 2 eq.) were dissolved in dry THF (35 ml) and the mixture was added dropwise to the solution of 4-nitrochloroformate. The resulting reaction mixture was stirred for 2 h at room temperature. Ethyl acetate (EA) was added and the organic phase was washed twice with brine before drying over sodium sulfate. The solvents were removed in vacuo and subsequent flash column chromatography (cHex:EA 4:1) yielded compound **8** as a yellow oil (1.30 g, 3.70 mmol, 74%).

^{1}H NMR (300 MHz, $CDCl_3$) δ 8.53 – 8.51 (m, 1H, H-1), 8.3 – 8.27 (m, 2H, H-8), 7.70 – 7.68 (m, 2H, H-3, H-4), 7.40 – 7.37 (m, 2H, H-7), 7.18 – 7.13 (m, 1H, H-2), 4.57 (t, J = 6.4 Hz, 2H, H-6), 3.18 (t, J = 6.4 Hz, 2H, H-5).

^{13}C NMR (75 MHz, $CDCl_3$) δ 159.17, 155.51, 152.34, 149.68, 145.61, 137.61, 126.31, 125.47, 121.88, 121.38, 120.56, 115.89, 66.80, 36.96.

APCI-MS: m/z 353.3 (calculated for $[M+H]^+$: 353.03)

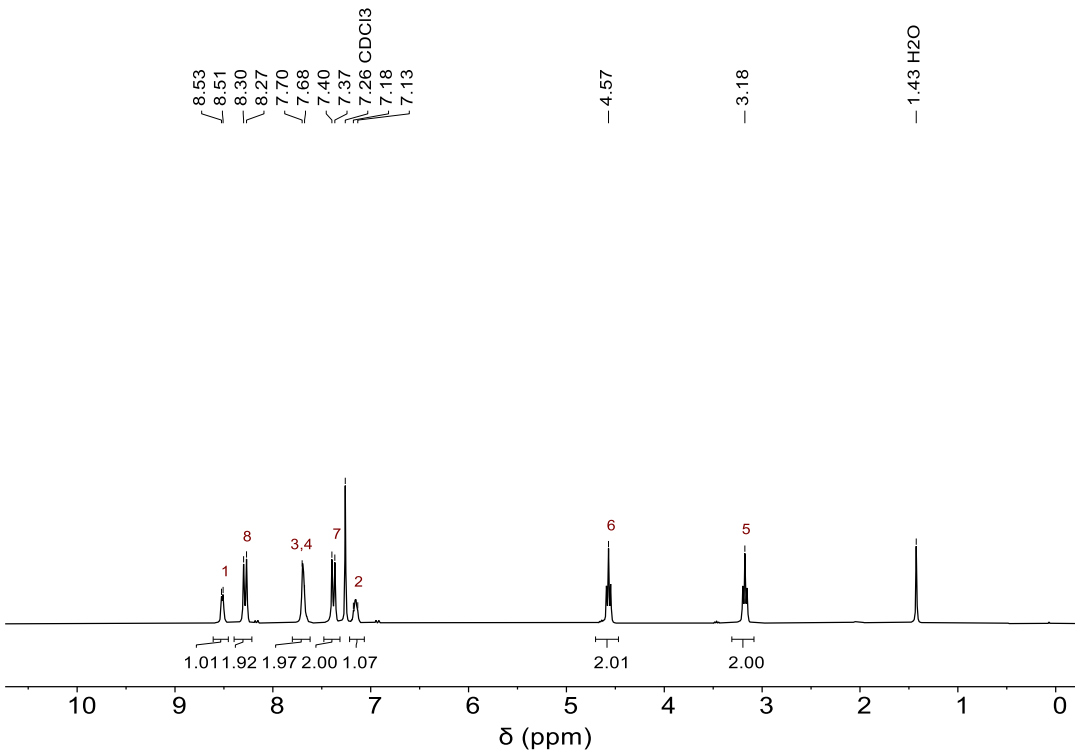

Figure S3.4 ^{1}H NMR spectrum (300 MHz, $CDCl_3$, 298 K) of compound 8.

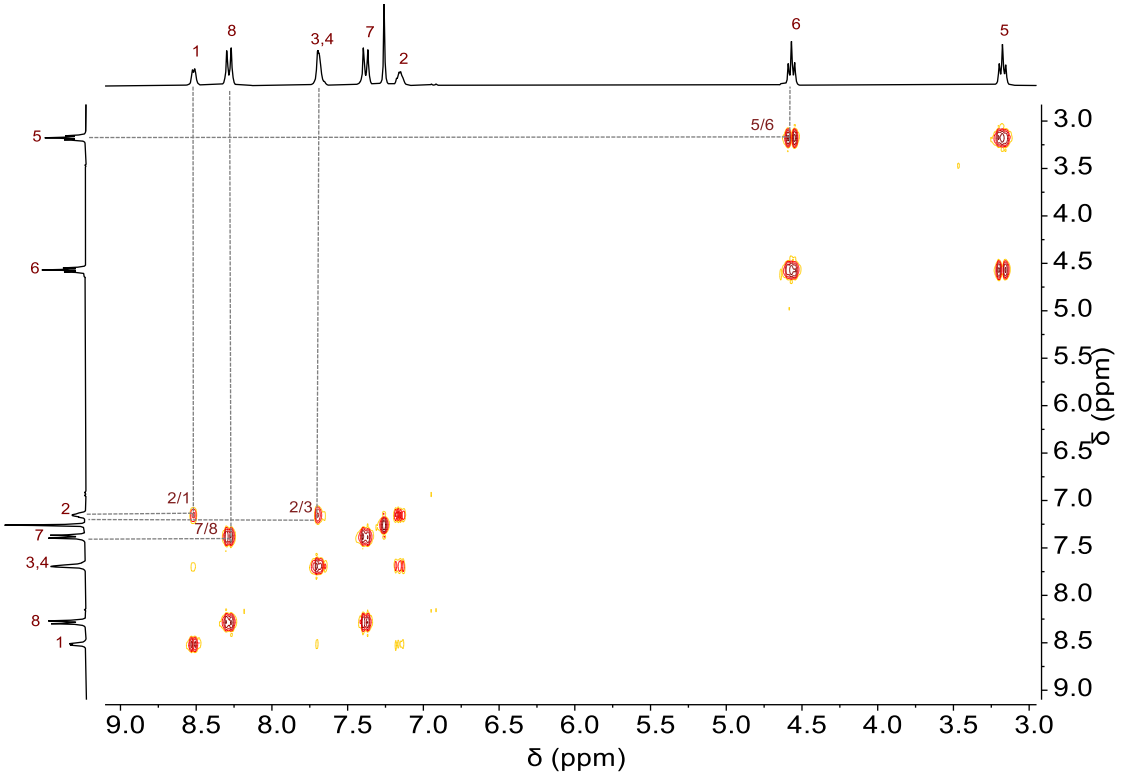

Figure S3.5 ^{1}H,^{1}H COSY NMR spectrum (300 MHz, $CDCl_3$, 298 K) of compound 8.

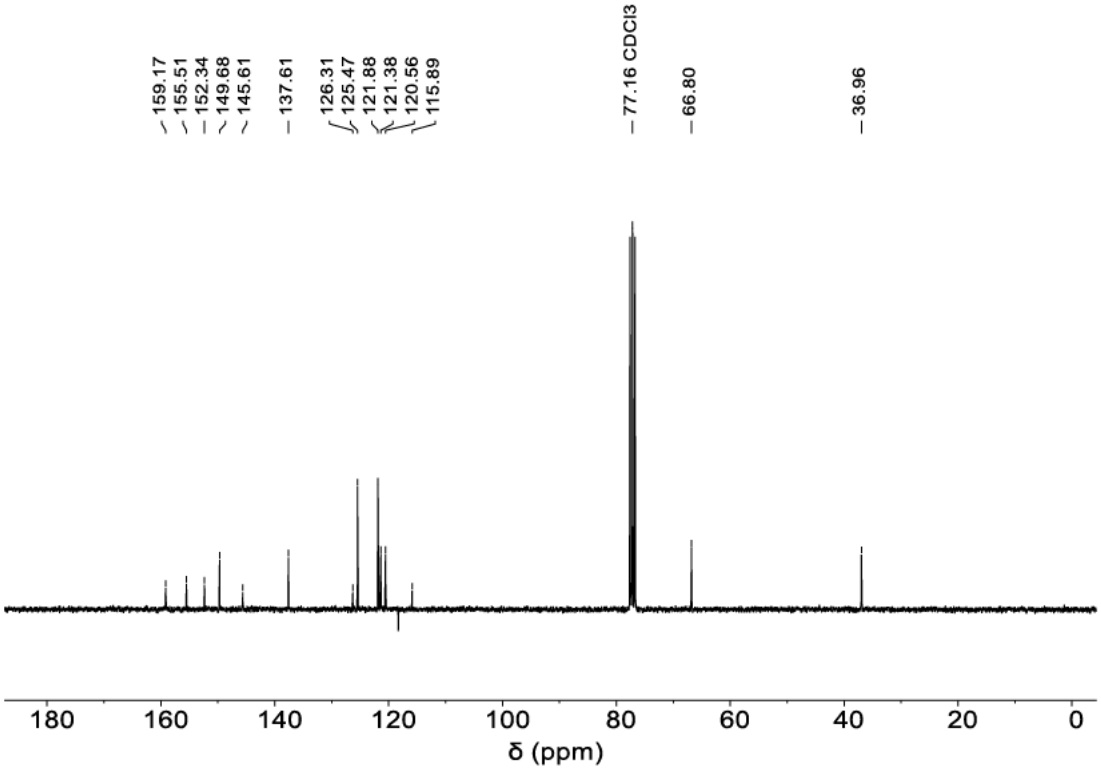

Figure S3.6 ^{13}C NMR spectrum (75 MHz, $CDCl_3$, 298 K) of compound 8.

2.1.1.3. Synthesis of compound 10

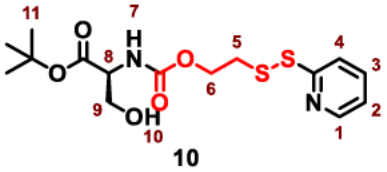

10

In a round-bottom flask *tert*-butyl protected serine hydrochloride (200 mg, 1.01 mmol, 1 eq.) was dissolved in dry DCM (10 ml) and dry DIPEA (654 mg, 881 µl, 5.06 mmol, 5 eq.) was added to the solution. Compound **8** was dissolved in dry DCM (5 ml) and added slowly to the mixture. The solution was stirred at room temperature overnight and then washed twice with water and with brine. The aqueous phase was extracted with EA and the combined organic phase was dried over sodium sulphate. The solvents were removed in vacuo and flash column chromatography (cHex:EA 1:1) yielded compound **10** as a colorless amorphous solid (316 mg, 0.84 mmol, 83%).

^{1}H NMR (400 MHz, $CDCl_3$) δ 8.44 (d, J = 4.8 Hz, 1H, H-1), 7.72 (d, J = 8.1 Hz, 1H, H-3), 7.66 (td, J = 7.7, 1.8 Hz, 1H, H-4), 7.10 (ddd, J = 7.3, 4.9, 1.2 Hz, 1H, H-2), 5.61 – 5.59

(m, 1H, H-7), 4.43 – 4.37 (m, 1H, H-6), 4.30 – 4.24 (m, 2H, H-6', H-8), 3.95 – 3.88 (m, 2H, H-9), 3.11 – 2.96 (m, 2H, H-5), 2.84 – 2.81 (m, 1H, H-10), 1.48 (s, 9H, H-11).

^{13}C NMR (101 MHz, $CDCl_3$) δ 169.46, 160.09, 155.89, 149.69, 137.33, 121.02, 120.11, 82.96, 63.66, 63.57, 56.76, 37.69, 28.14.

ESI-MS: *m/z* 375.1 (calculated for $[M+H]^+$: 375.10)

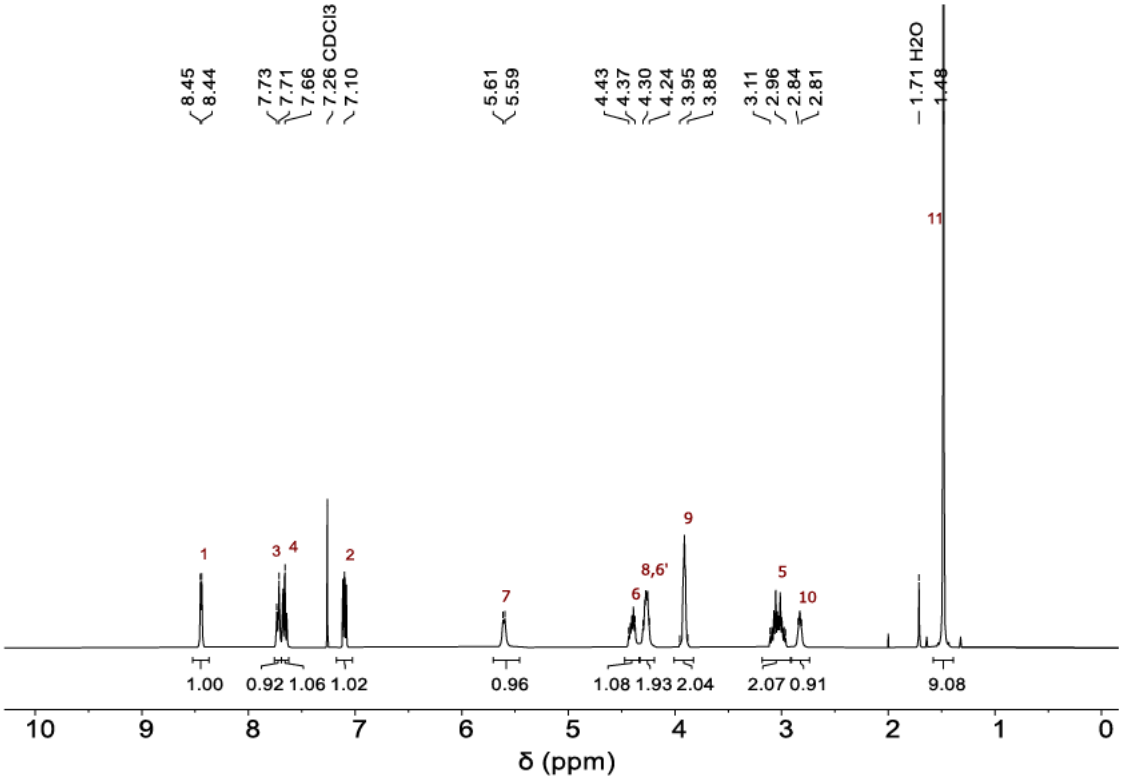

Figure S3.7 ^{1}H NMR spectrum (400 MHz, $CDCl_3$, 298 K) of compound 10.

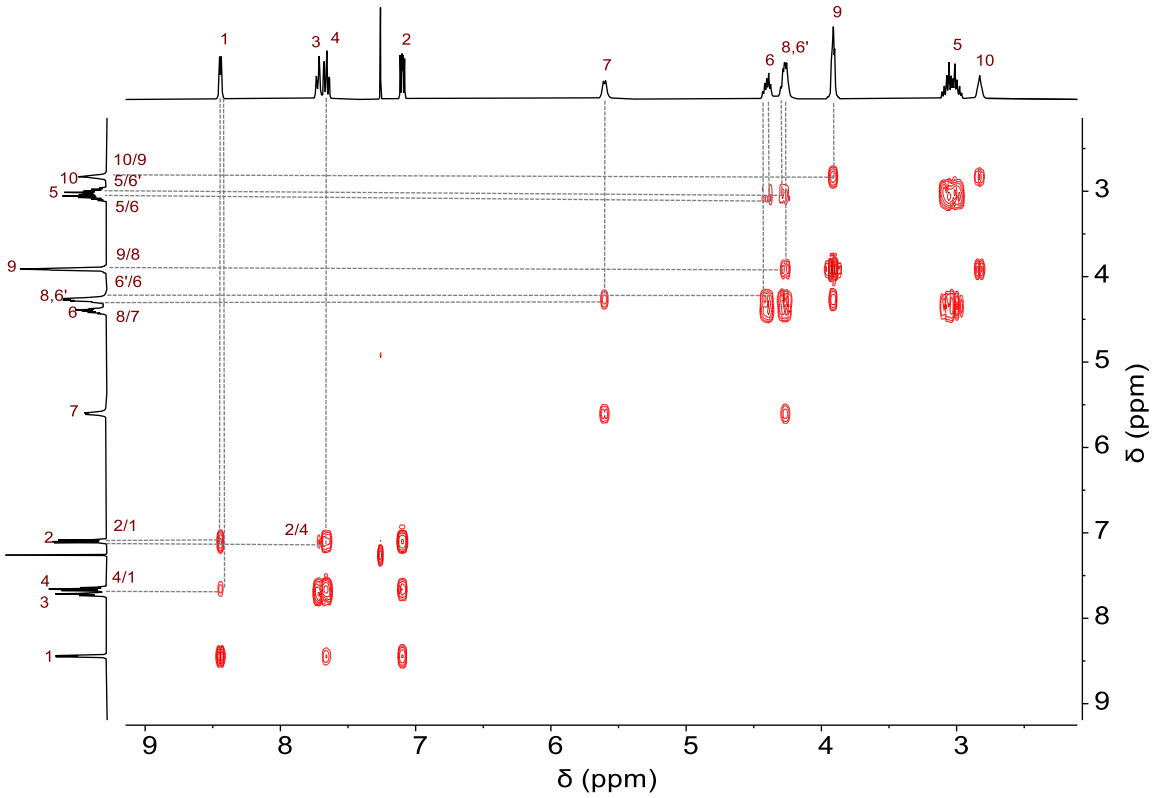

Figure S3.8 $^{1}H,^{1}H$ COSY NMR spectrum (400 MHz, $CDCl_3$, 298 K) of compound 10.

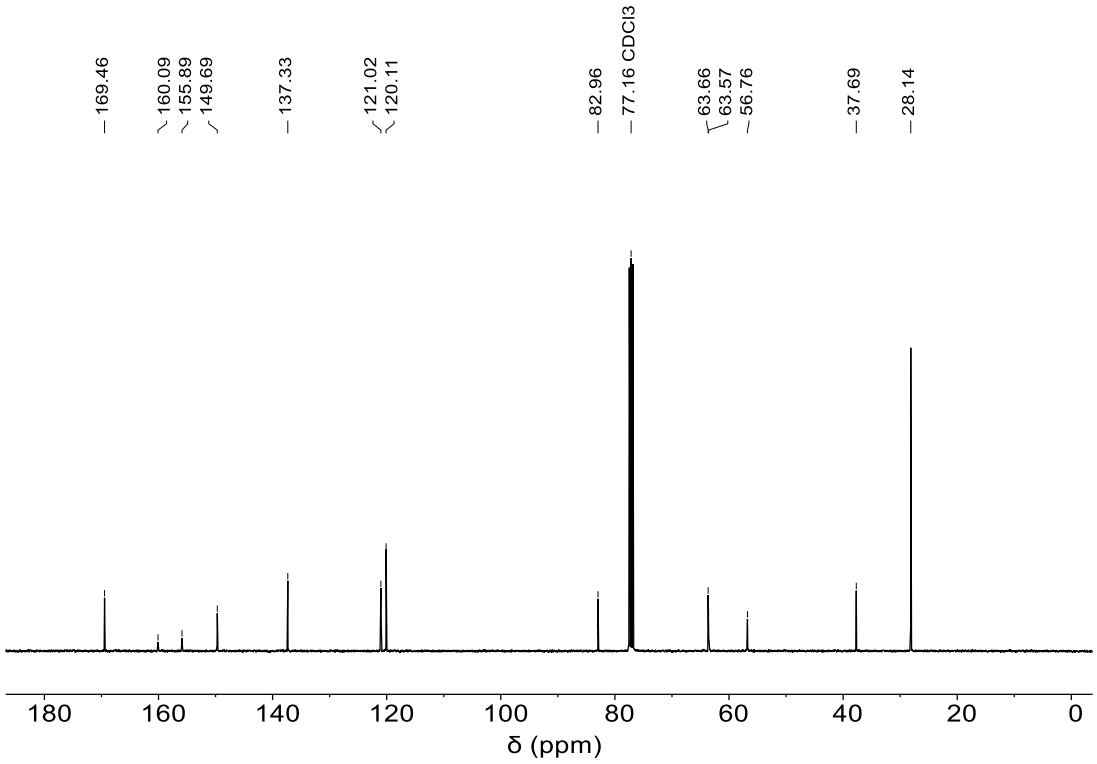

Figure S3.9 ^{13}C NMR spectrum (101 MHz, $CDCl_3$, 298 K) of compound 10.

2.1.1.4. Synthesis of compounds 11a

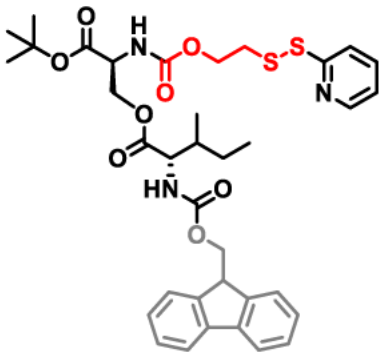

11a

In a round-bottom flask compound **10** (157 mg, 419 µmol, 1 eq.) was dissolved in dry DCM (5 ml) under N_2. Fmoc-Ile (274 mg, 774 µmol, 1.8 eq.), DMAP (23.6 mg, 193 µmol, 0.5 eq.) and DIC (98 mg, 774 µmol, 1.8 eq.) were dissolved in dry DCM (10 ml) and added dropwise to the solution of compound **10**. The reaction mixture was stirred at room temperature overnight. The solvent was removed in vacuo and flash column chromatography (cHex:EA 3:1) yielded compound **11a** as a colorless oil (291 mg, 410 µmol, 98%).

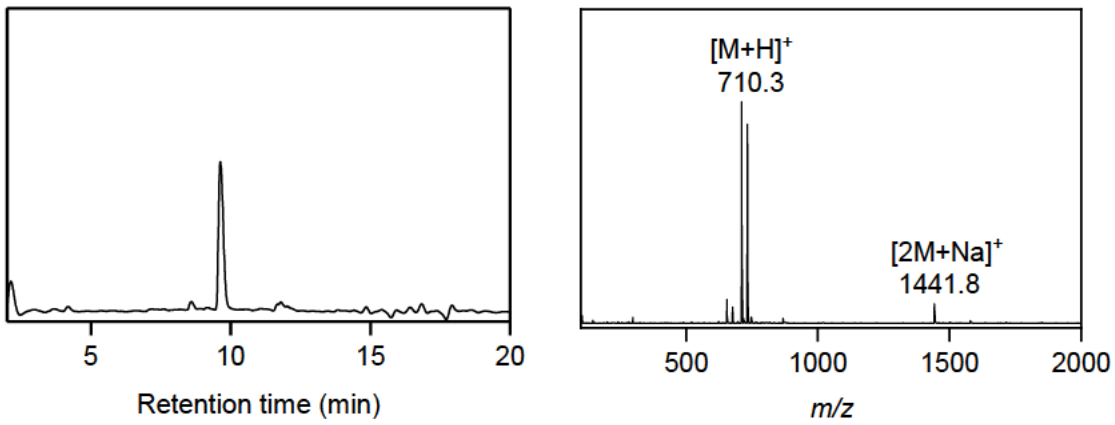

Figure S3.10 LC-MS data of compound 11a. Left: LC trace (214 nm) with t_R (11a) = 9.63 min. Right: Convoluted ESI-MS spectrum showing peaks of $[M+H]^+$ (calculated: 710.26) and $[2M+Na]^+$ (calculated: 1441.49).

2.1.1.5. Synthesis of compounds 11b

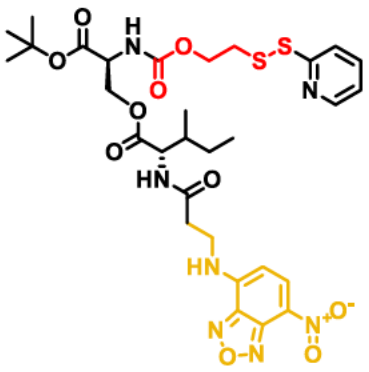

11b

In a round-bottom flask compound **10** (162 mg, 433 µmol, 1.2 eq.) was dissolved in dry DCM (4 ml) under N_2. Nitrobenzoxadiazole (NBD)-β-Ala-Ile (132 mg, 361 µmol, 1 eq.), DMAP (88 mg, 722 µmol, 2 eq.) and DIC (91 mg, 722 µmol, 2 eq.) were dissolved in dry DCM (5 ml) and added dropwise to the solution of compound **10**. The reaction mixture was stirred at room temperature overnight. The solvent was removed in vacuo and flash column chromatography (EA:cHex 2:1) yielded compound **11b** as a bright yellow oil (141 mg, 195 µmol, 54%).

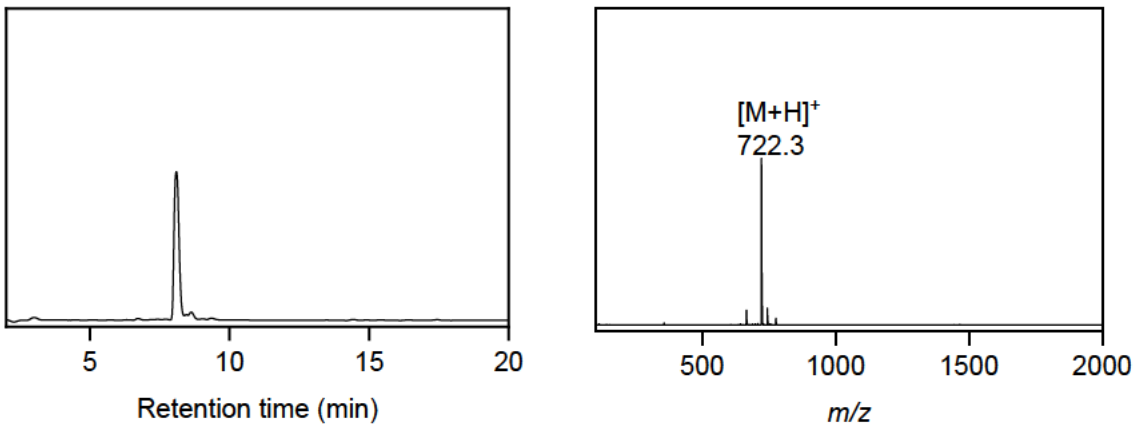

Figure S3.11 LC-MS data of compound 11b. Left: LC trace (214 nm) with t_R (11b) = 8.63 min. Right: Convoluted ESI-MS spectrum showing the peak of $[M+H]^+$ (calculated: 722.23).

2.1.1.5. Synthesis of compounds 11c

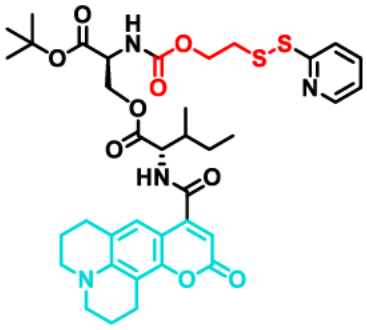

11c

In a round-bottom flask compound **10** (80 mg, 214 µmol, 1 eq.) was dissolved in dry DCM (4 ml) under N_2. Coumarin 343-Ile (126 mg, 316 µmol, 1.5 eq.), DMAP (26.1 mg, 214 µmol, 1 eq.) and DIC (40 mg, 320 µmol, 1.5 eq.) were dissolved in dry DCM (5 ml) and added dropwise to the solution of compound **10**. The reaction mixture was stirred at room temperature overnight. The solvent was removed in vacuo and flash column chromatography (cHex:EA 3:2) yielded compound **11c** as a bright green oil (126 mg, 167 µmol, 78%).

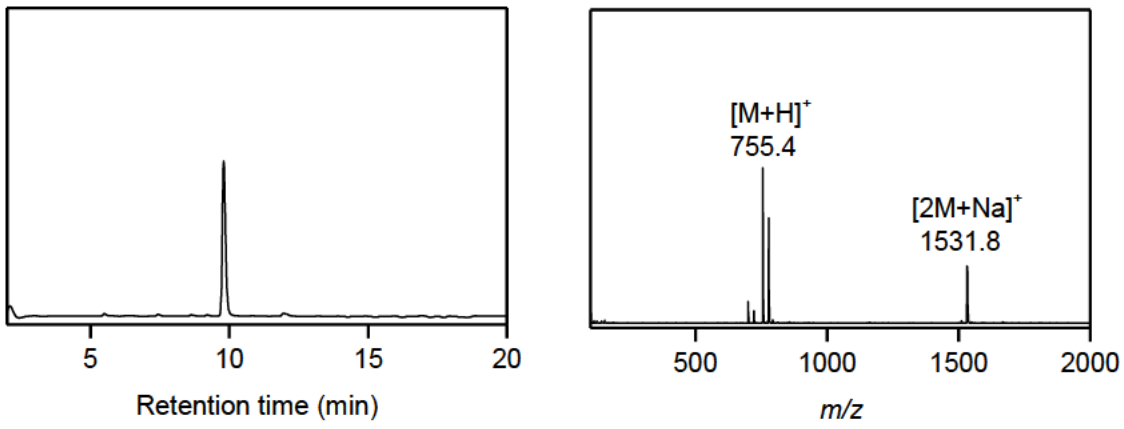

Figure S3.12 LC-MS data of compound 11c. Left: LC trace (214 nm) with t_R (11c) = 9.80 min. Right: Convoluted ESI-MS spectrum showing peaks of $[M+H]^+$ (calculated: 755.28) and $[2M+Na]^+$ (calculated: 1531.53).

2.1.1.6. Synthesis of compound 12a

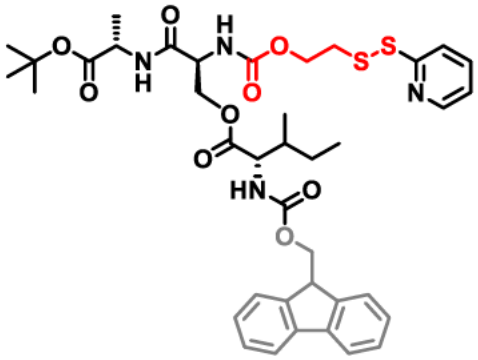

12a

In a round-bottom flask compound **11a** (280 mg, 394 µmol, 1 eq.) was dissolved in a 1:1-mixture of TFA and DCM (4 ml:4ml) and stirred for 6 h. The solvents were removed in vacuo. The remaining colorless oil was dissolved in dry DCM (15 ml) and DIPEA (329 mg, 443 µl, 2.54 mmol, 6 eq.) was added under N_2. Afterwards, PyBOP (441 mg, 847 µmol, 2.2 eq.) and *tert*-butyl-protected alanine hydrochloride (154 mg, 847 µmol, 2.2 eq.) were added and the reaction mixture was stirred for 3 h. The solution was washed with water and extracted with EA. The combined organic phase was dried over sodium sulphate and the solvents were evaporated. Flash column chromatography (EA:cHex 4:3) yielded compound **12a** as a colorless oil (255 mg, 327 µmol, 83%).

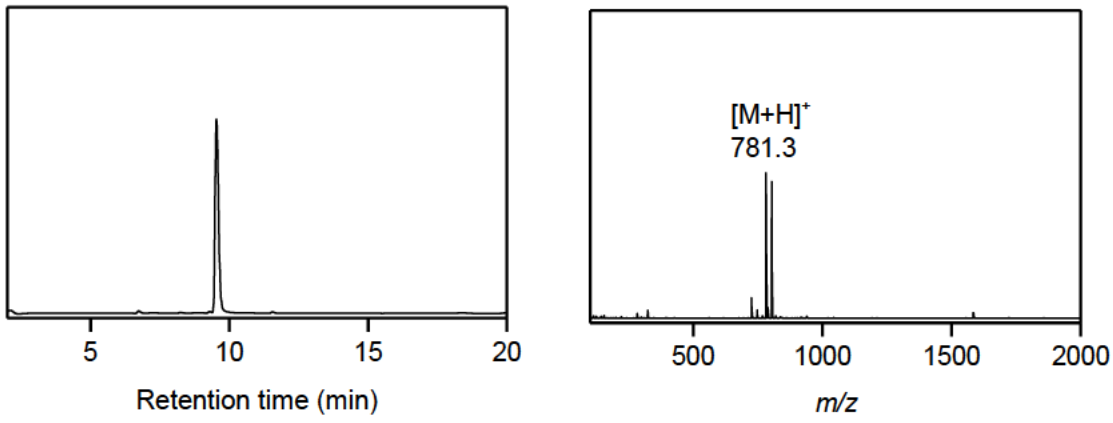

Figure S3.13 LC-MS data of compound 12a. Left: LC trace (214 nm) with t_R (12a) = 9.53 min. Right: Convoluted ESI-MS spectrum showing peaks of $[M+H]^+$ (calculated: 781.29).

2.1.1.9. Synthesis of compound 12b

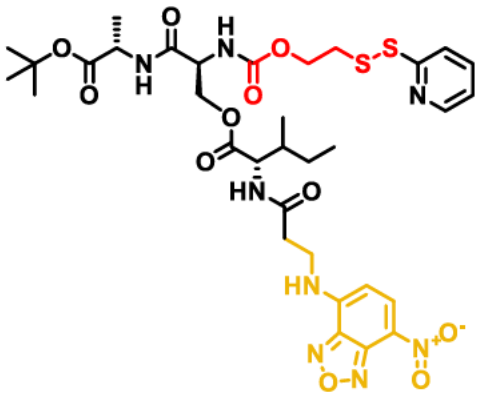

12b

In a round-bottom flask compound **11b** (141 mg, 195 µmol, 1 eq.) was dissolved in a 1:1-mixture of TFA and DCM (2 ml:2ml) and stirred for 4 h. The solvents were removed in vacuo. The remaining bright yellow oil was dissolved in dry DCM (10 ml) and DIPEA (153 mg, 206 µl, 1.18 mmol, 6 eq.) was added under N_2. Afterwards, PyBOP (205 mg, 393 µmol, 2 eq.) and *tert*-butyl-protected alanine hydrochloride (71 mg, 393 µmol, 2 eq.) were added and the reaction mixture was stirred for 3 h. The solvent was evaporated. The product was purified via HPLC using the Phenomenex Gemini column. The gradient started with 10% CH_3CN in H_2O (+0.1% TFA) and this solvent ratio was kept for 3 min after which the CH_3CN content was increased to 100% over 12 min. The purification yielded **12b** as a bright yellow solid (55 mg, 69 µmol, 35%).

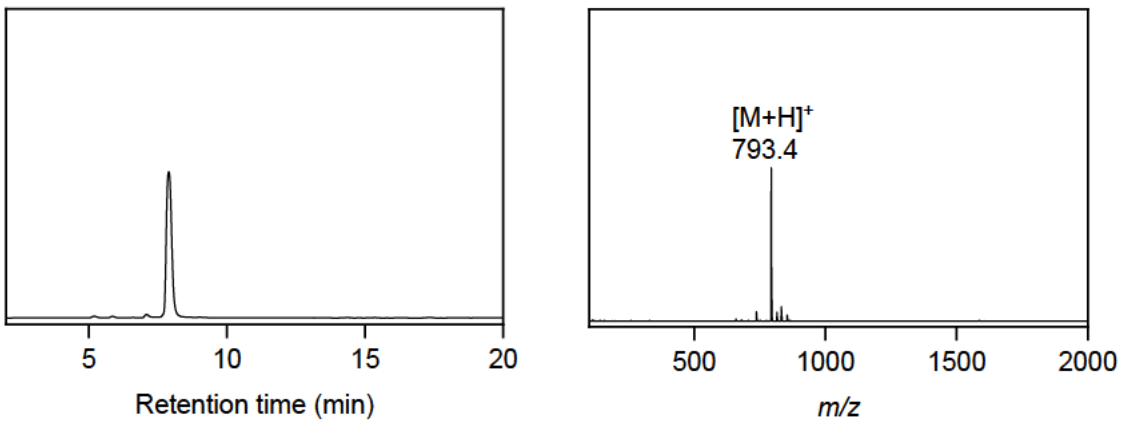

Figure S3.14 LC-MS data of compound 12b. Left: LC trace (214 nm) with t_R (12b) = 7.89 min. Right: Convoluted ESI-MS spectrum the showing peak of $[M+H]^+$ (calculated: 793.26).

2.1.1.8. Synthesis of compound 12c

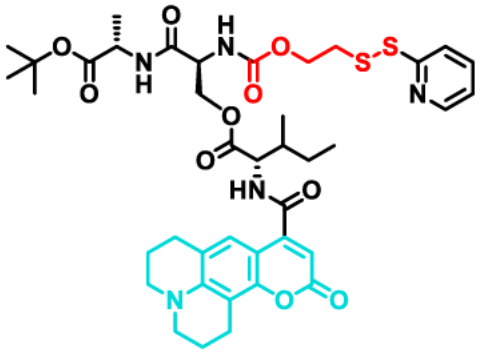

12c

In a round-bottom flask compound **11c** (126 mg, 167 µmol, 1 eq.) was dissolved in a 1:1-mixture of TFA and DCM (2 ml:2ml) and stirred for 4 h. The solvents were removed in vacuo. The remaining bright green oil was dissolved in dry DCM (10 ml) and DIPEA (297 mg, 400 µl, 2.30 mmol, 13.7 eq.) was added under N_2. Afterwards, PyBOP (718 mg, 1.38 mmol, 8.2 eq.) and *tert*-butyl-protected alanine hydrochloride (267 mg, 1.47 mmol, 8.8 eq.) were added and the reaction mixture was stirred for 3 h. The solution was washed with water and brine and extracted with EA. The combined organic phase was dried over sodium sulphate and the solvents were evaporated. Flash column chromatography (EA:cHex 4:1) yielded compound **12c** as a bright green oil (122 mg, 148 µmol, 88%).

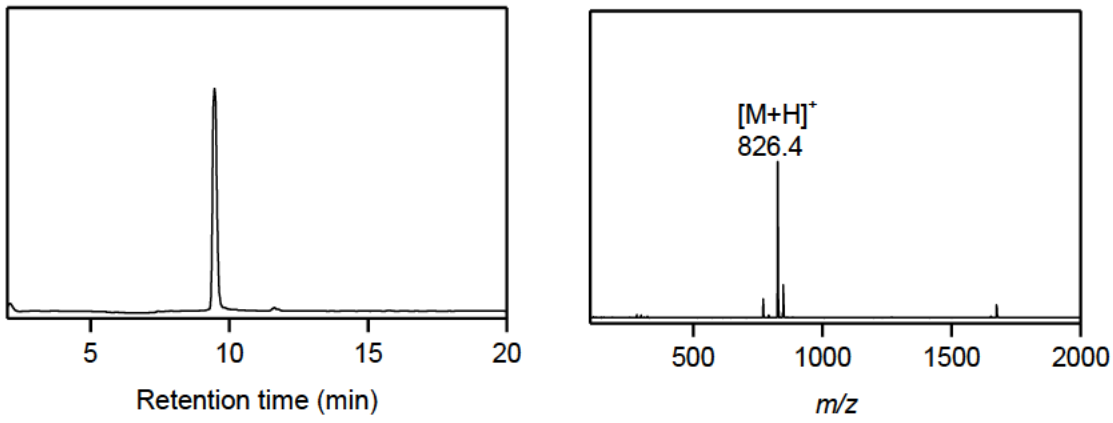

Figure S3.15 LC-MS data of compound 12c. Left: LC trace (214 nm) with t_R (12c) = 9.47 min. Right: Convoluted ESI-MS spectrum showing peaks of $[M+H]^+$ (calculated: 826.32).

2.1.1.8. Synthesis of compound 12d

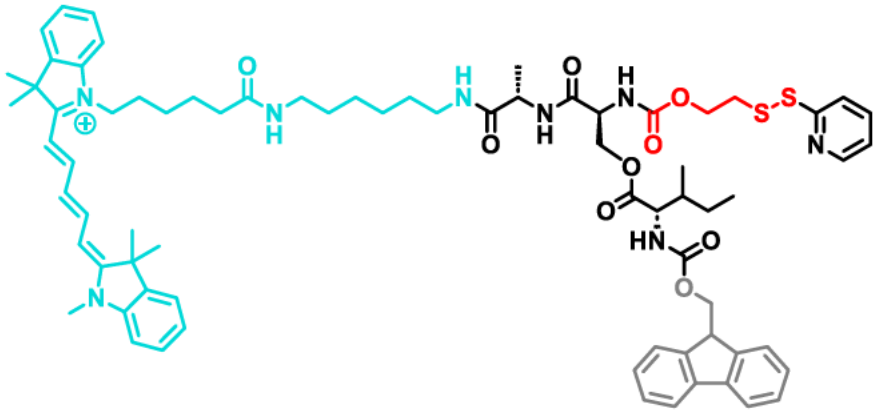

12d

In a round-bottom flask compound **12a** (30 mg, 38.4 µmol, 1 eq.) was dissolved in a 1:1-mixture of TFA and DCM (2 ml:2ml) and stirred for 4 h. The solvents were removed in vacuo. Next, cyanine5-amine hydrochloride (10 mg, 15.3 µmol, 0.5 eq.) was dissolved in DCM (4 ml) and DIPEA (11.9 mg, 16.0 µml, 91.9 µmol, 3 eq.) was added to the solution under N_2. The remaining colorless oil of the deprotected **12a** was dissolved in dry DCM (3 ml) and PyBOP (47.8 mg, 400 µl, 2.30 mmol, 13.7 eq.) was added to the solution of cyanine5-amine under N_2. The reaction mixture was stirred at room temperature overnight. The solvent was evaporated and purification via HPLC yielded compound **12d** as a bright blue solid (10 mg, 7.8 µmol, 51%).

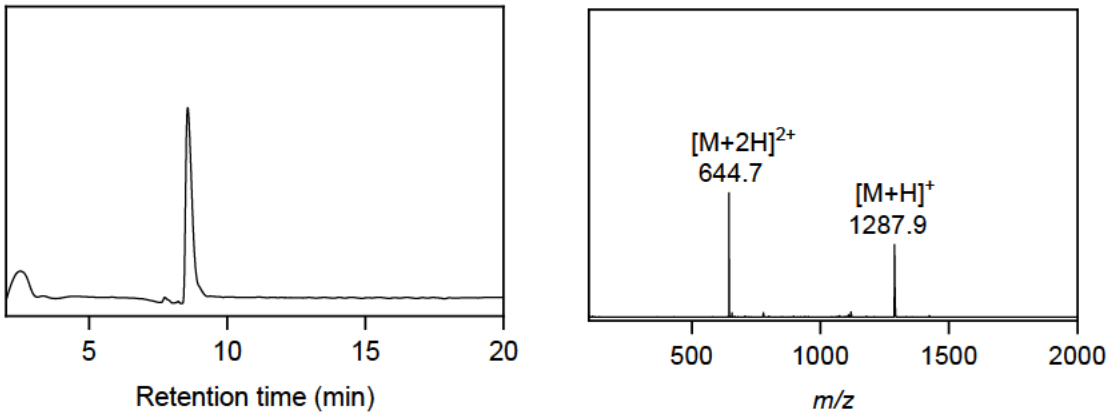

Figure S3.16 LC-MS data of compound 12d. Left: LC trace (214 nm) with t_R (12d) = 8.57 min. Right: Convoluted ESI-MS spectrum showing peaks of $[M+2H]^{2+}$ and $[M+H]^+$ (calculated: 1288.70).

2.1.2. Solid phase supported synthesis of TAT-modified glutathione-responsive isopeptides

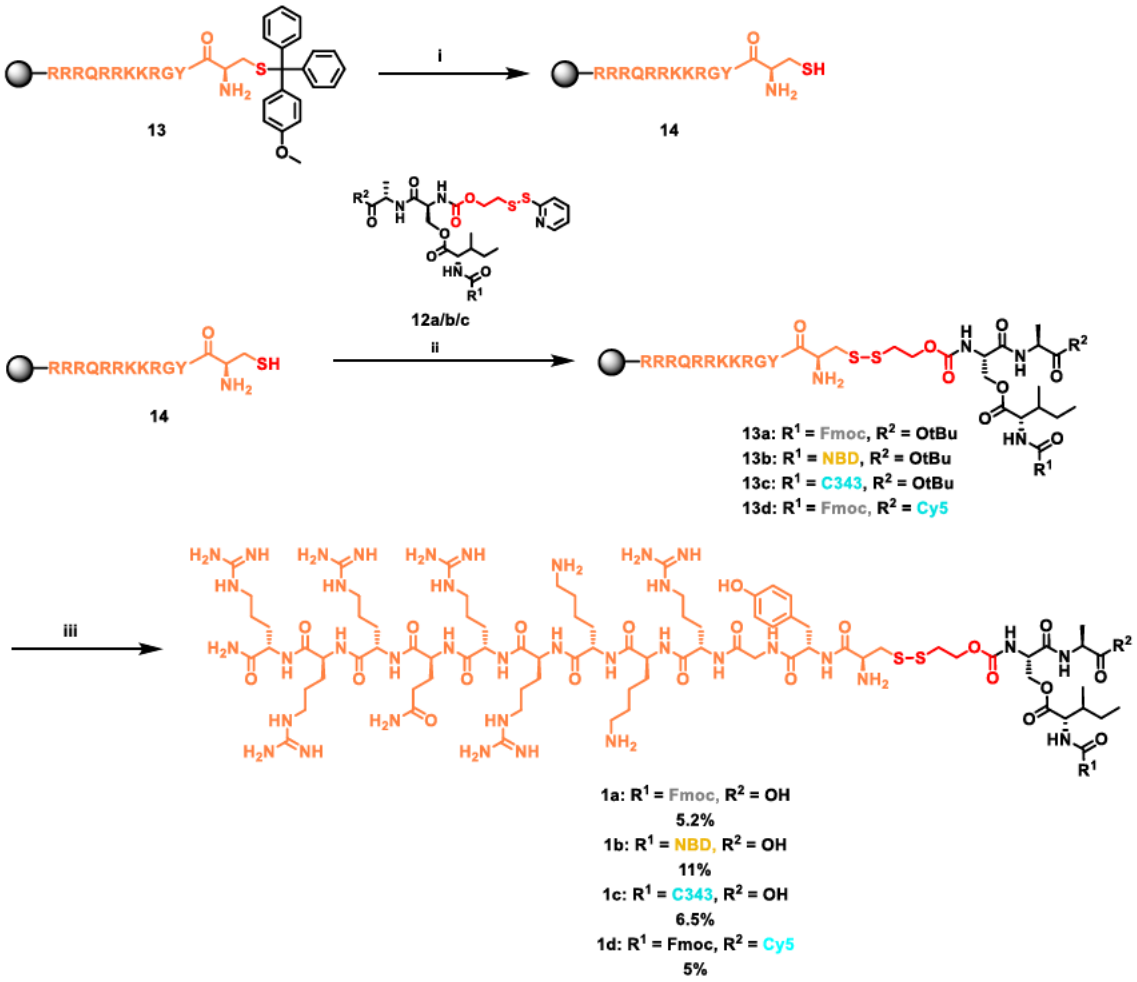

Scheme S3.2 Synthesis of TAT-modified glutathione-responsive isopeptides. i) TFA, TIPS, DCM (2% : 5% : 93%, 5x8 min, RT); ii) 12a/b/c/d, DMF, 2 h, RT; iii) TFA, TIPS, H_2O (95% : 2.5% : 2.5%), 2.5 h, RT.

The peptide TAT with an additional *N*-terminal cysteine **13** was synthesized via solid phase supported peptide synthesis using Rink amide resin at a scale of 0.05 mmol or 0.1 mmol. The resin was swollen in DMF for 1 h before the synthesis. Before every coupling step and as the final deprotection, the *N*-terminal Fmoc group was cleaved by two deprotection steps using 20% piperidine in DMF (3 ml) for 15 s and 50 s at 75 °C and 90 °C respectively. Fmoc-Gln(Trt), Fmoc-Lys(Boc), Fmoc-Gly, Fmoc-Tyr(*t*Bu) and Fmoc-Cys(Mmt) (5 eq. in 1.25 ml) were coupled for 15 s and 110 s at 75 °C and 90 °C respectively using DIC (0.25 M) and Oxyma (0.5 M) in a total of 2.75 ml DMF. For Fmoc-Arg(Pbf) the coupling steps were performed as double couplings.

The acid labile Mmt-protecting group of the cysteine side chain was removed by adding a mixture of 2% TFA with TIPS (5%) in DCM (93%) to the resin (5 ml each time) and shaking it for 8 min under N_2 before draining the solution. This procedure was repeated 5 times (i). Afterwards, the resin was thoroughly washed with DCM and dry DMF (5 ml) was added under N_2. Compound **12a** (82 mg, 0.11 mmol, 2.1 eq.) or **12b** (56 mg, 0.068 mmol, 1.4 eq.) or **12c** (56 mg, 0.068 mmol, 1.4 eq.) was dissolved in dry DMF (5 ml) and added to the resin. The mixture was shaken for 2 h at room temperature (ii). The solution was drained and the resin was washed with DMF and DCM. The cleavage solution (5 ml of 95% TFA, 2.5% TIPS, 2.5% H_2O) was added and the mixture was shaken for 2.5 h at room temperature (iii). Afterwards the peptide solution was collected by filtering out the resin and the resin was additionally washed with TFA (1 ml). The combined solution was added dropwise to ice cold diethyl ether to precipitate the product. After centrifugation for 20 min at 4,000 rpm at 0 °C, the supernatant was removed and the pellet was dried. The products **1a**, **1b**, **1c** and **1d** were each purified via HPLC using the Phenomenex Gemini column at a flowrate of 25 ml/min. The gradient started with 5% CH_3CN in H_2O (+0.1% TFA) and this solvent ratio was kept for 4 min after which the CH_3CN content was increased to 50% over 31 min. The compound **1a** was received as a white powder after lyophilization (5.9 mg, 5.2% overall yield). The compound **1b** was received as a yellow powder after lyophilization (7.6 mg, 6.5% overall yield). The compound **1c** was received as a yellow powder after lyophilization (9.0 mg, 11% overall yield). The compound **1d** was received as a blue powder after lyophilization (6 mg, 5% overall yield).

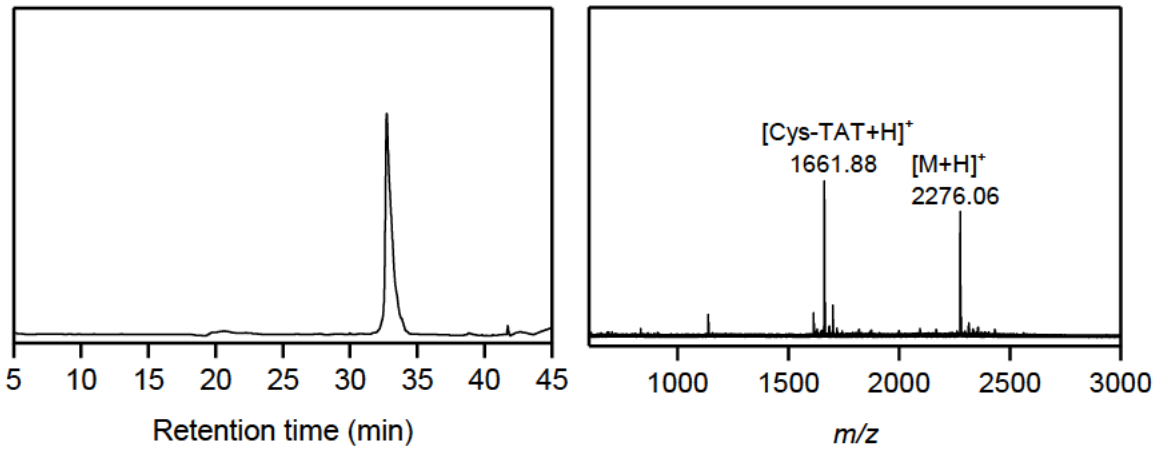

Figure S3.17 Analytical data of compound 1a. Left: Analytical HPLC trace (214 nm) with t_R (1a) = 32.73 min. For the analysis a Zorbax Eclipse XDB-C18 HPLC column was used. The gradient started with 5% CH_3CN in H2O (+0.1% TFA) and this solvent ratio was kept for 15 min after which the CH_3CN content was increased to 50% over 20 min. Right: MALDI TOF spectrum showing peaks of $[M+H]^+$ (calculated: 2276.70) and the product of disulfide cleavage $[Cys\text{-}TAT+H]^+$ (calculated: 1661.98).

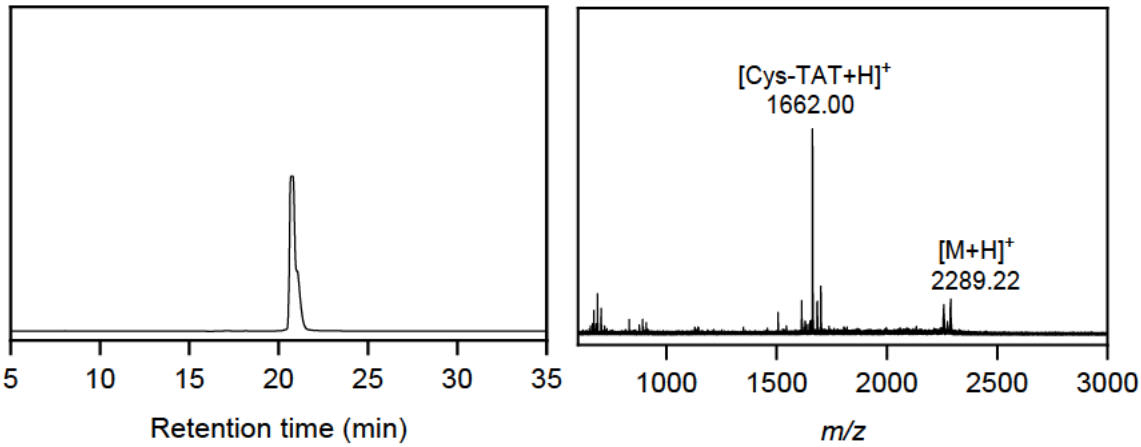

Figure S3.18 Analytical data of compound 1b. Left: Analytical HPLC trace (214 nm) with t_R (1b) = 20.78 min. For the analysis a Zorbax Eclipse XDB-C18 HPLC column was used. The gradient started with 0% CH_3CN in H_2O (+0.1% TFA) and this solvent ratio was kept for 8 min after which the CH_3CN content was increased to 45% over 15 min. Right: MALDI TOF spectrum showing peaks of $[M+H]^+$ (calculated: 2288.63) and the product of disulfide cleavage $[Cys\text{-}TAT+H]^+$ (calculated: 1661.98).

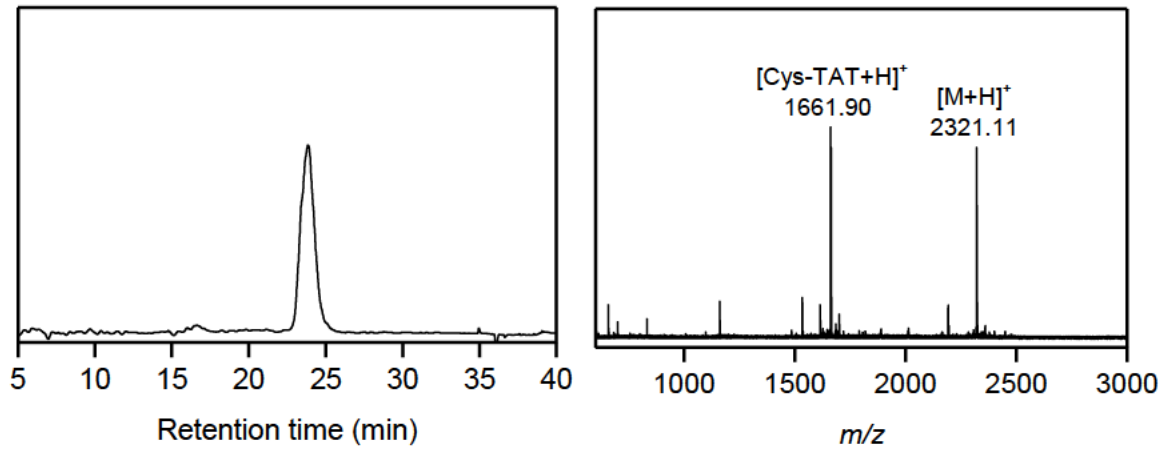

Figure S3.19 Analytical data of compound 1c. Left: Analytical HPLC trace (214 nm) with t_R (1c) = 23.84 min. For the analysis a Zorbax Eclipse XDB-C18 HPLC column was used. The gradient started with 5% CH_3CN in H_2O (+0.1% TFA) and this solvent ratio was kept for 1 min after which the CH_3CN content was increased to 50% over 29 min. Right: MALDI TOF spectrum showing peaks of $[M+H]^+$ (calculated: 2321.74) and the product of disulfide cleavage $[Cys\text{-}TAT+H]^+$ (calculated: 1661.98).

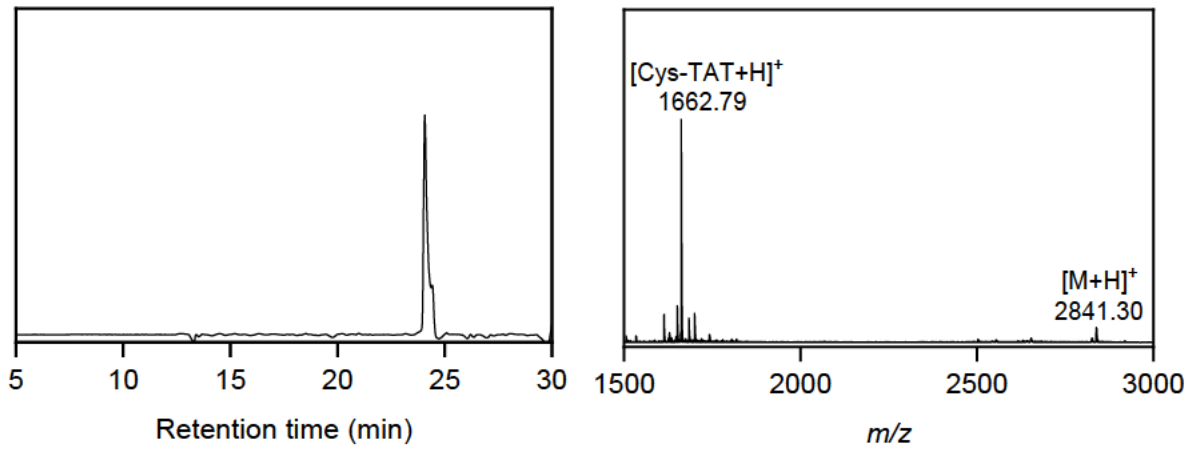

Figure S3.20 Analytical data of compound 1d. Left: Analytical HPLC trace (214 nm) with t_R (1d) = 25.09 min. For the analysis a Zorbax Eclipse XDB-C18 HPLC column was used. The gradient started with 5% CH_3CN in H_2O (+0.1% TFA) and this solvent ratio was kept for 1 min after which the CH_3CN content was increased to 50% over 20 min and then to 100% over 3 min. Right: MALDI TOF spectrum showing peaks of $[M+H]^+$ (calculated: 2840.56) and the product of disulfide cleavage $[Cys\text{-}TAT+H]^+$ (calculated: 1661.98).

3. Glutathione-Induced Transformation of Isopeptides

3.1. General procedure of LC-MS kinetic analysis

The glutathione-induced conversion of the bioresponsive isopeptides **1a** and **1b** was analyzed via an LC-MS kinetic study. The samples were prepared by mixing 300 µl of a solution of the respective isopeptide **1a** in methanol (0.1 mg/ml) with 300 µl of NH_4HCO_3 buffer (50 mM, pH 7.4) that contained glutathione (c(reduced glutathione) = 20 mM; c(oxidized glutathione) = 2 mM). The resulting samples (c(**1a**) = 0.05 mg/ml; c(reduced glutathione) = 10 mM; c(oxidized glutathione) = 1 mM) were immediately injected into an LC-MS set-up. The samples were shaken at room temperature and subsequently analyzed at different time points to monitor the degradation reaction of the isopeptides.

4. Analysis of Secondary Structure and Self-Assembly Behavior

4.1. Temperature-dependent ^{1}H-NMR analysis of linear Fmoc-ISA 5a

For the temperature-dependent NMR analysis a solution of the linear peptide **5a** was prepared containing 0.5 mg peptide in 0.5 ml deuterated solvent. The deuterated solvent consisted of a 9:1-mixture of phosphate buffer (50 mM) prepared from D_2O and DMSO-d_6. The sample was then immediately analyzed via ^{1}H-NMR spectroscopy at 293 K and the temperature was increased stepwise to 323 K. At each temperature the sample was equilibrated for 20 min before the measurement.

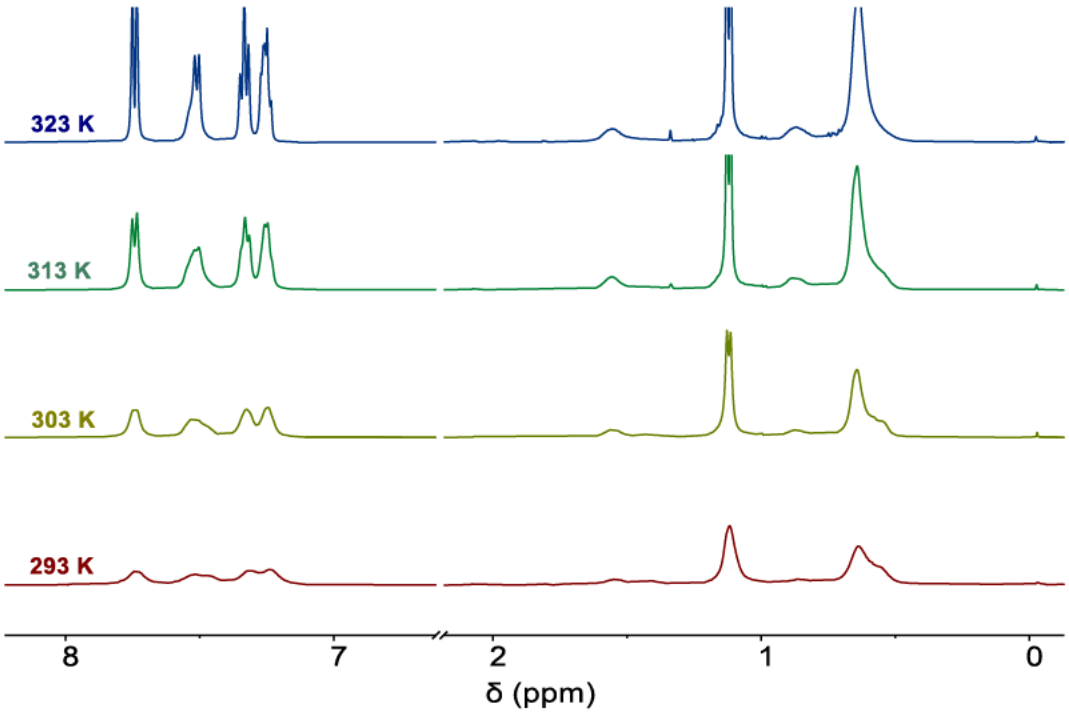

Figure S3.21 Temperature-dependent ^{1}H-NMR analysis of linear Fmoc-ISA 5a in phosphate buffer (50 mM) prepared from D_2O and DMSO-d_6 (9:1).

4.2. CD spectra of Fmoc-ISA 5a and kinked assembly precursor 1a

The linear peptide **5a** or the kinked assembly precursor **1a** were dissolved in phosphate buffer (10 mM, pH 7.4) to yield a peptide concentration of 500 µM. The solutions were sonicated to dissolve the peptides completely. The samples were subsequently measured, and the spectra were recorded at wavelengths from 300 to 180 nm with a bandwidth of 1 nm, data pitch of 0.2 nm, and scanning speed of 5 nm/min. The spectra were measured three times and accumulated.

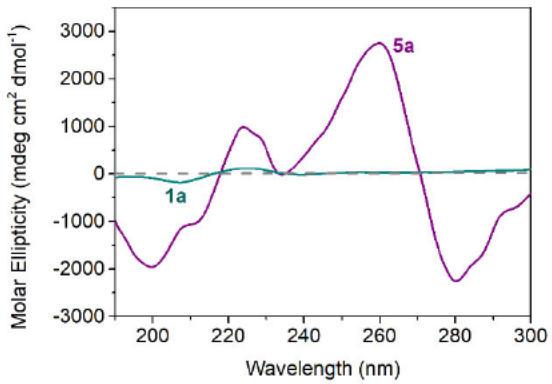

Figure S3.22 CD spectra of linear peptide 5a and assembly precursor 1a at 500 µM in phosphate buffer (10 mM, pH 7.4).

4.3. TEM analysis of linear Fmoc-ISA 5a

The linear peptide **5a** was dissolved in DMSO (10 mM) and diluted with DPBS at a ratio of 1:99 to yield a 100 μM peptide solution. The solution was incubated for 24 h and TEM grids were prepared by pipetting 3 μL of the solution onto a Formvar-coated copper grid and incubated for 5 min. After the incubation, the solutions were removed with filter paper, and the grids were stained with 7 μL 4% uranyl acetate solution for 2.5 min. The grids were washed three times with MilliQ water and dried before being measured.

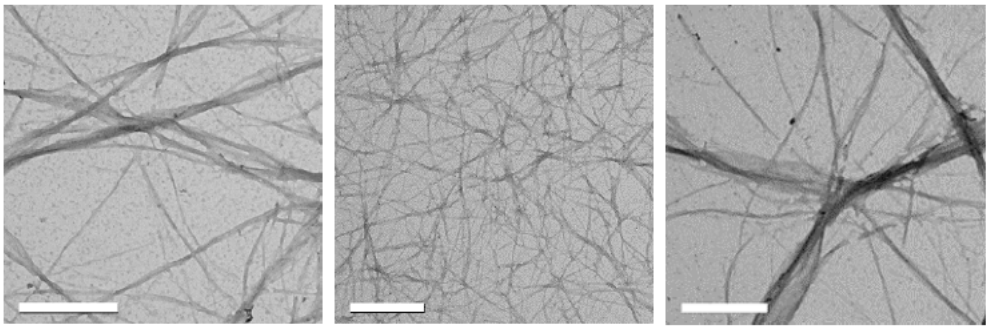

Figure S3.23 TEM images of nanofibers formed by 5a (100 μM) in DPBS (pH 7.4) and DMSO (99:1). Scale bar 500 nm.

4.4. TEM analysis of linear peptides and kinked precursors

The linear peptides **5a**, **5b** and **5c** were each dissolved in DMSO to achieve stock solution with 10 mM or 50 mM concentration. The respective DMSO stock solutions were mixed yielding the stock solutions of the mixed linear peptides: for Fmoc-ISA **5a** and Coumarin343-ISA **5c** at a 5:1 ratio and for Fmoc-ISA **5a** and Fmoc-ISA-Cy5 **5d** at a 99:1 ratio. The same was done for the kinked assembly precursors **1a** and **1c/1d**. The DMSO stock solutions of the mixed linear peptides and the mixed isopeptides were diluted with DPBS at a 1:99 ratio to yield 500 µM or 100 µM peptide solutions. The same was done for the stock solutions of the linear NBD-ISA **5c** and the control isopeptide **1c**. The TEM samples were prepared as described in section 1.2.8.

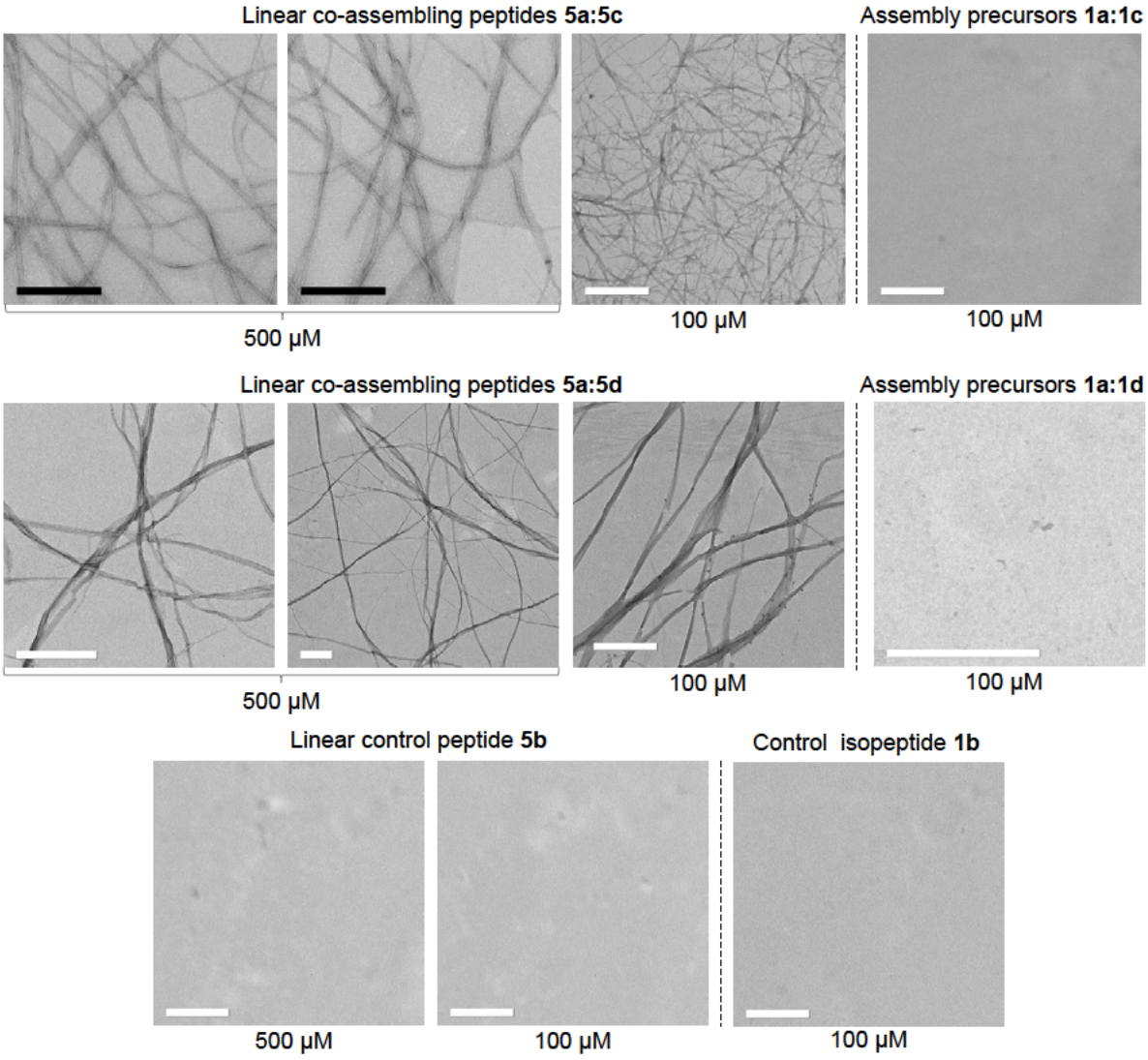

Figure S3.24 TEM images showing nanofibers formed by co-assembling peptides 5a:5c (5:1 ratio) and by 5a:5d (99:1 ratio), at concentrations of 500 µM and 100 µM in DPBS (pH 7.4) with 1% DMSO. For comparison, TEM images of non-assembling assembly precursors 1a:1c (5:1 ratio) and by 1a:1d (99:1 ratio) at 100 µM are shown.

Additionally, images of the linear control peptide 5b and the control isopeptide 1b at 500 μM and 100 μM, respectively, in DPBS (pH 7.4) with 1% DMSO are included. Scale bar 500 nm.

4.5. Cryo-TEM analysis of linear Fmoc-ISA 5a

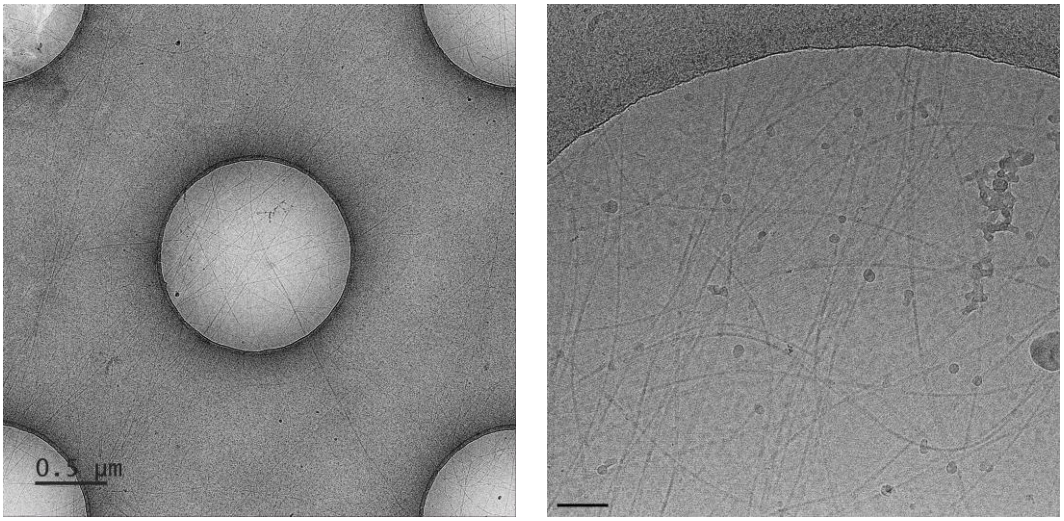

Figure S3.25 Cryo-TEM images of nanofibers formed by self-assembling peptide 5a (1 mg/ml) in DPBS (pH 7.4) and DMSO (99:1). Scale bars 500 nm (left) and 100 nm (right).

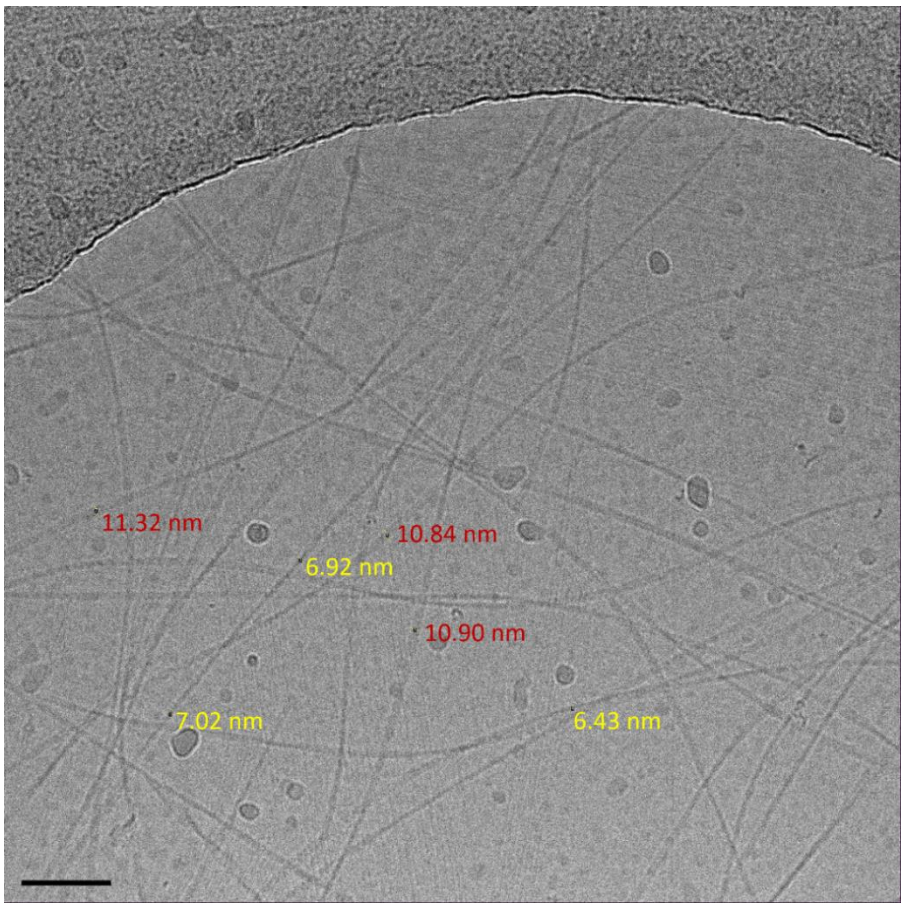

Figure S3.26 Cryo-TEM image of nanofibers formed by self-assembling peptide 5a (1 mg/ml) in DPBS (pH 7.4) and DMSO (99:1). The twisted fibers exhibit an average thickness of 6.8±0.3 nm at the twists (yellow) and 11.0±0.2 nm (red) at the non-twisted areas. Scale bar 100 nm.

4.6. Proteostat assay for the determination of the critical aggregation concentration

For the analysis of the critical aggregation concentration of the linear peptides **5a**, **5a:5c** (5:1) and **5a:5d** (99:1) the commercial Proteostat protein aggregation assay kit by *Enzo Life Sciences, Inc.* was used. The peptide samples were prepared by diluting DMSO stock solutions of the linear peptides **5a**, **5a:5c** (5:1) and **5a:5d** (99:1) in various concentrations (1 to 100 µM) with DPBS in a 1:99 ratio. The resulting peptide samples were incubated for 24 h at room temperature while shaking. The Proteostat working solution was prepared by mixing 0.52 µl of the Proteostat stock solution with 98.48 µl MilliQ water and 1 µl assay buffer. After the incubation, 27 µl of each peptide solution were mixed with 3 µl of the Proteostat working solution. 9 µl of each solution were pipetted into a well of a Greiner 384 flat black well plate (3 wells per sample of each peptide concentration). The plate was incubated in the dark for 15 min while shaking. The fluorescence intensity of the Proteostat dye was subsequently measured with an excitation and emission bandwidth of 20 nm and an emission wavelength of 600 nm after excitation at 550 nm.

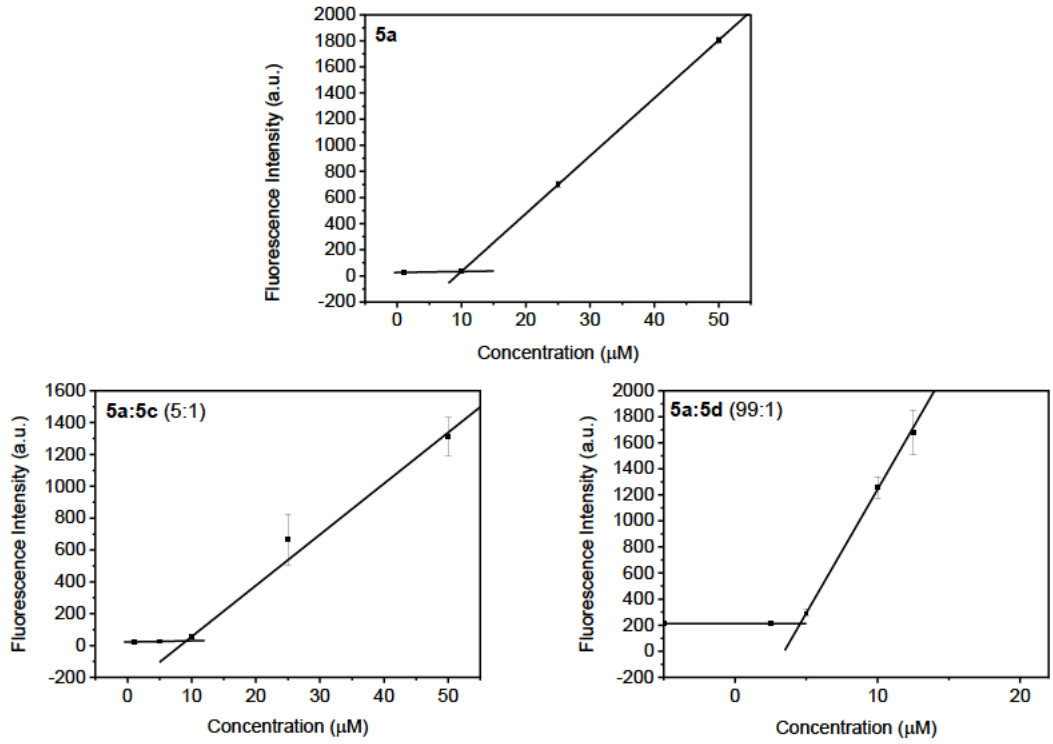

Figure S3.27 Proteostat aggregation assay of the linear Fmoc-ISA 5a (left) and of the mixed linear peptides Fmoc-ISA 5a and Fmoc-ISA-Cy5 5d (99:1) (right) in DPBS:DMSO (99:1). The samples were incubated at room temperature for 24 h before the analysis. By calculating the intersection of the linear fits, the critical aggregation concentration of 5a was determined to be 10 µM, while the critical aggregation concentration of the mixed linear peptides 5a:5b was 9.2 µM and of 5a:5d was 4.6 µM.

5. T Cell Experiments

5.1. Cell culture and activation of T cells

$CD8^+$ T cells were isolated from clinically healthy donors (LRS cones) via negative selection (https://www.stemcell.com/products/rosettesep-human-cd8-t-cell-enrichment-cocktail.html). After isolation, cells were counted and transferred into RPMI medium (+30%FBS, +1%P/S, +1% L-Glutamine, +1% NEAA, +12 mM HEPES) supplemented with 10% DMSO and frozen at -80°C. 3 days before the experiment, T cells were thawed and transferred to RPMI culture medium (+10%FBS, +1%P/S, +1% L-Glutamine, +1% NEAA, +12 mM HEPES) supplemented with 50 U/mL recombinant IL-2 and cultured overnight. Cells were then washed in culture medium and incubated with anti CD3/CD28 T cell activation DynaBeads at a 1:2 cell to bead ratio for 2 days. Inactivated control T cells were cultured without DynaBeads.

5.2. Cell uptake of isopeptides in T cells and confocal microscopy

After activation, DynaBeads were magnetically separated from the cells and the cells were transferred into fresh culture medium to a final concentration of $1x10^6$/mL (+50 U/mL rec. IL-2) for treatment with the peptides. Peptides were added at the indicated concentrations and incubated with active and resting control cells for 1 hour. Cells were then washed by centrifugation, resuspended in fresh cells culture medium and kept at 37 °C until further use for up to 24 hours.

Confocal microscopy was performed using a laser scanning microscope LSM 880 (Carl Zeiss AG). Images were acquired using a 20× (Plan-Apochromat 20x/0.8 M27, Carl Zeiss AG, Germany) and a 63× immersion oil objective (Plan-Apochromat 63x/1.4 Oil DIC M27, Carl Zeiss AG, Germany) and 488 nm, 543 nm and 647 nm laser lines. Images were analyzed using ImageJ (NIH) software. For imaging, dsLBs were dissolved 1:20 or 1:40 in 8-well Nunc LabTeK glass bottom chamber slides filled with 200 µL PBS.

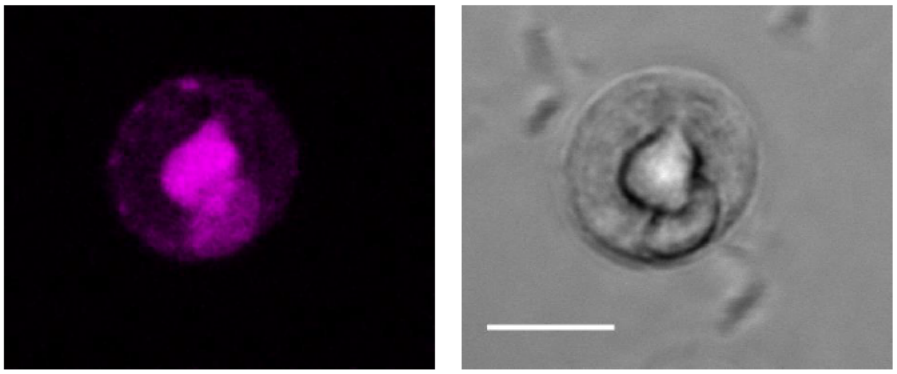

Figure S3.28 Confocal laser scanning microscopy (CLSM) images of activated T cells incubated with 5 µM of control isopeptide 1b (purple) for 1 hour. Scale bar: 15 µm.

5.3. Analysis of T cell cytotoxicity towards cancer cells

To assess bispecific T cell engager-mediated cancer cell killing, MCF-7 breast cancer cells were seeded at a density of 20,000 cells per 150 µL in 96-well plates. After allowing the cells to attach for 24 hours, the culture medium was replaced with RPMI 1640 containing L-Glutamine, supplemented with 1% fetal bovine serum, 1% penicillin/streptomycin, 1% non-essential amino acids, 50 mM HEPES, and 100 U/mL recombinant human IL-2. An anti-Her2-CD3 BiTE antibody (BSAB-002, Creative Biolabs, USA) was then added to the samples in a serial dilution. Pre-activated T cells, treated with different peptides concentrations as described previously, were introduced to the cancer cells at a 1:5 cancer-to-T cell ratio. To account for donor variation, T cells from two separate donors were used, each in technical duplicates. After 24 hours of co-culture at 37°C, 5% CO_2, and 100% humidity, the assay was terminated. Cells and supernatants were collected to measure T cell-induced cytotoxicity using LDH release analysis (9158-HA-010, Biotechne, USA) according to the manufacturer's instructions. Non-peptide treated T cells, single cultures of cancer cells and T cells as well as a human serum IgG antibody solution were used as controls. For positive controls, cancer cells were lysed by 10 mM SDS for 1 hour.

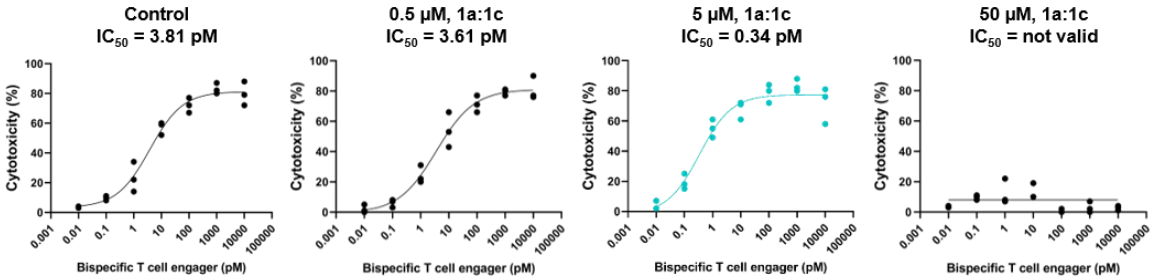

Figure S3.29 Dose-response curve showing the cytotoxic effect of activated T cells against HER2-expressing MCF7 cancer cells in relation to the concentration of a bispecific T cell engager targeting HER2 and CD3. The curves show data for T cells pre-treated with the isopeptides 1a:1c (5:1) at different concentrations for 1 hour, followed by washing and addition of the bispecific engager (n = 3 donors, mean of 2 technical replicates each).

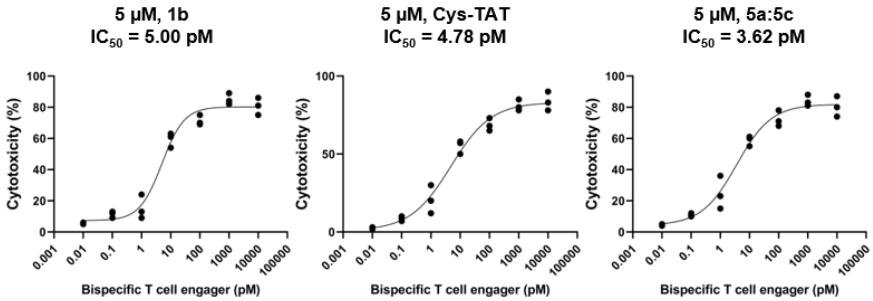

Figure S3.30 Dose-response curve showing the cytotoxic effect of activated T cells against HER2-expressing MCF7 cancer cells in relation to the concentration of a bispecific T cell engager targeting HER2 and CD3. The curves show data for T cells pre-treated with the control isopeptide 1b, the cell-penetrating transporter Cys-TAT and the linear peptides 5a:5c (5:1) at 5 µM each for 1 hour, followed by washing and addition of the bispecific engager (n = 3 donors, mean of 2 technical replicates each).

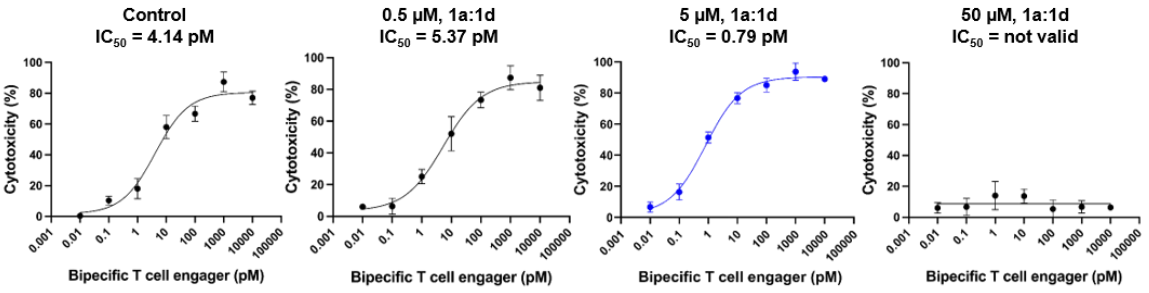

Figure S3.31 Dose-response curve showing the cytotoxic effect of activated T cells against HER2-expressing MCF7 cancer cells in relation to the concentration of a bispecific T cell engager targeting HER2 and CD3. The curves show data for T cells pre-treated with the isopeptides 1a:1d (99:1) at different concentrations for 1 hour, followed by washing and addition of the bispecific engager (n = 3 donors, mean of 2 technical replicates each).

5.4. Proteome profiler analysis

For proteome profiler analysis, pre-activated T cells were seeded at 100,000 cells per well and treated with the peptides as described above. Pre-activated cells that were not treated with peptides served as the negative control. To obtain sufficient final protein concentration, 40 technical replicates were prepared for each condition. After peptide treatment, the samples were washed with PBS and then pooled. The cells were subsequently lysed in Lysis Buffer 17, supplemented with 10 µg/mL of Aprotinin, Leupeptin hemisulfate, and Pepstatin A (all from R&D Systems, USA), for 30 minutes at 4°C under constant agitation. Cell debris was removed by centrifugation, and the protein concentration in the supernatant was measured using the BCA Protein Assay Kit (Merck, Germany) following the manufacturer's instructions. From each condition, 600 µg of protein was used to load the membranes of the Proteome Profiler Human Phospho-Kinase Array Kit (R&D Systems, USA). The assay was performed according to the manufacturer's protocol, with the Streptavidin-HRP replaced by IRDye 800CW Streptavidin (LI-COR Biotechnology, USA). Fluorescence intensity of the stained membranes was documented using an ODYSSEY M imaging system (LI-COR Biotechnology, USA) equipped with a 785 nm laser. Image analysis was carried out using ImageJ software (NIH).

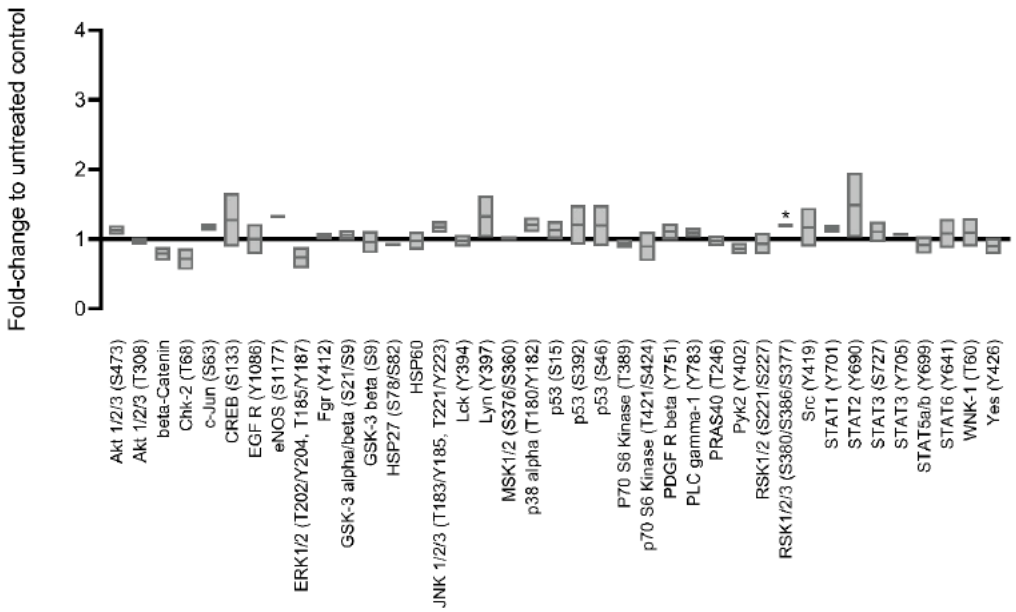

Figure S3.32 Proteome Profiler Human Phospho-Kinase Antibody Array analysis of T cells treated with the control isopeptide 1b at 5 µM for 1 hour (n = 2 donors, 2 on-membrane replicates).

5.5. Real-time deformation cytometry (RT-DC)

T cell deformation was measured by real-time deformation cytometry (RT-DC) using an AcCellerator (ZellMechanik Dresden, Germany). Deformation was induced by hydrodynamic stress as the T cells pass through a 15 µm x 15 µm channel within a microfluidic chip and driven by syringe pumps filled with RPMI cell culture medium at a flow rate of 0.06 µL/mL. The image-based analysis was performed using an inverted microscope (Axiovert 200M, ZEISS, Germany) and a CMOS camera (Mikrotron, Germany). The camera and the syringe pumps were controlled by the ShapeIn software (Zellmechanik Dresden, Germany). The analysis was performed with the ShapeOut 2 software (Zellmechanik Dresden, Germany). To exclude T cell debris the following limits were used: area >100 μm^2, circularity 0.960-0.995, deformation 0-0.0024 and porosity 1.0-1.4.

5.6. Correlative light and electron microscopy (CLEM) and structured illumination microscopy (SIM)

For post-embedding correlative light and electron microscopy (CLEM) of cryo-fixed human T cells (CTLs) was done as described previously.[1] Stimulated (24 h in culture) or resting CTLs were incubated with the glutathione-responsive isopeptides **1a** and **1d** (99:1) for 1 h at 37 °C. After several wash steps, CTLs were kept in RPMI medium supplemented with 30% FCS, 1% P/S, 1% NEAA, 50 U/ml IL-2, 50 mM HEPES and CellMask™ DeepRed (1:1000). Cells were then seeded on 1.4 mm sapphire discs coated with poly-L-ornithine (0.1 mg/ml) in flat specimen carriers (Leica) and vitrified in a high-pressure freezing system (EM PACT2, Leica). The frozen specimens were cryo-transferred into the precooled (-130 °C) freeze substitution chamber of the AFS2 (Leica). The temperature was increased from -130 to -90 °C for 2 h. Cryo-substitution was performed at -90 °C to -70 °C for 20 h in anhydrous acetone and at -70 to -60 °C for 24 h with 0.3% (wt/vol) uranyl acetate in anhydrous acetone. At -60 °C the samples were infiltrated with increasing concentrations (30, 60 and 100%; 1 h each) of Lowicryl® (3:1 K11M/HM20 mixture; Electron Microscopy Sciences). After a 5 h 100% Lowicryl infiltration, samples were UV polymerized at -60 °C for 24 h and for additional 15 h while temperature was raised linearly to 5 °C. Samples

were stored in the dark at 4 °C until further processing. After removing the membrane carriers, 100 nm ultrathin sections were cut using an EM UC7 (Leica) and collected on carbon-coated 200 mesh copper grids (Plano). 1 d after sectioning a grid was stained with DAPI for 3 min (1/1000), washed and sealed between a coverslip and a glass slide for high resolution SIM imaging. After fluorescence imaging, the grid was carefully removed, stained with uranyl acetate and lead citrate and recorded with a Tecnai12 Biotwin electron microscope. Only CTLs with well conserved membranes, cell organelles and nuclei were analyzed and used for correlation. The DAPI and/or the CellMask signals were used to find the best overlap with the electron microscope image. The final alignment defines the position of the fluorescent signals within the cell of interest. Images were overlaid in Corel DRAW X6.

Images for correlative fluorescence and electron microscopy (CLEM) were acquired with excitation light of 405, 488 and 642 nm wavelengths. Almost the entire field of view of a 200-mesh grid (around 90 µm^2) could be observed with a 63× Plan-Apochromat objective by SIM, allowing a perfect orientation relative to the grid bars. After adjusting the highest and lowest focus planes for z-stack analysis in brightfield, images were recorded with a step size of 100 nm. Fluorescent images were excited with 405 nm wavelengths to visualize DAPI. 488 nm wavelength was used for visualization of NBD and 642 nm for CellMask DeepRed or Cy5-labeled glutathione-responsive isopeptides. The DAPI image and the CellMask images were recorded to identify the nucleus, the plasma membranes of the CTL and the image plane. 3-10 images were recorded with a step size of 100 nm to scan the cells of interest. All the images were acquired with a 63× Plan-Apochromat (NA 1.4) and then processed to obtain higher resolutions by Zen 2012 (Zeiss).

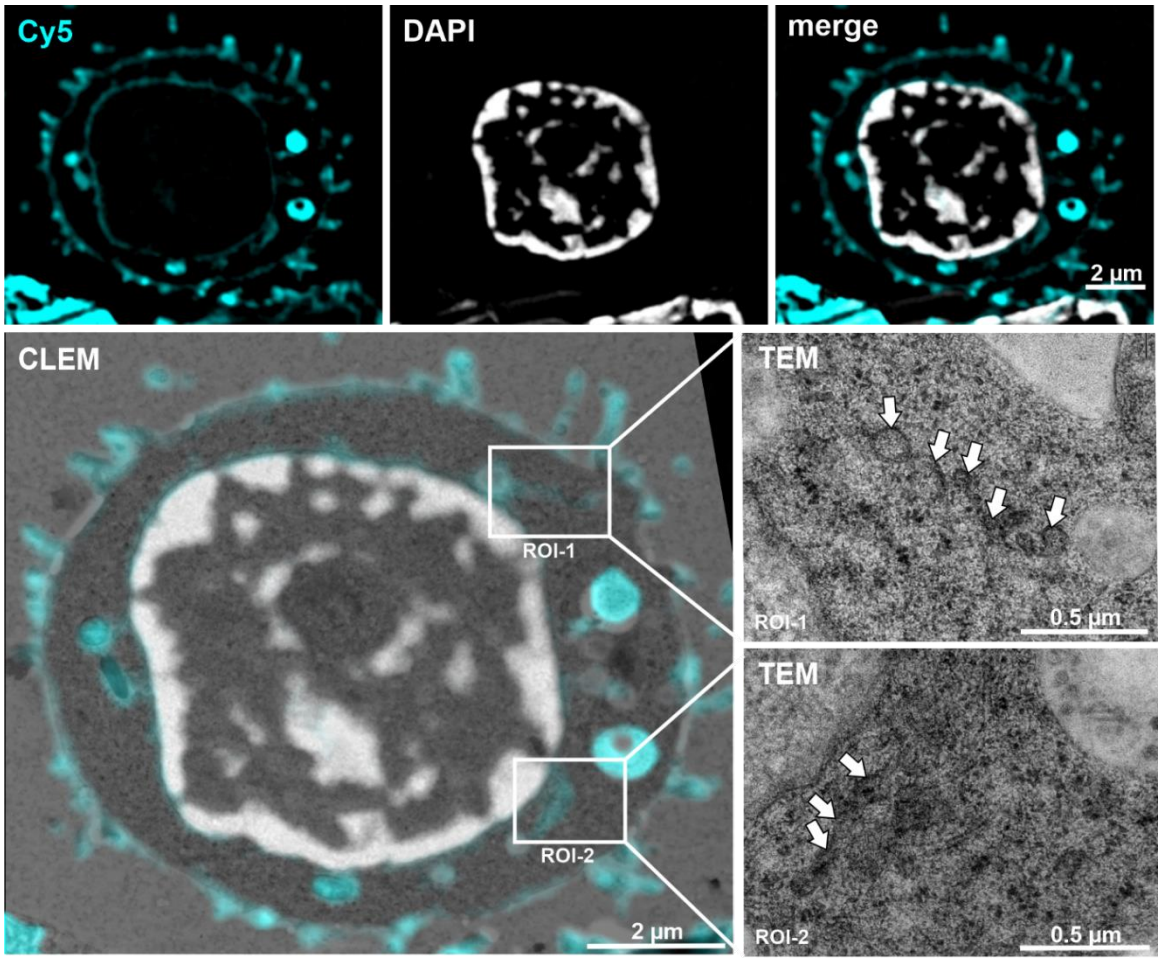

Figure S3.33 Correlative light and electron microscopy (CLEM) images of activated human $CD8^+$ T cells treated with 5 µM of glutathione-responsive isopeptides 1a and 1d (99:1) (cyan) for 1 hour before freezing.

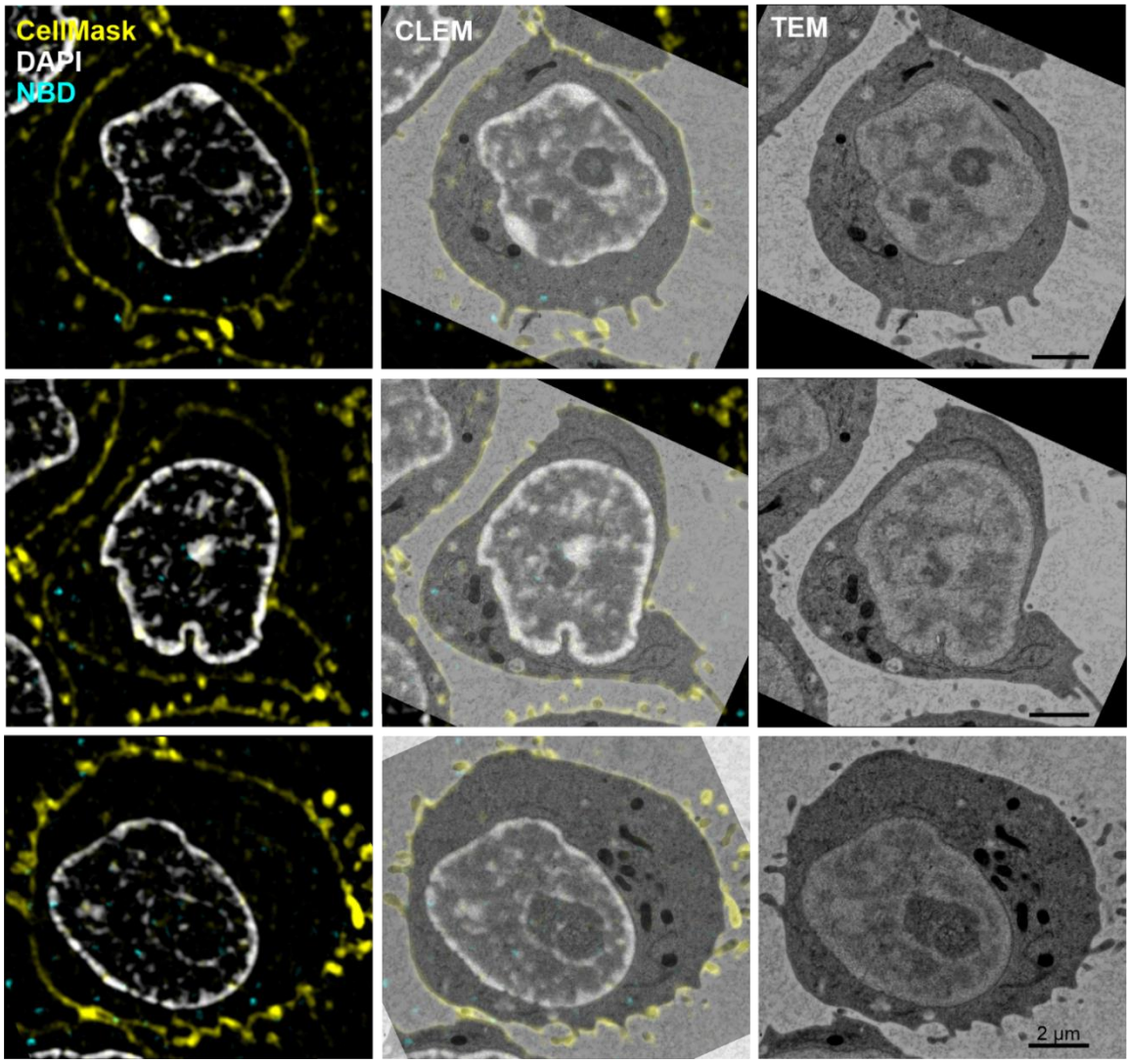

Figure S3.34 Correlative light and electron microscopy (CLEM) images of activated human CD8$^+$ T cells treated with 5 µM of control isopeptides 1b (cyan) for 1 hour before freezing.

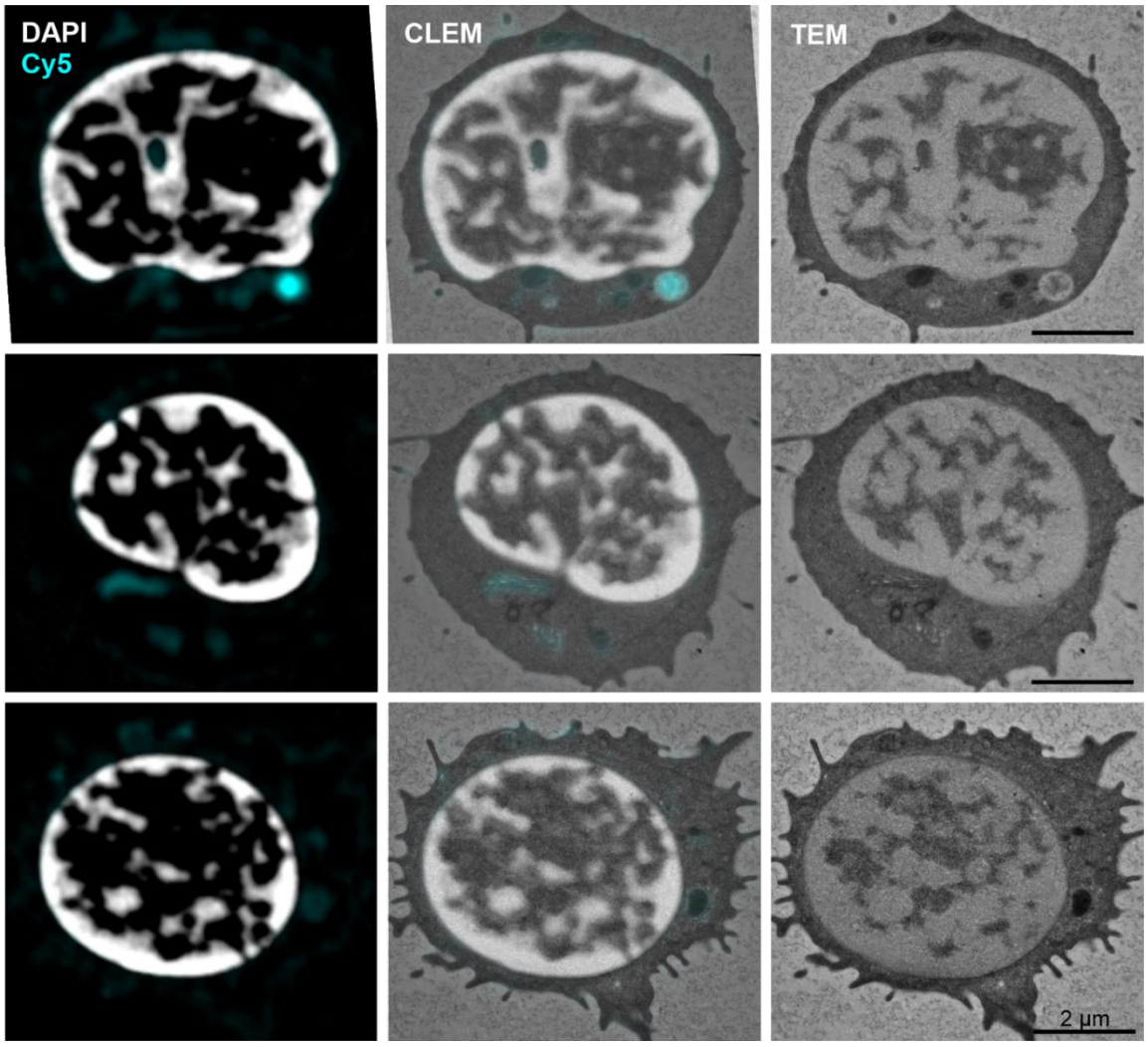

Figure S3.35 Correlative light and electron microscopy (CLEM) images of non-activated human $CD8^+$ T cells treated with 5 µM of glutathione-responsive isopeptides 1a and 1d (99:1) (cyan) for 1 hour before freezing.

References

1 Hsin-Fang Chang *et al.* Identification of distinct cytotoxic granules as the origin of supramolecular attack particles in T lymphocytes. *Nat. Commun.* 13, 1029 (2022).

4. Intracellular Formation of Synthetic Peptide Nanostructures Causes Mitochondrial Disruption and Cell Death in Tumor Spheroids

Authors

Sarah Chagri[‡], Konrad Maxeiner[‡], Lisa Förch, Julian Link, Patrick Roth, Raphael Meyer, Jana Fetzer, Anke Kaltbeitzel, Ingo Lieberwirth, Katharina Landfester, Manfred Wagner, David Y.W. Ng, and Tanja Weil

[‡] S. Chagri and K. Maxeiner contributed equally to this work.

Reproduced, with minor changes, from 'Chagri, S.[‡]; Maxeiner, K.[‡]; Förch, L.; Link, J.; Roth, P.; Meyer, R.; Fetzer, J.; Kaltbeitzel, A.; Lieberwirth, I.; Landfester, K.; Wagner, M.; Ng, D. Y. W.; Weil, T. Intracellular Formation of Synthetic Peptide Nanostructures Causes Mitochondrial Disruption and Cell Death in Tumor Spheroids. *ChemRxiv*, doi:10.26434/chemrxiv-2024-xkxpb (2024).'

Contributions

Sarah Chagri: Conceptualization, molecular design of peptides and planning of synthesis and experiments. Synthesis and characterization of peptides and associated molecules. CD measurements and NMR analysis. Cell uptake experiments and cell viability assays. Data analysis and interpretation of all corresponding results. Writing of the manuscript.

Konrad Maxeiner: Cell uptake experiments and cell viability assays. Metabolic analysis and tumor spheroid experiments. Data analysis and interpretation of all corresponding results. Writing of the manuscript.

Lisa Förch: Tumor spheroid experiments.

Julian Link: Synthesis of peptides.

Patrick Roth: TEM measurements for the analysis of peptide structure formation and interpretation of results.

Raphael Meyer: CD measurements and interpretation of results.

Jana Fetzer: Synthesis of peptides.

Anke Kaltbeitzel, Ingo Lieberwirth, Katharina Landfester: CLEM measurements and interpretation of results.

Manfred Wagner: Measuring and interpretation NMR spectra.

David Y. W. Ng: Design and discussion on the concept and results. Editing of the manuscript.

Tanja Weil: Acquiring funding for the project, design and discussion of the concept and results. Editing of the manuscript.

Abstract

Supramolecular assemblies found in nature demonstrate the concept of creating functionality through structure formation. In recent years, these complex natural architectures have inspired the development of materials for the formation of synthetic nanostructures within living cells. These intracellular assemblies have the potential to modulate cellular processes, yet their specific effects on cellular metabolism and three-dimensional (3D) cell networks, such as tumor spheroids, still remain underexplored. Herein, we correlate the glutathione-induced formation of synthetic nanostructures inside MDA-MB-231 triple negative breast cancer cells to the metabolic disruption and mitochondrial degradation observed in two-dimensional (2D) cell culture, as well as to cell death and size decrease in a three-dimensional (3D) tumor spheroid model. In 2D cell culture, material-cell interactions were examined through live-cell imaging and by quantifying changes in mitochondrial respiration. By studying the interplay between glutathione-responsive cytosolic peptide assembly and the implications on the integrity of the mitochondrial network, as well as on 3D cell networks, our work advances the understanding of how synthetic intracellular nanofibers impact vital functions of living cells.

4.1. Introduction

Intracellular nanostructures, such as the cytoskeleton, are naturally occurring protein assemblies that regulate fundamental processes involved in cell metabolism, division, and motility.[1] These intricate and dynamic protein assemblies span the cytosol, serving as a blueprint for the design of synthetic nanomaterials for intracellular structure formation. The creation of synthetic architectures within mammalian cells represents a milestone in synthetic biology and nanomedicine, as it offers a bottom-up understanding of how natural intracellular assemblies can be replicated based on molecular design principles. This knowledge offers new avenues for understanding the impact of such assemblies on cellular integrity, function and viability.[2]

Given the prevalence of the resistance to various chemotherapeutics in healthcare, the development of alternative strategies for effective treatment represents a vital objective in biomedical sciences.[3] Supramolecular approaches that involve forming synthetic nanostructures inside cells represent a unique strategy for mechanically inducing cell death by disrupting vital cellular processes.[4] The accumulation of larger aggregates inside cancer cells enhances the retention of synthetic materials, thereby improving pharmacokinetic properties and circumventing common drug resistance mechanisms, such as clearance driven by the overexpression of efflux pumps. However, preventing the premature assembly of the nanomaterial outside cells is crucial in the material design process. Tailoring synthetic nanomaterials to display bioresponsive properties ensures that the pro-assembling compounds transform into active monomers only in the presence of specific endogenous cues, enhancing spatiotemporal control over assembly formation.[2] Physiological stimuli, such as pH gradients[5], intracellular enzymes[6], and the high concentration of the reductive glutathione in the cytosol[7], can be exploited to selectively induce

structure formation. In cancerous cells, the intracellular glutathione concentration is often increased[8,9] which contributes to multidrug resistance due to the glutathionylation and subsequent elimination of small molecule drugs[10,11]. This biological phenomenon can be used to design pro-assembling precursors by introducing glutathione-responsive trigger groups with cleavable disulfide bridges[6,12,13], enabling the controlled formation of synthetic nanostructures inside living cells upon reduction.

In recent years, our group has developed a series of peptide-based pro-assembling precursors that undergo a multistep conversion process in response to two specific environmental cues: the acidifying environment inside endosomes upon cellular uptake and the presence of reactive oxygen species (ROS) in the cytosol upon endosomal escape.[4,14,15] Building upon this foundation, we have expanded the portfolio towards a glutathione-responsive system that activates immune cells through the formation of intracellular peptide nanostructures.[16] The glutathione-induced peptide assembly within activated cytotoxic T cells stimulates T cell effector function thereby increasing their cytotoxic activity towards cancer cells.[16] Despite this progress, detailed studies on the concentration- and time-dependent biological impacts of synthetic intracellular assemblies – particularly regarding their effects on cancer cell metabolism – have only recently emerged. It is therefore essential to investigate the uptake, distribution and intracellular conversion of assembly precursors over time to elucidate how the timeline of *in situ* structure formation correlates with the impact on cellular function.

To date, the analysis of in-situ intracellular structure formation has been mostly focused on cells cultured in conventional two-dimensional (2D) monolayers.[15,16] However, findings derived from 2D cell cultures often fail to accurately replicate *in vivo* conditions, primarily due to their oversimplified cell-cell and cell-extracellular

matrix interactions. In contrast, three-dimensional (3D) cell networks more closely emulate the complex interactions observed *in vivo*. Notably, multicellular tumor spheroids exhibit key characteristics of solid tumors, including gradients in oxygen and nutrients from the outer cell layers to the hypoxic core, as well as high cell density.[17]

Herein, we present the *in situ* formation of metabolism-disrupting nanostructures inside 2D-cultured cancer cells and 3D tumor spheroids using glutathione-responsive pro-assembling *iso*peptides. These peptides undergo a multistep reaction cascade into self-assembling linear peptides upon cellular uptake (Figure 4.1). This study introduces live-cell and fluorescent lifetime imaging to observe real-time changes in the mitochondrial network and integrity during the formation of fluorescent peptide nanostructures for the first time. With similar time resolution, the impact on mitochondrial respiration is quantified by measuring the cellular oxygen consumption rate (OCR) *via* an extracellular flux analyzer. These measurements allow us to discern the effect of intracellular structure formation on the oxidative phosphorylation and energy homeostasis of multidrug-resistant MDA-MB-231 triple negative breast cancer cells. Additionally, we investigate the toxicity of the glutathione-responsive isopeptides in three-dimensional MDA-MB-231 tumor spheroids, monitoring their size reduction to assess the biological impact of the *in situ* formed nanostructures.

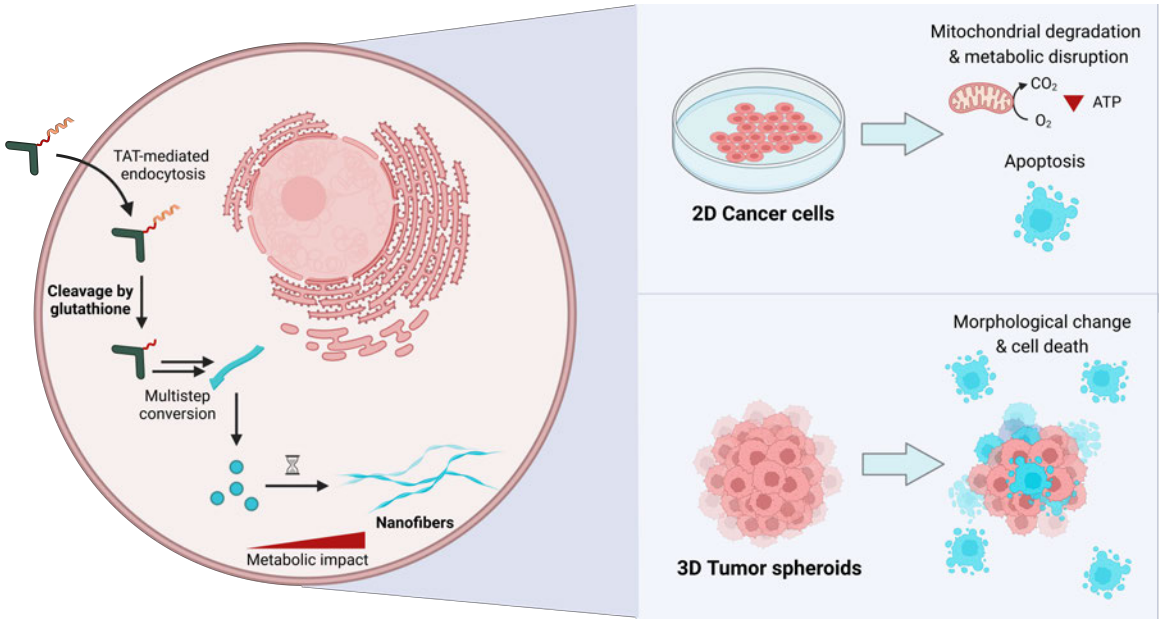

Figure 4.1 Schematic representation of glutathione-induced intracellular peptide assembly inside 2D-cultured cancer cells and 3D tumor spheroids. Glutathione-responsive isopeptides enter the cells via transactivator of transcription (TAT)-mediated endocytosis and are subjected to glutathione-induced cleavage in the cytosol, followed by a multistep conversion into linear self-assembling peptides. This intracellular transformation leads to the formation of nanostructures that disrupt the mitochondrial network causing cancer cell death and size decrease of tumor spheroids.

4.2. Results and Discussion

4.2.1. Design and transformation of glutathione-responsive isopeptides

The glutathione-responsive pro-assembling *iso*peptides **1a** and **1b** consist of three main structural components: (1) the cell-penetrating peptide sequence TAT (transactivator of transcription) derived from human immunodeficiency virus (HIV); (2) a glutathione-responsive trigger group capable of reductive degradation; and (3) the pro-assembling *iso*peptide with an aromatic *N*-terminal group that is necessary for self-assembly (Fmoc) and fluorescence (Coumarin 343), respectively (Figure 4.2a).[16] To assess the effects of glutathione-induced transformation without self-assembly, we synthesized the control *iso*peptide **1c** (Figure 4.2a). This control includes a nitrobenzodiazole (NBD) fluorophore at the *N*-terminus and is designed to enter cells and undergo glutathione-induced transformation but does not produce

self-assembling peptide monomers (Figure S4.18). Additionally, non-cell-penetrating control *iso*peptides **4a** (with Fmoc) and **4b** (with Coumarin 343) were synthesized with a triethylene glycol unit replacing the cell-penetrating TAT sequence (Figure 4.2a).

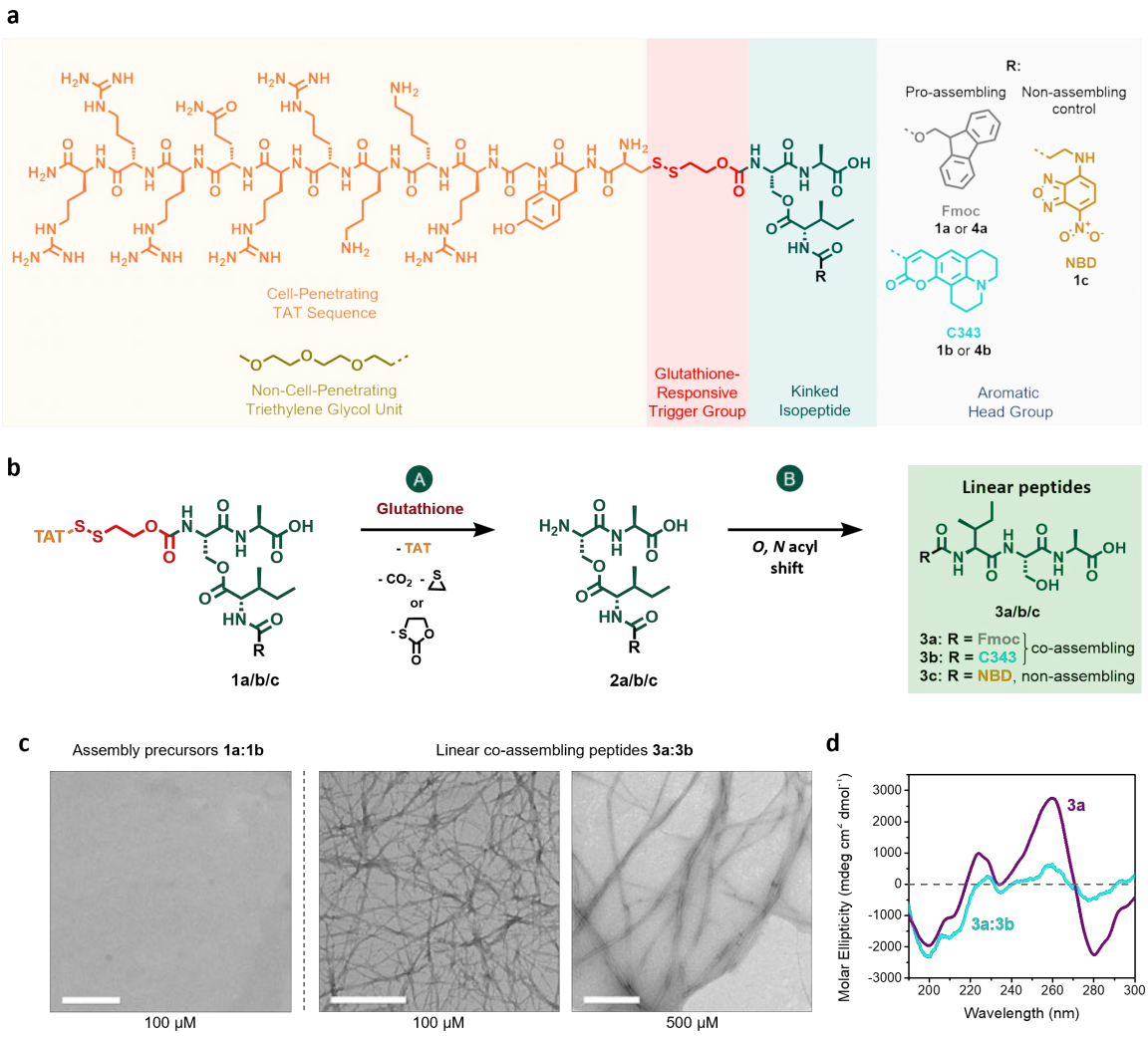

Figure 4.2 Chemical structures and multistep conversion of glutathione-responsive isopeptides into fibrillating peptide nanostructures. a) Chemical structure of glutathione-responsive pro-assembling *iso*peptides **1a** (with a Fmoc (9-fluorenylmethoxycarbonyl) group) and **1b** (with a C343 (Coumarin 343) moiety), as well as chemical structures of non-assembling control *iso*peptides **1c** (with an NBD (nitrobenzodiazole) unit), and triethylene glycol-modified non-cell-penetrating *iso*peptides **4a** and **4b**. **b)** Reaction scheme of the multistep conversion of glutathione-responsive *iso*peptides **1a/b/c** *via* the deprotected *iso*peptides **2a/b/c** into the co-assembling linear peptide monomers **3a** and **3b** or the non-assembling linear peptide **3c**. **c)** Transmission electron micrographs (TEM) of nanofibers formed by co-assembling peptides **3a** and **3b** (5:1 ratio at 500 µM and 100 µM) and TEM images of non-assembling assembly precursors **1a** and **1b** (5:1 ratio at 100 µM) in DPBS (pH 7.4) and DMSO (99:1). Scale bar 500 nm. **d)** Circular dichroism (CD) spectra of linear peptide **3a** (purple curve) and linear co-assembling peptides **3a** and **3b** (5:1 ratio) (cyan curve) at 500 µM in phosphate buffer (10 mM, pH 7.4).

To investigate the structure formation of the linear co-assembling peptides **3a** and **3b**, which are the final products of the glutathione-induced transformation of **1a** and **1b**, we used dry-state transmission electron microscopy (TEM) (Figure 4.2c and Figure S4.18). The TEM images revealed that the co-assembly of Fmoc-ISA **3a** and Coumarin 343-ISA **3b** formed elongated fibrillar peptide nanostructures at concentrations of 100 µM and 500 µM in a 5:1 ratio of **3a:3b** in DPBS (pH 7.4) with 1% DMSO. In contrast, the kinked pro-assembling isopeptides **1a** and **1b** did not form such supramolecular structures under similar conditions, underscoring their role as assembly precursors that require a stimulus to transform into the self-assembling monomers.

The circular dichroism (CD) spectra of both the self-assembling monomer Fmoc-ISA **3a** and the mixture of co-assembling linear peptides **3a** and **3b** (in a 5:1 ratio) both exhibited nanoscale chirality[18], featuring a peak at 260 nm indicative of $\pi \rightarrow \pi^*$ transitions in the aromatic head groups (see Figure 4.2d). Additionally, a secondary peak at 224 nm was observed, corresponding to the $n \rightarrow \pi^*$ transition of the carbonyl groups in the peptide backbone, which can be attributed to hydrogen bonding.[19,20] Notably, the CD spectrum of the co-assembled **3a:3b** mixture showed a slightly lower intensity at 260 nm compared to the spectrum of the self-assembling peptide **3a**. This reduction can be explained by the fact that the aromatic interactions between the Fmoc- and Coumarin 343-functionalized peptides **3a** and **3b** are weaker than the interactions solely between the Fmoc groups in peptide **3a**.

To complement these structural analyses and to assess the critical aggregation concentration (CAC) of the co-assembling peptides **3a** and **3b** (5:1 ratio), we conducted a Proteostat aggregation assay. This assay detects assemblies through an increase in fluorescence upon binding the Proteostat dye. The analysis indicated

a CAC of 9.2 µM for the linear peptides **3a** and **3b** in a 5:1 ratio in DPBS (pH 7.4) with 1% DMSO (Figure S4.19).

4.2.2. *In situ* formation of peptide nanostructures inside cancer cells

Next, we investigated the cellular uptake of the glutathione-responsive *iso*peptides, their subcellular distribution and the *in situ* formation of intracellular nanofibers. For this purpose, we incubated MDA-MB-231 breast cancer cells with a 5:1 mixture of Fmoc-substituted *iso*peptide **1a** and Coumarin 343-substituted *iso*peptide **1b** and examined the emergence of fluorescent intracellular nanostructures *via* confocal laser scanning microscopy (CLSM) (Figure 4.3).

Time-lapsed live-cell imaging revealed that the TAT-modified *iso*peptides **1a** and **1b** (5:1 ratio, 50 µM total peptide concentration) rapidly entered the cells and formed fluorescent peptide aggregates already within the first 15 minutes of incubation (Figure 4.3a). First, upon cell entry, we observed Coumarin 343-associated fluorescence in localized round areas distributed throughout the cytosol (Figure 4.3a). After ten minutes of incubation with **1a** and **1b**, we noticed fibrillar and directed peptide nanostructures growing in an aster-like pattern from the round areas of increased fluorescence extending into the surrounding cellular space (Figure 4.3a, ROI). The cells exhibiting these intracellular structures showed a decrease in overall size and change in shape after 15 minutes (Figure 4.3a).

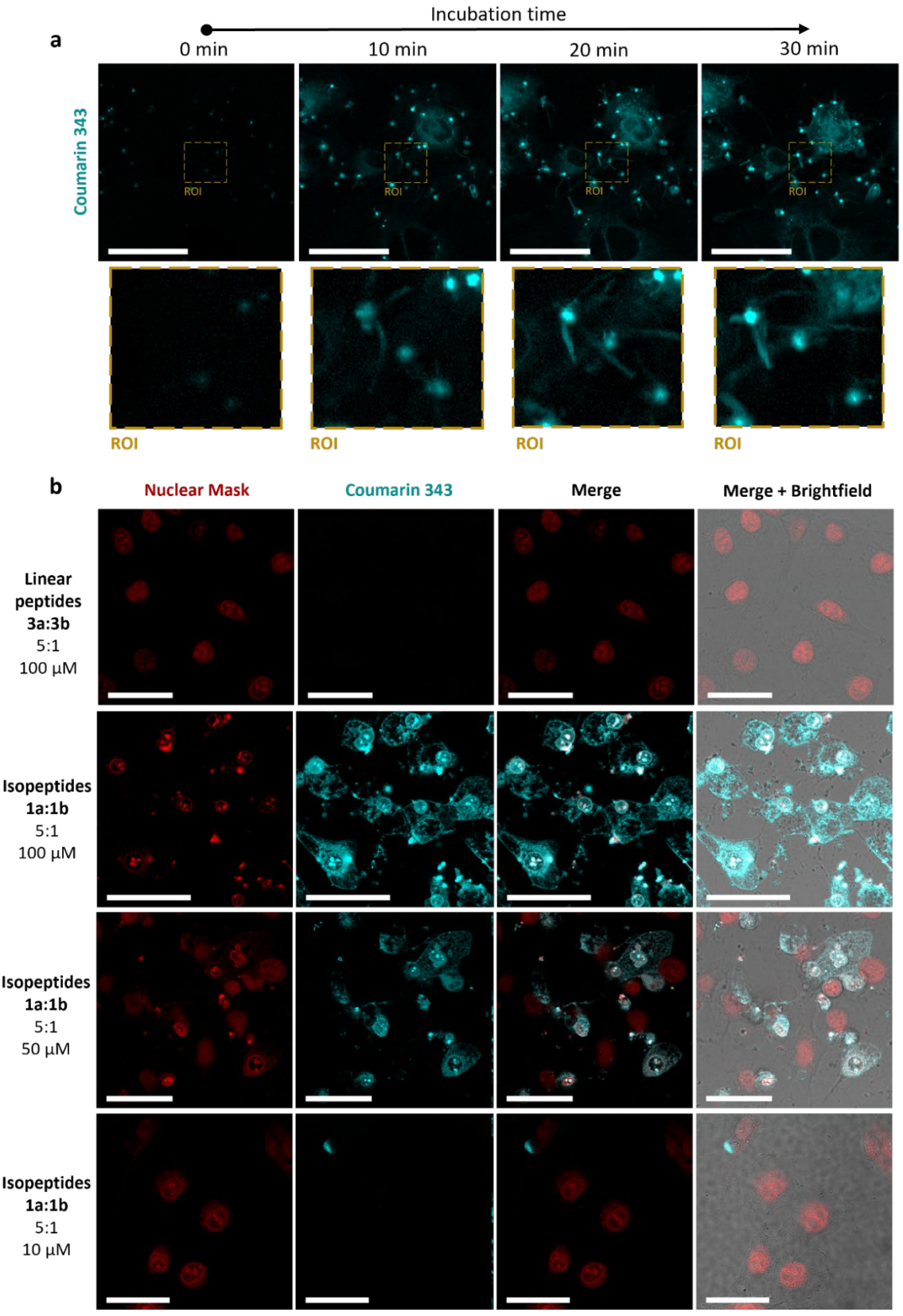

Figure 4.3 Cell uptake and intracellular peptide structure formation in cancer cells. a) Time-dependent live-cell imaging of MDA-MB-231 cells treated with 50 µM of the glutathione-responsive isopeptides **1a** and **1b** (5:1) (cyan). The rectangle indicates a region of interest (ROI) in which structure

transformation from globular peptide structures to fibrous nanostructures can be observed. Scale bars 50 µm. b) Confocal laser scanning microscopy (CLSM) images of MDA-MB-231 breast cancer cells after 4 h of incubation with glutathione-responsive isopeptides **1a** and **1b** (5:1) at 100 µM, 50 µM and 10 µM (cyan) (second to fourth row). As a control, cells were incubated with the linear peptides 3a and 3b (top row) at 100 µM. The nucleus was stained with HCS Nuclear Mask Deep Red (red). Scale bars 50 µm.

Further analysis of MDA-MB-231 breast cancer cells treated with the assembly precursors **1a:1b** at 100 µM and 50 µM for 4 h revealed the presence of highly fluorescent structures throughout the cytosol (Figure 4.3b, second and third row). Co-staining of the nucleus showed a strong Coumarin 343-fluorescence signal in the perinuclear and nuclear regions (Figure 4.3b, second and third row). This observation of co-localization could be explained by the inherent nucleus-targeting properties of TAT[24], which may result in residual non-cleaved assembly precursors accumulating in the proximity of the nucleus. Additionally, we observed that in the cells treated with **1a:1b** at 100 µM, the nucleus stain was most intense in small, condensed areas of the nuclear region (Figure 4.3b, second row). These observations are indicative of nuclear fragmentation, which is associated with decreased cell viability (Figure S4.25). For the lower *iso*peptide concentration of 10 µM, the peptides remained contained within small areas for 4 h (Figure 4.3b, bottom row), and no significant disruption of cellular integrity was evident.

The formation of intracellular peptide architectures was further investigated using correlative light and electron microscopy (CLEM) (Fig. S4.23). CLEM analysis of MDA-MB-231 cells treated with 100 µM of **1a:1b** for 4 h revealed fluorescent peptide assemblies within the cytosol, especially in the nuclear and perinuclear regions (Fig. S4.23). In close proximity to fluorescent peptide nanostructures, mitochondria with disrupted membranes were observed, indicating that cytosolic assembly has negative impacts on the integrity of these organelles (Fig. S4.23). The subcellular distribution observed *via* CLEM was consistent with CLSM analysis (Fig. 4.3), confirming the ability of *iso*peptides **1a:1b** to form nanostructures within living cells.

As a control, cells treated directly with the linear co-assembling peptides **3a:3b** (5:1 ratio), the final products of the glutathione-induced reaction cascade of **1a:1b**, did not show any uptake or impact on cellular morphology, underlining the importance of the TAT-mediated cell entry and the *in situ* intracellular transformation (Figure 4.3b, top row). For the non-assembly-inducing control *iso*peptide **1c**, internalization was observed but without impact on cellular integrity (Figure S4.20). This further supports that the *in situ* formation of supramolecular peptide nanostructures is necessary to elicit a biological response.

4.2.3. Peptide nanostructures disrupt the cytoskeleton of cancer cells

The cytoskeleton, particularly the actin filament network, plays a vital role in maintaining cell structure, movement and organization.[1] As we observed rapid morphological changes in cells in response to the formation of the peptide nanostructures, we seek to understand the relationship between the formation of synthetic peptide nanostructures and the loss of cytoskeletal integrity. Therefore, MDA-MB-231 cells were treated with varying concentrations of the *iso*peptides **1a:1b** for 4 h and their actin filaments were subsequently stained with Alexa Fluor™ 555 Phalloidin (Figure 4.4). At high concentrations of 100 or 50 µM of **1a:1b**, significant fragmentation of the actin filaments was observed (Figure 4.4, second to fourth row and Figure S4.24). Notably, in areas of very high Coumarin 343 fluorescence, there was a marked absence of phalloidin-stained actin filaments, suggesting that peptide nanostructure formation disrupts the cytoskeleton (Figure 4.4, second and third row, ROI). In cells incubated with 10 µM of the *iso*peptide mixture **1a:1b** (Figure 4.4, bottom row), no apparent changes to the integrity and density of the actin filaments were observed compared to the control cells treated with the linear peptides **3a:3b** (Figure 4.4, top row).

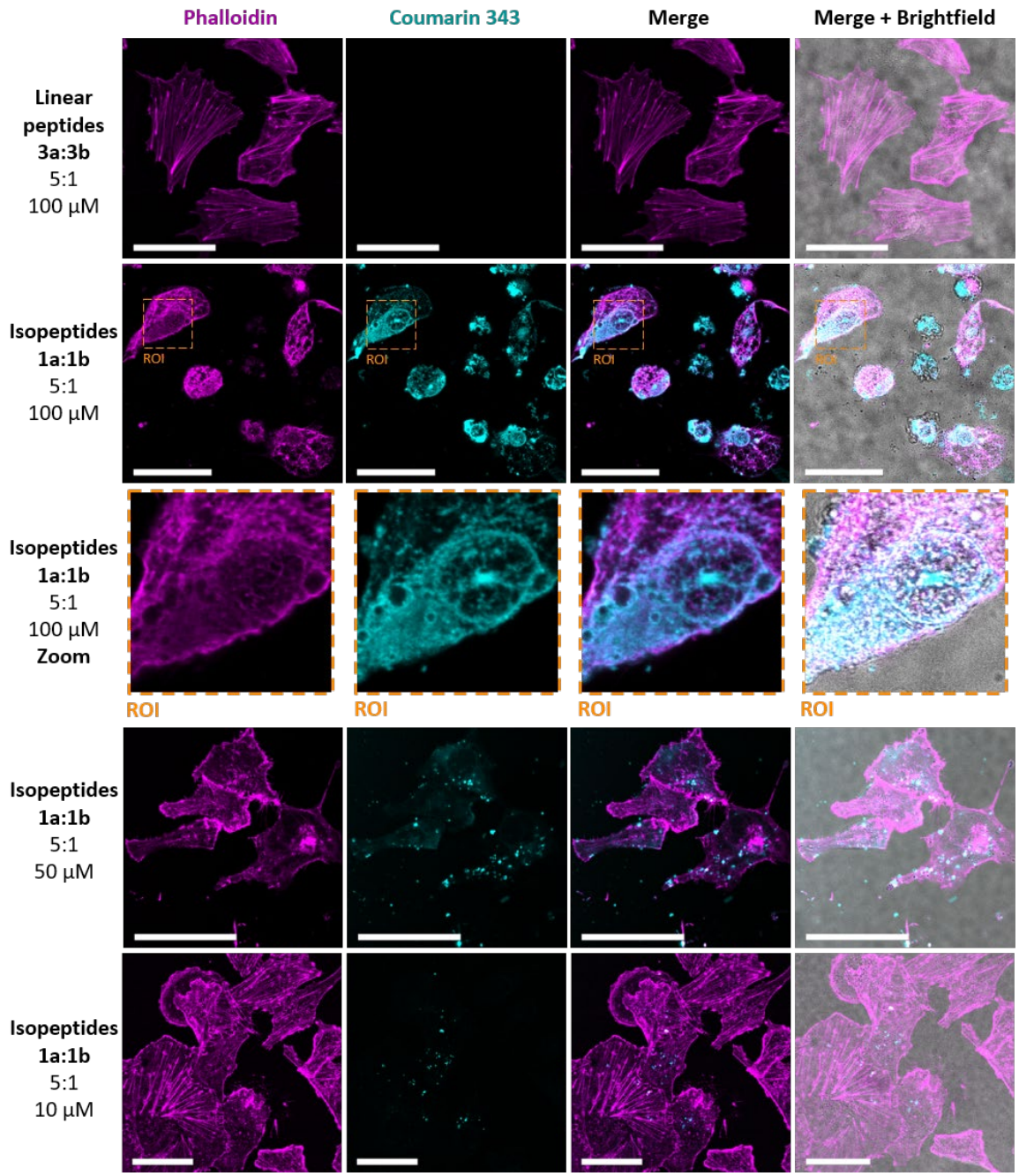

Figure 4.4 Disruption of actin filaments by *in situ* formed nanostructures. Confocal laser scanning microscopy (CLSM) images of MDA-MB-231 cells after 4 h of incubation with glutathione-responsive *iso*peptides **1a** and **1b** (5:1) (cyan) at different concentrations or the linear peptides **3a:3b** and additional staining with Alexa Fluor™ 555 Phalloidin (pink). Scale bars 50 µm.

4.2.4. Intracellular structure formation impacts metabolism and disrupts mitochondrial integrity

Analyzing the synthetic structure formation inside cells via CLSM and CLEM revealed morphological changes upon intracellular peptide assembly, which include blebbing, cell rounding and fragmentation of both nuclei and actin filaments (Figure 4.3 and 4.4). These findings indicate an effect on cell viability, which was determined in the next step using CellTiter-Glo Assay after a 4 h incubation with the pro-assembling precursors **1a:1b** at different concentrations. A concentration dependent effect on cell viability was observed and an IC_{50} of 36.4 ± 3.1 µM was calculated (Figure S4.25). In combination with the CLEM images, which revealed a localization of peptide nanofibers in close proximity to mitochondria with disrupted membranes, these results indicate that the peptide nanofibers impact energy metabolism of the cells. To gain further insights into the mechanism of how synthetic peptide nanostructures effect cell integrity, mitochondria function was investigated in more detail, as these organelles are essential for cell metabolism and dynamics, and maintaining energy homeostasis. To assess the impact of peptide assembly on mitochondrial structure and function, we performed live-cell imaging with cells that had been transfected with CellLight™ Mitochondria-RFP (Figure 4.5a and Figure S4.21). We observed that within the first 30 minutes of incubation with 50 µM of the *iso*peptides **1a:1b** the mitochondria of the cancer cells underwent significant changes: starting from an interconnected network of tubular-shaped organelles, their morphology transformed into shrunken, fragmented and more punctiform mitochondria (Figure 4.5a). These observations point towards mitochondrial fragmentation, which could be a result of changes in the rates of mitochondrial fusion and fission events[25] indicative of early stages of cell death[26]. To further investigate the mitochondrial disruption, we quantitatively assessed various aspect of mitochondrial respiration as a function of the formation of the

peptide nanostructures. Using a Seahorse XFe96 extracellular flux analyzer, we measured the oxygen consumption rate (OCR) of cells treated with various electron transport chain (ETC) modulators, providing further insights into cellular respiration. When adding the pro-assembling *iso*peptides **1a:1b** to the cells, we observed a concentration-dependent decrease in OCR already within the first 30 minutes of incubation (Figure 4.5b). For the lowest concentration of 10 µM, no effect on the OCR was found indicating cellular tolerance to this amount of assembly precursors. This correlates with the cell viability data (Figure S4.25), where no negative effect was observed at this concentration, as well as to the critical aggregation concentration of the co-assembling peptides (Figure S4.19).

However, starting at 25 µM total *iso*peptide concentration, a rapid reduction in OCR was observed, which was even more pronounced at 50 and 100 µM (Figure 4.5b). This showed that the addition of the assembly precursors **1a:1b** at concentrations capable of causing intracellular structure formation led to a significant decrease in basal respiration within less than 30 minutes. These quantitative findings aligned with the visual data from live-cell imaging of mitochondria-stained cells (Figure 4.5a), confirming mitochondrial dysfunction as a consequence of intracellular peptide assembly. Besides examining the cellular response to **1a:1b** in terms of basal respiration, we also studied the impact on ATP production and the spare respiratory capacity, as both properties are indicative of mitochondrial health and metabolic function (Figure 4.5c). Here we also noticed a concentration-dependent effect of the *iso*peptides **1a:1b** with cells being treated with ≥ 25 µM overall peptide concentration exhibiting a significantly reduced ATP production and spare respiratory capacity (Figure 4.5c). In contrast, no effect on mitochondrial function was observed for the linear peptides **3a:3b**, underscoring the importance of intracellular accumulation of assembly precursors and the propagation of resulting peptide assemblies to elicit a biological response.

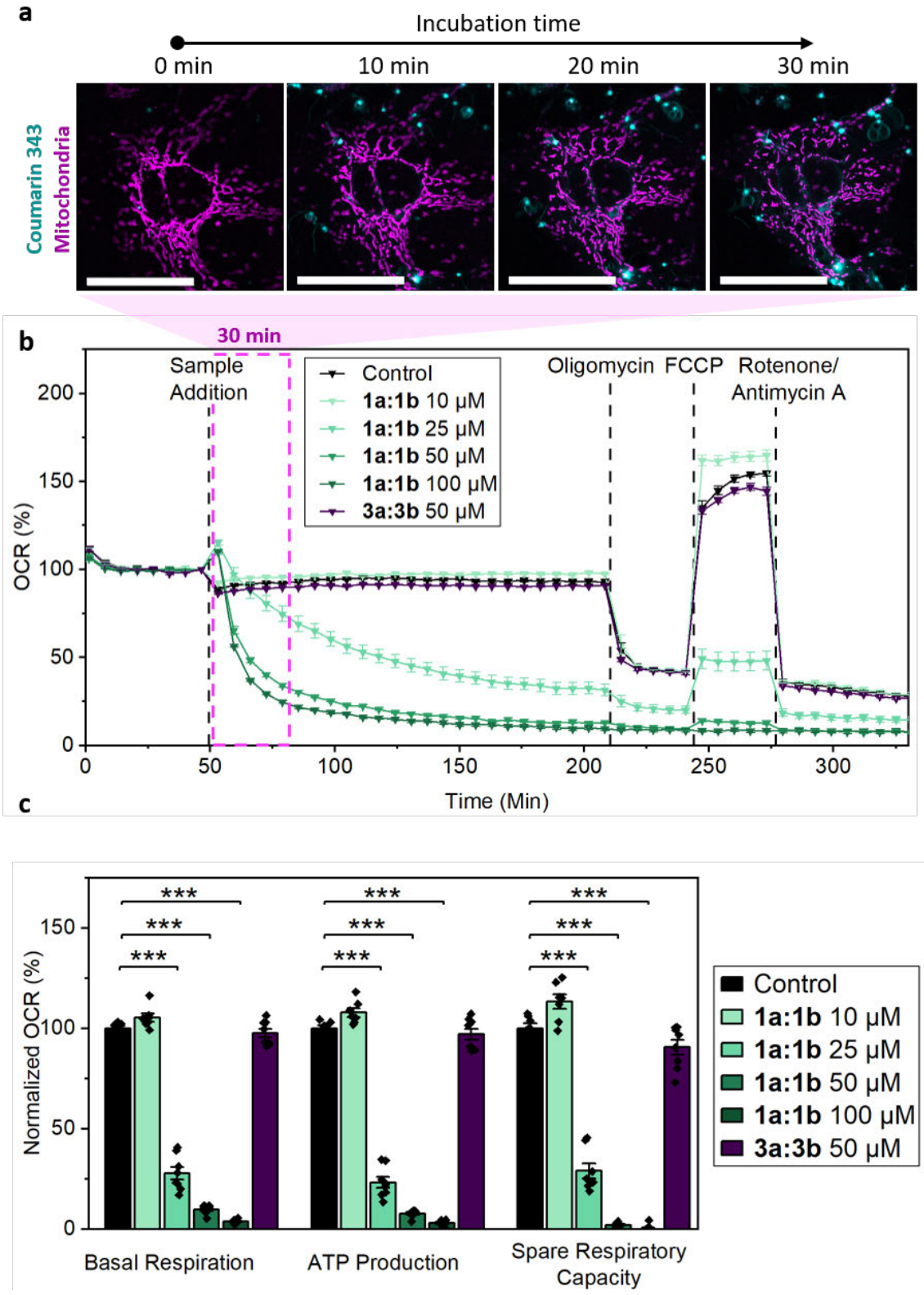

Figure 4.5 Effect of glutathione-responsive *iso*peptides on mitochondrial integrity and respiration. a) CLSM images of live-cell imaging of MDA-MB-231 cells treated with 50 μM of **1a:1b** (cyan). Cells were previously transfected with CellLight™ Mitochondria-RFP (pink). Scale bars 50 μm. **b)** Effect of isopeptide mixture **1a:1b** and of control compounds on the oxygen consumption rate (OCR) of MDA-MB-231 cells during the Mito Stress Test Assay. At different time points specific modulators of

the electron transport chain (ETC) were added to investigate the influence of the samples on cellular respiration in more detail: (1) oligomycin inhibits ATP synthase, (2) FCCP (carbonyl cyanide 4-(trifluoromethoxy)phenylhydrazone) disrupts the mitochondrial membrane potential, (3) rotenone inhibits complex I and antimycin A inhibits complex III of the ETC.[27] The last measurement before treatment injection of the compound is set as 100%. **c)** Effect of isopeptide mixture **1a:1b** and of control compounds on basal respiration, ATP production and spare respiratory capacity. Values are normalized towards the untreated control group. Data are presented as mean ± s.e.m., n ≥ 5. Statistical significance was calculated by ANOVA with a Tukey post hoc test. *p < 0.05, **p < 0.01, ***p < 0.001.

In addition to examining mitochondrial fragmentation via genetically encoded fluorescence labeling of the organelle, MitoTracker DeepRed was used as a co-staining reagent (Figure 4.6). Unexpectedly, we observed that the dye underwent a change in fluorescence lifetime (FL) within cells exposed to the pro-assembling isopeptides **1a:1b** during live-cell imaging. Initially, the FL signal of the stain was uniform with signal component decay at 0.65 ns and could be observed homogeneously in all examined cells. However, the addition of the *iso*peptides **1a:1b** at 50 µM caused a shift in the FL of MitoTracker DeepRed to 1.20 ns, particularly in those cells exhibiting high Coumarin 343 fluorescence of the peptide nanostructures (Figure 4.6). The observed shift in the photochemical properties of the dye is likely caused by changes in its chemical environment, which appear to correlate with the degradation of the mitochondrial network as a result of the intracellular formation of peptide nanostructures.

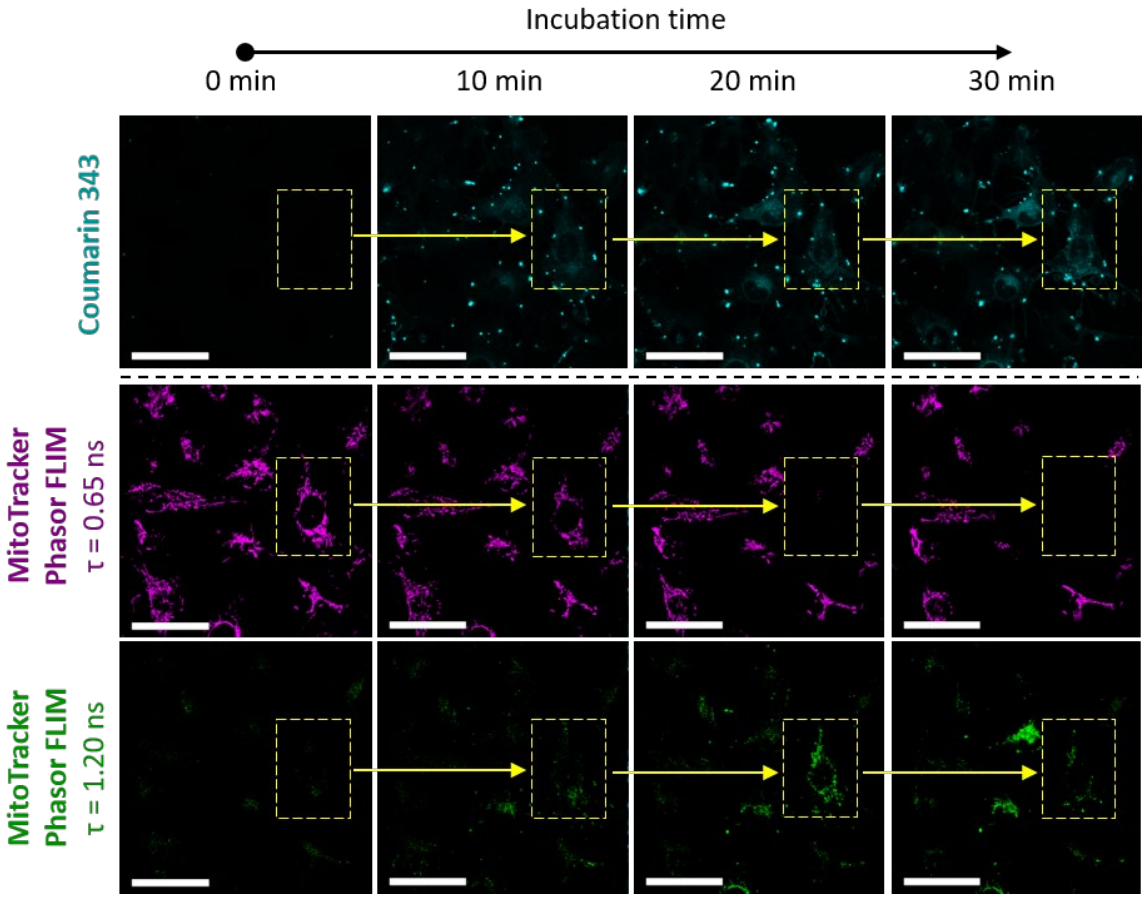

Figure 4.6 Changes in fluorescence lifetime of mitochondrial stain following intracellular structure formation. CLSM images show live-cell imaging of MDA-MB-231 cells treated with 50 µM of **1a:1b** (peptide fluorescence shown in cyan). Cells were previously stained with MitoTracker DeepRed. Fluorescence lifetime measurements of the stain were conducted concurrently with fluorescence imaging, revealing two distinct fluorescence lifetime signals for MitoTracker DeepRed over time. The corresponding phasor plots are provided in the SI (Figure S4.22). Scale bars 50 µm.

4.2.5. Intracellular peptide nanostructures have a toxic effect on tumor spheroids and cause size reduction

After observing the impact of intracellular assemblies on cellular organelles such as the cytoskeleton and mitochondria in 2D cell culture, we next investigated their effects on 3D cell networks. To assess the impact of intracellular peptide assembly on cell networks, we treated tumor spheroids derived from MDA-MB-231 breast cancer cells with glutathione-sensitive assembly precursors **1a:1b** and monitored their uptake after 4 h with fluorescence microscopy. After the incubation with the peptide precursors, spheroids were stained with propidium iodide (PI), which is unable to pass the membrane of healthy cells, to further investigate the impact on cell viability (Figure 4.7a,b).

Consistent with the 2D cell experiments, incubation with the **1a:1b** precursors at 100 µM resulted in a strong Coumarin 343 fluorescence signal within the spheroids (Figure 4.7b, second row). Cellular uptake was observed uniformly on the surface of the spheroids. (Figure 4.7b-c) In contrast, spheroids treated with the linear peptides **3a:3b** did not show any internalization, showing the necessity for the TAT-facilitated cellular uptake and intracellular activation cascade to obtain intracellular structures that directly affect cell integrity. Spheroids treated with the non-assembling peptide **1c** showed a weak fluorescence signal, indicating uptake without subsequent assembly (Figure S4.30).

In comparison to the control spheroids, those incubated with **1a:1b** at 50 or 100 µM exhibited a significant decrease in size after 4 h of incubation (Figure 4.7d, Figure S4.29-S4.31). While spheroids incubated with **1a:1b** at 100 and 50 µM decreased in size by 7.9 ± 0.5 % and 3.8 ± 0.5 %, respectively, spheroids incubated with the linear peptides **3a:3b** or non-assembling NBD-labeled peptides **1c** did not show any size changes during the incubation period (Figure 4.7d). This suggests

that the uptake of the assembly precursors into cells localized at the surface of the spheroids could lead to cell death, resulting in a decrease in size, whereas no effects on the spheroid stability were observed for the treatment with the linear or non-assembling control peptides **3a:3b** and **1c**.

Furthermore, the dead staining with propidium iodide (PI) revealed a stronger fluorescence signal for spheroids incubated with the glutathione-responsive *iso*peptides **1a:1b** at 100 µM compared to the spheroids incubated with **1a:1b** at 50 µM or the spheroids incubated with **3a:3b** at 100 µM (Figure 4.7b). Upon cellular internalization and glutathione-induced transformation, the intracellular peptide assemblies cause cell death, as already described for two-dimensional cell studies. The residual fluorescence signal for propidium iodide for untreated and control spheroids is due to the natural necrotic core of the spheroids.[17] The co-localization of Coumarin 343 fluorescence and the PI stain for spheroids incubated with the *iso*peptides **1a:1b** at 100 µM confirms that uptake and intracellular transformation of the *iso*peptides causes cell death, thereby disrupting the overall spheroid integrity (Figure 4.7b,d).

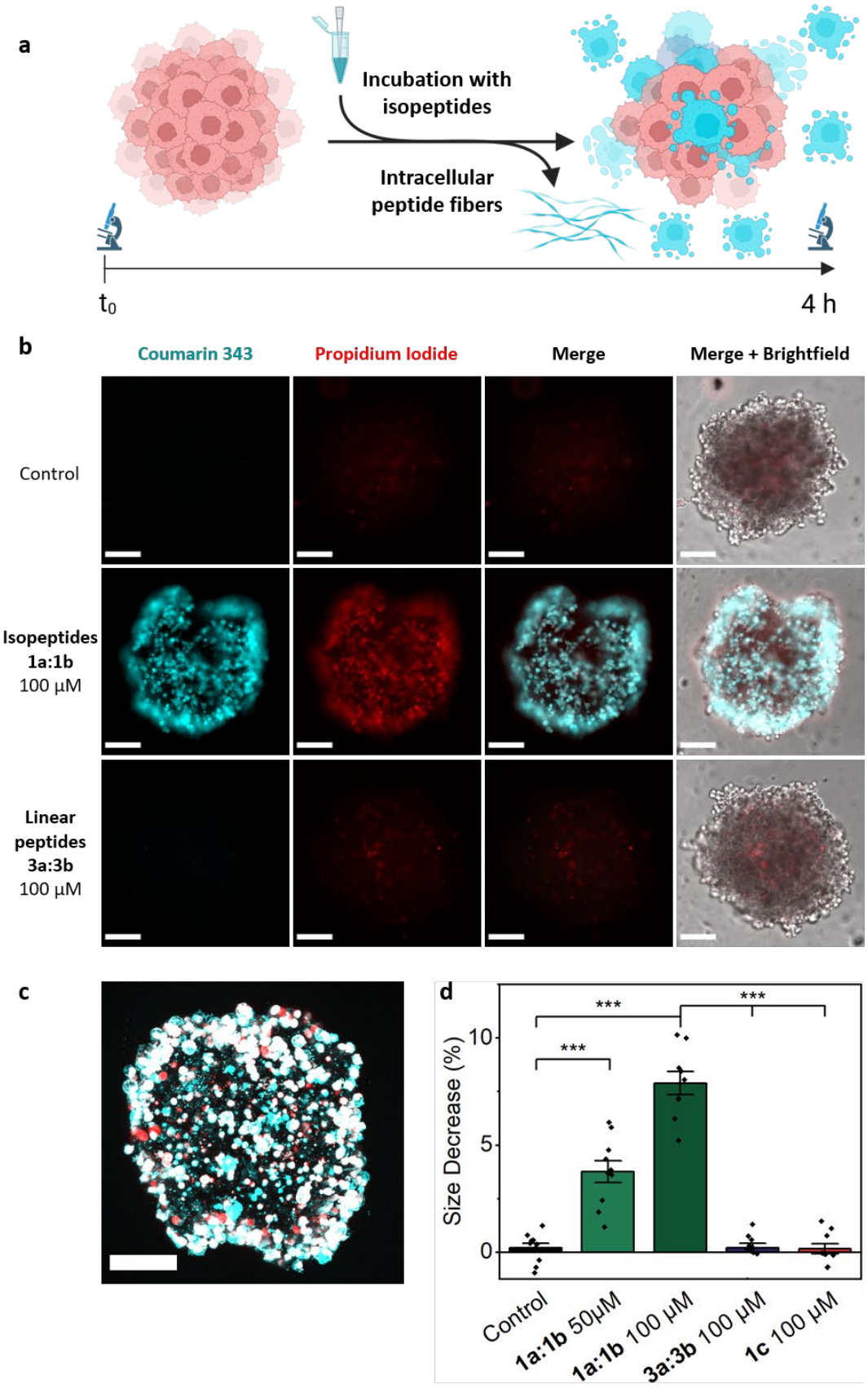

Figure 4.7 Intracellular peptide assembly disrupts tumor spheroids. a) Schematic representation of tumor spheroid treatment with glutathione-responsive isopeptides and subsequent toxic intracellular assembly formation. **b)** Fluorescence microscopy images of uptake and dead staining of tumor spheroids.

Coumarin 343 fluorescence is shown in cyan and propidium iodide-stained dead cells are red. Scale bars 100 µm **c)** Maximum projection of a z-stack of a spheroid incubated with **1a:1b** at 100 µM for 4 h. Scale bar 100 µm **d)** Spheroid size was measured before and after incubation with glutathione-responsive isopeptides using brightfield images in ImageJ. Diameter of each spheroid was measured at 4 different places (Figure S4.31). Data are presented as mean ± s.e.m., n=10. Statistical significance was calculated by ANOVA with a Tukey post hoc test. *$p < 0.05$, **$p < 0.01$, ***$p < 0.001$.

4.3. Conclusion

In conclusion, using glutathione-responsive *iso*peptides as assembly precursors has enabled us to assemble intracellular nanofibers that disrupt the energy homeostasis of MDA-MB-231 breast cancer cells and cause rapid cell death. The efficient cellular uptake and the fast glutathione-induced transformation of the kinked *iso*peptides into the linear self-assembling monomers allows the controlled formation of synthetic architectures within the complex cellular environment, both in 2D-cultured cells and 3D tumor spheroids. These nanostructures effectively disrupt essential subcellular structures and processes, such as mitochondrial function and the actin cytoskeleton, which results in cell death and a significant reduction in spheroid size. By combining qualitative time-dependent microscopy with quantitative metabolic analysis of oxygen consumption rates and mitochondrial stress, we established a clear link between structural alterations in the mitochondrial network and the functional decline in mitochondrial respiration. Furthermore, using tumor spheroids as a model for three-dimensional cellular networks provides a more complex and relevant context for studying the biological effects of intracellular synthetic nanostructures. By continuing to explore these interactions, we can gain important insights into the fundamental principles that govern cellular responses to synthetic assemblies.

References

1 Alberts, B. *et al. Molecular Biology of the Cell*. 6. edn, (W. W. Norton & Company, 2014).

2 Chagri, S., Ng, D. Y. W. & Weil, T. Designing bioresponsive nanomaterials for intracellular self-assembly. *Nat. Rev. Chem.* **6**, 320-338 (2022).

3 Persidis, A. Cancer multidrug resistance. *Nat. Biotechnol.* **17**, 94–95 (1999).

4 Zhou, Z. *et al.* In Situ Assembly of Platinum(II)-Metallopeptide Nanostructures Disrupts Energy Homeostasis and Cellular Metabolism. *J. Am. Chem. Soc.* **144**, 12219–12228 (2022).

5 Cheng, Z. *et al.* Self-assembly of pentapeptides into morphology-adaptable nanomedicines for enhanced combinatorial chemo-photodynamic therapy. *Nano Today* **33**, 100878 (2020).

6 Liang, G., Ren, H. & Rao, J. A biocompatible condensation reaction for controlled assembly of nanostructures in living cells. *Nat. Chem.* **2**, 54–60 (2009).

7 Quinn, J. F., Whittaker, M. R. & Davis, T. P. Glutathione responsive polymers and their application in drug delivery systems. *Polym. Chem.* **8**, 97–126 (2016).

8 Gamcsik, M. P., Kasibhatla, M. S., Teeter, S. D. & Colvin, O. M. Glutathione levels in human tumors. *Biomarkers* **17**, 671–691 (2012).

9 Carretero, J. *et al.* Growth-associated changes in glutathione content correlate with liver metastatic activity of B16 melanoma cells. *Clin. Exp. Metastasis* **17**, 567–574 (1999).

10 Depeille, P., Cuq, P., Passagne, I., Evrard, A. & Vian, L. Combined effects of GSTP1 and MRP1 in melanoma drug resistance. *Br. J. Cancer* **93**, 216–223 (2005).

11 Bradshaw, D. M. & Arceci, R. J. Clinical relevance of transmembrane drug efflux as a mechanism of multidrug resistance. *J. Clin. Oncol.* **16**, 3674–3690 (1998).

12 Qiao, S.-L., Ma, Y., Wang, Y., Lin, Y.-X. & Wang, H. General Approach of Stimuli-Induced Aggregation for Monitoring Tumor Therapy. *ACS Nano* **11**, 7301–7311 (2017).

13 An, H.-W. *et al.* Bio-orthogonally Deciphered Binary Nanoemitters for Tumor Diagnostics. *ACS Appl. Mater. Interfaces* **8**, 19202-19207 (2016).

14 Pieszka, M. *et al.* Controlled Supramolecular Assembly inside Living Cells by Sequential Multi-staged Chemical Reactions. *J. Am. Chem. Soc.* **142**, 15780-15789 (2020).

15 Ren, Y. *et al.* Supramolecular Assembly in Live Cells Mapped by Real-Time Phasor-Fluorescence Lifetime Imaging. *J. Am. Chem. Soc.* **146**, 11991–11999 (2024).

16 Chagri, S. *et al.* Synthetic intracellular nanostructures enhance cytotoxic T cell function via assembly-driven chemical engineering. *ChemRxiv*, doi:10.26434/chemrxiv-2024-3lxgk (2024).

17 Costa, E. C. *et al.* 3D tumor spheroids: an overview on the tools and techniques used for their analysis. *Biotechnol. Adv.* **34**, 1427–1441 (2016).

18 Smith, D. K. Lost in translation? Chirality effects in the self-assembly of nanostructured gel-phase materials. *Chem. Soc. Rev.* **38**, 684–694 (2009).
19 Tao, K., Levin, A., Adler-Abramovich, L. & Gazit, E. Fmoc-modified amino acids and short peptides: simple bio-inspired building blocks for the fabrication of functional materials. *Chem. Soc. Rev.* **45**, 3935–3953 (2016).
20 Roth, P. *et al.* Supramolecular assembly guided by photolytic redox cycling. *Nat. Synth.* **2**, 980–988 (2023).

Supplementary Information

1. General Information

1.1. Materials

Reagents and solvents were purchased from commercial sources and were used without further purification. Peptide synthesis grade reagents were used for synthesizing the peptides. HPLC was performed using acetonitrile (CH_3CN) in HPLC grade (containing 0.1% trifluoroacetic acid (TFA)) and water for HPLC (containing 0.1% TFA) and reactions was obtained from a Millipore purification system. Flash column chromatography was carried out using Macherey-Nagel silica gel 0.04–0.063 mm.

1.2. Instruments

1.2.1. Microwave Peptide Synthesizer

Linear peptides were synthesized in a Liberty Blue Automated Microwave Peptide Synthesizer by CEM Corporation.

1.2.2. Liquid Chromatography-Mass Spectrometry (LC-MS)

Compounds were analyzed by HPLC-ESI-MS on a LC-MS 2020 by Shimadzu using a Kinetex 2.6 µm EVO C18 100 Å LC 50 × 2.1 mm column. MilliQ water acidified with 0.1% formic acid and CH_3CN were used as solvents for all measurements. The solvent gradient started with 5% CH_3CN and 95% water. This solvent ratio was kept constant for 2 min, then the CH_3CN content was linearly increased to 95% in 14 min. Data were processed in LabSolutions and OriginPro 9.

1.2.3. Atmospheric-Pressure Chemical Ionization Mass Spectrometry (APCI-MS)

All APCI-MS spectra were recorded on a Advion Expression-L Compact mass spectrometer. Data processing was performed in Advion Data Express.

1.2.4. Nuclear Magnetic Resonance Spectroscopy (NMR)

NMR spectra of small molecules and peptides were recorded on a Bruker Avance II 300 MHz spectrometer and a Bruker Avance 400 MHz spectrometer. The solvent signal was

used as a reference (deuterated chloroform $CDCl_3$ δ =7.26 ppm for ^1H, 77.16 ppm for ^{13}C and for DMSO-d_6 2.50 ppm and 39.52 ppm respectively). The data was processed in MestReNova.

1.2.5. Transmission Electron Microscopy (TEM)

TEM images of the peptide samples were recorded on a JEOL 1400 transmission electron microscope at a voltage of 120 kV. Formvar/carbon-film coated copper grids (300 mesh) by Plano GmbH were used to prepare the samples. The images were processed in Fiji ImageJ or Icy.

1.2.6. 2D Cell Culture

MDA-MB-231 cells were cultured at 37 °C and 5% CO_2 in Dulbecco's Modified Eagle's Medium (DMEM, high glucose), supplemented with 10% fetal bovine serum (FBS). The cells were cultured in T75 culture flask and subcultivated two to three times per week.

1.2.7. Tumor Spheroid Culture

MDA-MB-231 cells were seeded in Ultra-Low-Attachment (ULA) 96-well plates (Corning, Ref. 4520) at a cell density of 10,000 cells/well. The plate was centrifuged (1,200 rpm, RT, 5 min) to allow formation of pre-clusters facilitating sphere development over time. Spheroids were cultured for 7 days in complete medium (DMEM high glucose with glutamine supplemented with 10 % FBS) at controlled humidified atmosphere (37 °C, 5% CO_2).

1.2.8. Fluorescence Microscopy

Fluorescence images of the tumor spheroids were taken using a Keyence BZ-X810 fluorescence microscope using a 20x LD PH lens. Propidium iodide staining for dead imaging of tumor spheroids was analyzed using Cy5 filter with the following wavelength settings: Ex. 470/40 nm, Em. 525/50 nm. For Coumarin 343 imaging of the peptide co-assemblies a GFP filter was used: Ex.: 470/40 nm, Em.: 525/50 nm.

1.2.9. Confocal Laser Scanning Microscopy (CLSM)

Cells were imaged live using an incubator-equipped Leica Stellaris® 8 microscope (40x/1.25 glycerol immersion objective) with fast lifetime contrast (FALCON) module (Leica

Microsystems GmbH). The incubator (okolab) is set and held constant at 37 °C, 5% CO_2 and a relative humidity of 90% throughout all measurements. For the detection of Coumarin 343 fluorescence, samples were excited using a 40 MHz pulsed white light laser tuned to 440 nm. Emitted photons were detected using HyD® S2 (GaAsP hybrid photocathode) detector with a filter window at *475 nm – 550 nm*. The IRF standard used is fluorescein sodium salt.

Fluorescence lifetime imaging (FLIM) was performed on living cells at *2.5*-minute intervals, with a scanning resolution of 1024 x 1024 pixels at 200 Hz, accumulating *15* frames per acquisition. Adaptive focusing was applied to each frame and well position. A total of 100 frames were captured. Photon counting was conducted using a FALCON-modified time-correlated single photon counting (TCSPC) method.

Each pixel was converted into a phasor plot using the following equation:

$$g_{i,j}(\omega) = \int_0^T I(t) \cdot \cos(n\omega t)\mathrm{d}t \Big/ \int_0^T I(t)\mathrm{d}t$$

$$s_{i,j}(\omega) = \int_0^T I(t) \cdot \sin(n\omega t)\mathrm{d}t \Big/ \int_0^T I(t)\mathrm{d}t$$

In this equation, $g_{i,j}(\omega)$ and $s_{i,j}(\omega)$ represent the x and y coordinates of the phasor plot, n and ω are the harmonic and angular frequencies of excitation, respectively, and T is the acquisition's repeat frequency. The frequency domain data acquired from each pixel can be transformed into phasor points using the following transformations:

$$g_{i,j}(\omega) = m_{i,j} \cdot \cos\left(\phi_{i,j}\right)$$

$$s_{i,j}(\omega) = m_{i,j} \cdot \sin\left(\phi_{i,j}\right)$$

In these transformations, $m_{i,j}(\omega)$ and $\varphi_{i,j}(\omega)$ represent the modulation and phase shift of the frequency domain measurement at pixel *i,j*. The decay at each pixel is thus mapped to a point in the phasor plot. Phasor components were identified and separated using LAS X software, and photons outside the defined phasor region were excluded from the images.

2. Synthesis

2.1. Synthesis of glutathione-responsive isopeptides

The synthesis of the glutathione-responsive isopeptides described in the following subsections have been reported previously by our group.[1]

2.1.1. Synthesis of isopeptides with activated disulfide bond

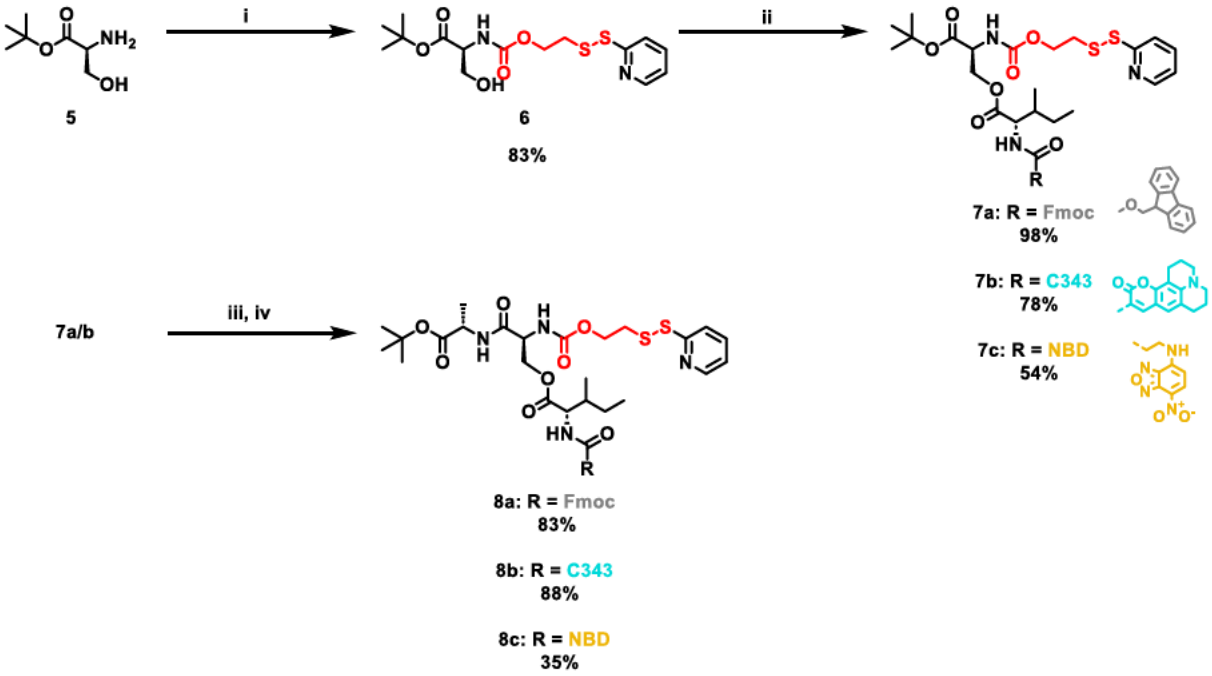

Scheme S4.1 Synthesis of isopeptides with activated disulfide-bonds. i) 4-nitrophenyl 2-(pyridin-2-yldisulfanyl)ethyl carbonate, DIPEA, DCM, overnight, RT; ii) Fmoc/C343/NBD-Ile, DIC, DMAP, DCM, overnight, RT; iii) TFA, DCM, 4 h, RT; iv) Ala-tBuO, PyBOP, DIPEA, DCM, 3 h, RT.

2.1.1.1. Synthesis of compound 6

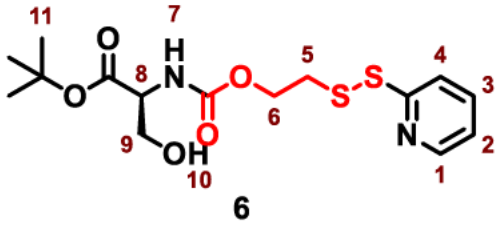

6

In a round-bottom flask, *tert*-butyl protected serine hydrochloride (200 mg, 1.01 mmol, 1 eq.) was dissolved in dry DCM (10 ml), and dry DIPEA (654 mg, 881 µL, 5.06 mmol, 5 eq.) was added to the solution. Separately, 4-nitrophenyl 2-(pyridin-2-yldisulfanyl)ethyl carbonate was dissolved in dry DCM (5 ml) and slowly added to the reaction mixture. The

solution was stirred at room temperature overnight, then washed twice with water and brine. The aqueous layer was extracted with ethyl acetate (EA), and the combined organic layers were dried over sodium sulfate. After solvent removal under reduced pressure, flash column chromatography (cHex:EA, 1:1) afforded compound **6** as a colorless amorphous solid (316 mg, 0.84 mmol, 83% yield).

^{1}H NMR (400 MHz, $CDCl_3$) δ 8.43 (d, J = 4.9 Hz, 1H, H-1), 7.74 – 7.64 (m, 3H, H-3, H-4), 7.10 (ddd, J = 6.8, 4.9, 1.4 Hz, 1H, H-2), 5.73 (d, J = 7.6 Hz, 1H, H-7), 4.40 – 4.21 (m, 3H, H-6, H-6', H-8), 3.90 (dd, J = 3.6, 2.3 Hz, 1H, H-9), 3.32 (s, 1H, H-10), 3.10 – 2.94 (m, 2H, H-5), 1.46 (s, 9H, H-11).

^{13}C NMR (101 MHz, $CDCl_3$) δ 169.51, 163.21, 159.90, 155.89, 149.41, 137.59, 126.22, 121.08, 120.21, 115.82, 82.80, 63.41, 63.38, 56.74, 37.70, 28.09.

ESI-MS: m/z 375.1 (calculated for $[M+H]^+$: 375.10)

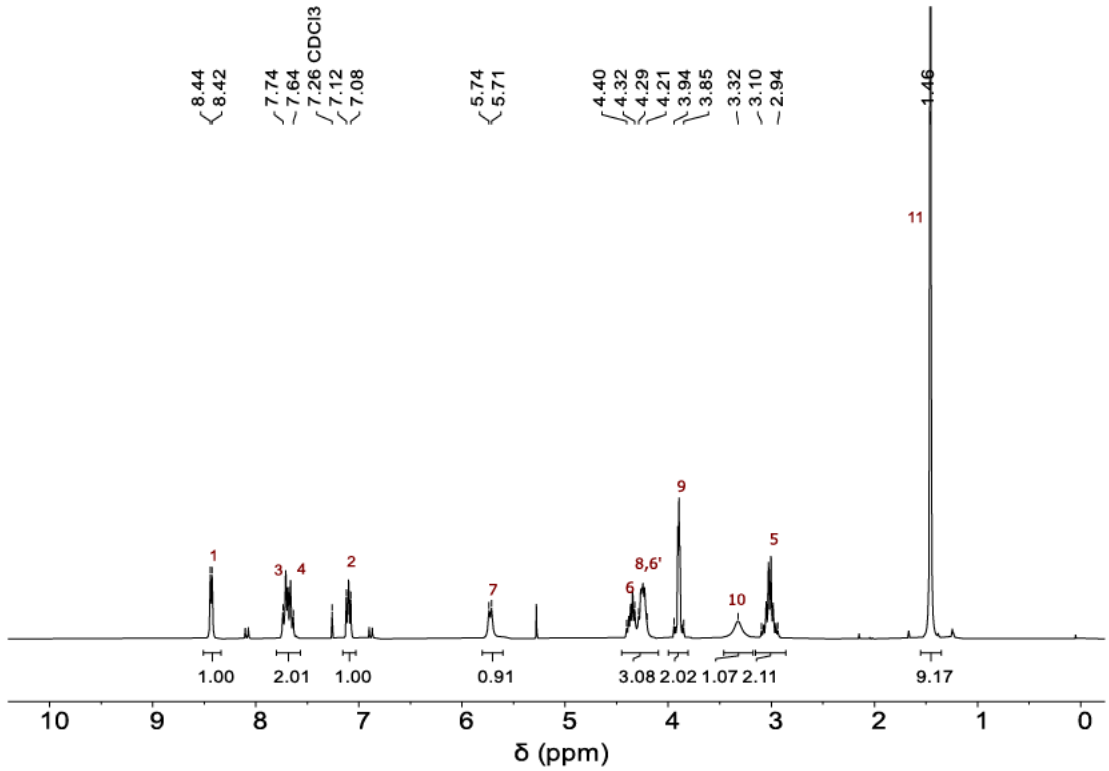

Figure S4.1 ^{1}H NMR spectrum (300 MHz, $CDCl_3$, 298 K) of compound 6.

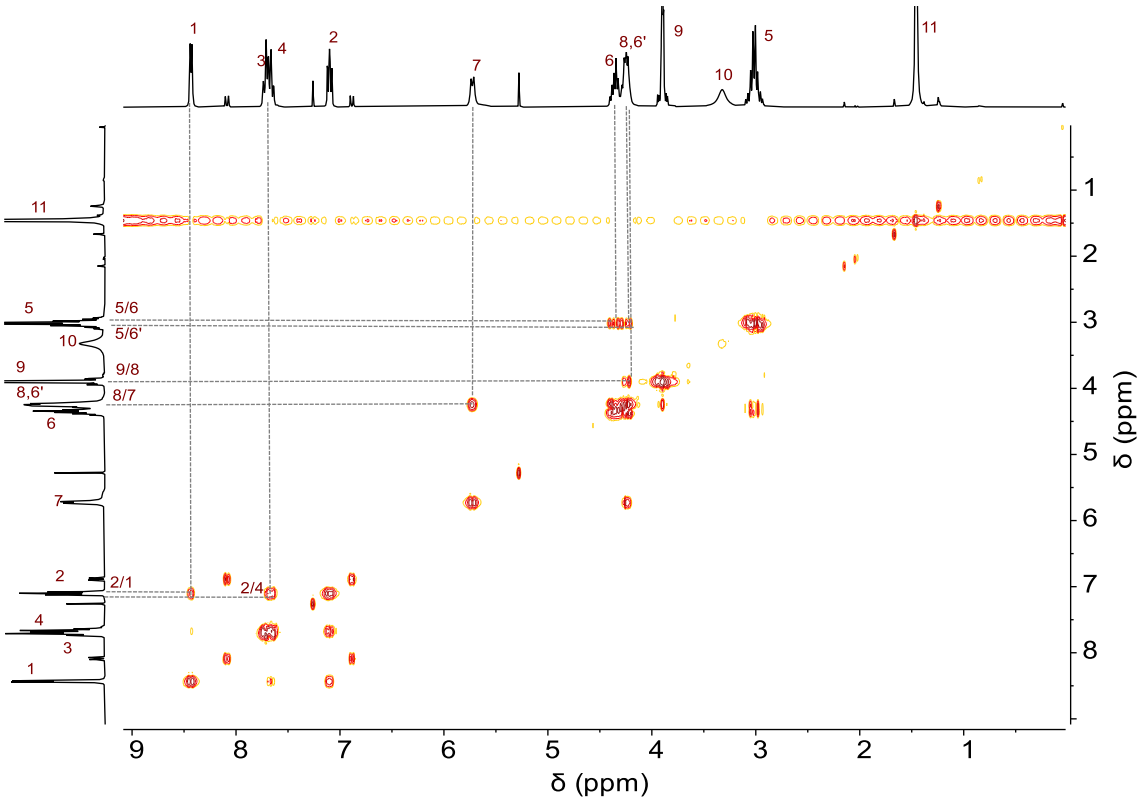

Figure S4.2 $^{1}H,^{1}H$ COSY NMR spectrum (300 MHz, $CDCl_3$, 298 K) of compound 6.

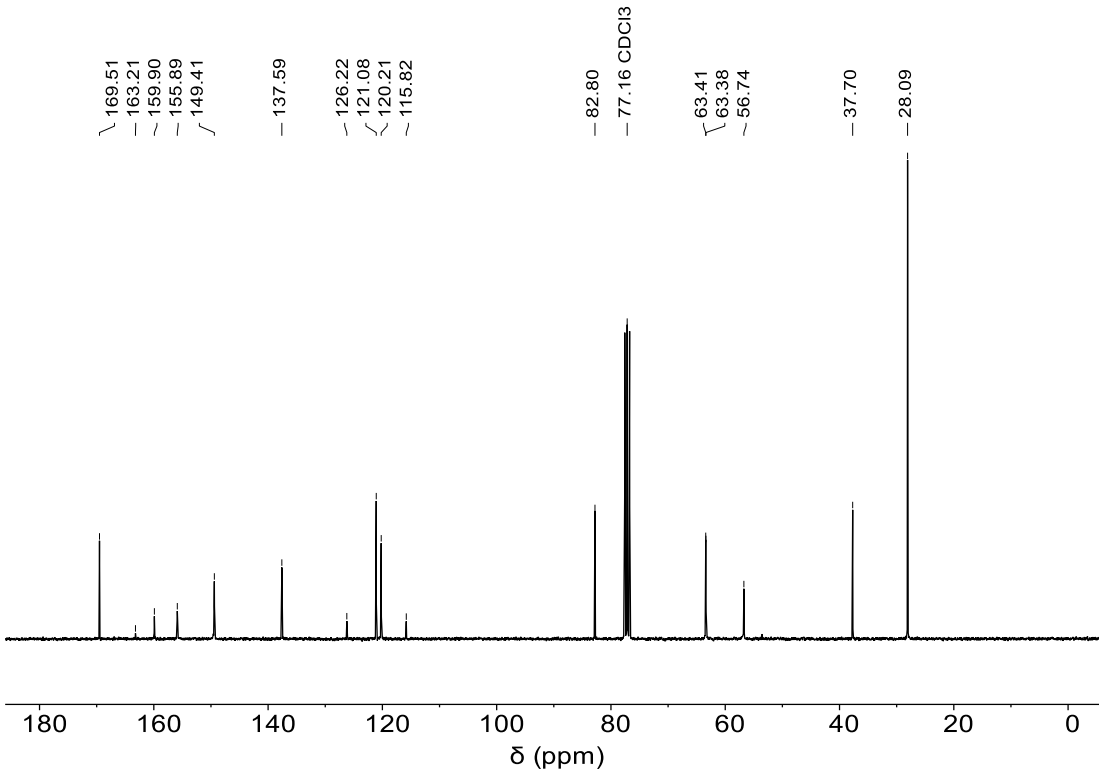

Figure S4.3 ^{13}C NMR spectrum (101 MHz, $CDCl_3$, 298 K) of compound 6.

2.1.1.2. Synthesis of compounds 7a

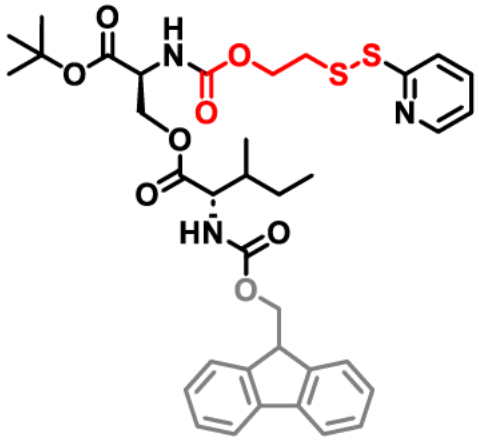

7a

In a round-bottom flask, compound **6** (157 mg, 419 µmol, 1 eq.) was dissolved in dry DCM (5 ml) under a nitrogen atmosphere. Fmoc-Ile (274 mg, 774 µmol, 1.8 eq.), DMAP (23.6 mg, 193 µmol, 0.5 eq.), and DIC (98 mg, 774 µmol, 1.8 eq.) were dissolved in dry DCM (10 ml) and added dropwise to the solution of compound **6**. The reaction mixture was stirred at room temperature overnight. After solvent removal under reduced pressure, flash column chromatography (cHex:EA, 3:1) afforded compound **7a** as a colorless oil (291 mg, 410 µmol, 98% yield).

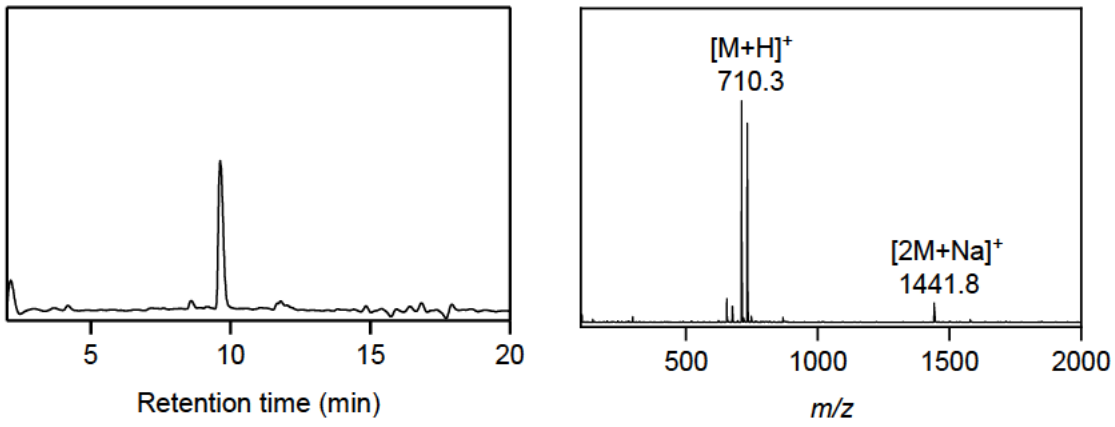

Figure S4.4 LC-MS data of compound 7a. Left: LC trace (214 nm) with t_R (7a) = 9.63 min. Right: Convoluted ESI-MS spectrum showing peaks of $[M+H]^+$ (calculated: 710.26) and $[2M+Na]^+$ (calculated: 1441.49).

2.1.1.3. Synthesis of compounds 7b

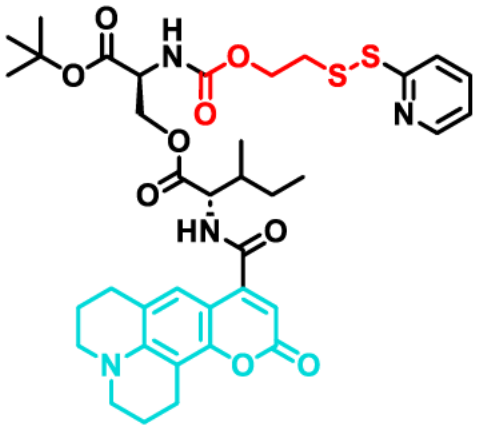

7b

In a round-bottom flask, compound **6** (80 mg, 214 µmol, 1 eq.) was dissolved in dry DCM (4 ml) under a nitrogen atmosphere. Coumarin 343-Ile (126 mg, 316 µmol, 1.5 eq.), DMAP (26.1 mg, 214 µmol, 1 eq.), and DIC (40 mg, 320 µmol, 1.5 eq.) were dissolved in dry DCM (5 ml) and added dropwise to the solution of compound 6. The reaction mixture was stirred at room temperature overnight. After solvent removal under reduced pressure, flash column chromatography (cHex:EA, 3:2) afforded compound **7b** as a bright green oil (126 mg, 167 µmol, 78% yield).

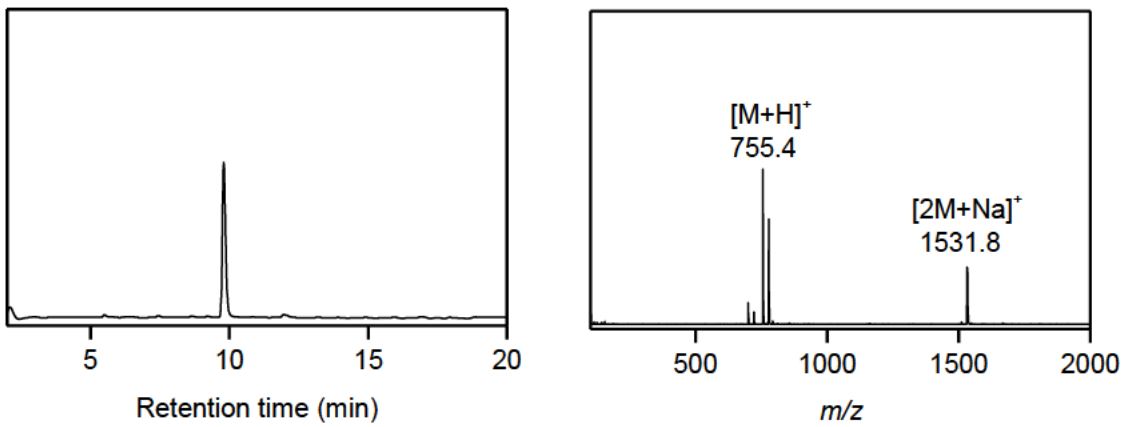

Figure S4.5 LC-MS data of compound 7b. Left: LC trace (214 nm) with t_R (7b) = 9.80 min. Right: Convoluted ESI-MS spectrum showing peaks of $[M+H]^+$ (calculated: 755.28) and $[2M+Na]^+$ (calculated: 1531.53).

2.1.1.4. Synthesis of compounds 7c

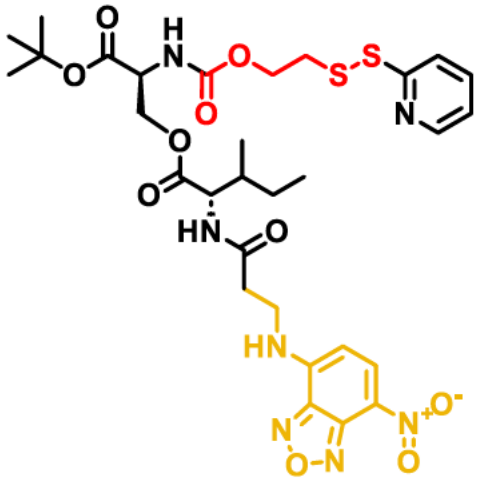

7c

In a round-bottom flask, compound **6** (162 mg, 433 µmol, 1.2 eq.) was dissolved in dry DCM (4 ml) under a nitrogen atmosphere. Nitrobenzoxadiazole (NBD)-β-Ala-Ile (132 mg, 361 µmol, 1 eq.), DMAP (88 mg, 722 µmol, 2 eq.), and DIC (91 mg, 722 µmol, 2 eq.) were dissolved in dry DCM (5 ml) and added dropwise to the solution of compound **6**. The reaction mixture was stirred at room temperature overnight. After solvent removal under reduced pressure, flash column chromatography (EA:cHex, 2:1) afforded compound **7c** as a bright yellow oil (141 mg, 195 µmol, 54% yield).

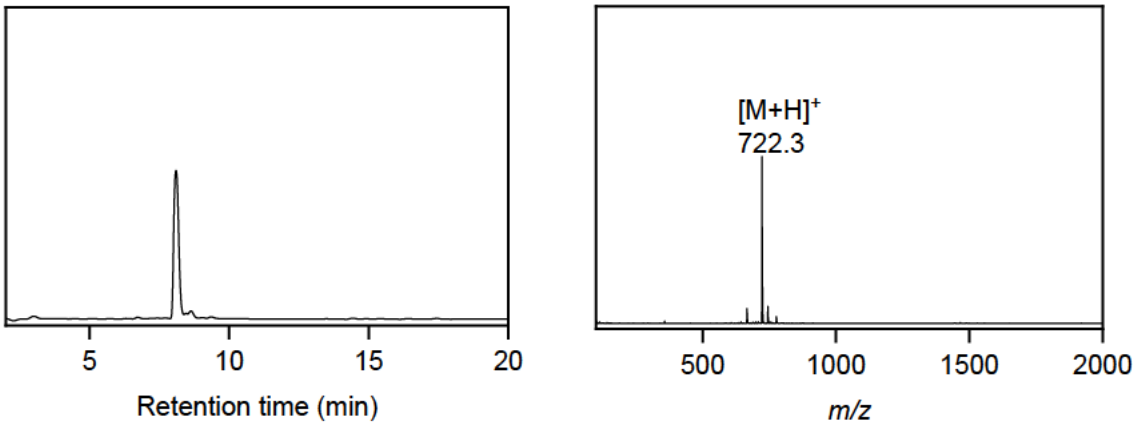

Figure S4.6 LC-MS data of compound 7c. Left: LC trace (214 nm) with t_R (7c) = 8.63 min. Right: Convoluted ESI-MS spectrum showing the peak of $[M+H]^+$ (calculated: 722.23).

2.1.1.5. Synthesis of compound 8a

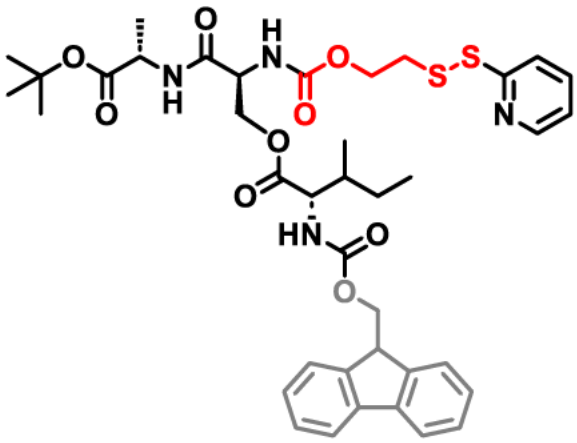

8a

In a round-bottom flask, compound **7a** (280 mg, 394 µmol, 1 eq.) was dissolved in a 1:1 mixture of TFA and DCM (4 ml:4 ml) and stirred for 6 hours. The solvents were removed under reduced pressure. The resulting colorless oil was dissolved in dry DCM (15 ml), and DIPEA (329 mg, 443 µL, 2.54 mmol, 6 eq.) was added under a nitrogen atmosphere. PyBOP (441 mg, 847 µmol, 2.2 eq.) and *tert*-butyl-protected alanine hydrochloride (154 mg, 847 µmol, 2.2 eq.) were then added, and the reaction mixture was stirred for 3 hours. The solution was washed with water, and the organic phase was extracted with ethyl acetate (EA). The combined organic layers were dried over sodium sulfate, and the solvents were evaporated. Flash column chromatography (EA:cHex, 4:3) yielded compound **8a** as a colorless oil (255 mg, 327 µmol, 83% yield).

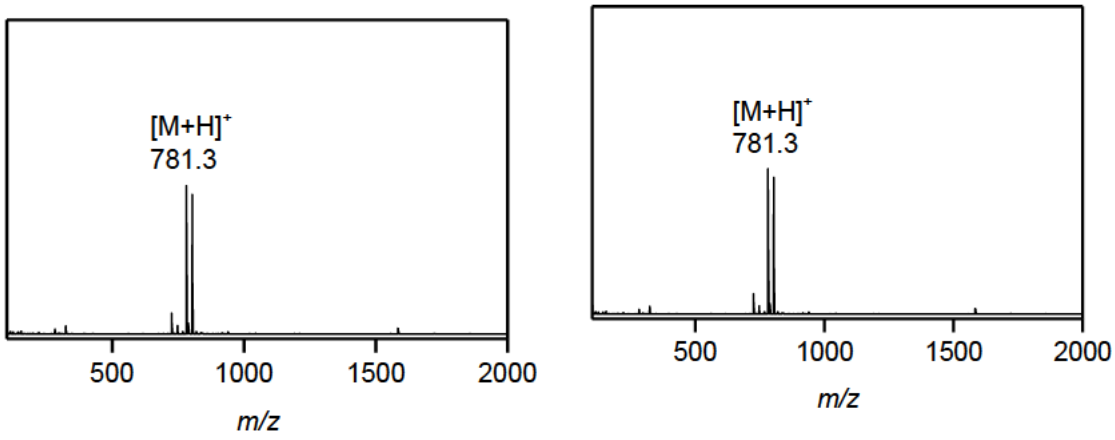

Figure S4.7 LC-MS data of compound 8a. Left: LC trace (214 nm) with t_R (8a) = 9.53 min. Right: Convoluted ESI-MS spectrum showing peaks of $[M+H]^+$ (calculated: 781.29).

2.1.1.6. Synthesis of compound 8b

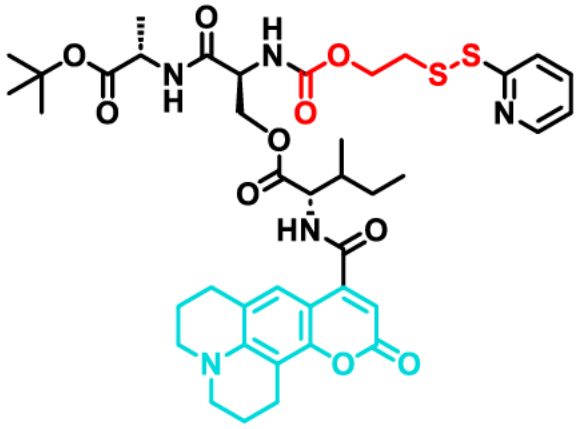

8b

In a round-bottom flask, compound **8b** (126 mg, 167 µmol, 1 eq.) was dissolved in a 1:1 mixture of TFA and DCM (2 ml:2 ml) and stirred for 4 hours. The solvents were removed under reduced pressure. The resulting bright green oil was dissolved in dry DCM (10 ml), and DIPEA (297 mg, 400 µL, 2.30 mmol, 13.7 eq.) was added under a nitrogen atmosphere. PyBOP (718 mg, 1.38 mmol, 8.2 eq.) and tert-butyl-protected alanine hydrochloride (267 mg, 1.47 mmol, 8.8 eq.) were then added, and the reaction mixture was stirred for 3 hours. The solution was washed with water and brine, and the organic phase was extracted with ethyl acetate (EA). The combined organic layers were dried over sodium sulfate, and the solvents were evaporated. Flash column chromatography (EA:cHex, 4:1) afforded compound **8b** as a bright green oil (122 mg, 148 µmol, 88% yield).

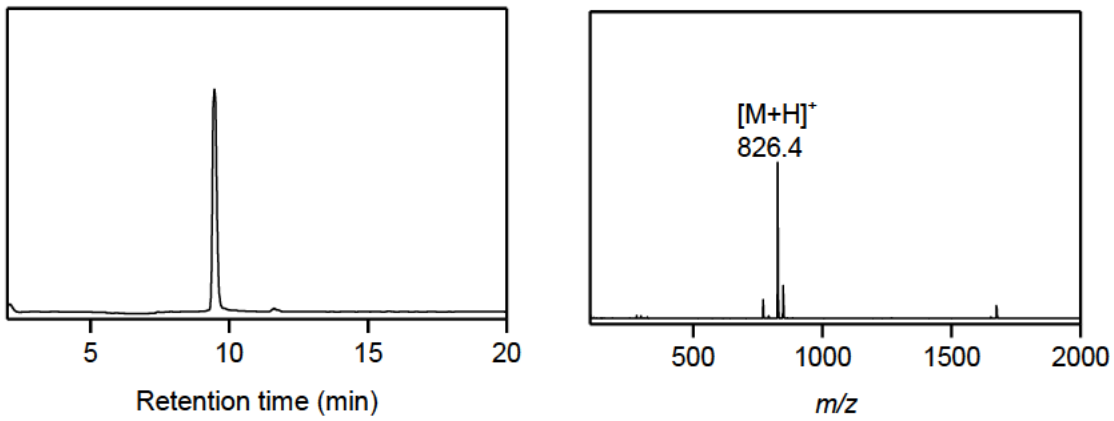

Figure S4.8 LC-MS data of compound 8b. Left: LC trace (214 nm) with t_R (8b) = 9.47 min. Right: Convoluted ESI-MS spectrum showing peaks of $[M+H]^+$ (calculated: 826.32).

2.1.1.7. Synthesis of compound 8c

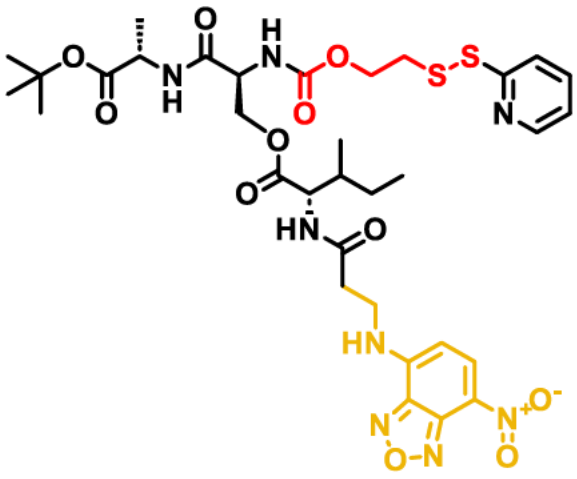

8c

In a round-bottom flask, compound **7c** (141 mg, 195 µmol, 1 eq.) was dissolved in a 1:1 mixture of TFA and DCM (2 ml:2 ml) and stirred for 4 hours. The solvents were removed under reduced pressure. The resulting bright yellow oil was dissolved in dry DCM (10 ml), and DIPEA (153 mg, 206 µL, 1.18 mmol, 6 eq.) was added under a nitrogen atmosphere. PyBOP (205 mg, 393 µmol, 2 eq.) and *tert*-butyl-protected alanine hydrochloride (71 mg, 393 µmol, 2 eq.) were then added, and the reaction mixture was stirred for 3 hours. After solvent evaporation, the product was purified via HPLC using a Phenomenex Gemini column. The gradient began with 10% CH_3CN in H2O (+0.1% TFA), held for 3 minutes, followed by a linear increase of CH_3CN to 100% over 12 minutes. This purification afforded compound **8c** as a bright yellow solid (55 mg, 69 µmol, 35% yield).

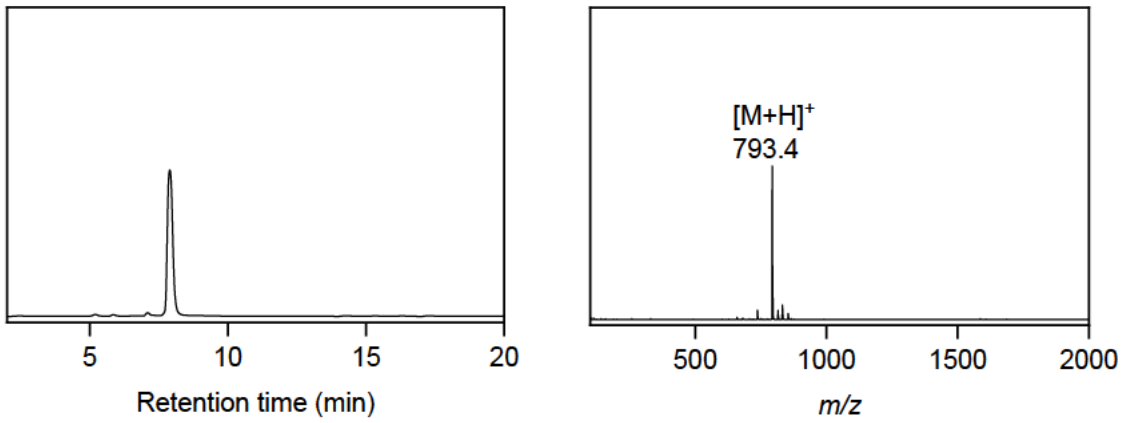

Figure S4.9 LC-MS data of compound 8c. Left: LC trace (214 nm) with t_R (8c) = 7.89 min. Right: Convoluted ESI-MS spectrum the showing peak of $[M+H]^+$ (calculated: 793.26).

2.1.2. Solid phase supported synthesis of TAT-modified glutathione-responsive isopeptides

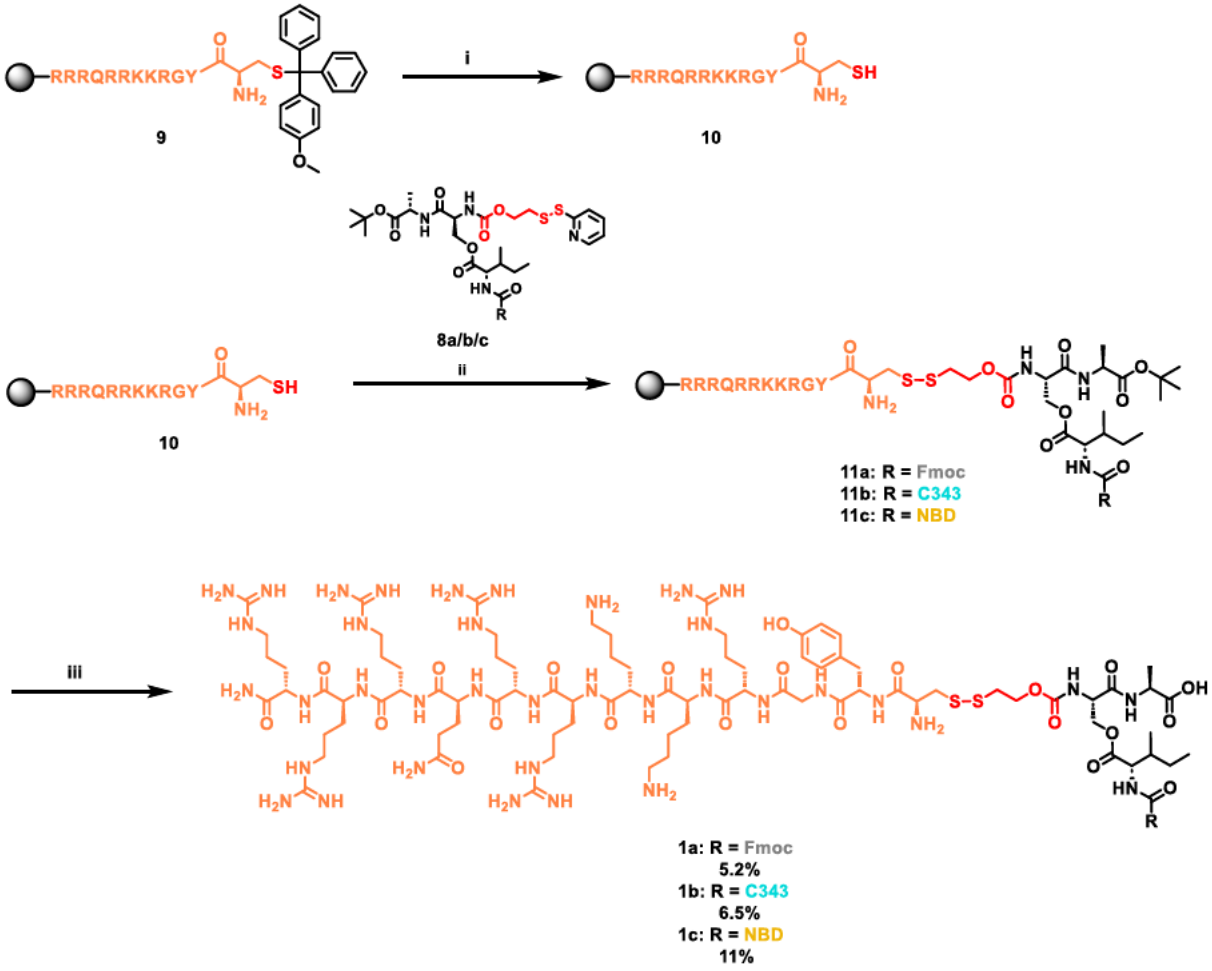

Scheme S4.2 Synthesis of TAT-modified glutathione-responsive isopeptides. i) TFA, TIPS, DCM (2% : 5% : 93%, 5x8 min, RT); ii) 8a/b/c, DMF, 2 h, RT; iii) TFA, TIPS, H_2O (95% : 2.5% : 2.5%), 2.5 h, RT.

The peptide TAT, with an additional N-terminal cysteine **9**, was synthesized via solid-phase peptide synthesis (SPPS) on a Rink amide resin at a 0.05 mmol scale. The resin was first swollen in DMF for 1 hour before starting the synthesis. Prior to each coupling step, as well as during the final deprotection, the N-terminal Fmoc group was removed using two deprotection steps: 20% piperidine in DMF (3 ml) was applied for 15 seconds at 75 °C, followed by 50 seconds at 90 °C. Fmoc-protected amino acids (Fmoc-Gln(Trt), Fmoc-Lys(Boc), Fmoc-Gly, Fmoc-Tyr(tBu), and Fmoc-Cys(Mmt)) were coupled in a 5-fold molar excess (5 eq. in 1.25 ml) for 15 seconds and 110 seconds at 75 °C and 90 °C, respectively, using a solution of DIC (0.25 M) and Oxyma (0.5 M) in 2.75 ml DMF. Fmoc-Arg(Pbf) was coupled using double coupling steps for better efficiency.

The acid-labile Mmt-protecting group on the cysteine side chain was removed by treating the resin with a mixture of 2% TFA and 5% TIPS in 93% DCM (5 ml each time). This mixture was added to the resin and shaken for 8 minutes under nitrogen before draining the solution. This process was repeated five times (step i). The resin was then thoroughly washed with DCM, and dry DMF (5 ml) was added under nitrogen. Compound **8a** (82 mg, 0.11 mmol, 2.1 eq.), **8b** (56 mg, 0.068 mmol, 1.4 eq.), or **8c** (56 mg, 0.068 mmol, 1.4 eq.) was dissolved in dry DMF (5 ml) and added to the resin, with the mixture shaken for 2 hours at room temperature (step ii). The solution was drained, and the resin was washed with DMF and DCM. To cleave the peptide from the resin, a cleavage solution (5 ml of 95% TFA, 2.5% TIPS, 2.5% H_2O) was added, and the mixture was shaken for 2.5 hours at room temperature (step iii). The peptide solution was collected by filtering out the resin, and the resin was washed with 1 ml of TFA. The combined solutions were added dropwise to ice-cold diethyl ether to precipitate the product. After centrifugation at 4,000 rpm for 20 minutes at 0 °C, the supernatant was removed, and the pellet was dried.

The resulting products (**1a**, **1b** and **1c**) were each purified via HPLC using a Phenomenex Gemini column at a flow rate of 25 ml/min. The gradient began with 5% CH_3CN in H_2O (+0.1% TFA), held for 4 minutes, followed by an increase in CH_3CN to 50% over 31 minutes. Compound **1a** was eluted after 23.69 minutes and was obtained as a white powder after lyophilization (5.9 mg, 5.2% overall yield). Compound **1b** eluted after 23.87 minutes and was obtained as a yellow powder (7.6 mg, 6.5% overall yield). Compound **1c** eluted after 20.78 minutes and was obtained as a yellow powder (9.0 mg, 11% overall yield).

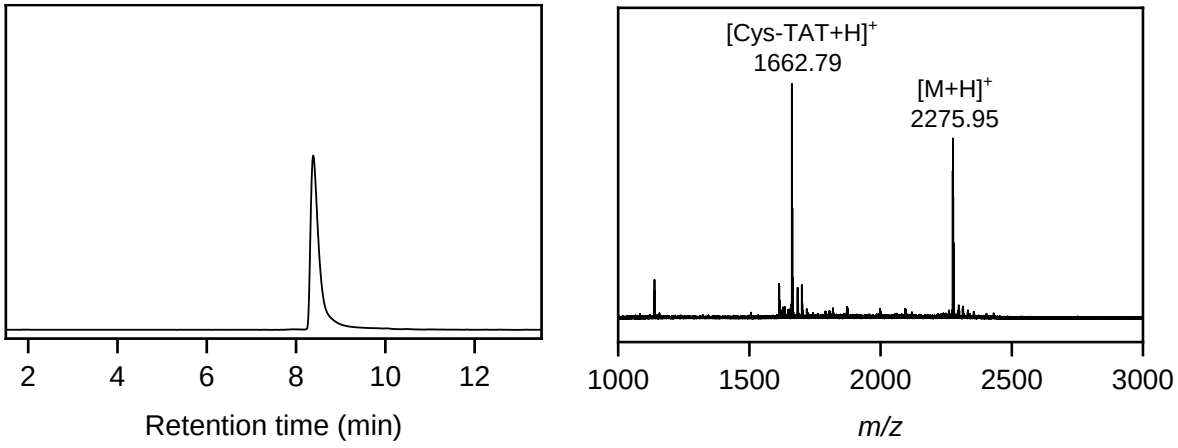

Figure S4.10 Analytical data of compound 1a. Left: LC trace (214 nm) with t_R (1a) = 8.38 min. Right: MALDI TOF spectrum showing peaks of $[M+H]^+$ (calculated: 2276.70) and the product of disulfide cleavage $[Cys\text{-}TAT+H]^+$ (calculated: 1661.98).

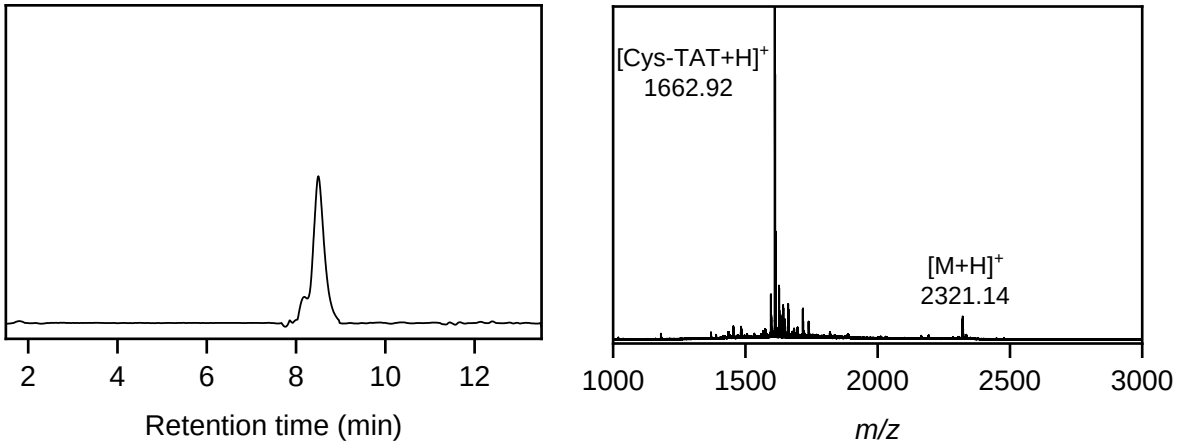

Figure S4.11 Analytical data of compound 1b. Left: LC trace (214 nm) with t_R (1b) = 8.50 min. Right: MALDI TOF spectrum showing peaks of $[M+H]^+$ (calculated: 2321.74) and the product of disulfide cleavage $[Cys\text{-}TAT+H]^+$ (calculated: 1661.98).

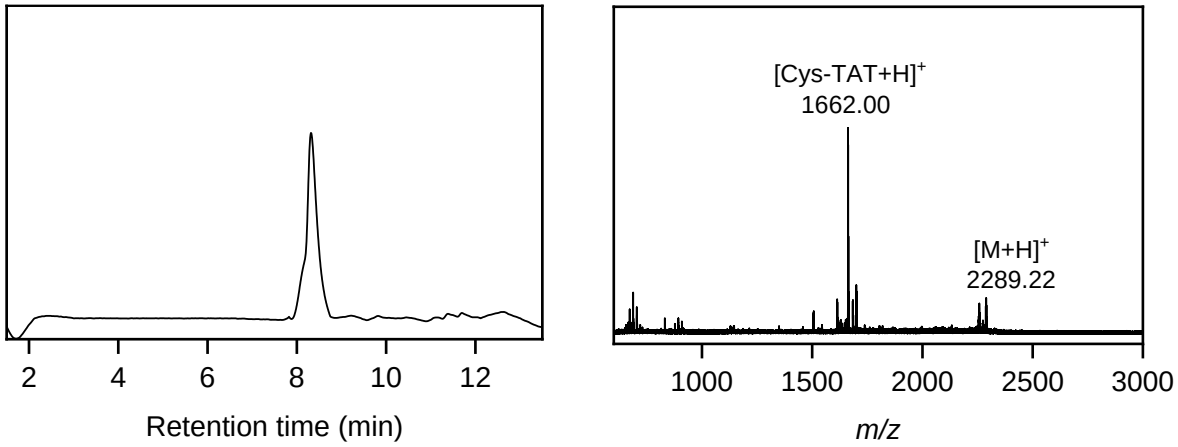

Figure S4.12 Analytical data of compound 1c. Left: LC trace (214 nm) with t_R (1c) = 8.31 min. Right: MALDI TOF spectrum showing peaks of $[M+H]^+$ (calculated: 2288.63) and the product of disulfide cleavage $[Cys\text{-}TAT+H]^+$ (calculated: 1661.98).

2.2. Synthesis of control compounds

2.2.1. Synthesis of triethylene glycol-modified control isopeptides

2.2.1.1. Synthesis of compound 12

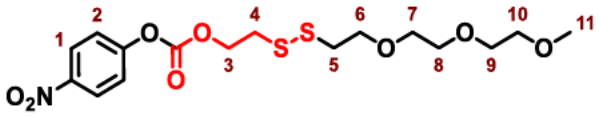

12

In a round-bottom flask 4-nitrophenyl (2-(pyridin-2-yldisulfaneyl)ethyl) carbonate (287 mg, 815 µmol, 1.4 eq.) was dissolved in a mixture of EtOH:MeOH:AcOH (85:15:5 ml) under N_2. 2-(2-(2-methoxyethoxy)ethoxy)ethane-1-thiol (106 mg, 588 µmol, 1.0 eq.) was dissolved in EtOH:AcOH (40:2 ml) under N_2 and the mixture was added dropwise to the solution of 4-nitrophenyl (2-(pyridin-2-yldisulfaneyl)ethyl) carbonate. The resulting reaction mixture was stirred for 24 h at room temperature. The solvents were removed in vacuo and subsequent flash column chromatography (cHex:EA 2:1) yielded compound **12** as a colorless oil (221 mg, 524 µmol, 89%).

^{1}H NMR (300 MHz, $CDCl_3$) δ 8.29 (d, J = 9.2 Hz, 2H), 7.39 (d, J = 9.2 Hz, 1H), 4.55 (t, J = 6.5 Hz, 2H), 3.75 (t, J = 6.5 Hz, 2H), 3.66 – 3.53 (m, 9H), 3.38 (s, 3H), 3.03 (t, J = 6.6 Hz, 2H), 2.94 (t, J = 6.5 Hz, 2H).

^{13}C NMR (176 MHz, CDCl3) δ 155.56, 152.46, 145.58, 125.49, 121.94, 121.91, 70.72, 70.53, 69.77, 69.58, 67.05, 66.87, 59.20, 38.74, 38.50, 36.87, 36.70.

APCI-MS: m/z 439.1 (calculated for $[M+NH_4]^+$: 439.12).

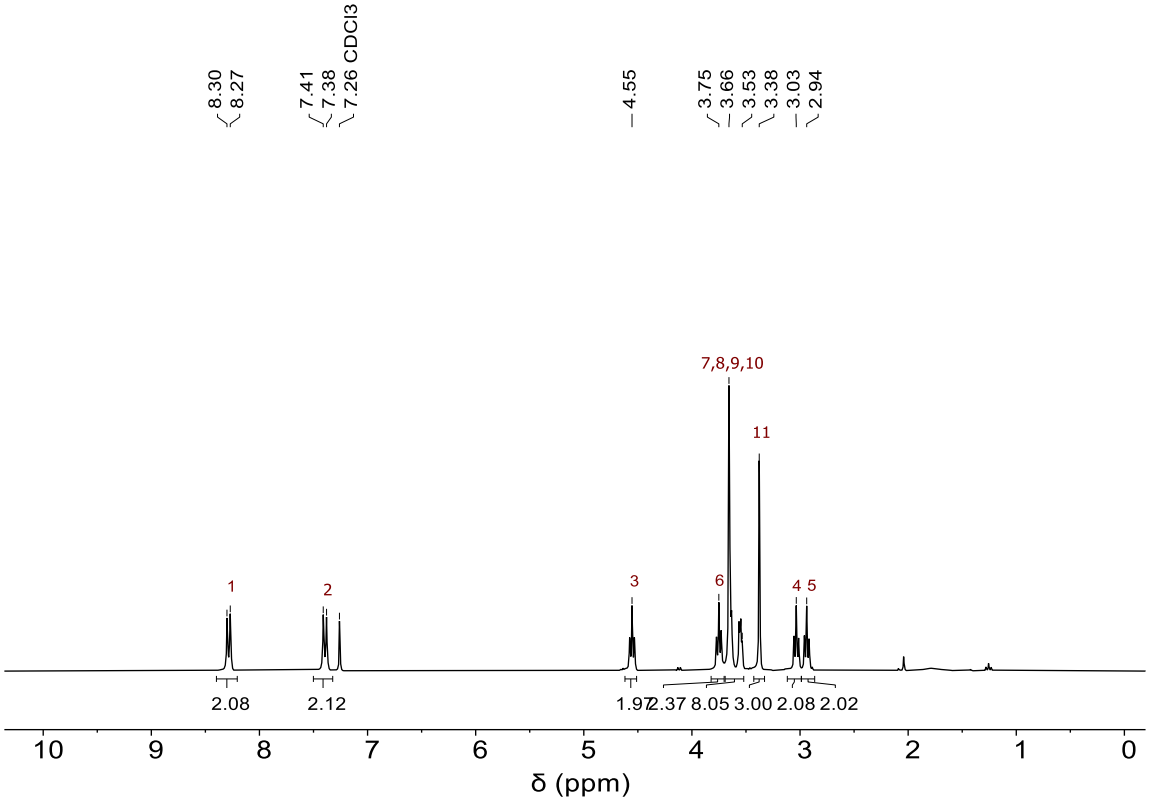

Figure S4.13 ^{1}H NMR spectrum (300 MHz, $CDCl_3$, 298 K) of compound 12.

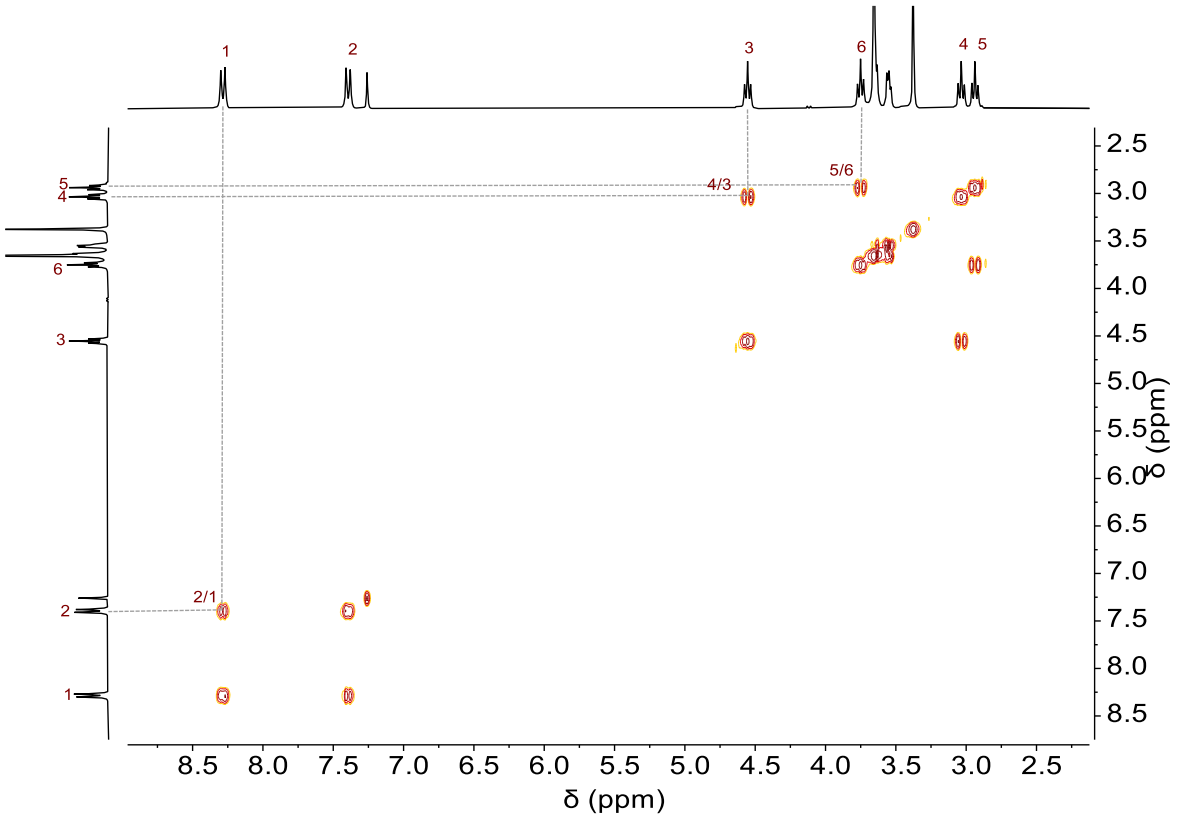

Figure S4.14 ^{1}H,^{1}H COSY NMR spectrum (300 MHz, $CDCl_3$, 298 K) of compound 12.

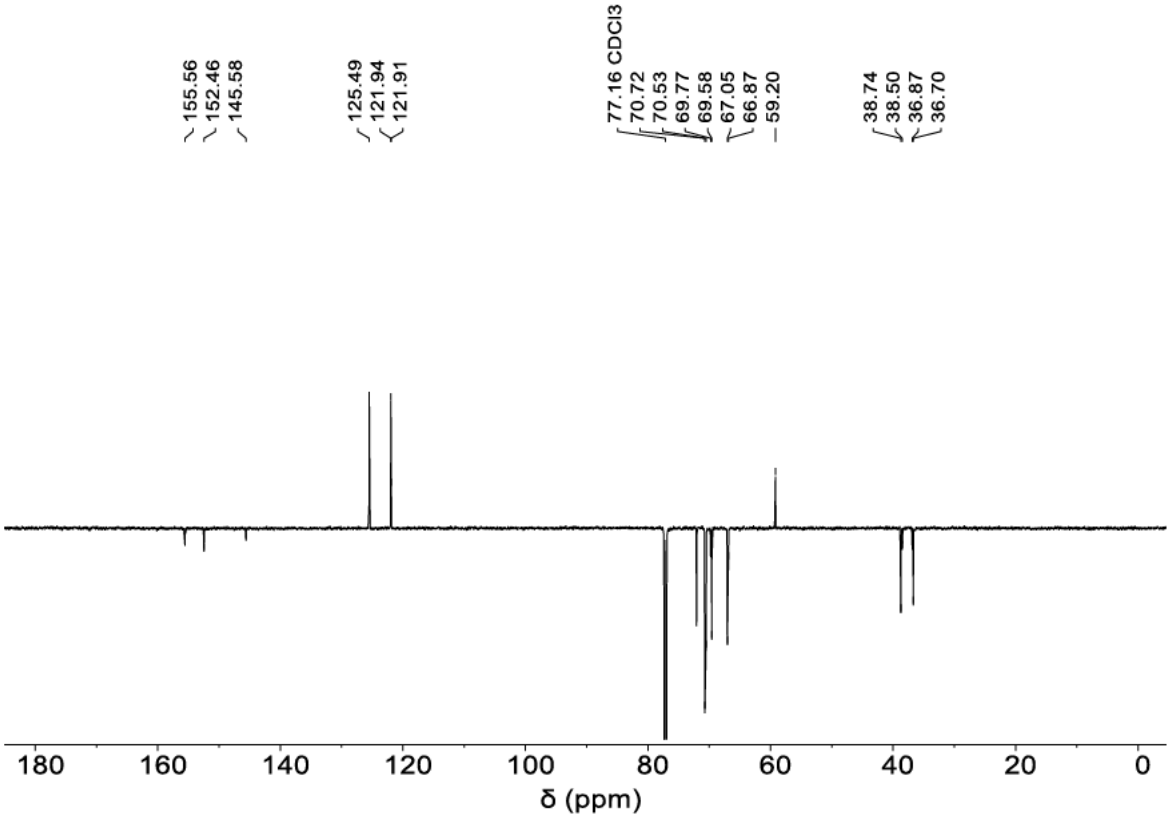

Figure S4.15 ^{13}C NMR spectrum (176 MHz, $CDCl_3$, 298 K) of compound 12.

2.2.1.2. Synthesis of compound 4a

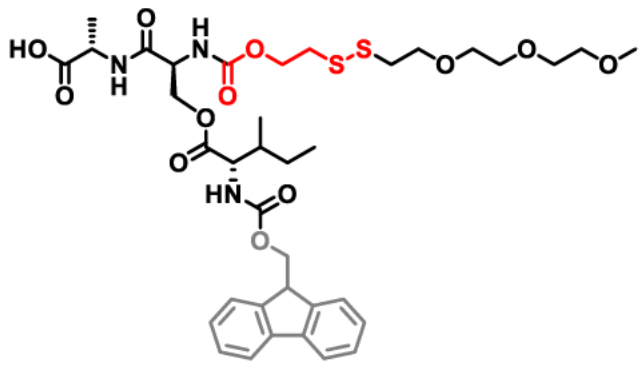

4a

The isopeptide **4a** was synthesized via solid phase supported peptide synthesis using Fmoc-Ala Wang resin at a scale of 0.5 mmol. The resin was swollen in DMF for 1 h before the synthesis. Before the coupling step and as the final deprotection, the *N*-terminal Fmoc group was cleaved by two deprotection steps using 20% piperidine in DMF (10 ml) for 25 s and 65 s at 70 °C and 90 °C respectively. Fmoc-serine without side chain protecting group (4 eq. in 10 ml) was coupled for 30 s and 120 s at 70 °C and 90 °C respectively using

DIC (0.5 M) and Oxyma (1 M) in a total of 16 ml DMF. Afterwards, the resin was washed with DCM and DMF and suspended in dry DMF (5 ml) under N_2. To the suspension dry DIPEA (323 mg, 0.44 ml, 2.5 mmol, 5 eq.) was added. A solution of compound **12** (289 mg, 686 µmol, 1.4 eq.) in dry DMF (5 ml) was added dropwise to the suspended resin. The suspension was shaken at room temperature overnight and subsequently washed repeatedly with DMF. In a second step, the resin was suspended again in dry DMF (3 ml) and Fmoc-Ile (530 mg, 1.5 mmol, 3 eq.), DMAP (61 mg, 0.5 mmol, 1 eq.) and DIC (189 mg, 0.22 ml, 1.5 mmol, 3 eq.) in dry DMF (5 ml) was added dropwise. After two hours the solution was drained and the same reactants in dry DMF (5 ml) were added again. After shaking at room temperature overnight, the solution was drained and the resin was washed repeatedly with DMF and DCM. Afterwards, the cleavage solution (5 ml of 95% TFA, 2.5% TIPS, 2.5% H_2O) was added and the mixture was shaken for 2 h at room temperature. The peptide solution was collected by filtering out the resin and the resin was additionally washed with TFA (1 ml). The solvent was removed in vacuo and flash chromatography (EA:cHex 3:1 + 1% formic acid) yielded compound **4a** as a colorless solid (83 mg, 524 µmol, 21%).

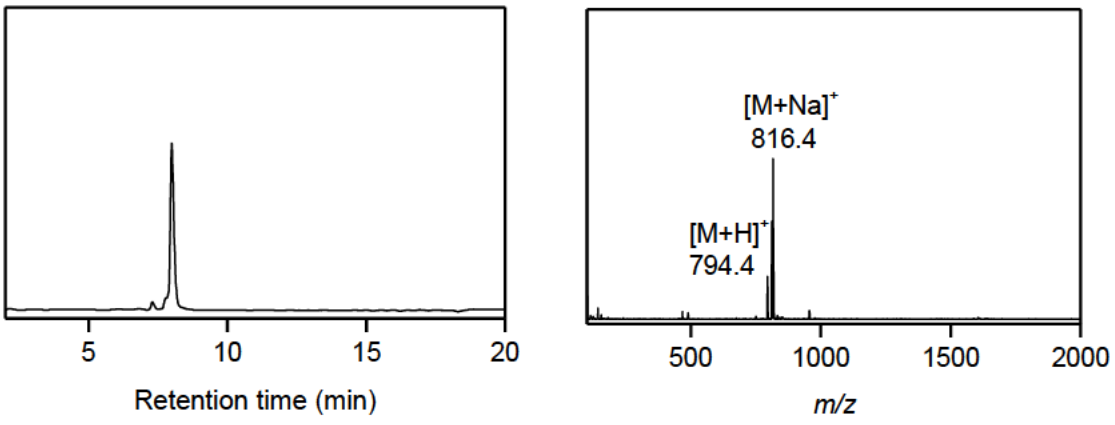

Figure S4.16 LC-MS data of compound 4a. Left: LC trace (214 nm) with t_R (4a) = 7.99 min. Right: Convoluted ESI-MS spectrum showing peaks of $[M+H]^+$ (calculated: 794.30) and $[M+Na]^+$ (calculated: 816.28).

2.2.1.3. Synthesis of compound 4b

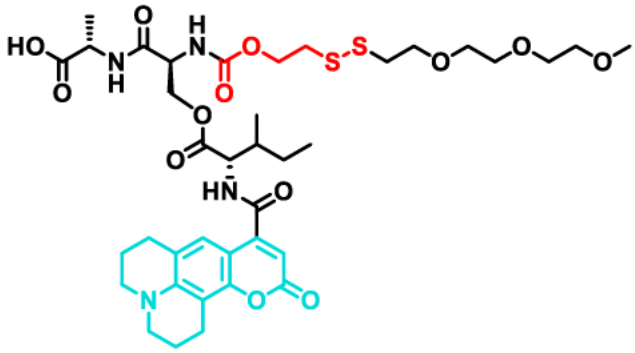

4b

In a round-bottom flask compound **8b** (55 mg, 67 µmol, 1 eq.) was dissolved in a 1:1-mixture of TFA and DCM (4 ml:4ml) and stirred for 4 h. The solvents were removed in vacuo. The remaining bright green oil was dissolved in EtOH:AcOH (1:20, 10 ml) under N_2. Afterwards, 2-(2-(2-methoxyethoxy)ethoxy)ethane-1-thiol (46 mg, 255 µmol, 3.8 eq.) was dissolved in EtOH:AcOH (5:2, 3.5 ml) under N_2 and the mixture was added dropwise to the solution of **8b**. The resulting reaction mixture was stirred for 24 h at room temperature. The solvents were removed in vacuo and subsequent flash column chromatography (DCM: MeOH 10:1) yielded compound **4b** as a bright green solid (27 mg, 524 µmol, 47%).

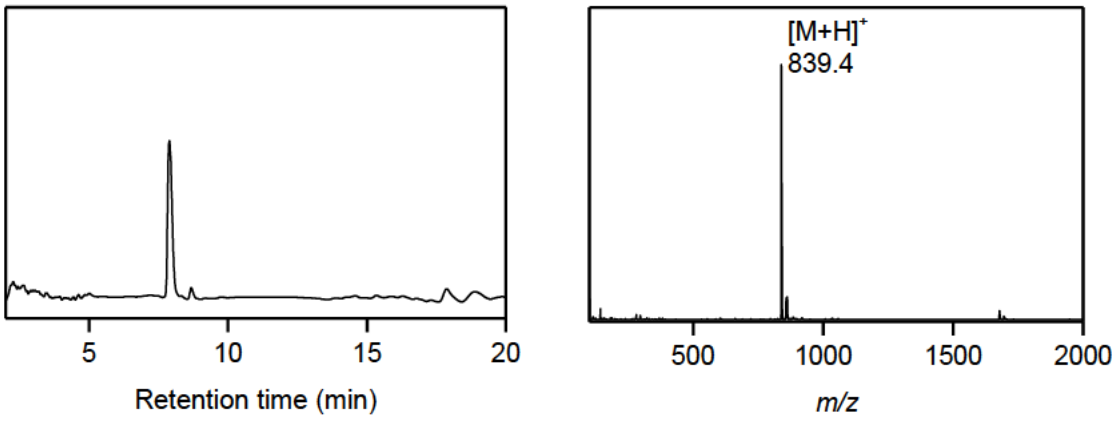

Figure S4.17 LC-MS data of compound 4b. Left: LC trace (214 nm) with t_R (4b) = 8.68 min. Right: Convoluted ESI-MS spectrum showing peaks of $[M+H]^+$ (calculated: 839.32).

3. Analysis of secondary structure and self-assembly behavior

3.1. TEM analysis

The linear peptides **3a**, **3b** and **3c** were each dissolved in DMSO to achieve stock solution with 10 mM or 50 mM concentration. The respective DMSO stock solutions were mixed at a 5:1 ratio of Fmoc-ISA **3a** and Coumarin 343-ISA **3b** yielding the stock solutions of the mixed linear peptides. The same was done for the kinked assembly precursors **1a** and **1b**. The DMSO stock solutions of the mixed linear peptides **3a** and **3b** and the mixed isopeptides **1a** and **1b** were diluted with DPBS at a 1:99 ratio to yield 500 µM or 100 µM peptide solutions. The same was done for the stock solutions of the linear NBD-ISA **3c** and the control isopeptide **1c**. The TEM samples were prepared as described in section 1.2.5.

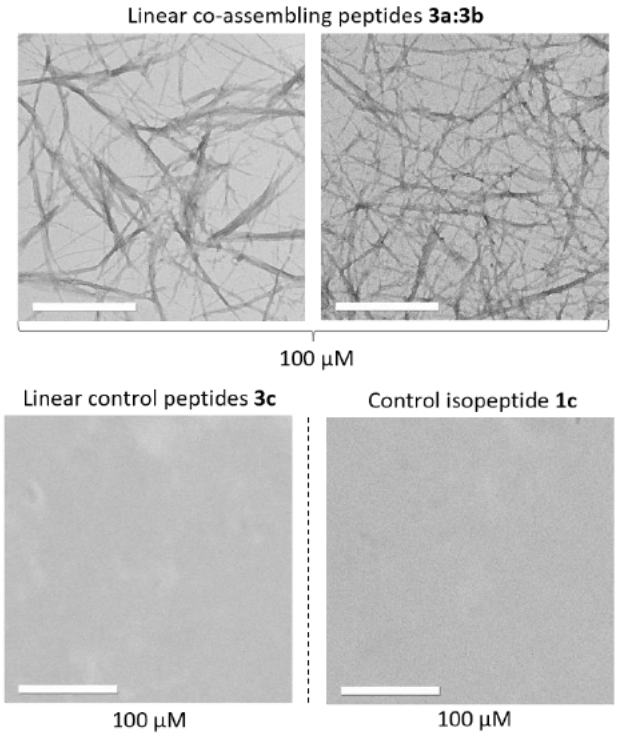

Figure S4.18 TEM images of nanofibers formed by co-assembling peptides 3a and 3b (5:1 ratio at 100 µM) in DPBS (pH 7.4) and DMSO (99:1). TEM images of linear control peptide 3c (100 µM) and TEM images of control *iso*peptide 1c (100 µM) in DPBS (pH 7.4) and DMSO (99:1). Scale bar 500 nm.

3.2. Proteostat assay for the determination of the critical aggregation concentration

For the analysis of the critical aggregation concentration of the linear peptides **3a:3b** (5:1) the commercial Proteostat protein aggregation assay kit by *Enzo Life Sciences, Inc.* was used as previously shown in a study by our group.[1] The peptide samples were prepared by diluting DMSO stock solutions of the linear peptides **3a:3b** (5:1) in various concentrations (1 to 100 µM) with DPBS in a 1:99 ratio. The resulting peptide samples were incubated for 24 h at room temperature while shaking. The Proteostat working solution was prepared by mixing 0.52 µl of the Proteostat stock solution with 98.48 µl MilliQ water and 1 µl assay buffer. After the incubation, 27 µl of each peptide solution were mixed with 3 µl of the Proteostat working solution. 9 µl of each solution were pipetted into a well of a Greiner 384 flat black well plate (3 wells per sample of each peptide concentration). The plate was incubated in the dark for 15 min while shaking. The fluorescence intensity of the Proteostat dye was subsequently measured with an excitation and emission bandwidth of 20 nm and an emission wavelength of 600 nm after excitation at 550 nm.

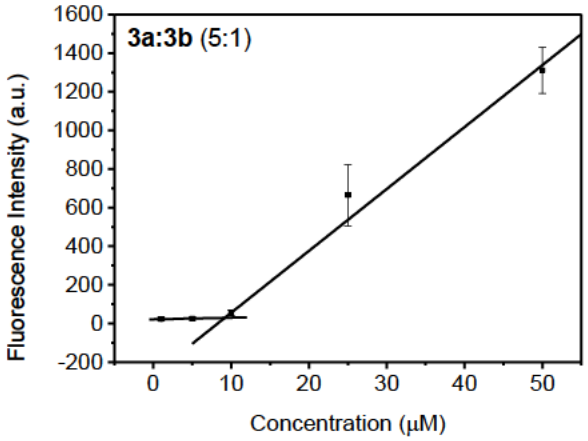

Figure S4.19 Proteostat aggregation assay of the mixed linear peptides Fmoc-ISA 3a and C343-ISA 3b (5:1) in DPBS:DMSO (99:1). The samples were incubated at room temperature for 24 h before the analysis. By calculating the intersection of the linear fits, the critical aggregation concentration of the mixed linear peptides 3a:3b was determined to be 9.2 µM.

4. Cell Experiments in 2D cell culture

4.1. Cell uptake analysis

MDA-MB-231 cells were seeded at a density of 20,000 cells/well in an 8-well confocal plate. After adhering for 24 h, cells were treated with the samples containing either **1a:1b** or the control compounds **1c**, **3a:3b** or **4a:4b** at different concentrations and incubated for 4 h at 37 °C. The sample solutions were prepared by dissolving the respective compounds in DMSO to prepare different stock solutions (100x) containing **1a:1b**, **3a:3b** or **4a:4b** in a 5:1 molar ratio or **1c**. These stocks were each diluted with DPBS in a 9:1 ratio yielding the DPBS:DMSO stocks (10x). Another dilution with DMEM (9:1) gave the final samples (total DMSO content: 1%) which were added to the cells after removing the old medium. After the incubation time of 4 h was over, the cells were fixed for 15 min at room temperature using 4% paraformaldehyde solution. The nucleus was stained with HCS Nuclear Mask Deep Red Stain for 20 min at room temperature. The staining solution was removed, and fresh DPBS was added to the cells before they were imaged by confocal laser scanning microscopy.

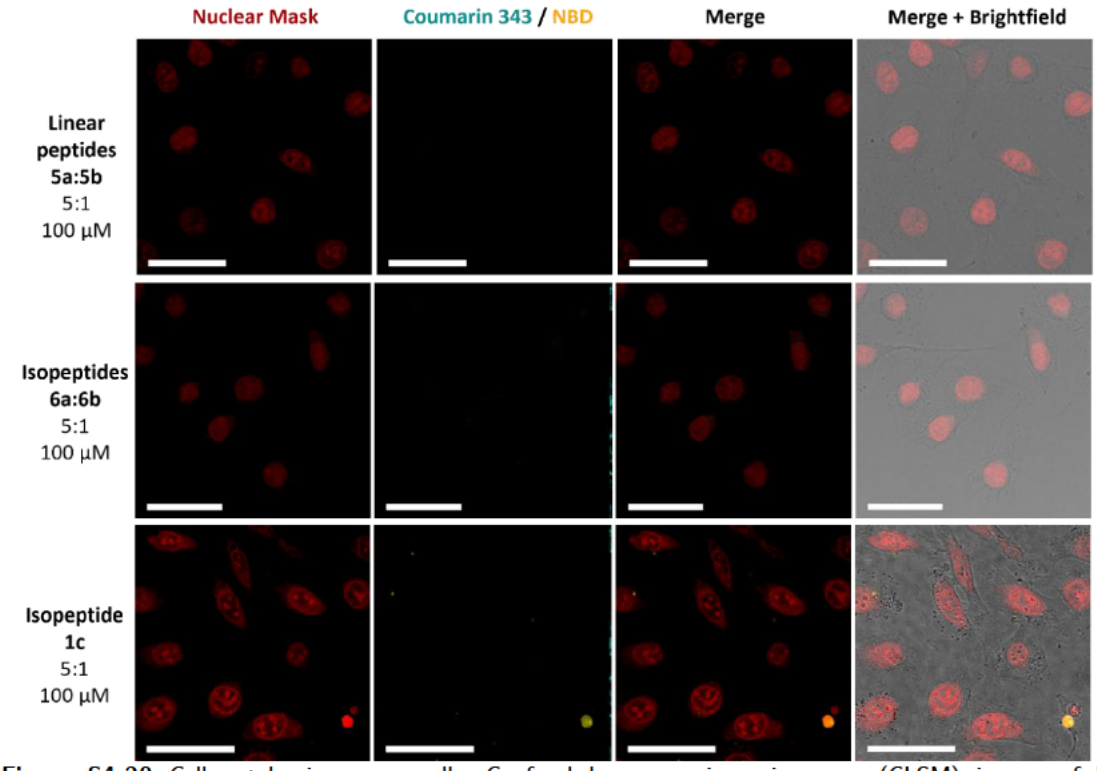

Figure S4.20 Cell uptake in cancer cells. Confocal laser scanning microscopy (CLSM) images of MDA-MB-231 breast cancer cells after 4 h of incubation with control compounds 3a:3b, 4a:4b (5:1) or 1c at 100 µM. The nucleus was stained with HCS Nuclear Mask Deep Red (red). Scale bars 50 µm.

4.2. Live-cell imaging

MDA-MB-231 cells were cultured in an 8-well confocal plate at a density of 20,000 cells per well in DMEM and allowed to adhere overnight at 37°C, 5% CO_2. The medium was removed and the sample of **1a:1b** in DMEM/DPBS/DMSO (90%/9%/1%) was introduced into a well. The cells were imaged live using an incubator-equipped Leica Stellaris® 8 microscope (40x glycerol immersion objective) with fast lifetime contrast (FALCON) module (Leica Microsystems GmbH). The incubator (okolab) is set and held constant at 37 °C, 5% CO_2 and a relative humidity of 90% throughout all measurements.

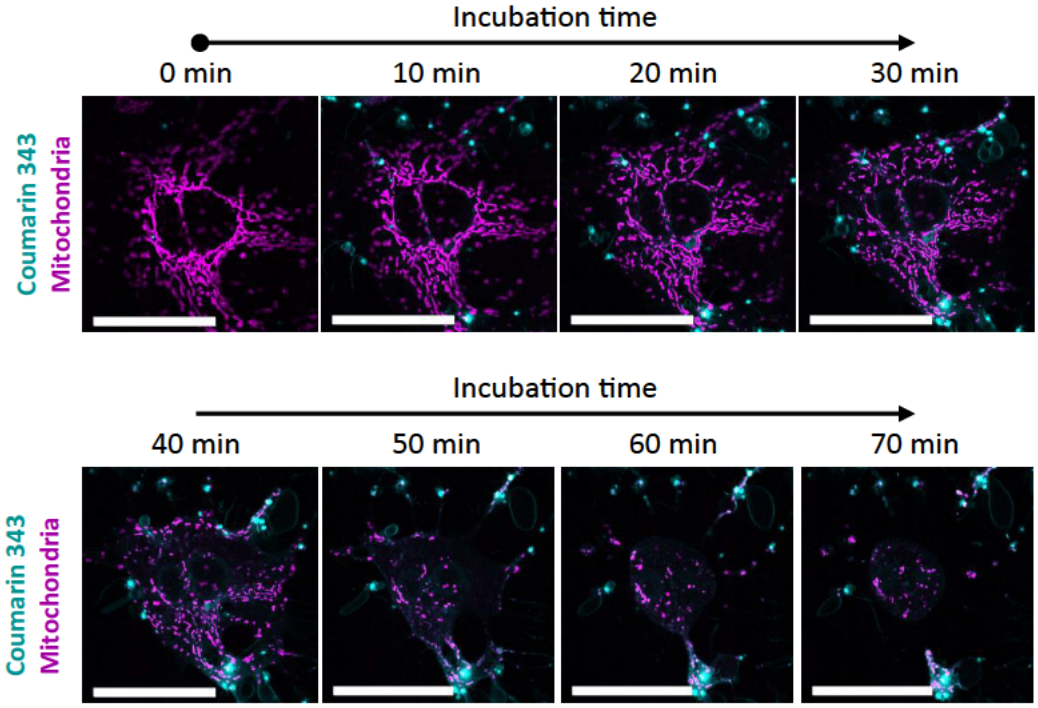

Figure S4.21 Live cell imaging of mitochondria-stained cancer cells. CLSM images of live-cell imaging of MDA-MB-231 cells treated with 50 µM of 1a:1b (cyan). Cells were previously transfected with CellLight™ Mitochondria-RFP (pink). Scale bars 50 µm.

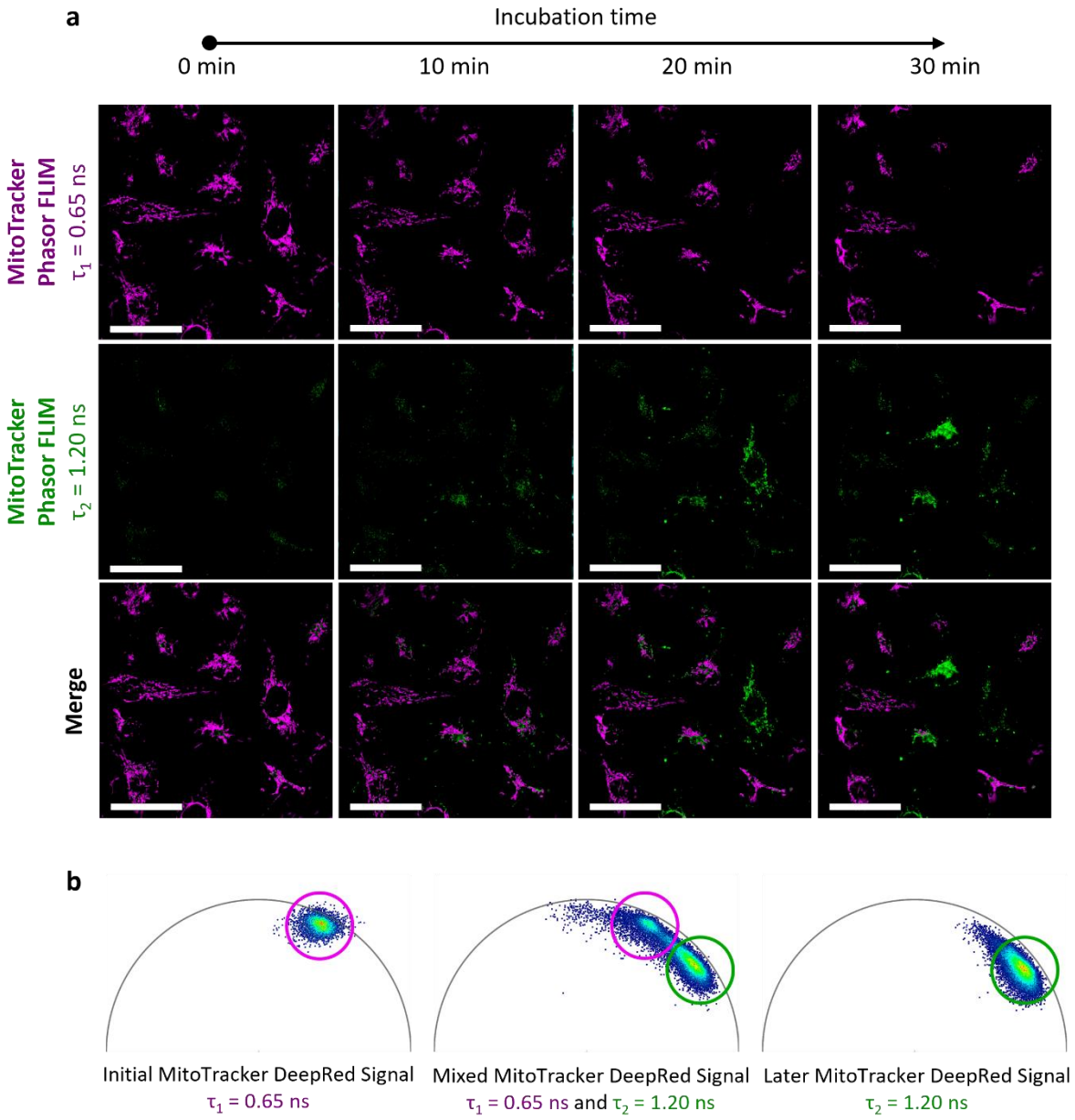

Figure S4.22 Phasor plots of MitoTracker DeepRed FLIM measurements. Live-cell imaging of MDA-MB-231 cells treated with 50 µM of 1a:1b. Cells were previously stained with MitoTracker DeepRed. Fluorescence lifetime measurements of the stain were conducted concurrently with fluorescence imaging, revealing two distinct fluorescence lifetime signals for MitoTracker DeepRed over time. Scale bars 50 µm.

4.3 Correlative light- and electron microscopy (CLEM) of cells

For electron microscopy (EM) studies correlated with confocal light microscopy, MDA-MB-231 cells were seeded at a density of 20,000 cells per well on sapphire disks and incubated with 100 µM of **1a:1b** for 4 h. After incubation, the cells on the sapphire disks were frozen using high-pressure freezing (Wohlwendt HPF 01). Freeze substitution followed, with the cells stained at low temperatures using OsO_4 and uranyl acetate for EM examination. The cells were then embedded in epoxy resin (EPON), and ultrathin sections were prepared with an ultramicrotome (Leica FC7) using a diamond knife (Diatome). The section thickness and substrate were adjusted for subsequent EM investigation: for TEM, sections (100 nm thick) were transferred to Cu grids; Fluorescence of the co-assembling peptides was first measured in a confocal laser scanning microscope (Leica SP5) (458 nm excitation, 470-500 nm emission detection bandwidth). The same thin section was then examined in TEM (FEI Tecnai F20). To identify the fluorescent peptide assemblies, we correlated fluorescence with EM images by superimposing the images using the "Landmark correspondence" plugin in ImageJ 1.53e.

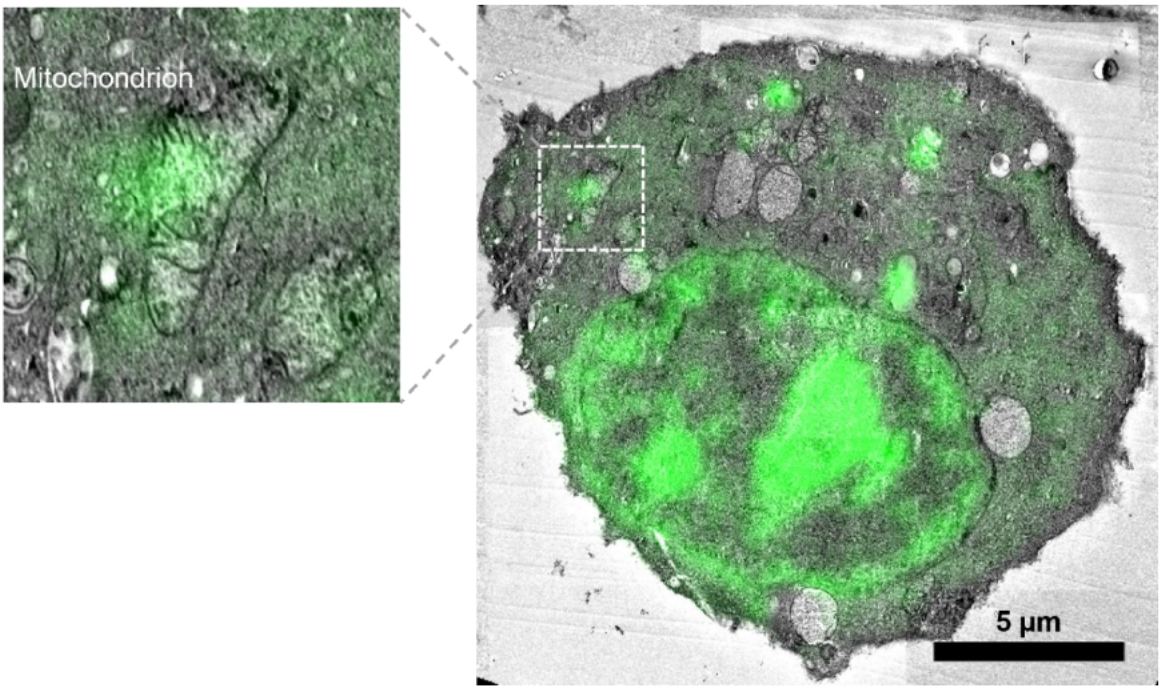

Figure S4.23 Correlative light- and electron microscopy (CLEM) image of MDA-MB-231 cell incubated with 1a:1b (100 µM) (green) for 4 h.

4.4. Co-staining of actin filaments

For the co-staining of actin filaments MDA-MB-231 cells were seeded at a density of 20,000 cells/well in an 8-well confocal plate. After adhering for 24 h, cells were treated with the samples containing **1a:1b** at different concentrations and incubated for 4 h at 37 °C. The sample preparation is described in section 3.1. After the incubation the medium was removed and the cells were washed with DPBS and fixed for 15 min at room temperature using 4% paraformaldehyde solution. After rinsing with DPBS three times, the actin filament stain Alexa Fluor™ 555 Phalloidin was added to the cells (diluted 1:20 in DPBS) and incubated for 15 min at room temperature. Afterwards the cells were washed once with DPBS and fresh DPBS was added before imaging.

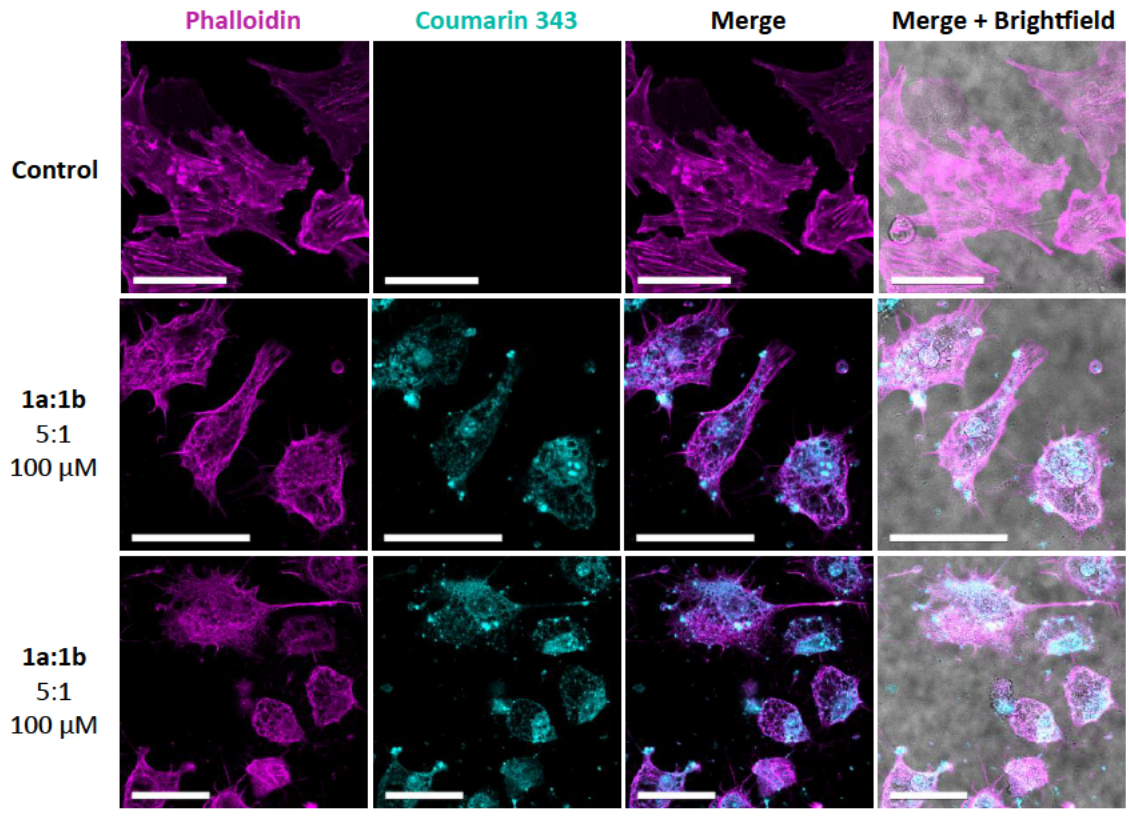

Figure S4.24 Disruption of actin filaments by in-situ formed nanostructures. Confocal laser scanning microscopy (CLSM) images of MDA-MB-231 cells after 4 h of incubation with glutathione-responsive isopeptides 1a and 1b (5:1) (cyan) and additional staining with Alexa Fluor™ 555 Phalloidin (pink). Scale bars 50 µm.

4.5. Cell viability assay

MDA-MB-231 cells were seeded at a density of 2,500 cells/well in a white half area 96-well plate and incubated at 37°C overnight to allow them to adhere. The following day, different concentrations of the glutathione-responsive isopeptides **1a:1b,** the glutathione-responsive non-assembly-inducing isopeptide **1c** or the other control compounds. For each condition, quadruplicates were performed. Cells were incubated with 50 µL of the sample for 4 h. After the treatment, CellTiter-Glo® Assay solution (50 µL) was added to each well, and the plate was placed on an orbital shaker for 2 minutes and subsequently incubated 10 minutes at room temperature. Luminescence was measured using a Promega GloMax®-Multi Detection System using the manufacturer's protocol.

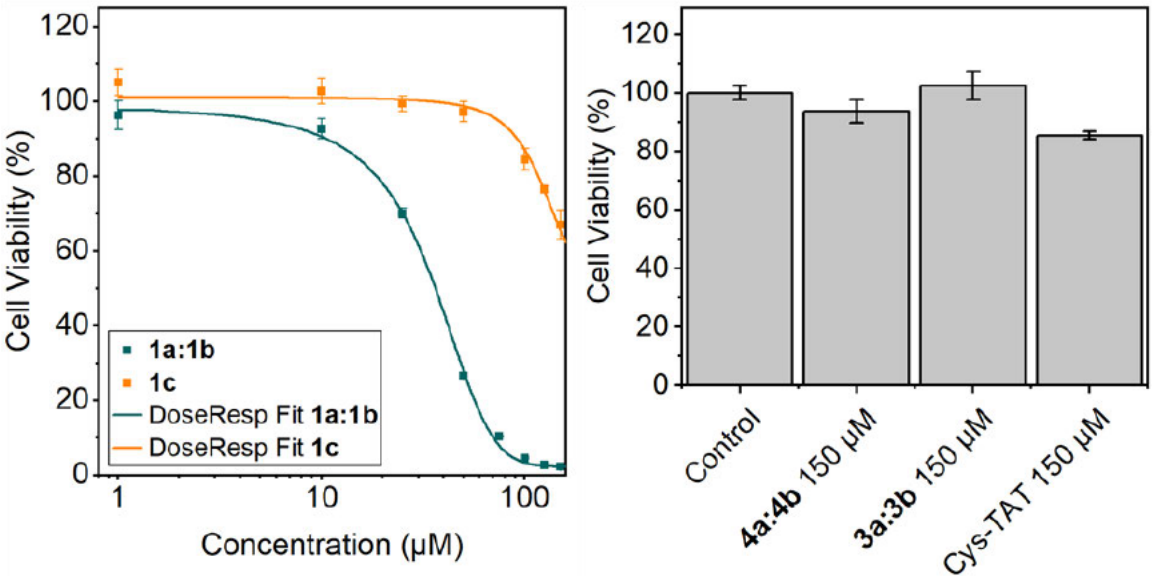

Figure S4.25 Cell viability of MDA-MB-231 cells incubated with 1a:1b (green curve) or 1c (orange curve) for 4 h (left) and with the other control compounds (right). The IC_{50} value of 1a:1b for MDA-MB-231 cells is 36.4±3.1 µM.

5. Analysis of Metabolic Disruption

5.1. Mito stress test

The effect of the compounds on the metabolism of MDA-MB-231 cells was investigated using the Seahorse XFe96 Analyzer (Agilent Technologies). The Seahorse XF Cell Mito Stress Test Kit was used following the manufacture's protocol to determine the respiratory activity of the cells. Cells were seeded at a density of 20,000 cell/well one day before the assay and incubated overnight at 37°C, 5% CO_2 in DMEM, high glucose supplemented with 10% FBS. The cartridge for sample loading was loaded with calibration solution (200 µL per well) and incubated at 37°C in a non-CO_2 incubator. On the day of the assay, Seahorse XF DMEM, pH 7.4 was supplemented with pyruvate (1 mM), glutamine (2 mM), and glucose (10 mM). Cells were washed twice with XF DMEM (2x 100 µL) and the medium was substituted with fresh XF DMEM (180 µL) and placed in a 37°C non-CO_2 incubator for 45 to 60 minutes before loading the plate into the instrument. Assay components of the Mito Stress Test Assay were prepared as described in the manufacturer's protocol. Briefly, Oligomycin was resuspended in 630 µL, Carbonyl cyanide-p-trifluoromethoxyphenylhydrazone (FCCP) in 720 µL and Rotenone/ Antimycin A (Rot/AA) in 540 µL supplemented XF DMEM and vortexed vigorously to ensure complete dissolution. Stocks were diluted to 3 ml total; Oligomycin: 450 µL stock in 2,550 µL XF DMEM (final concentration 1.5 µM); FCCP: 300 µL in 2,700 µL XF DMEM (final concentration 1 µM); Rot/AA: 300 µL in 2,700 µL XF DMEM (final concentration 0.5 µM). Samples were prepared at 10x stocks with 10% DMSO in XF DMEM. The cartridge was prepared by loading the samples (20 µL) in Port A of the designated wells and the components of the Mito Stress Test Assay in Ports B-D of each well. The cartridge and 96-well plate with the cells were loaded in the instrument and the content of the ports was injected sequentially according to the specific assay. The oxygen concentration, to monitor the oxygen consumption rate (OCR), was constantly measured throughout the entire time of the assay. The Mito Stress Assay were performed in two independent experiments with n=4. Bar graphs are shown for the mean ± standard error of the mean (s.e.m.) for raw and processed data. For the processed data, all values were set to 100%

OCR for the last measurement prior to sample addition before calculating the results. Additionally, the values were normalized to the control for each independent experiment, before calculating the mean value and SEM. Statistical significance was calculated by ANOVA with a Tukey post hoc test and was defined as $^{*}p < 0.05$, $^{**}p < 0.01$, $^{***}p < 0.001$.

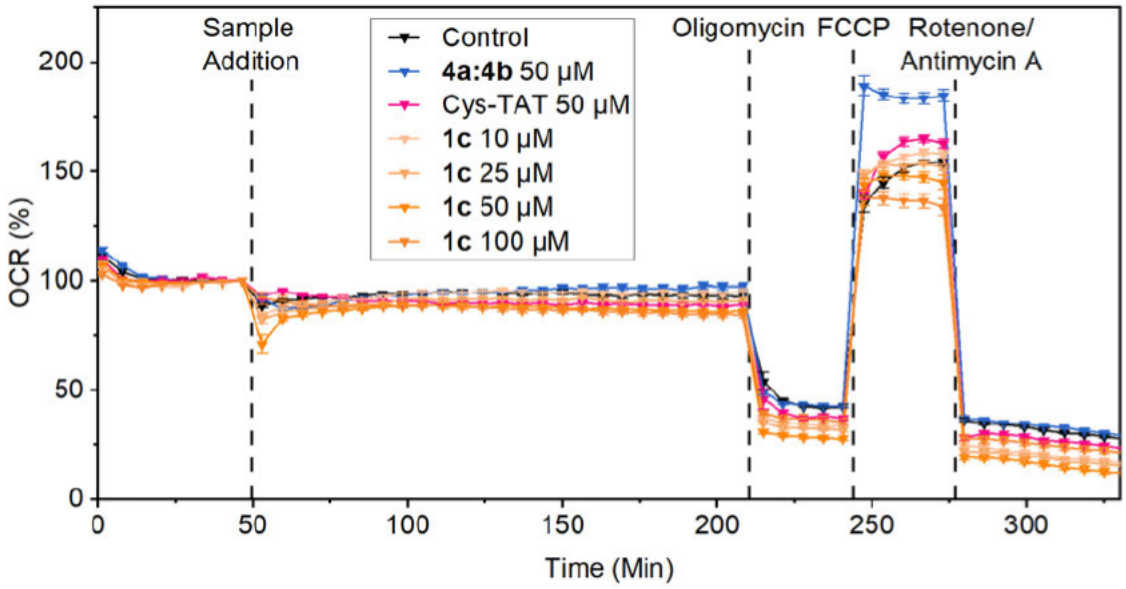

Figure S4.26 Effect on the oxygen consumption rate (OCR) of MDA-MB-231 cells treated with the control compounds 1c, 4a:4b and Cys-TAT for 4 hours total. During the last 1.5 hours Mito Stress Test was performed. At different time points specific modulators of the electron transport chain (ETC) were added to investigate the influence of the samples on cellular respiration in more detail: (1) oligomycin inhibits ATP synthase, (2) FCCP (carbonyl cyanide 4-(trifluoromethoxy)phenylhydrazone) disrupts the mitochondrial membrane potential, (3) rotenone inhibits complex I and antimycin A inhibits complex III of the ETC.27 The last measurement before treatment injection of the compound is set as 100%. Data are presented as mean ± s.e.m., n ≥ 8.

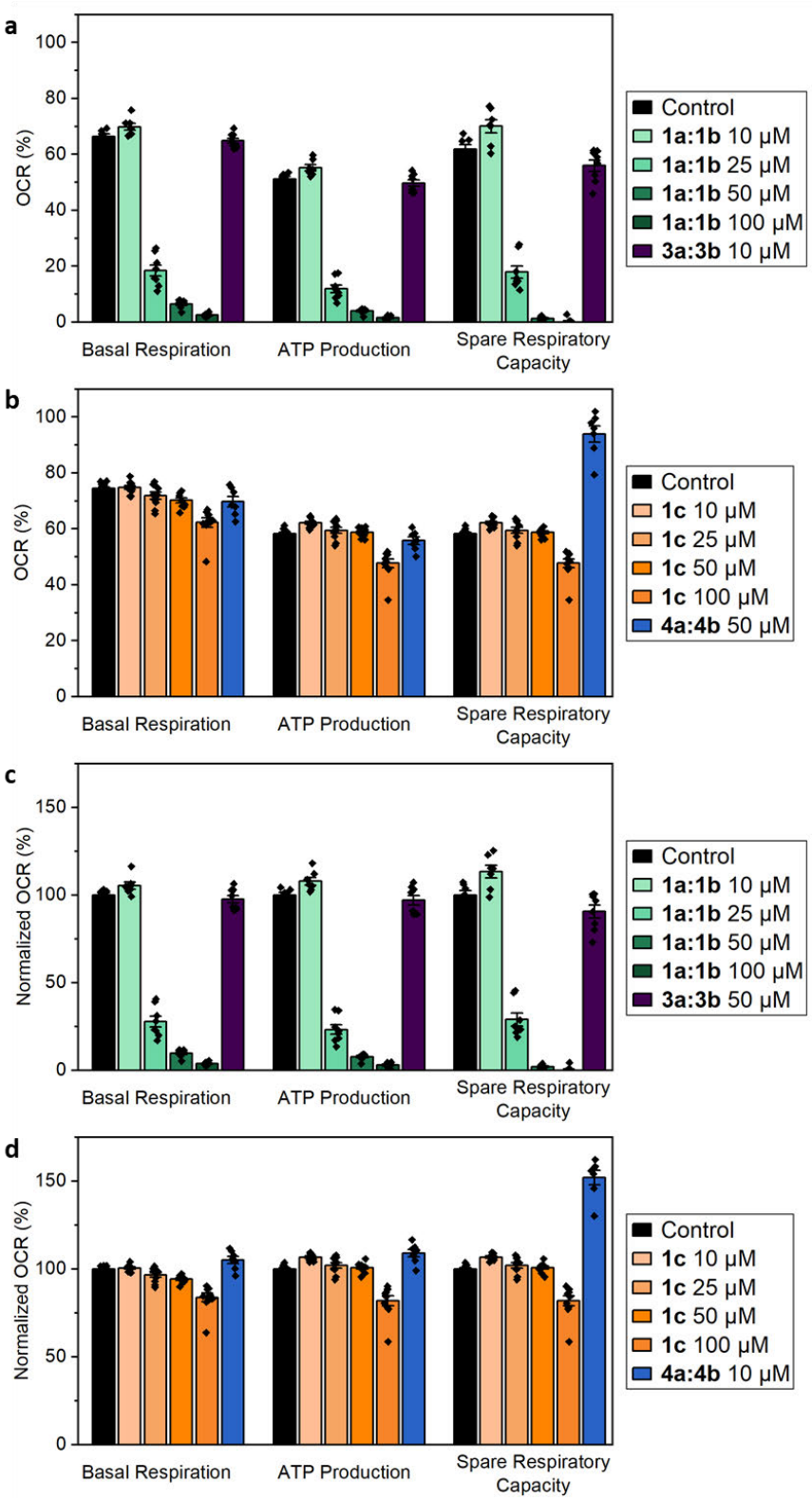

Figure S4.27 Comparison of the effect of 1a:1b, 1c, 3a:3b and 4a:4b on characteristic values of mitochondrial function after 4 h total incubation. Basal Respiration, ATP Production and Spare Respiratory Capacity are shown. Values were calculated using the data from graphs with the last measurement before sample addition set to 100% OCR and are presented as OCR (%) (a and b). Additionally, the data was normalized to the control of each experiment and data are shown as Normalized OCR (%) (c and d). Data are presented as mean ± s.e.m., n ≥ 6.

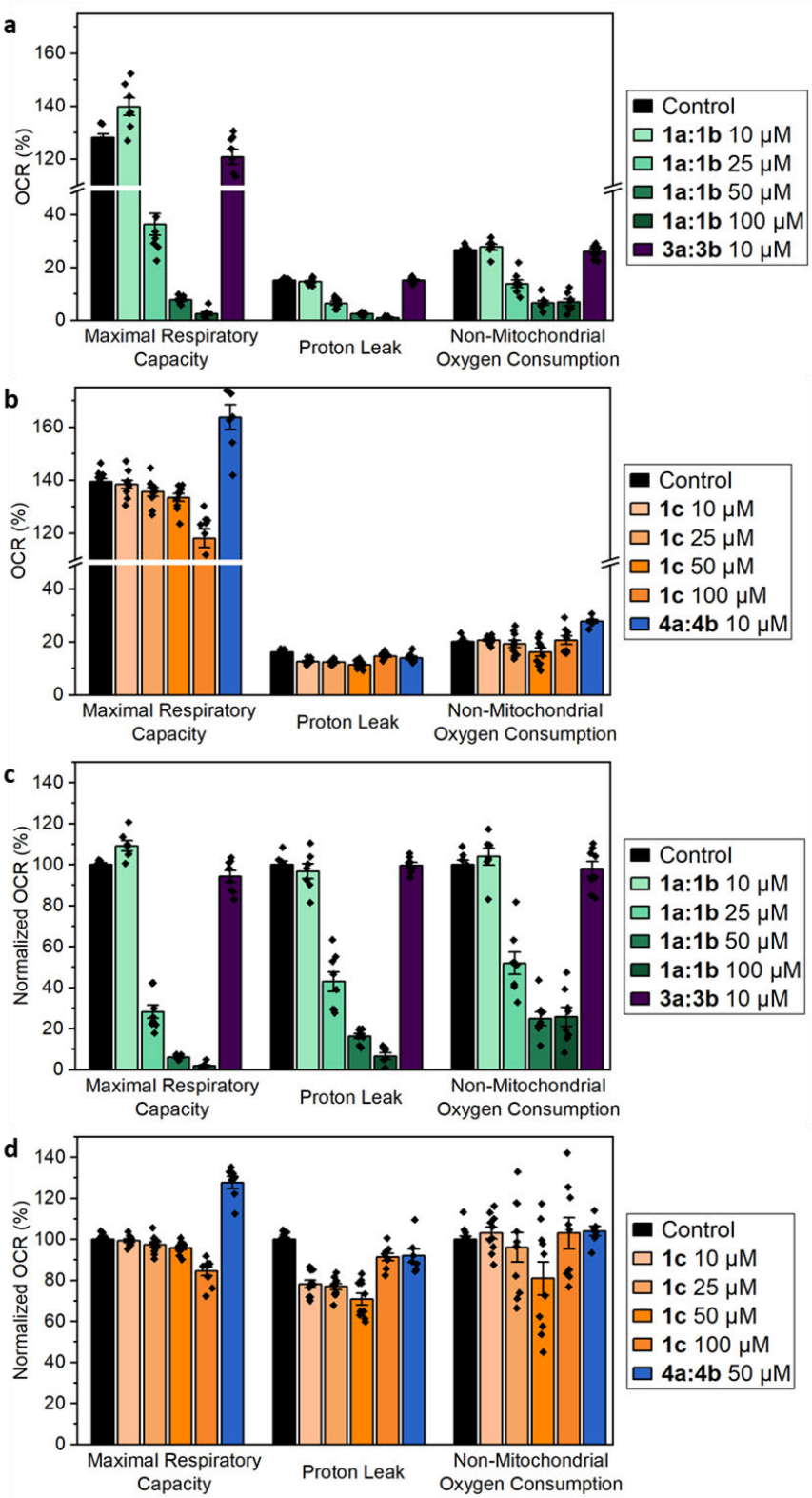

Figure S4.28 Comparison of the effect of 1a:1b, 1c, 3a:3b and 4a:4b on characteristic values of mitochondrial function after 4 h total incubation. Maximal Respiratory Capacity, Proton Leak and Non-Mitochondrial Oxygen Consumption are shown. Values were calculated using the data from graphs with the last measurement before sample addition set to 100% OCR and are presented as OCR (%) (a and b). Additionally, the data was normalized to the control of each experiment and data are shown as Normalized OCR (%) (c and d). Data are presented as mean ± s.e.m., n ≥ 6.

6. Tumor Spheroid Experiments

6.1. Evaluation of uptake and toxicity on MDA-MB-231 spheroids

Prior to treatment, fully developed MDA-MB-231 spheroids were imaged using a Keyence BZ-X810 fluorescence microscope. Subsequently, spheroids were treated with the synthesized and previously characterized compounds (**1a:1a** (100and 50 µM), **1c** (100 µM), **3a:3b** (100 µM) and **4a:4b** (100 µM) in a final volume of 100 µL/well and incubated at 37°C, 5% CO_2. Untreated spheroids were used as experimental control where the medium was substituted with fresh DMEM containing 1% DMSO. Cellular uptake after 4 h incubation was observed using the GFP filter of a Keyence BZ-X810 microscope. Growth and morphological changes were monitored by brightfield imaging using a Keyence BZ-X810 microscope after 4 h incubation. At the end of the incubation time spheroids were washed with DPBS to remove treatment residuals and incubated with Propidium Iodide (8 µg/ml; Sigma-Aldrich, P4864). After incubation with the staining solutions spheroids were washed with DMEM FluoroBrite and imaged using either a Keyence BZ-X810 or a Leica Stellaris® 8 microscope. Experiments were carried out on two independent cultures with internal replicates (n≥5).

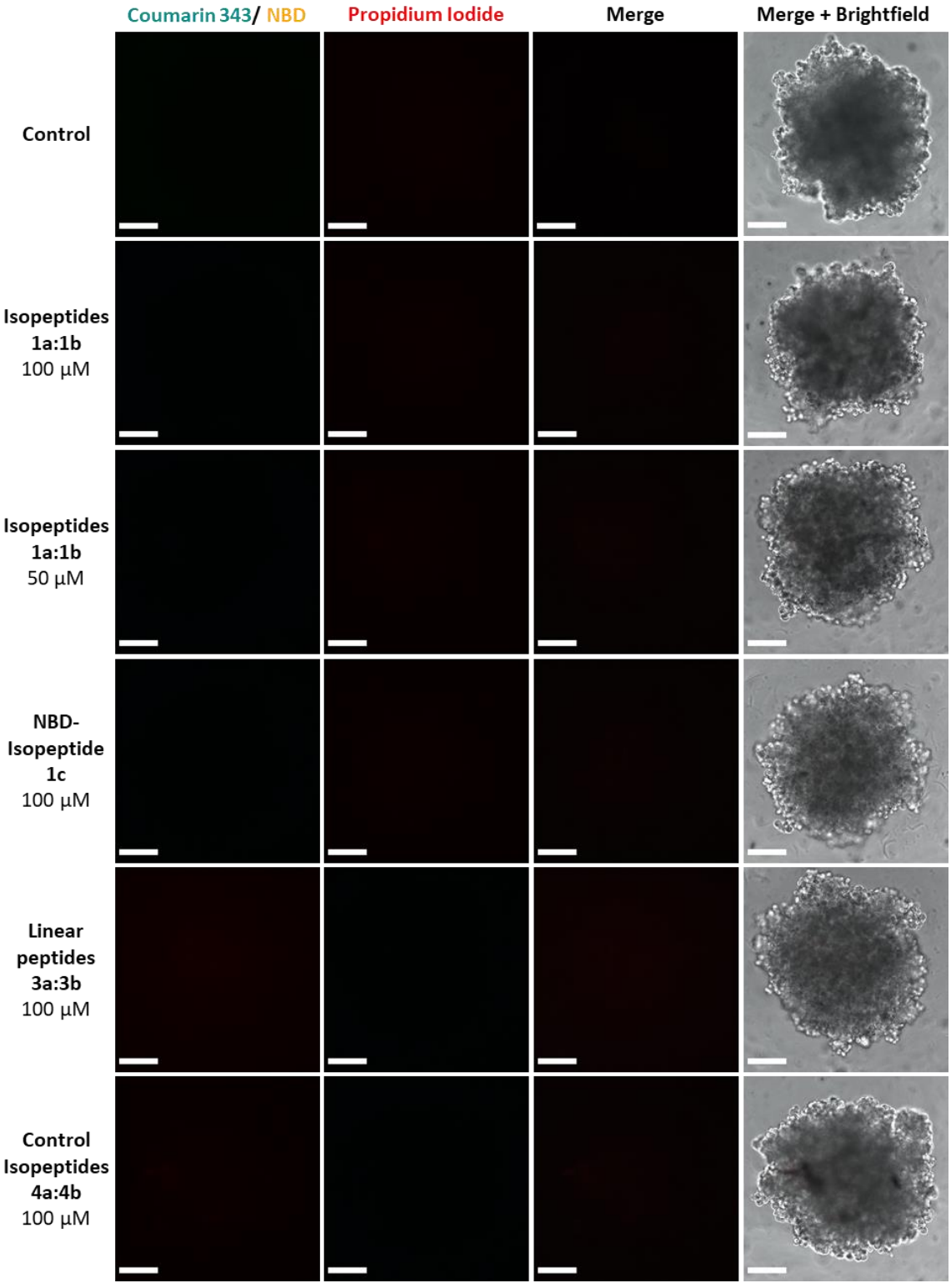

Figure S4.29 Fluorescence microscopy images of MDA-MB-231 tumor spheroids before treatment. Coumarin 343 (cyan) and propidium iodide (red) fluorescence were imaged using GFP and Cy5 filter settings. Scale bars 100 µm.

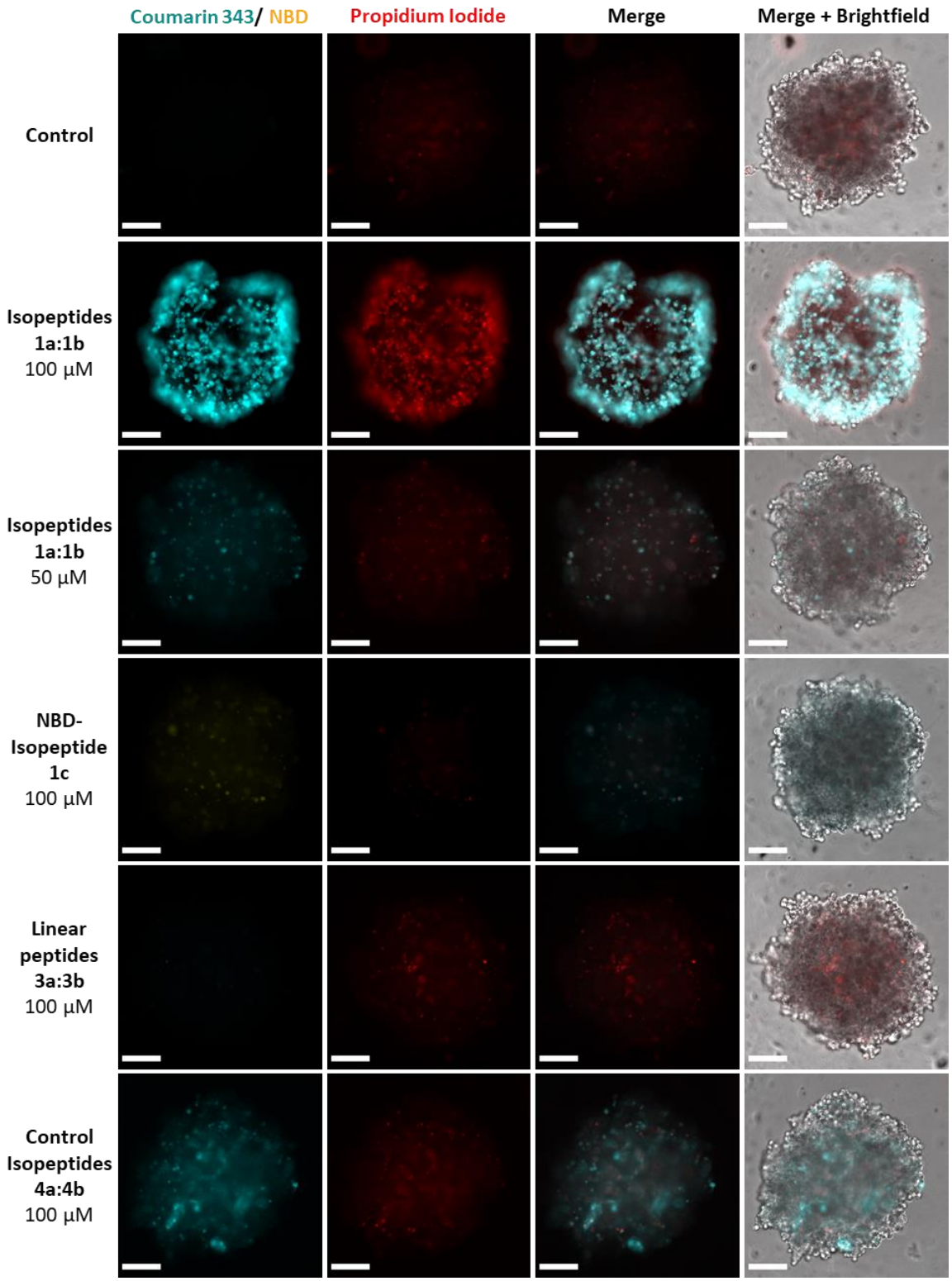

Figure S4.30 Fluorescence microscopy images of MDA-MB-231 tumor spheroids after 4 h treatment with 1a:1b at 100 and 50 µM and 1c , 3a:3b and 4a:4b at 100 µM. Coumarin 343 (cyan) or NBD (yellow) and propidium iodide (red) fluorescence were imaged using GFP and Cy5 filter settings. Scale bars 100 µm.

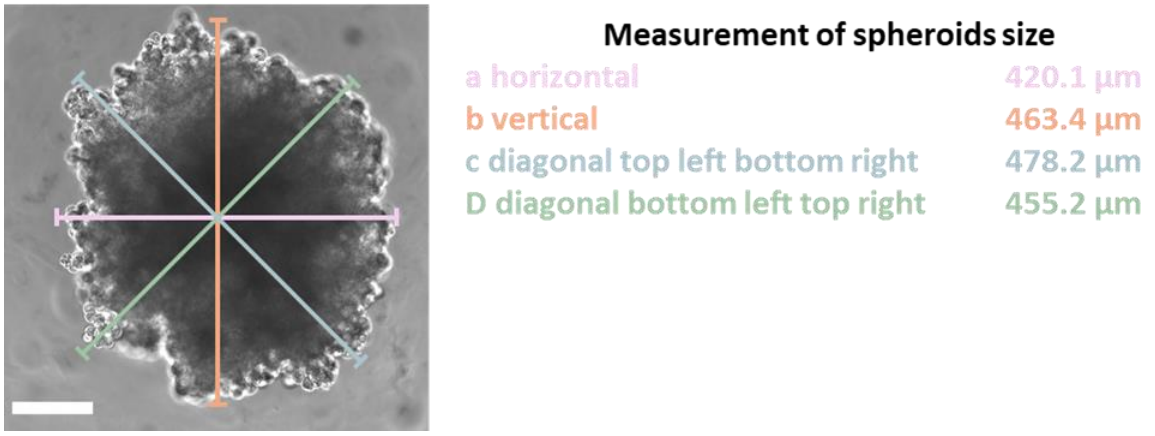

Figure S4.31 Measurement of spheroid size shown for the example of an untreated control spheroid at t_0. For each spheroid the size was measured at four different positions at t_0 and after 4 h incubation with compounds. To ensure comparability, the size of each spheroid was measured horizontally, vertically and diagonally. The mean of the four measurements was used to evaluate the change in size within the 4 h incubation time. Images were processed using ImageJ. Scale bar 100 µm.

References

1 Chagri, S.; Burgstaller, A.; Schirra, C.; Link, J.; Zhou, Z.; Roth, P.; Meyer, R.; Fetzer, J.; Ren, Y.; Si, S.; Mazzotta, F.; Wagner, M.; Lieberwirth, I.; Landfester, K.; Ng, D. Y. W.; Staufer, O.; Weil, T. Synthetic intracellular nanostructures enhance cytotoxic T cell function via assembly-driven chemical engineering. *ChemRxiv*, doi:10.26434/chemrxiv-2024-3lxgk (2024).

5. Programming Nanostructure Formation through Furin-Triggered Isopeptide Conversion and Peptide Self-Assembly

Authors

Sarah Chagri[‡], Jana Fetzer[‡], Patrick Roth, Albin Lahu, Jian Zhang, Manfred Wagner, Shutian Si, Ingo Lieberwirth, Katharina Landfester, David Y. W. Ng, Tanja Weil

[‡] S. Chagri and J. Fetzer contributed equally to this work.

Contributions

Sarah Chagri: Conceptualization, molecular design of peptides and planning of synthesis and experiments. Synthesis and characterization of peptides. Fluorescence microscopy of peptide fiber samples. Data analysis and interpretation of results. Writing of the manuscript.

Jana Fetzer: Synthesis, purification and characterization of peptides. Analysis of enzymatic conversion via HPLC. Characterization of secondary structure via CD spectroscopy. Preparation of samples for TEM, cryo-EM and NMR analysis. Data analysis and interpretation of results. Writing of the manuscript.

Patrick Roth: Dry-state TEM measurements for the analysis of peptide structure formation and interpretation of results.

Albin Lahu: Dry-state TEM measurements for the analysis of time-dependent structure formation and interpretation of results.

Jian Zhang: AFM measurements for the analysis of peptide structure formation and interpretation of results.

Manfred Wagner: Measurement and interpretation of variable temperature ^{1}H-NMR spectra.

Shutian Si, Ingo Lieberwirth, Katharina Landfester: Cryo-EM measurements and interpretation of results.

David Y. W. Ng: Discussion on the concept and results.

Tanja Weil: Acquiring funding for the project, design and discussion of the concept and results.

Abstract

The stimulus-induced creation of synthetic nanostructures within biological environments requires the precise chemical design of assembly precursors to program their in situ transformation and subsequent structure formation. By incorporating a bioresponsive moiety sensitive to a specific enzyme into the molecular design of the assembly precursor, greater specificity in subcellular localization and enhanced cell targeting can be achieved, based on the expression of the enzyme. Furin, a Golgi-associated endoprotease, is upregulated in many types of cancers, making it an interesting endogenous stimulus to target for bioresponsive assembly formation. Herein, we examine the furin-triggered enzymatic cleavage of a kinked isopeptide with the recognition sequence RVRR and its subsequent conversion into a self-assembling linear peptide, capable of forming fibrillar nanostructures. We analyze the enzymatic conversion of the kinked isopeptide assembly precursor over time to validate its responsiveness to furin and compare it to a non-cleavable control isopeptide with the scrambled sequence RRRV. The material properties of the linear fiber-forming peptide are characterized using circular dichroism spectroscopy, fluorescence and electron microscopy, as well as nuclear magnetic resonance spectroscopy. This study provides insights into the furin-induced transformation of a kinked isopeptide for the controlled formation of nanostructures and elucidates the specific material characteristics of the resulting self-assembling peptide, highlighting the potential for future biological applications.

5.1. Introduction

Over the past decade, significant research has been conducted on the formation of intracellular synthetic nanostructures via bioresponsive material transformation.[1-5] A major focus of this field has been on leveraging the intracellular assemblies to disrupt cellular processes, providing alternative strategies for cancer treatment.[6] From a perspective of bottom-up synthetic biology, there is also a compelling interest in the bioresponsive formation of artificial structures within cells that allows for controlled cell-material-interactions.

The biological impact of intracellular synthetic nanostructure formation is potentially influenced by three main factors: (1) the abundance of an endogenous stimulus that triggers nanostructure formation within the cell, (2) the kinetics of the intracellular conversion from assembly precursor to the self-assembling monomer and (3) the supramolecular characteristics of the resulting nanostructures. The first parameter represents an important variable, as many endogenous chemical and biological stimuli have been exploited to create intracellular nanostructures with significant differences in cellular outcomes.[5] Typically, chemical triggers that are abundant throughout the cell, such as the ubiquitous reducing agent glutathione,[7] cause immediate transformation of the assembly precursor upon cell entry, resulting in a high local concentration of the self-assembling molecule.[8,9]

Using naturally occurring enzymes to trigger bioresponsive transformation offers the advantage of achieving spatiotemporal control over the conversion that is dependent on the localized subcellular enzyme activity.[10] Following cellular uptake, an enzyme-responsive assembly precursor must first be transported to the subcellular compartment associated with the respective enzyme. This transport introduces a delay in the in situ formation of the self-assembling molecule, in

contrast to systems directly sensitive to pH changes during endocytosis[11,12] or to the intracellular redox environment.[8,13,14]

Furin is an endoprotease associated with the Golgi apparatus in eukaryotic cells.[15] The enzyme catalyzes the cleavage of substrates downstream of the polybasic recognition motif RX(R/K)R (Figure 5.1b).[15] This cleavage process is vital for the processing and activation of various proteins, including hormones and growth factors,[16] but it also plays a pivotal role in pathogenesis, including cancer progression[17] and viral infections like SARS-CoV-2.[18] As furin is frequently overexpressed in many cancers,[17] it represents an attractive target for triggering intracellular material transformation and assembly.[19-21] Furin-triggered in situ structure formation has previously been used for imaging of furin-overexpressing tumors, for instance via photoacoustic imaging[22], micro-positron emission tomography[23] or magnetic resonance imaging[20].

Another factor influencing the timeline of the intracellular structure formation is the kinetics of the intracellular conversion of the assembly precursor into the self-assembling monomer. While many systems for intracellular assembly rely on a single stimulus-induced cleavage step, a multistep conversion for in situ generation of the self-assembling molecule offers greater control over the entire reaction kinetics, as this can increase the options for tailoring the individual reaction steps to a specific chemical environment.[24] In our previous studies, we used kinked isopeptides featuring an oxidation-sensitive phenyl boronic acid group, which acts both as a stimulus-responsive element and as a point of attachment for a cell-penetrating peptide.[25-27] In the acidic environment of the endosome, the cell-penetrating peptide is removed. Once in the cytosol, hydrogen peroxide causes the removal of the redox-sensitive phenyl boronic acid group, triggering a rearrangement that linearizes the isopeptide, resulting in the formation of cytotoxic

peptide fibers within the cell.[25-27] An enzyme-induced approach to convert an isopeptide into a linear, self-assembling peptide would potentially offer better spatiotemporal control over assembly formation by leveraging intracellular gradients of furin activity. This strategy could not only enable more precise control of nanostructure formation but also restrict the assembly to cells that overexpress furin, thereby introducing cell specificity based on protein expression levels. Herein, we introduce a furin-responsive kinked isopeptide designed for the controlled formation of nanostructures via the enzyme-triggered multistep transformation into a self-assembling linear peptide (Figure 5.1a,c). The enzymatic cleavage and subsequent rearrangement of the kinked isopeptide into a linear peptide were monitored using time-dependent high-performance liquid chromatography (HPLC). To characterize the supramolecular and structural properties of the linear peptide monomer, we employed a range of techniques, including fluorescence microscopy, transmission electron microscopy (TEM), cryogenic transmission electron microscopy (cryo-TEM), circular dichroism (CD) and nuclear magnetic resonance (NMR) spectroscopy. Our findings highlight the potential of enzyme-responsive isopeptide-based systems for the controlled formation of peptide nanostructures.

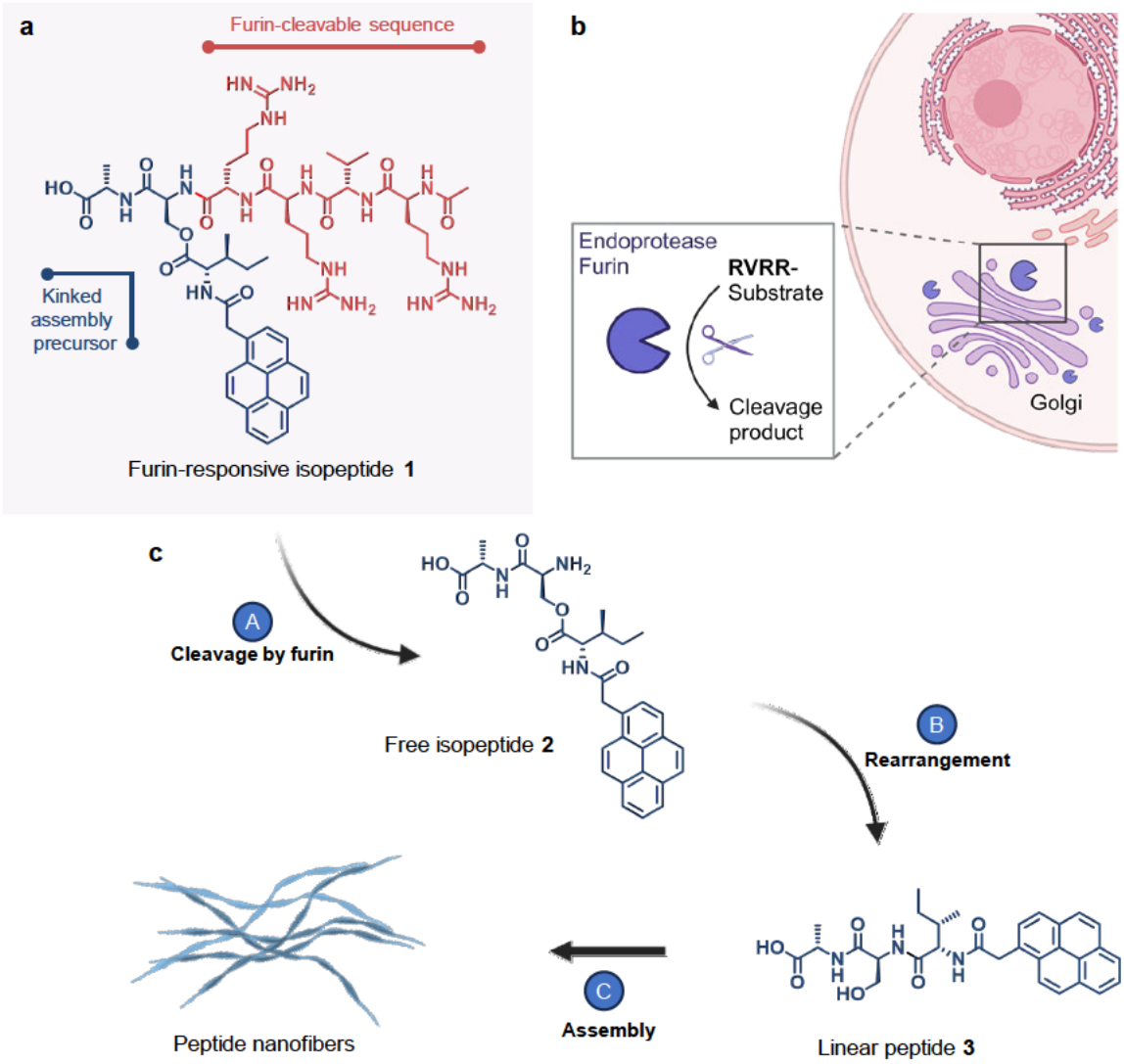

Figure 5.1 Chemical structure of furin-responsive isopeptide, subcellular localization of furin and enzyme-induced multistep reaction cascade. **a)** The furin-responsive kinked isopeptide **1** is composed of a pro-assembling *iso*-tripeptide with pyrene as fluorescent *N*-terminal substituent and the enzyme-cleavable sequence RVRR. **b)** Furin is a Golgi-associated endoprotease capable of cleaving downstream of its recognition sequence RVRR. **c)** The isopeptide assembly precursor **1** can be cleaved by furin (A), resulting in the rearrangement of the free isopeptide **2** (B). The linear peptide **3** can assemble into fibrillar nanostructures (C).

5.2. Results and discussion

5.2.1. Design, synthesis and transformation of isopeptides

The furin-responsive isopeptide **1** consists of three main structural components: (1) the furin-cleavable sequence RVRR, (2) a pro-assembling *iso*-tripeptide and (3) the pyrene moiety that is necessary for self-assembly and fluorescence (Figure 5.2a). Additionally, we prepared the non-cleavable isopeptide $\mathbf{1}_{scr}$ with a scrambled enzyme recognition sequence (RRRV) as a control compound (Figure 5.2b). The synthesis of these isopeptides was conducted via solid-phase-supported peptide synthesis (Scheme S5.1).

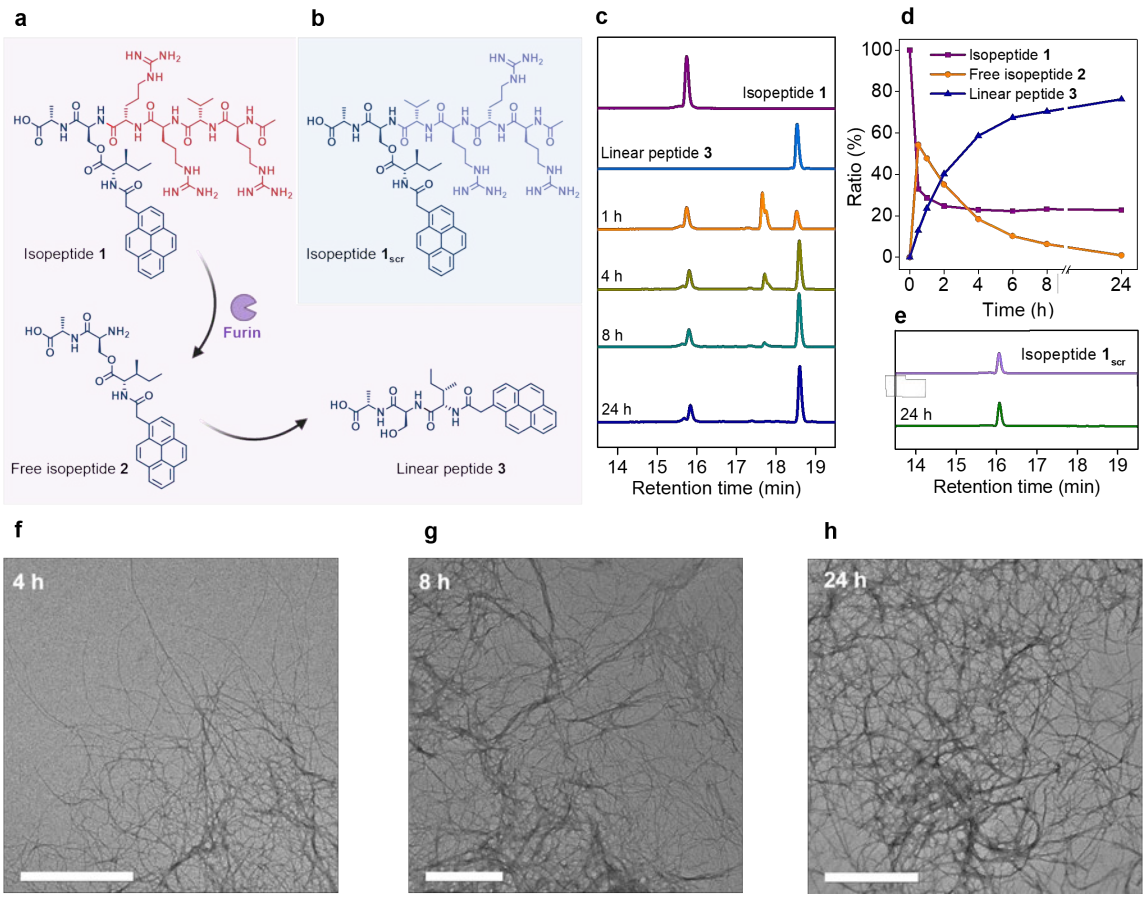

Figure 5.2 Analysis of furin-induced conversion of an enzyme-responsive isopeptide. a) Reaction scheme of furin-induced cleavage of isopeptide **1** downstream of the RVRR cleavage site resulting in free isopeptide **2** which subsequently undergoes a rearrangement via *O,N* acyl shift to form linear peptide **3**. b) Chemical structure of non-cleavable control isopeptide $\mathbf{1}_{scr}$ (RRRV). c) HPLC study of the kinetics of enzyme-induced conversion of isopeptide **1** (20 µM) in the presence of the protease furin (1 nmol/U) in buffered solution over time (HEPES (100 mM), $CaCl_2$ (1 mM), TCEP (1 mM)). d) Molar ratio of isopeptide **1**, free isopeptide **2** and linear peptide **3** over time based on the peak intensity at 340 nm.

e) HPLC study of the scrambled control isopeptide $\mathbf{1}_{scr}$ (20 µM) in the presence of furin in buffered solution. Due to the scrambled enzyme-recognition sequence (RRRV) no enzymatic cleavage was detected. f),g),h) Transmission electron micrographs of reaction solution of isopeptide **1** (200 µM) in the presence of furin (1 nmol/U) in buffered solution (HEPES (100 mM), $CaCl_2$ (1 mM), TCEP (1 mM)) after incubation for 4 h (f), 8 h (g) and 24 h (h) at 37 °C. Scale bars: 500 nm.

To investigate the furin-induced transformation of isopeptide **1**, we analyzed the kinetics of this multistep reaction cascade in the presence of commercial furin using HPLC. Isopeptide **1** was dissolved at a concentration of 20 µM in a buffer solution (HEPES (100 mM), $CaCl_2$ (1 mM), TCEP (1 mM)) containing the enzyme furin (1 nmol/U) and incubated at 37 °C. By analyzing the mixture at various time points, we observed a rapid degradation of isopeptide **1** (t_R = 15.74 min), with the signal for the linearized peptide **3** (t_R = 18.54 min) already appearing within the first hour. A peak with a retention time of 17.65 min was attributed to the intermediate free isopeptide **2**, which had undergone enzymatic cleavage but had not yet rearranged into linear peptide **3**. By 24 h, 76% of isopeptide **1** had transformed into the final product, the linear peptide **3**. The observation of less than 100% conversion could be attributed to the accumulation of formed fibers, which might sequester free isopeptide monomers, rendering the cleavage motifs inaccessible. . Additionally, the enzyme activity may decline over time. Analysis of the reaction solution at different time points via transmission electron microscopy (TEM) revealed the formation of fibrillar nanostructures already after 4 h of incubation (Figure 5.2f and Figure S5.11). After 8 h and 24 h of incubation, when the majority of isopeptide 1 is converted to the linear peptide 3 according to the HPLC kinetics analysis, bundled networks of peptide fibers were observed in the TEM analysis (Figure 5.2g,h and Figure S5.11). In contrast to the kinetics analysis of the degradation of isopeptide **1**, the control isopeptide $\mathbf{1}_{scr}$, which contains a scrambled version of the furin-recognition sequence (RRRV instead of RVRR), showed no furin-induced degradation over the 24-hour period (t_R = 16.07 min) (Figure 5.2e).

Overall, these results demonstrate that furin effectively cleaves downstream of the RVRR sequence even within the branched isopeptide **1**, despite the presence of an ester bond on the serine side chain connected to a bulky pyrene-modified isoleucine. This experiment provides proof of concept for the enzyme-triggered transformation of a kinked isopeptide into a linearized peptide, which can function as a supramolecular monomer for programmed structure formation. The combination of the kinetics analysis of the enzyme-induced conversion of isopeptide **1** into linear peptide **3** with the visualization of peptide structures formed by **3** via TEM supports the idea that the furin-induced conversion of a kinked assembly precursor can lead to in situ structure formation.

5.2.2. Analysis of peptide nanostructures

Next, the supramolecular behavior and structure formation of linear peptide **3** were studied using CD and NMR spectroscopy, as well as fluorescence and electron microscopy.

Temperature-dependent ^{1}H-NMR spectroscopy provided insights into the dynamic assembly of the linear peptide **3**. The spectrum measured at room temperature (298 K) revealed significant peak broadening, which is characteristic of supramolecular interactions between peptide monomers in aqueous solution (deuterated phosphate buffer (50 mM) and DMSO-d_6 (9:1)) (Figure 5.3a,c). Upon heating to 353 K, the appearance of sharp signals corresponding to the aromatic pyrene moiety and side chain groups suggested an increased amount of monomeric peptide **3** in solution at elevated temperatures.

CD spectroscopy gives information on the secondary structure and chirality of peptides. While the spectrum of the kinked isopeptide **1** displayed a single minimum at 201 nm indicative of an overall random coil structure, the CD spectrum of linear peptide **3** exhibited a more complex profile with a minimum at 191 nm and two

maxima at 206 nm and 233 nm (Figure 5.3b). The negative band at 191 nm can be attributed to the π→π* transition of peptide bonds within the backbone, while the strong positive band at 206 nm likely reflects π→π* transitions modulated by the *N*-terminal pyrene moiety. The positive signal at 233 nm is suggestive of the n→π* electronic transition associated with the aromatic pyrene group, underscoring its significant role in the overall conformation of the peptide. To determine the critical aggregation concentration of the linear peptide **3**, a fluorescence-based Proteostat aggregation assay was conducted. Solutions of the linear peptide **3** at varying concentrations were prepared in DPBS and DMSO (9:1) and incubated over 24 h, before adding the aggregation-sensitive Proteostat dye. Fluorescence measurements revealed a critical aggregation concentration of approximately 48 µM for the linear peptide **3** (Figure 5.3d).

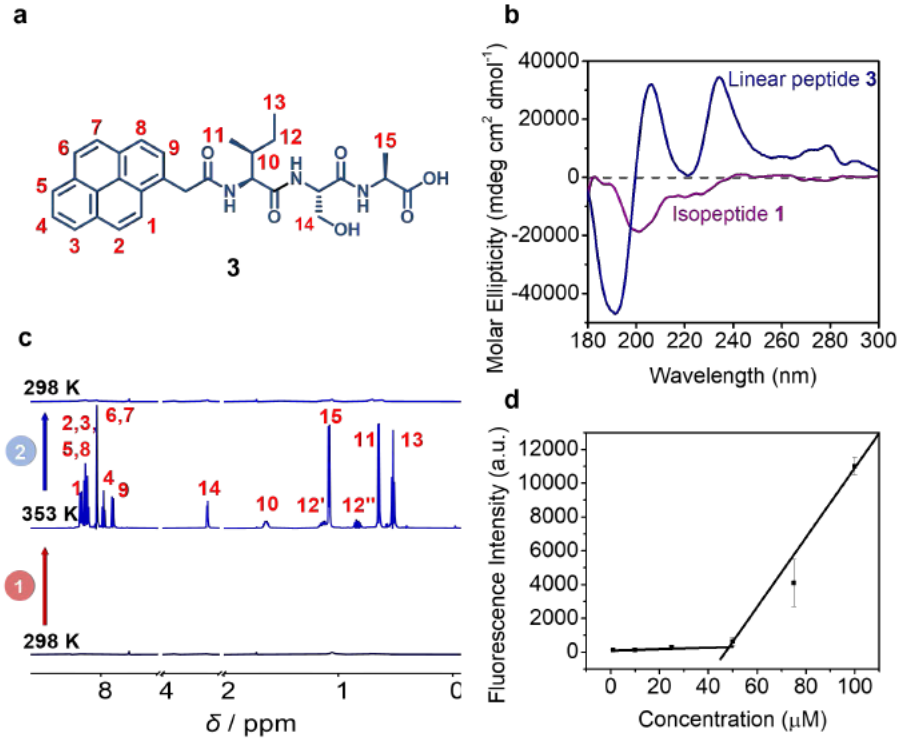

Figure 5.3 Supramolecular characterization of linear peptide **3**. a) Chemical structure of linear peptide **3** with labeled protons. b) Circular dichroism (CD) spectra of linear peptide 3 and kinkedisopeptide **1** (100 µM) in phosphate buffer (10 mM, pH 7.4). **c)** ^{1}H NMR analysis of the self-assembly behavior of linear peptide **3** (1 mg/mL) in deuterated phosphate buffer (50 mM) and DMSO-d_6 (9:1) at 298 K (bottom), after heating to 353 K (middle), and after cooling back to 298 K (top). **d)** Proteostat aggregation assay of linear peptide **3** in DPBS and DMSO (9:1). The critical aggregation concentration of linear peptide **3** was determined to be 48 µM by calculating the intersection of the linear fits.

Fluorescence microscopy of an aqueous solution of linear peptide **3** at 100 µM in phosphate buffer (pH 7.4) and DMSO (9:1) showed the spontaneous formation of thin fibers extending several micrometers in length (Figure 5.4a,b). Cryo-electron microscopy (cryo-EM) images confirmed the presence of elongated fibrillar nanostructures at both 500 µM and 100 µM peptide concentrations (Figure 5.4d). Transmission electron microscopy (TEM) in the dry state also visualized bundled fibrillar assemblies (Figure 5.4c). Atomic force microscopy (AFM) was used to further characterize the nanofibers, revealing a twisted morphology indicative of their structural configuration (Figure 5.4e and Figure S.5.14). The observed formation of peptide nanostructures via the assembly of linear peptide **3** is a critical prerequisite for their application in enzyme-induced peptide nanostructure formation within biological contexts.

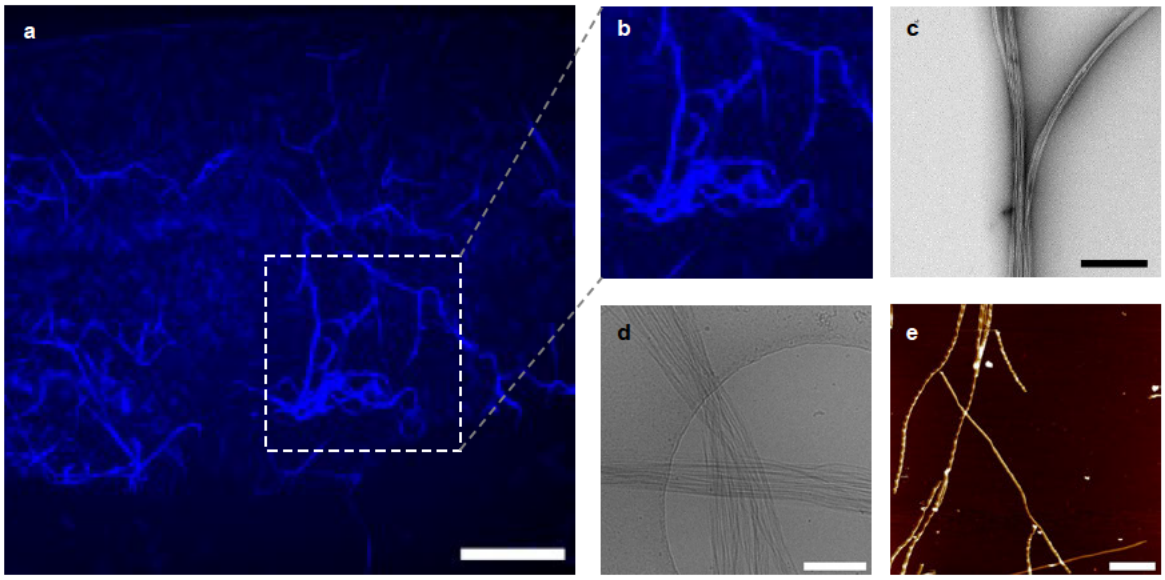

Figure 5.4. Characterization of nanofiber formation by linear peptide 3. a) Fluorescence microscopy image of linear peptide **3** (100 µM) in DPBS and DMSO (9:1). Scale bar: 50 µm. **b)** Enlarged view of the fluorescence microscopy image of linear peptide **3** (100 µM) in DPBS and DMSO (9:1). **c)** Dry-state TEM image showing nanofiber bundles formed by linear peptide **3** (100 µM) in DPBS (pH 7.4) and DMSO (9:1). Scale bar: 500 nm. **d)** Cryo-EM image of peptide nanofibers formed by linear peptide **3** (500 µM) in DPBS (pH 7.4) and DMSO (9:1). Scale bar: 250 nm. e) AFM image of peptide nanofibers formed by linear peptide **3** (100 µM) in DPBS (pH 7.4) and DMSO (9:1). Scale bar: 500 nm.

5.3. Conclusion and Outlook

This study demonstrates the successful synthesis and characterization of a furin-responsive kinked isopeptide designed for the enzyme-triggered transformation into a linear self-assembling peptide. We confirmed that furin efficiently catalyzes the conversion of the isopeptide into a linear peptide despite the kinked structure of the precursor molecule. The linear peptide resulting from the enzyme-induced transformation can assemble into elongated fibrillar nanostructures with a distinct twisted morphology, which was studied using various microcopy characterization techniques,. Leveraging proteolytic enzyme activity for the conversion of a kinked isopeptide to achieve controlled nanostructure formation offers significant potential for targeted biological applications. Therefore, future exploration should focus treating furin-overexpressing cells with the furin-responsive isopeptides to analyze the intracellular conversion and structure formation, as well as the impact on cellular function. Cell lines with low furin expression could be employed as a control or even co-cultured with furin-overexpressing cells to investigate potential cell-specific effects of the isopeptide.

Beyond the simple chemical design presented in the chapter, incorporating other fluorescent groups with superior optical properties and varying the peptide sequence could enable the generation of new nanomaterials with diverse fluorescent properties, different supramolecular characteristics and morphologies. Overall, enzyme-responsive isopeptides could offer a range of opportunities for both biological applications and further chemical design exploration.

References

1 Zheng, R. *et al.* Controllable Self-Assembly of Peptide-Cyanine Conjugates In Vivo as Fine-Tunable Theranostics. *Angew. Chem. Int. Ed.* **60**, 7809–7819 (2021).

2 Ye, D. *et al.* Bioorthogonal cyclization-mediated in situ self-assembly of small-molecule probes for imaging caspase activity in vivo. *Nat. Chem.* **6**, 519–526 (2014).

3 Hai, Z. & Liang, G. Intracellular Self-Assembly of Nanoprobes for Molecular Imaging. *Adv. Biosyst.* **2**, 1800108 (2018).

4 Qi, G.-B., Gao, Y.-J., Wang, L. & Wang, H. Self-Assembled Peptide-Based Nanomaterials for Biomedical Imaging and Therapy. *Adv. Mater.* **30**, 1703444 (2018).

5 Chagri, S., Ng, D. Y. W. & Weil, T. Designing bioresponsive nanomaterials for intracellular self-assembly. *Nat. Rev. Chem.* **6**, 320-338 (2022).

6 An, H.-W. *et al.* A tumour-selective cascade activatable self-detained system for drug delivery and cancer imaging. *Nat. Commun.* **10**, 4861 (2019).

7 Estrela, J. M., Ortega, A. & Obrador, E. Glutathione in Cancer Biology and Therapy. *Crit. Rev. Clin. Lab. Sci.* **43**, 143–181 (2006).

8 Guo, W.-W. *et al.* Intracellular Restructured Reduced Glutathione-Responsive Peptide Nanofibers for Synergetic Tumor Chemotherapy. *Biomacromolecules* **21**, 444–453 (2020).

9 An, H.-W. *et al.* Bio-orthogonally Deciphered Binary Nanoemitters for Tumor Diagnostics. *ACS Appl. Mater. Interfaces* **8**, 19202-19207 (2016).

10 Feng, Z., Wang, H. & Xu, B. Instructed Assembly of Peptides for Intracellular Enzyme Sequestration. *J. Am. Chem. Soc.* **140**, 16433–16437 (2018).

11 Waqas, M. *et al.* pH-Dependent In-Cell Self-Assembly of Peptide Inhibitors Increases the Anti-Prion Activity While Decreasing the Cytotoxicity. *Biomacromolecules* **18**, 943–950 (2017).

12 Li, M. *et al.* Proline Isomerization-Regulated Tumor Microenvironment-Adaptable Self-Assembly of Peptides for Enhanced Therapeutic Efficacy. *Nano Lett.* **19**, 7965–7976 (2019).

13 Cheng, D.-B. *et al.* Endogenous Reactive Oxygen Species-Triggered Morphology Transformation for Enhanced Cooperative Interaction with Mitochondria. *J. Am. Chem. Soc.* **141**, 7235–7239 (2019).

14 Du, W. *et al.* Increasing Photothermal Efficacy by Simultaneous Intra- and Intermolecular Fluorescence Quenching. *Adv. Funct. Mater.* **30**, 1908073 (2020).

15 Molloy, S. S., Bresnahan, P. A., Leppla, S. H., Klimpel, K. R. & Thomas, G. Human furin is a calcium-dependent serine endoprotease that recognizes the sequence Arg-X-X-Arg and efficiently cleaves anthrax toxin protective antigen. *J. Biol. Chem.* **267**, 16396–16402 (1992).

16 Dubois, C. M., Laprise, M.-H., Blanchette, F., Gentry, L. E. & Leduc, R. Processing of Transforming Growth Factor β1 Precursor by Human Furin Convertase *J. Biol. Chem.* **270**, 10618–10624 (1995).

17 Jaaks, P. & Bernasconi, M. The proprotein convertase furin in tumour progression. *Int. J. Cancer* **141**, 654–663 (2017).
18 Bestle, D. *et al.* TMPRSS2 and furin are both essential for proteolytic activation of SARS-CoV-2 in human airway cells. *Life Sci. Alliance* **3**, e202000786 (2020).
19 Yuan, Y. *et al.* Intracellular Self-Assembly of Taxol Nanoparticles for Overcoming Multidrug Resistance. *Angew. Chem. Int. Ed.* **54**, 9700–9704 (2015).
20 Yuan, Y. *et al.* Furin-mediated intracellular self-assembly of olsalazine nanoparticles for enhanced magnetic resonance imaging and tumour therapy. *Nat. Mater.* **18**, 1376–1383 (2019).
21 Chen, J. *et al.* Furin-Instructed Intracellular Gold Nanoparticle Aggregation for Tumor Photothermal Therapy. *Adv. Funct. Mater.* **30**, 2001566 (2020).
22 Dragulescu-Andrasi, A., Kothapalli, S.-R., Tikhomirov, G. A., Rao, J. & Gambhir, S. S. Activatable Oligomerizable Imaging Agents for Photoacoustic Imaging of Furin-Like Activity in Living Subjects. *J. Am. Chem. Soc.* **135**, 11015–11022 (2013).
23 Liu, Y. *et al.* Enzyme-Controlled Intracellular Self-Assembly of 18F Nanoparticles for Enhanced MicroPET Imaging of Tumor. *Theranostics* **5**, 1058 (2015).
24 Chen, Z., Chen, M., Zhou, K. & Rao, J. Pre-targeted Imaging of Protease Activity through In Situ Assembly of Nanoparticles. *Angew. Chem. Int. Ed.* **59**, 7864–7870 (2020).
25 Pieszka, M., Sobota, A. M., Gacanin, J., Weil, T. & Ng, D. Y. W. Orthogonally Stimulated Assembly/Disassembly of Depsipeptides by Rational Chemical Design. *Chembiochem* **20**, 1376-1381 (2019).
26 Ren, Y. *et al.* Supramolecular Assembly in Live Cells Mapped by Real-Time Phasor-Fluorescence Lifetime Imaging. *J. Am. Chem. Soc.* **146**, 11991–11999 (2024).
27 Zhou, Z. *et al.* In Situ Assembly of Platinum(II)-Metallopeptide Nanostructures Disrupts Energy Homeostasis and Cellular Metabolism. *J. Am. Chem. Soc.* **144**, 12219–12228 (2022).

Supplementary Information

1. General Information

1.1. Materials

Reagents and solvents were purchased from commercial sources and were used without further purification. Peptide synthesis grade reagents were used for synthesizing the peptides. HPLC was performed using acetonitrile (CH_3CN) in HPLC grade (containing 0.1% trifluoroacetic acid (TFA)) and water for HPLC (containing 0.1% TFA) and reactions was obtained from a Millipore purification system. Flash column chromatography was carried out using Macherey-Nagel silica gel 0.04–0.063 mm. Furin (2,000 units/mL) was purchased from *New England Biolabs*.

1.2. Instruments

1.2.1. Microwave Peptide Synthesizer

Linear peptides were synthesized in a Liberty Blue Automated Microwave Peptide Synthesizer by CEM Corporation.

1.2.2. High-Performance Liquid Chromatography (HPLC)

The peptides were purified by preparative HPLC using a setup by Shimadzu. For purification either a Zorbax Eclipse XDB-C18 HPLC column (9.4 × 250 mm, 5 μm) was used at a flowrate of 4 ml/min or a Phenomenex Gemini 5 μm NX-C18 110 Å 150 × 30 mm was used at a flowrate of 25 ml/min. For analytical measurements a Waters Atlantis T3, C18 column (5 μm, 100 Å, 4.6 x 100 mm) was used.

1.2.3. Liquid Chromatography-Mass Spectrometry (LC-MS)

Compounds were analyzed by HPLC-ESI-MS on a LC-MS 2020 by Shimadzu using a Kinetex 2.6 μm EVO C18 100 Å LC 50 × 2.1 mm column. MilliQ water acidified

with 0.1% formic acid and CH_3CN were used as solvents for all measurements. The solvent gradient started with 5% CH_3CN and 95% water. This solvent ratio was kept constant for 2 min, then the CH_3CN content was linearly increased to 95% in 14 min. Data were processed in *LabSolutions* and *OriginPro 9*.

1.2.4. Matrix-Assisted Laser Desorption/Ionisation-Time of Flight Mass Spectrometry (MALDI-TOF)

All MALDI-TOF spectra were recorded on either a rapifleX MALDI-TOF/TOF from Bruker or MALDI Synapt G2-SI from Waters. Samples were mixed with a saturated solution of the matrix S7 α-cyano-4-hydroxycinnamic acid (CHCA) in H_2O/CH_3CN 1/1 + 0.1% TFA. Data processing was performed in *mMass* and *OriginPro 9*.

1.2.5. Nuclear Magnetic Resonance Spectroscopy (NMR)

NMR spectra of small molecules and peptides were recorded on a Bruker Avance 400 MHz spectrometer and an Avance III 850 MHz spectrometer. The solvent signal was used as a reference (deuterated chloroform $CDCl_3$ δ =7.26 ppm for ^1H, 77.16 ppm for ^{13}C, D_2O 4.65 ppm and for DMSO-d_6 2.50 ppm and 39.52 ppm respectively). The data was processed in *MestReNova*.

1.2.6. Circular Dichroism Spectroscopy (CD)

CD spectra were recorded on a JASCO J-1500 spectrometer in a 0.1 cm High Precision Cell by *HellmaAnalytics*. The recorded data was processed in Spectra Analysis by *JASCO* and *OriginPro9*.

1.2.7. Transmission Electron Microscopy (TEM)

TEM images of the peptide samples were recorded on a JEOL 1400 transmission electron microscope at a voltage of 120 kV. Formvar/carbon-film coated copper grids (300 mesh) by Plano GmbH were used to prepare the samples. The images were processed in *Fiji ImageJ*.

1.2.8. Cryogenic Transmission Electron Microscopy (cryo-TEM)

For cryo-TEM examination the samples were vitrified using a Vitrobot Mark V (Thermo Fisher, Hilsboro Oregon) plunging device. 3 µl of the sample dispersion was applied to a Quantifoil® R 1.2/1.3 300 Mesh, Cu, that has been glow discharged in an oxygen plasma cleaner (Diener Nano®, Diener electronic, Germany) shortly before. After removing excess sample solution with a filter paper, the grid is immediately plunged into liquid ethane. For the subsequent examination, the specimen is transferred to a TEM (FEI Titan Krios G4) keeping cryogenic conditions. Conventional TEM imaging was done using an acceleration voltage of 300 kV. Micrographs were acquired with a 4k Direct Electron Detection Camera (Gatan K3) under low dose conditions.

1.2.9. Fluorescence Microscopy

Fluorescence images of peptide nanostructures were taken using a Keyence BZ-X810 fluorescence microscope using a 20x LD PH lens and a DAPI filter: Ex.: 360/40 nm, Em.: 460/50 nm.

1.2.10. Atomic Force Microscopy (AFM)

40 µL of a [100 µM] Py-ISA peptide solution was dropped on a freshly peeled mica. After waiting for 10 min at room temperature to adsorb, additional 260 µL PBS containing 10 % DMSO was added gently. Peptide samples were imaged by using an AFM Instrument (Dimension Fast Scan Bio, Bruker Corporation, Inc.) in liquid tapping mode with Fastscan D tips. The scan rates were between 1 and 3 Hz. Obtained images were further analyzed by using *Nanoscope Analysis 1.9* software.

2. Synthesis

2.1. Synthesis of isopeptides

2.1.1. Synthesis of isopeptides with RVRR or RRRV sequence

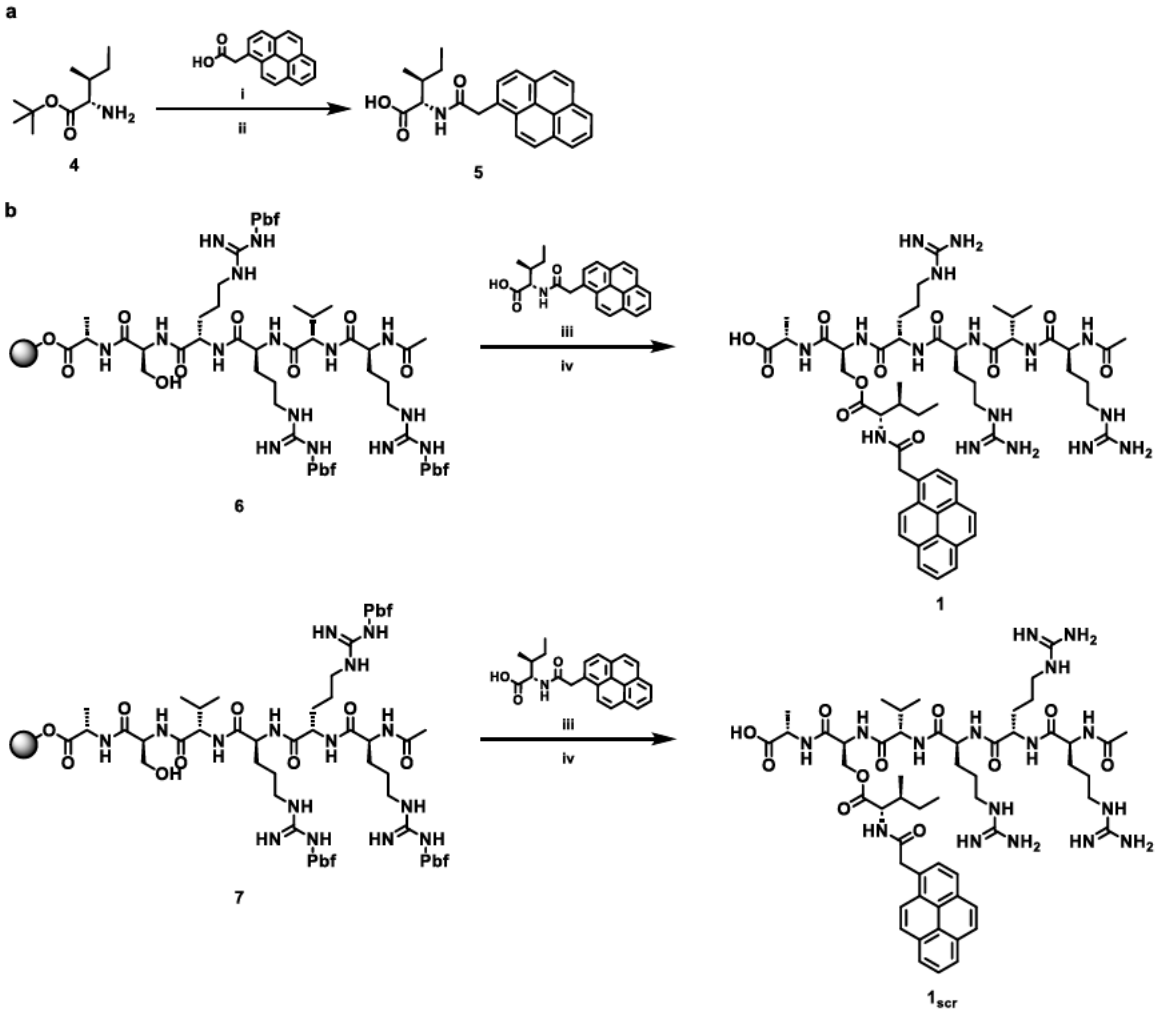

Scheme S5.1 a) Synthesis of pyrene-modified isoleucine: i) PyBOP, DIPEA, DCM, 3 h, RT; ii) TFA:DCM (1:1), 4 h, RT. b) Synthesis of isopeptides with RVVR and RRRV sequences: iii) DIC, DMAP, DCM, overnight, RT; iv) TFA, TIPS, H_2O (95:2.5:2.5), 2.5 h, RT.

2.1.1.1. Synthesis of pyrene-modified isoleucine (Py-Ile) 5

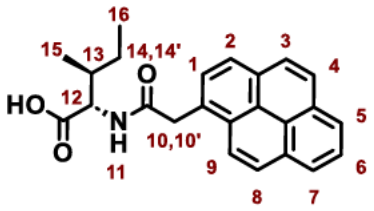

5

1-Pyreneacetic acid (130.15 mg, 0.50 mmol, 1.0 eq.) was dissolved in dry DMF (5 mL), then DIPEA (0.50 mL, 3.00 mmol, 6.0 eq.) was added. Subsequently, PyBOP (520.4 mg, 1.00 mmol, 2.0 eq.) and *tert*-butyl-protected isoleucine hydrochloride (111.87 mg, 0.50 mmol, 1.0 eq.) were dissolved in dry DMF (5 mL) and added to solved 1-pyreneacetic acid. The reaction mixture was stirred at room temperature for 3 h before the solvent was removed under reduced pressure. The crude product was purified via column chromatography (CH/EA, 2:1) yielding *tert*-butyl-protected Py-Ile as a colorless solid (191.5 mg, 0.44 mmol, 89%). Last, the protecting group was removed by adding a mixture of DCM/TFA (10 mL, 1:1). After stirring at room temperature for 3 h the solvent was removed under reduced pressure and the product **5** was used for further synthesis.

^{1}H NMR (400 MHz, DMSO-d_6) δ/ppm = 8.53 (d, J = 8.5 Hz, 1H, H-11), 8.43 (d, J = 9.2 Hz, 1H, H-aromat), 8.28 (ddd, J = 7.8, 4.8, 1.2 Hz, 2H, H-aromat), 8.26 – 8.17 (m, 2H, H-aromat), 8.15 (s, 2H, H-aromat), 8.10 – 8.01 (m, 2H, H-aromat), 4.35 (d, J = 14.7 Hz, 1H, H-10), 4.30 – 4.18 (m, 2H, H-10', H-12), 1.96 – 1.73 (m, 1H, H-13), 1.55 – 1.40 (m, 1H, H-14), 1.34 – 1.17 (m, 1H, H-14'), 0.88 – 0.83 (m, 6H, H-15, H-16).

^{13}C NMR (101 MHz, DMSO-d_6) δ/ppm = 173.13, 170.40, 131.20, 130.84, 130.38, 129.70, 128.95, 128.71, 127.42, 127.10, 126.83, 126.20, 125.09, 124.93, 124.72, 124.16, 124.10, 123.94, 56.39, 36.49, 24.74, 15.68, 11.29.

ESI m/z: $[M+H]^+$ 374.2 (calc. 374.2), $[2M+H]^+$ 747.5 (calc. 747.3).

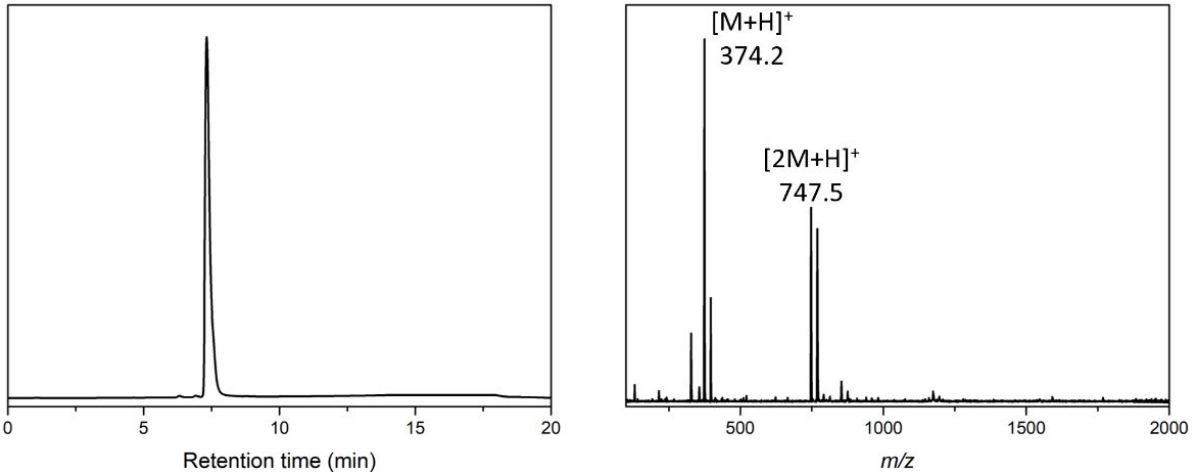

Figure S5.1 LC-MS data of Py-Ile. Left LC trace (254 nm) with $t_R = 7.33$ min. Right Convoluted ESI-MS spectrum.

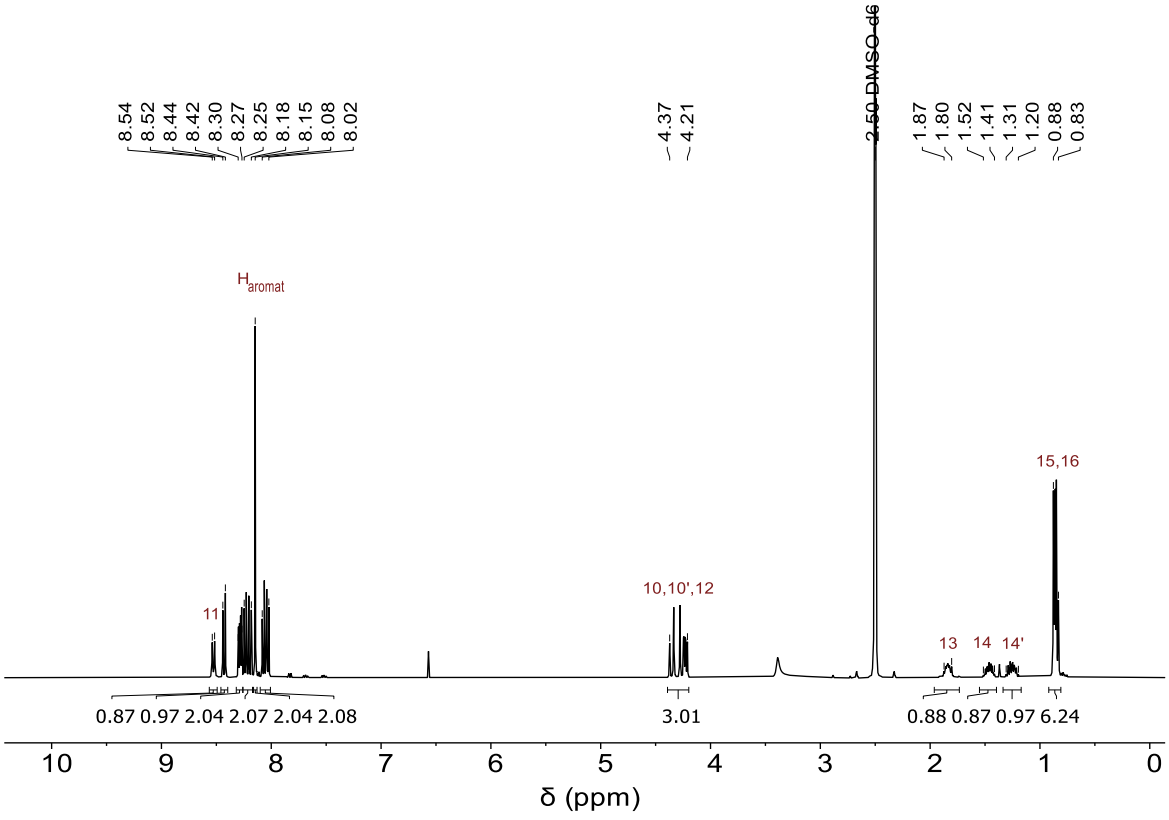

Figure S5.2 ^{1}H NMR spectrum (400 MHz, DMSO-d_6, 298 K) of Py-Ile 5.

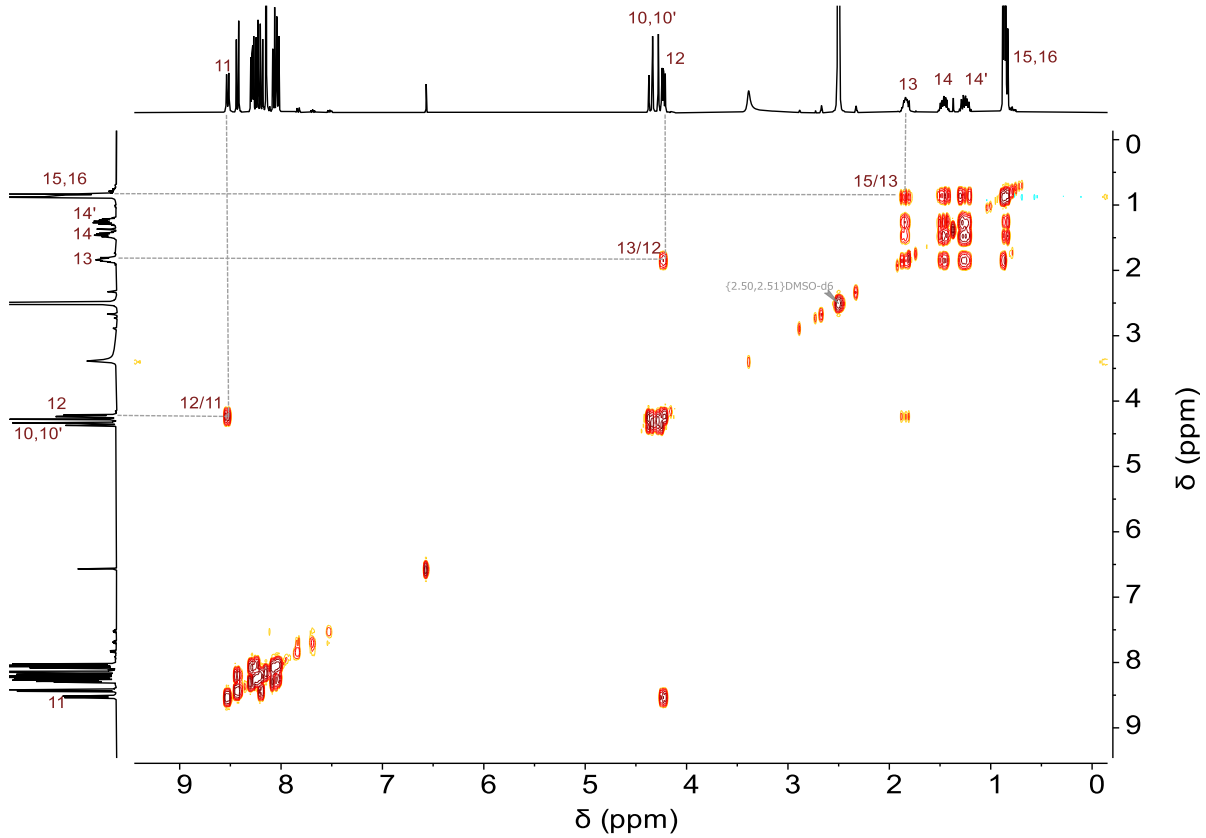

Figure S5.3 ^{1}H,^{1}H COSY NMR spectrum (400 MHz, DMSO-d$_6$, 298 K) of Py-Ile 5.

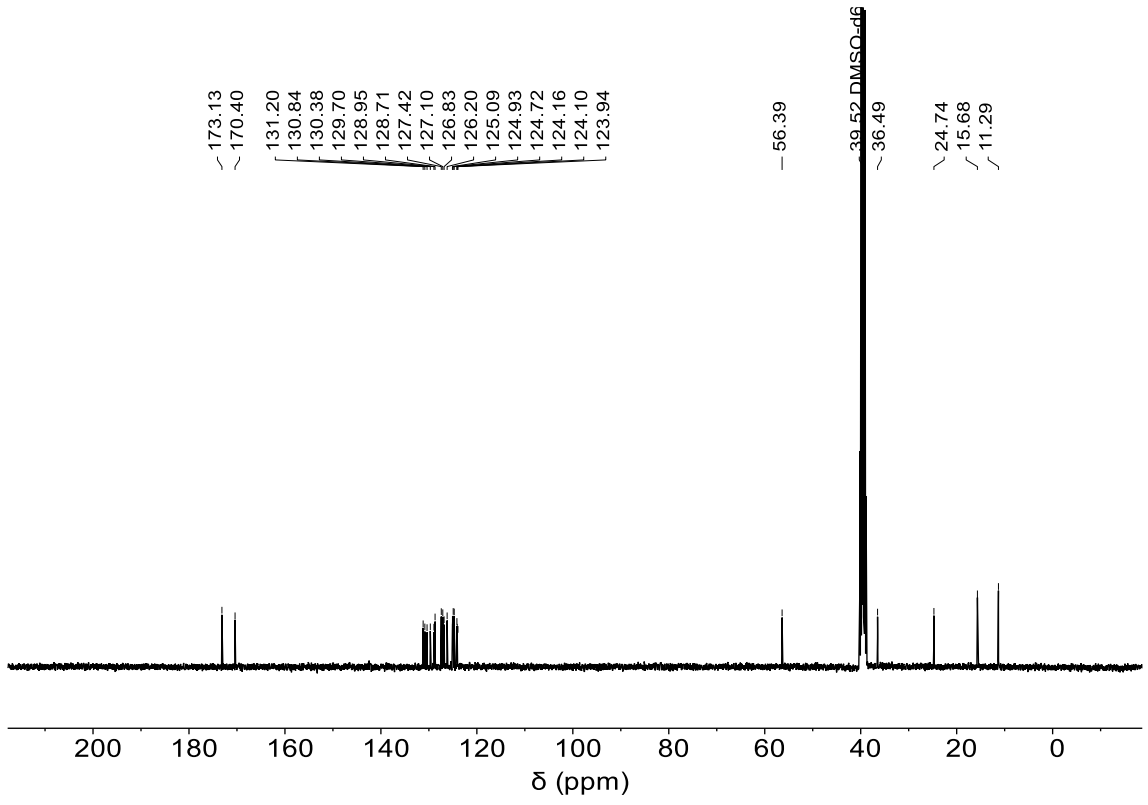

Figure S5.4 ^{13}C NMR spectrum (101 MHz, DMSO-d$_6$, 298 K) of Py-Ile 5.

2.1.2. Solid phase supported synthesis of isopeptides

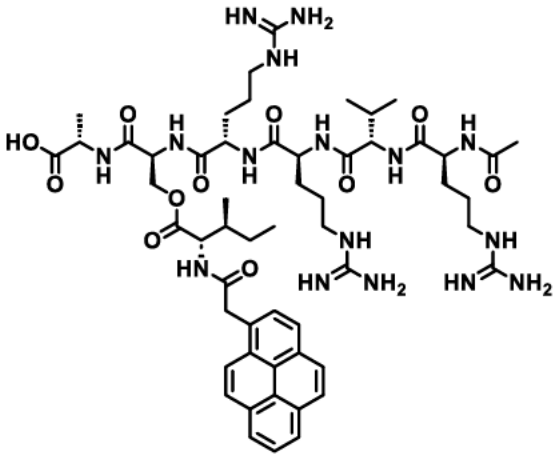

1

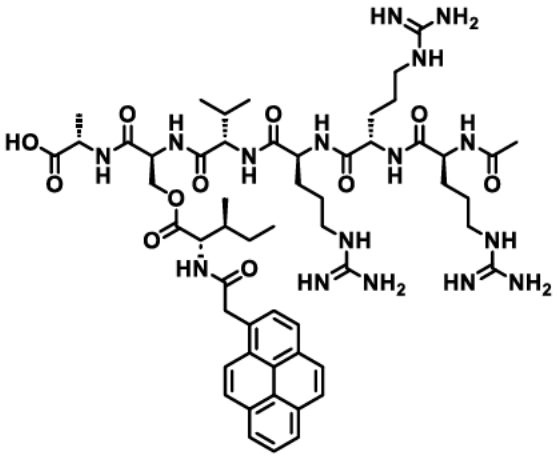

1_{scr}

The peptides were synthesized using a microwave assisted solid-phase peptide synthesizer. The Wang resin preloaded with Fmoc-Ala (0.705 g, 0.5 mmol) was covered and swollen in DMF for 1 h. Before every coupling step, the *N*-terminal Fmoc group was cleaved by two deprotection steps using 20% piperidine in DMF (3 ml) for 15 s and 50 s at 75 °C and 90 °C, respectively. Fmoc-Ser(OH), Fmoc-Arg(Pbf) (2x), Fmoc-Val and Ac-Arg(Pbf) (5 eq. in 1.25 ml) were coupled for 15 s and 110 s at 75 °C and 90 °C respectively using DIC (0.5 M) and Oxyma (1 M) in a total of 2.75 ml DMF. For Fmoc-Arg(Pbf) and Ac-Arg(Pbf) the coupling steps were performed as double couplings with additional washing steps. The resin was removed from the reaction vessel and washed with DMF and DCM. Before the next coupling step the resin was halved.

Py-Ile (102.70 mg, 0.275 mmol, 1.1 eq.) and DMAP (30.54 mg, 0.25 mmol, 1.0 eq.) were dissolved in dry DCM (5 mL), then DIC (0.16 mL, 1.00 mmol, 4 eq.) was added to the solution. Dry DCM (3 mL) was added to the resin (0.25 mmol) loaded with Ac-RVRRSA and the previously prepared Py-Ile solution was added dropwise. The resin was shaken over night at room temperature. The peptide sequence was cleaved from the resin by adding a mixture of TFA (4.75 mL, 95 %), TIPS (0.125 mL, 2.5 %) and H2O (0.125 mL, 2.5 %) and shaken for 2.5 h at room

temperature. The cleavage cocktail was drained and the resin washed with TFA. The peptide was precipitated in ice-cold Et_2O. After centrifugation for 20 minutes at 4k rpm the supernatant was removed and the crude product was dissolved in water and ACN and purified via HPLC (10 % to 100 % ACN in 20 min). After lyophilisation the product was received as a beige solid (9.4 mg, 8.23 µmol, 3 %).

MALDI-TOF m/z: $[M+H]^+$ 1141.4 (calc. 1141.63) (Isopeptide **1**) and $[M+H]^+$ 1141.6 (calc. 1141.63) (Isopeptide $\mathbf{1}_{scr}$)

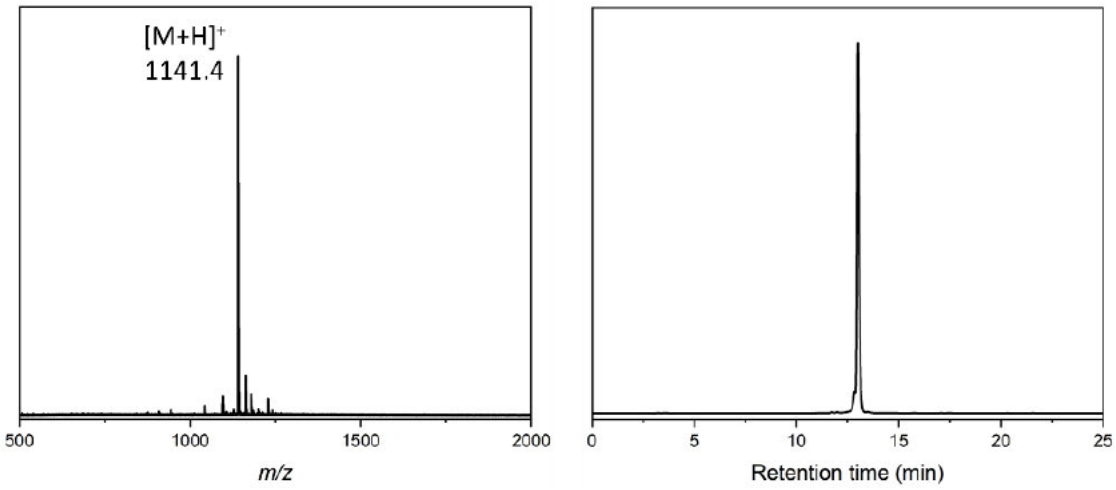

Figure S5.5 MALDI-TOF spectrum (left) and HPLC trace (right, 340 nm) of Isopeptide 1 with $t_R = 13.0$ min.

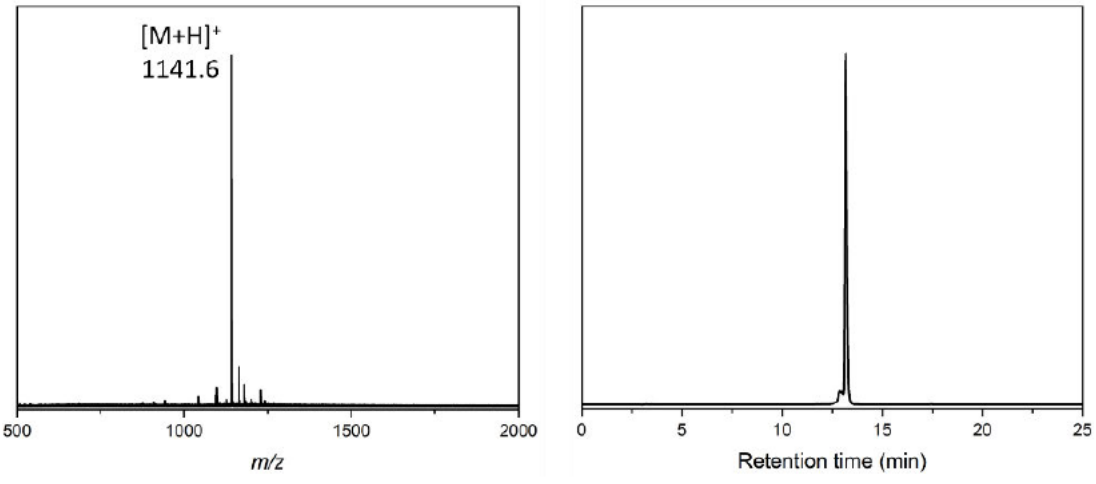

Figure S5.6 MALDI-TOF spectrum (left) and HPLC trace (right, 340 nm) of Isopeptide $\mathbf{1}_{scr}$ with $t_R = 13.2$ min.

2.2. Synthesis of linear Py-ISA 3

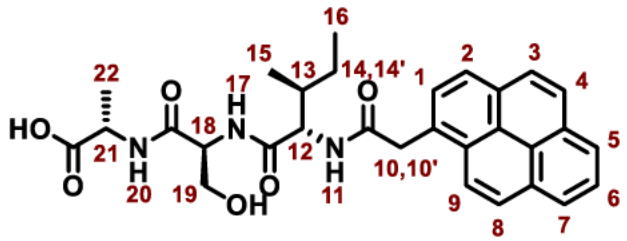

3

The peptide was synthesized using a microwave assisted solid-phase peptide synthesizer. The Wang resin preloaded with Fmoc-Ala (0.705 g, 0.5 mmol) was covered and swollen in DMF for 1 h. Before every coupling step and as the final deprotection, the *N*-terminal Fmoc group was cleaved by two deprotection steps using 20% piperidine in DMF (3 ml) for 15 s and 50 s at 75 °C and 90 °C, respectively. Fmoc-Ser(OH) and Fmoc-Ile (5 eq. in 1.25 ml) were coupled for 15 s and 110 s at 75 °C and 90 °C respectively using DIC (0.5 M) and Oxyma (1 M) in a total of 2.75 ml DMF. The resin was removed from the reaction vessel and washed with DMF and DCM.

1-Pyreneacetic acid (156.17 mg, 0.600 mmol, 1.2 eq.) and PyBOP (520.4 mg, 1.00 mmol, 2.0 eq.) were dissolved in dry DMF (5 mL) and DIPEA (0.35 mL, 2.00 mmol, 4 eq.) was added to the solution. To the ISA-loaded resin (0.50 mmol) dry DMF (3 mL) was added and the previously prepared 1-pyreneacetic acid-containing solution was added dropwise. The resin was shaken for 2.5 h at room temperature. The solution was drained and the resin was subsequently washed with DMF and DCM. The peptide sequence was cleaved from the resin by adding a mixture of TFA (4.75 mL, 95 %), TIPS (0.125 mL, 2.5%) and H_2O (0.125 mL, 2.5 %) and shaken for 2.5 h at room temperature. The cleavage cocktail was drained and the resin washed with TFA. The peptide was precipitated in ice-cold Et_2O. After centrifugation for 20 minutes at 4k rpm the supernatant was removed and the crude product was dissolved in water and ACN and purified via HPLC (10 % to

100 % ACN in 20 min). After lyophilization the product was received as a colorless solid (26 mg, 48.9 µmol, 10 %).

^{1}H-NMR, COSY (850 MHz, DMSO) δ/ppm = 8.41 (d, J = 9.15 Hz, 1H, H-9), 8.39 (d, J = 8.93 Hz, 1H, H-11), 8.28 (t, J = 7.28 Hz, 2H, H-29, H-5), 8.24 (d, J = 7.71 Hz, 1H, H-2), 8.20 (d, **J** = 9.17 Hz, 1H, H-8), 8.15 (s, 2H, H-34, H-3), 8.07 (d, J = 7.51 Hz, 1H, H-6), 8.05 (t, J = 8.50 Hz, 1H, H-17), 8.02 (d, J = 7.73 Hz, 1H, H-1), 7.95 (m, 1H, H-19), 4.37 (d, J = 15.00 Hz, 1H, H-10), 4.33 (q, J = 6.42 Hz, 1H, H-18), 4.27 (dd, J = 7.20 Hz, 8.95 Hz, 1H, H-12), 4.23 (d, J = 15.00 Hz, 1H, H-10'), 4.18 (m, 1H, H-21), 3.57 (m, 2H, H-19), 1.78 (m, 1H, H-13), 1.46 (m, 1H, H-14), 1.21 (d, J = 7.29 Hz, 3H, H-22), 1.12 (m, 1H, H-14'), 0.84 (d, J = 6.83 Hz, 3H, H-15), 0.78 (t, J = 7.43 Hz, 3H, H-16).

ESI m/z: $[M+H]^+$ 532.2 (calc. 532.2), $[2M+H]^+$ 1063.4 (calc. 1063.5).

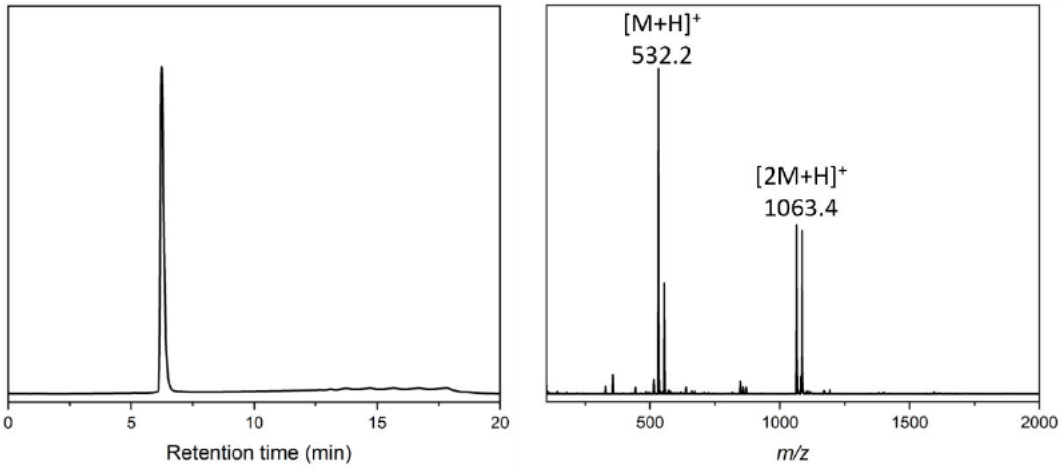

Figure S5.7 LC-MS data of linear Py-ISA 3. Left LC trace (254 nm) with t_R = 6.27 min. Right Convoluted ESI-MS spectrum.

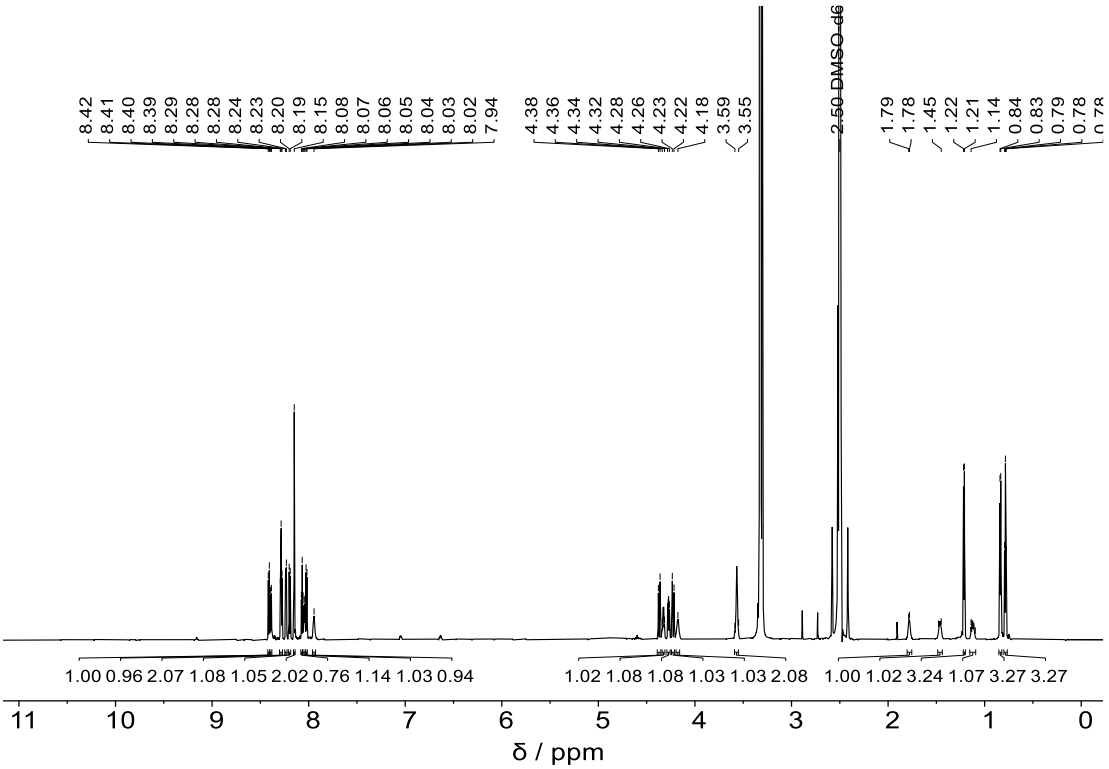

Figure S5.8 ^{1}H NMR spectrum (850 MHz, DMSO-d_6, 298 K) of linear Py-ISA 3.

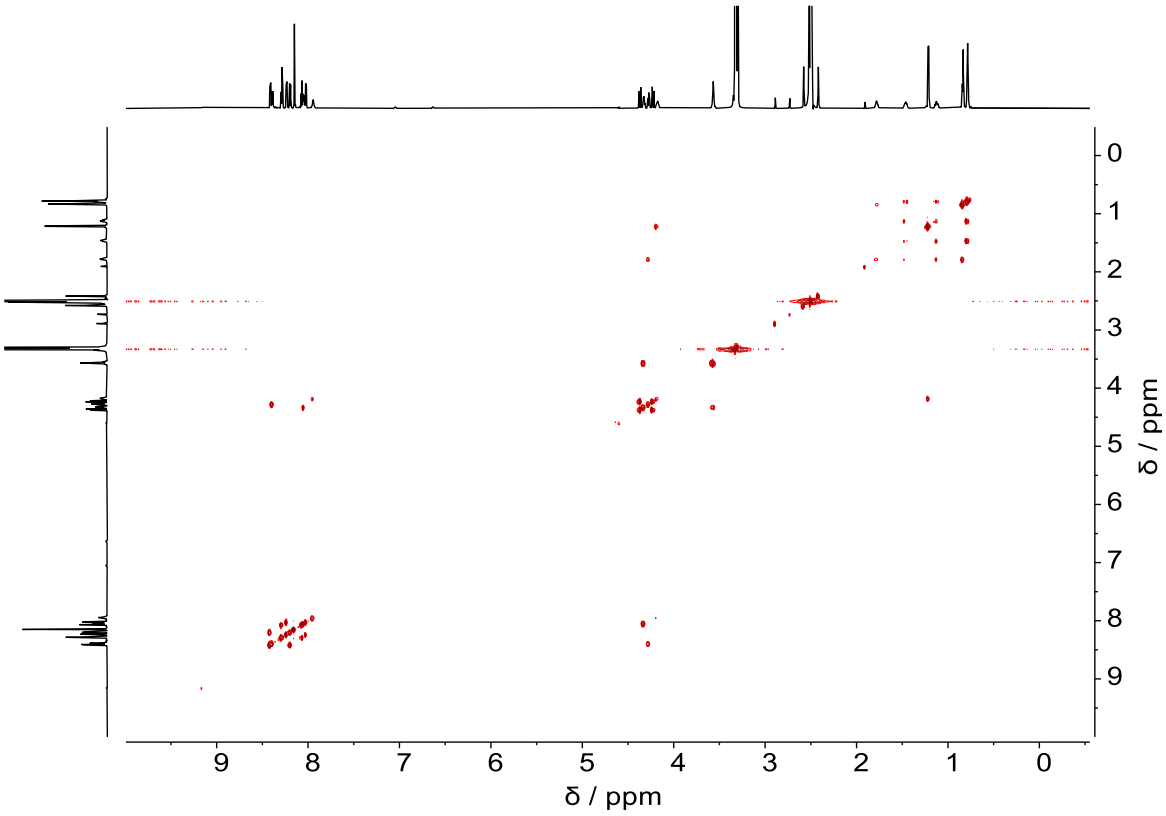

Figure S5.9 ^{1}H,^{1}H COSY NMR spectrum (850 MHz, DMSO-d6, 298 K) of linear Py-ISA 3.

3. Furin-Induced Transformation of Isopeptides

3.1. General procedure of HPLC kinetic analysis

The furin-induced conversion of the isopeptide **1** and $\mathbf{1}_{scr}$ was analyzed via an analytical HPLC kinetic study. The samples were prepared by adding the enzyme (1 nmol/U) to the isopeptide **1** (20 μM) in a buffered aqueous solution containing HEPES (100 mM), TCEP (1 mM) and $CaCl_2$ (1 mM). The pH of the buffer was adjusted to 7.4 using 1M NaOH. The control sample was prepared by dissolving the isopeptide $\mathbf{1}_{scr}$ in the same buffered aqueous solution. Samples were measured after 0.5 h, 1 h, 2 h, 4 h, 6 h, 8 h and 24 h by mixing 50 μL of the sample with 50 μL of methanol. After centrifugation of 5 minutes at 12,000 rpm, 50 μL of the supernatant was injected into the analytical HPLC to monitor the conversion process.

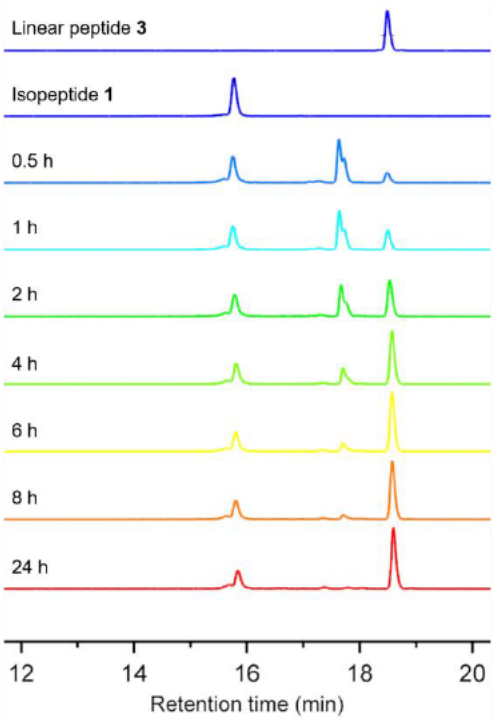

Figure S5.10 HPLC study of the kinetics of enzyme-induced conversion of isopeptide 1 (20 μM) in the presence of the protease furin in buffered solution over time (HEPES (100 mM), $CaCl_2$ (1 mM), TCEP (1 mM)).

3.2 General procedure of TEM kinetic analysis

The furin-induced structure formation of isopeptide **1** was analyzed via TEM kinetic study. The samples were prepared by adding the enzyme (1 nmol/U) to the isopeptide **1** (200 μM) in a buffered aqueous solution containing HEPES (100 mM), TCEP (1 mM) and $CaCl_2$ (1 mM). The pH of the buffer was adjusted to 7.4 using 1 M NaOH. TEM grids were prepared after 0.5 h, 1h, 2h, 4h, 6h, 8h and 24h by adding 3 μL by pipetting 3 μL of the solution onto a Formvar-coated copper grid and incubating for 5 min. After the incubation, the solutions were removed with filter paper, and the grids were stained with 10 μL 4% uranyl acetate solution for 2.5 min. The grids were washed three times with MilliQ water and dried before being measured.

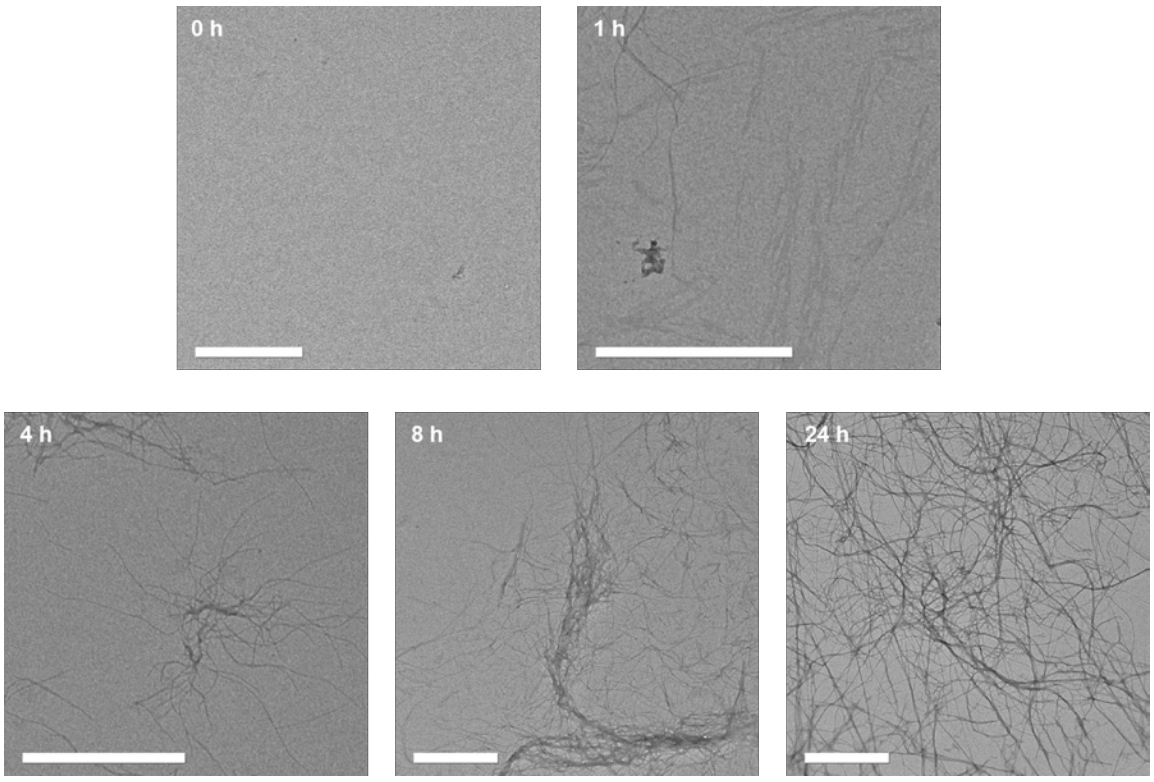

Figure S5.11 Dry-state TEM images of reaction solution of isopeptide **1** (200 μM) in the presence of furin in buffered solution (HEPES (100 mM), $CaCl_2$ (1 mM), TCEP (1 mM)) after incubation for 0 h, 1 h, 4 h, 24 h at 37 °C. Scale bars 500 nm.

4. Analysis of Secondary Structure and Self-Assembly Behavior

4.1. Temperature-dependent ^{1}H-NMR analysis of linear Py-ISA 3

For the temperature-dependent NMR analysis a solution of the linear peptide **3** was prepared containing 0.23 mg peptide in 0.5 ml deuterated solvent. The deuterated solvent consisted of a 9:1-mixture of phosphate buffer (50 mM) prepared from D_2O and DMSO-d_6. The sample was then immediately analyzed via ^{1}H-NMR spectroscopy at 298 K and the temperature was increased in 5 °C steps to 353 K. At each temperature the sample was equilibrated for 20 min before the measurement.

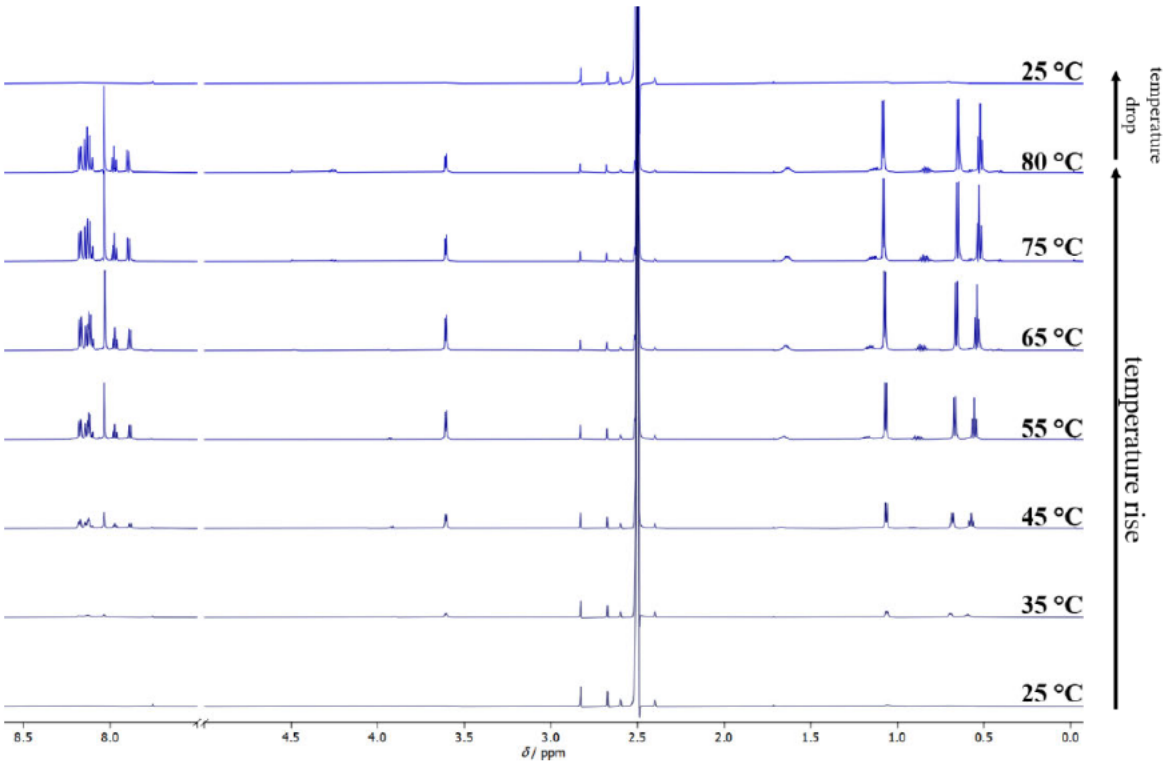

Figure S5.12 Temperature-dependent ^{1}H-NMR analysis of linear Py-ISA 3 in phosphate buffer (50 mM) prepared from D_2O and DMSO-d_6 (9:1).

4.2. CD spectra of Py-ISA 3 and kinked assembly precursor 1

The linear peptide **3** or the kinked assembly precursor **1** were dissolved in phosphate buffer (10 mM, pH 7.4) to yield a peptide concentration of 100 µM. The solutions were sonicated to dissolve the peptides completely. The samples were subsequently

measured, and the spectra were recorded at wavelengths from 380 to 180 nm with a bandwidth of 1 nm, data pitch of 0.2 nm, and scanning speed of 5 nm/min. The spectra were measured three times and accumulated.

4.3. TEM analysis of linear Py-ISA 3 and kinked assembly precursor 1

The linear peptide **3** or the isopeptides **1** and $\mathbf{1}_{scr}$ were dissolved in DMSO (1 mM) and diluted with DPBS at a ratio of 1:9 to yield a 100 µM peptide solution. The solution was incubated for 24 h and TEM grids were prepared by pipetting 3 µL of the solution onto a Formvar-coated copper grid and incubated for 5 min. After the incubation, the solutions were removed with filter paper, and the grids were stained with 10 µL 4% uranyl acetate solution for 2.5 min. The grids were washed three times with MilliQ water and dried before being measured.

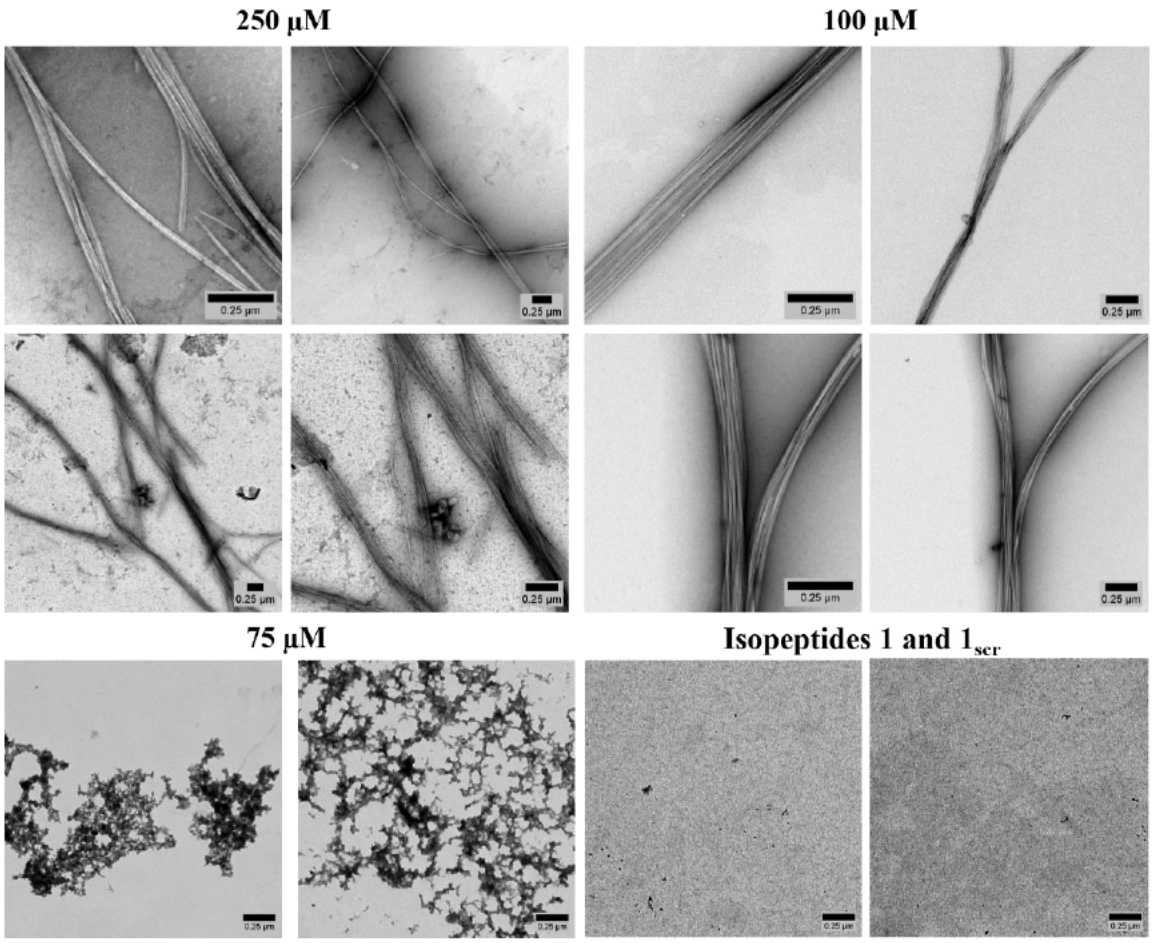

Figure S5.13 Dry-state TEM images showing nanofiber bundles and aggregates formed by linear peptide 3 (250 µM, 100 µM, 75 µM) in DPBS (pH 7.4) and DMSO (9:1) and dry-state TEM images of Isopeptides 1 and 1_{scr} showing the absence of aggregate or structure formation. Scale bar: 250 nm.

4.5. Cryo-TEM analysis of linear peptide 3

The linear peptide **3** was dissolved in DMSO (1 mM) and diluted with DPBS at a ratio of 1:9 to yield a 100 µM peptide solution. The solution was incubated for 24 h before 3 µL of the sample was used for further sample preparation as described in 1.2.8.

4.6. Proteostat aggregation assay

For the analysis of the critical aggregation concentration of the linear peptide **3** the commercial Proteostat protein aggregation assay kit by *Enzo Life Sciences, Inc.* was used. The peptide samples were prepared by diluting DMSO stock solutions of

the linear peptide **3** in various concentrations (1 µM to 100 µM) with DPBS in a 1:9 ratio. The resulting peptide samples were incubated for 24 h at room temperature while shaking. The Proteostat working solution was prepared by mixing 0.52 µl of the Proteostat stock solution with 98.48 µl MilliQ water and 1 µl assay buffer. After the incubation, 27 µl of each peptide solution were mixed with 3 µl of the Proteostat working solution. 9 µl of each solution were pipetted into a well of a Greiner 384 flat black well plate (3 wells per sample of each peptide concentration). The plate was incubated in the dark for 15 min while shaking. The fluorescence intensity of the Proteostat dye was subsequently measured with an excitation and emission bandwidth of 20 nm and an emission wavelength of 600 nm after excitation at 550 nm.

4.7. AFM

The linear peptide **3** was dissolved in DMSO (1 mM) and diluted with DPBS at a ratio of 1:9 to yield a 100 µM peptide solution. The solution was incubated for 24 the sample was used for imaging.

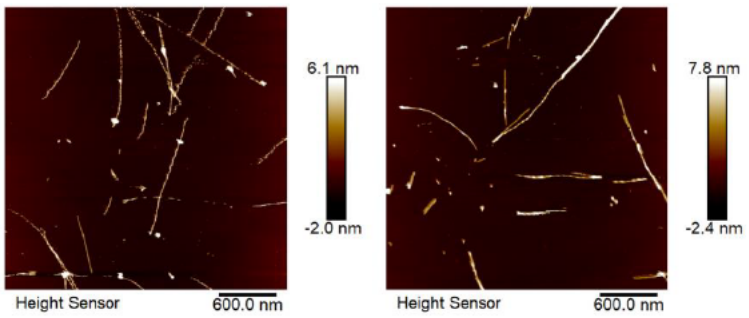

Figure S5.14 AFM images of peptide nanofibers formed by linear peptide 3 (100 µM) in DPBS (pH 7.4) and DMSO (9:1). Scale bar: 600 nm.

6. Summary and Outlook

The design of bioresponsive nanomaterials for intracellular assembly is aimed at exploiting physiological stimuli for the programmed formation of synthetic structures inside living cells. By emulating the supramolecular assemblies observed in nature, it is possible to construct artificial architectures within the intricate and confined intracellular environment, consequently impacting biological processes and cellular behavior. This thesis explored the chemical design, synthesis and characterization of bioresponsive isopeptides and their application for intracellular structure formation in different cell types, with a particular focus on studying the resulting material-cell interactions and their impact on cellular functions.

In Chapter 3, the design and synthesis of glutathione-responsive isopeptides for intracellular structure formation was presented. The glutathione-induced peptide assembly in human cytotoxic T cells was explored, revealing enhanced T cell effector function and increased cytotoxic activity against cancer cells. Unlike the commonly used cancer cell models, cytotoxic T cells were selected to investigate the non-disruptive, functional effects of synthetic intracellular assemblies. This is of significant relevance for modern immunotherapies that demand a deeper understanding of the modulation of T cell activity. The study demonstrated an increase in cancer cell death mediated by cytotoxic T cells after pre-treatment with the assembly-inducing isopeptides. Correlative light and electron microscopy confirmed the presence of synthetic peptide assemblies within the cytosol and

perinuclear region of the T cells. Furthermore, mechanobiological analysis using real-time deformation cytometry revealed increased stiffness and reduced deformability in treated T cells, which are crucial parameters for effective interaction with target cells. These findings, along with the observed upregulation of proteins associated with T cell activation and effector function, suggest that synthetic intracellular nanostructures can enhance the natural cytotoxic effector function. Thus, this work represents significant progress in the modulation of immune cell behavior, with important implications for immunotherapies.

Chapter 4 explored the use of glutathione-responsive isopeptides for intracellular structure formation in drug-resistant MDA-MB-231 breast cancer cells. The reductive glutathione-induced transformation and assembly of the peptides were studied in relation to their impact on cancer cell metabolism, focusing on mitochondrial function. By correlating live-cell imaging, which provided qualitative analysis of mitochondrial integrity, with quantitative measurements of oxygen consumption rates, we examined how intracellular structure formation within the crowded intracellular environment can disrupt mitochondrial respiration, a critical component of cellular metabolism. Additionally, the investigation of biological impact was extended by using a tumor spheroid model, complementing the traditional two-dimensional cell culture methods. This approach allowed for further exploration of the effects of peptide structure formation in more complex, three-dimensional cell networks, which possess distinct biological characteristics such as increased cell-cell interaction and uneven distribution of nutrients and oxygen. In the tumor spheroid models, incubation with the glutathione-responsive isopeptide assembly precursors resulted in a decrease in overall spheroid size, attributed to cell death caused by the uptake of isopeptides and subsequent intracellular structure formation.

Chapter 5 focused on the development of a furin-responsive kinked isopeptide designed for controlled nanostructure formation through enzyme-triggered transformation. The bioresponsive design and the synthesis of the isopeptide were presented, along with a kinetic analysis of its furin-induced multistep conversion into a self-assembling linear peptide. The results demonstrated the effectiveness of furin in cleaving the kinked isopeptide despite its unnatural structure. The fibrillar nanostructures formed by the linearized peptide were characterized regarding their secondary structure and supramolecular properties. This novel isopeptide-based system for furin-induced assembly formation adds to the growing toolbox of nanomaterials designed for bioresponsive structure formation.

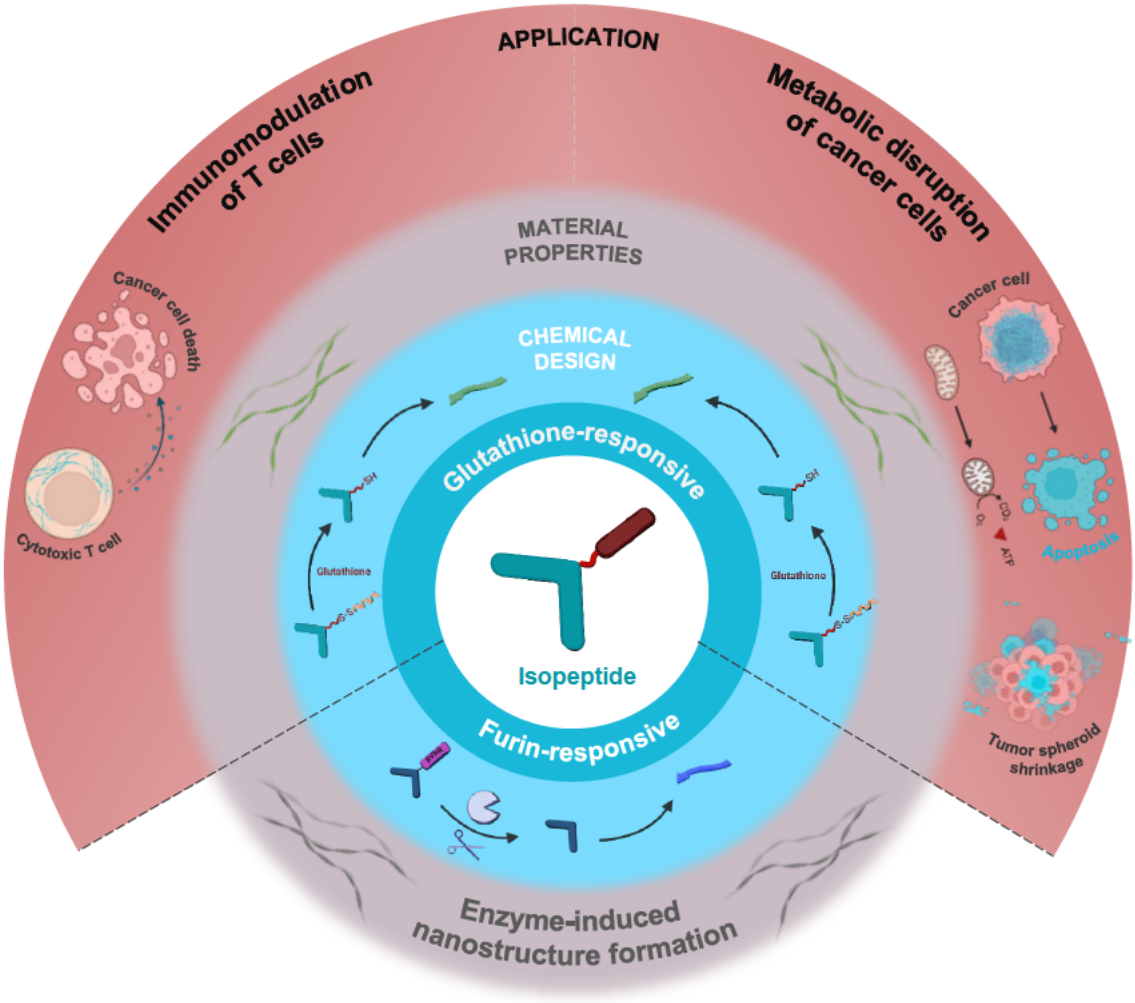

Figure 6.1 Summary of research projects discussed in this thesis.

In summary, this thesis demonstrated the design of bioresponsive nanomaterials for intracellular structure formation and examined how they can modulate cellular functions and behaviors in different cell types.

Several challenges remain in this field that need to be addressed in future research. For instance, the complexity of intracellular environments presents difficulties in predicting and controlling the localization and impact of synthetic materials. Therefore, future research should focus on refining the specificity and responsiveness of these nanomaterials to target cell types or subcellular regions more precisely. One potential approach could involve incorporating several bioresponsive protecting groups into the chemical design of the assembly precursors, thereby making them responsive to multiple stimuli. Consequently, multiple transformations, triggered by cell- or organelle-specific stimuli, would be required to initiate assembly formation, potentially enhancing both cellular and subcellular specificity. Furthermore, integrating additional bioactive components, such as signaling peptides or small molecule drugs, into the molecular design could synergistically increase the impact of the nanomaterial on cellular processes. For instance, while this thesis has already demonstrated that intracellular peptide assembly can boost T cell effector function, combining it with the release of immunostimulatory drugs, such as checkpoint inhibitors that prevent T cell inactivation, could further amplify the desired enhancement of cellular function. Moreover, investigating the role of different assembly morphologies in driving the functional effects on immune cells would provide valuable insights into which aspects of *in situ* supramolecular structure formation are most critical in modulating immune cell activity.

From a synthetic biology perspective, advancing methodologies that emulate natural processes by incorporating non-equilibrium assemblies – potentially coupled with cellular feedback dynamics – would hold great promise for inducing reversible

changes in cellular behavior. Such systems would be particularly valuable for modulating cellular functions instead of disrupting cellular integrity, with potential applications in addressing cell senescence or improving environmental adaptation. Developing synthetic materials that mimic the reversible nature of biological supramolecular assemblies would mark a major advancement in the ability to program material-cell interactions, enabling us to better understand and manipulate the fundamental processes that govern cellular behavior.

Appendix

List of Peer-Reviewed Publications and Preprints

Chagri, S., Ng, D. Y. W. & Weil, T. Designing bioresponsive nanomaterials for intracellular self-assembly. *Nat. Rev. Chem.* **6**, 320-338 (2022).

Giubertoni, G.‡; **Chagri, S.**‡; Argudo, P. G.; Prädel, L.; Maltseva, D.; Greco, A.; Caporaletti, F.; Pavan, A.; Ilie, I. M.; Ren, Y.; Ng, D. Y. W.; Bonn, M.; Weil, T.; Woutersen, S. Structural adaptability and surface activity of peptides derived from tardigrade proteins. *Protein Sci.* **33**, e5135 (2024). (‡ These authors contributed equally to this work.)

Chagri, S.; Burgstaller, A.; Schirra, C.; Link, J.; Zhou, Z.; Roth, P.; Meyer, R.; Fetzer, J.; Ren, Y.; Si, S.; Mazzotta, F.; Wagner, M.; Lieberwirth, I.; Landfester, K.; Ng, D. Y. W.; Staufer, O.; Weil, T. Synthetic intracellular nanostructures enhance cytotoxic T cell function via assembly-driven chemical engineering. *ChemRxiv*, doi:10.26434/chemrxiv-2024-3lxgk (2024).

Chagri, S.‡; Maxeiner, K.‡; Förch, L.; Link, J.; Roth, P.; Meyer, R.; Fetzer, J.; Kaltbeitzel, A.; Lieberwirth, I.; Landfester, K.; Wagner, M.; Ng, D. Y. W.; Weil, T. Intracellular Formation of Synthetic Peptide Nanostructures Causes Mitochondrial Disruption and Cell Death in Tumor Spheroids. *ChemRxiv*, doi:10.26434/chemrxiv-2024-xkxpb (2024). (‡ These authors contributed equally to this work.)

[redacted]

[redacted]

[redacted]

[redacted]

[redacted]

[redacted]

[redacted]

[redacted]

[redacted]

[redacted]

[redacted]